

The
Vortex-Induced Vibrations
of
Tethered Bodies

by

Hyeok Lee

A Thesis submitted to Monash University
for the degree of
Doctor of Philosophy

April 2009

Department of Mechanical and Aerospace Engineering
Monash University

To my wife Suk Hyun

Statement of Originality

I, Hyeok Lee, declare that this thesis is my own work and contains no material that has been accepted for the award of a degree or diploma in this or any other university. To the best of my knowledge and belief, this thesis contains no material previously published or written by another person except where due reference is made in the text of this thesis.

Hyeok Lee

April, 2009

First of all one must observe that each pendulum has its own time of vibration, so definite and determinate that it is not possible to make it move with any other period than that which nature has given it. On the other hand one can confer motion upon even a heavy pendulum which is at rest simply by blowing against it. By repeating these blasts with a frequency which is the same as that of the pendulum one can impart considerable motion.

Galileo Galilei, *Discorsi a Due*
Nuove Scienze, 1638

Abstract

The current study consists of two main parts. The first part explores the response of neutrally buoyant tethered bluff bodies undergoing vortex-induced vibrations (VIV) using both well-resolved numerical simulations and a restricted series of experiments. The second part numerically investigates the effect of an elastic tether on the vortex-induced vibration of buoyant tethered bluff bodies. The bodies chosen for this study are a circular cylinder and a sphere.

Neutrally buoyant bodies were the focus for the first part of this study because they represent a special case connecting previous research on vortex-induced vibration research on bodies at higher and lower mass ratios, and because previous restricted experimental studies had indicated that the neutrally buoyant sphere underwent fundamentally different behaviour.

It is found through numerical experiments that a neutrally buoyant tethered cylinder exhibits three response regimes (Regime I to III) as the Reynolds number (Re) is increased from 10 to 300. Relative to the response of non-neutrally buoyant cylinders, a neutrally buoyant cylinder shows a rapid transition to non-periodic motion as the Reynolds number is increased.

For a neutrally buoyant sphere, through a combination of numerical simulations and experiments it is found that there exist seven different response regimes (Regime I to VII) within the range of $Re = 50 - 8000$. These regimes were determined based on changes in the time-mean position of the body, its amplitude and the frequency of oscillation. Importantly, the present study identifies that the vortex-induced vibration behaviour of a neutrally buoyant tethered sphere is closer to that of a non-buoyant sphere tethered in a vertical flow than that of a buoyant sphere tethered in a horizontal flow, in that both evolve towards quasi-circular motion as the Reynolds number is increased. Simulations for a buoyant sphere covering a range of the conventional reduced velocity (U^*), while keeping Re constant, reveal that Re has an effect on the maximum oscillation amplitude and response branches of vortex-induced vibration of a tethered sphere. The response is quantified for the restricted parameter space investigated.

In the second part of the present study, the effect of making the tether elastic was studied by introducing a spring parameter k_t , both for the cylinder and the sphere. The results show that the elasticity of the tether greatly affects the behaviour of both bluff bodies, and that there is a critical value of k_t above which the response is significantly

different to that of inelastically tethered bodies. When k_t exceeds its critical value, the oscillation amplitude is greatest at low U^* , whereas the amplitude is greatest at high U^* for the inelastically tethered case.

Acknowledgements

I would like to firstly thank my two supervisors, Prof. Mark Thompson, Prof. Kerry Hourigan for their guidance and direction throughout my candidature. Both Mark and Kerry warmly welcome me to Monash, and have provided continual support not only through academic stimulation but also through their caring attitude. It is really unforgettable.

Mention must be made also of the contribution of other staff of FLAIR. Prof. John Sheridan allowed me to use the water channel for the sphere experiments. My thanks go to Dr. David Lo Jacono for his great help throughout the sphere experiments and introducing me Debian. Dr. Greg Sheard and Dr. Kris Ryan have organised in-group seminars and given me opportunities to make my communication skill better.

Financial support for this research has been gratefully received through a Monash International Postgraduate Scholarship, and a Monash Graduate Scholarship from the Monash Research Graduate School. Other resources have been provided by the Department of Mechanical and Aerospace Engineering at Monash, the Australian Partnership for Advanced Computing, who have provided computing time on their high performance machines, and from the Department Workshop, who have prepared the spheres for the experiments necessary to complete this work.

During my candidature there have been several people who have always made themselves available to discuss ideas and share thoughts on various topics. For their personal and professional assistance during this time I would like to acknowledge, in no particular order, Dr. Justin Leontini, Dr. Bronwyn Stewart, Dr. Martin Griffith, Dr. Karlis Atvars, Dr. Jon Dusting, Miss Naomi Brammer, Mr. Joe Berry, Mr. Owen Gould, Mr. Patryk Burka, Mr. Mehdi Nazarinia and Ms. Elham Tolouei.

A special thank you must also be given Drs. Justin Leontini and Bronwyn Stewart for proof-reading parts of the thesis manuscript, and Mr. Mehdi Nazarinia and Ms. Elham Tolouei for the couple's care on my family.

I would like to thank my parents, Eun Ja and Han Young Lee, and my brother, Wook Lee for the love and support that they have offered throughout this time. To my wife Suk Hyun and two sons, Won and Yoon, you have encouraged and given me enormous energy during the last few years of my study in Melbourne. Thank you.

Finally, I would like to thank God for guiding and holding me throughout my life. He truly raised me up to more than I can be.

List publications relating to this thesis

LEE, HYEOK, THOMPSON, M.C. & HOURIGAN, K. 2007 Vortex-induced vibrations of a neutrally buoyant tethered sphere. *In proceedings of the 16th Australasian Fluid Mechanics Conference (16AFMC)*, Gold Coast, Australia, December 2007.

LEE, HYEOK, THOMPSON, M.C. & HOURIGAN, K. 2008 Flow-induced vibrations of a non-buoyant sphere. *In proceedings of the 9th International Conference on Flow-Induced Vibration (FIV 2008)*, Prague, Czech Republic, July 2008.

LEE, HYEOK, THOMPSON, M.C. & HOURIGAN, K. 2008 Vortex-induced vibrations of a tethered sphere with neutral buoyancy. *In proceedings of the XXII International Congress of Theoretical and Applied Mechanics (ICTAM 2008)*, Adelaide, Australia, August 2008.

LEE, HYEOK, THOMPSON, M.C. & HOURIGAN, K. 2008 Flow around a tethered neutrally-buoyant sphere. *In proceedings of the XXII International Congress of Theoretical and Applied Mechanics (ICTAM 2008)*, Adelaide, Australia, August 2008.

LEE, HYEOK, THOMPSON, M.C. & HOURIGAN, K. 2009 Vortex-induced vibrations of a neutrally buoyant tethered sphere. *J. Fluid Mech.* **In Preparation.**

LEE, HYEOK, THOMPSON, M.C. & HOURIGAN, K. 2009 Vortex-induced vibrations of a cylinder attached to elastic tethers. *J. Fluid Mech.* **In Preparation.**

LEE, HYEOK, THOMPSON, M.C. & HOURIGAN, K. 2009 Flow-induced vibrations of a non-buoyant tethered cylinder. *Phys. Fluids* **In Preparation.**

Nomenclature

Symbol	Description
§	Thesis section
DES	Detached eddy simulation
DNS	Direct numerical simulation
DOF	Degree-of-freedom
GLL	Gauss-Lobatto-Legendre
LES	Large eddy simulation
MWR	Method of weighted residuals
RMS	Root-mean-square
VIV	Vortex-induced vibration
∇	Vector gradient operator
\mathcal{F}	Fourier transform
\mathcal{F}_m	Fourier transform in the in the cylindrical coordinate ϕ
α	Alpha parameter, $\frac{\pi gD}{2U^2}$ (Cylinder) or $\frac{4gD}{3U^2}$ (Sphere) Angle of attack
β	Beta parameter, $1/m^*$
γ	Gamma parameter, $\frac{2U^2}{\pi D}$ (Cylinder) or $\frac{3U^2}{4D}$ (Sphere)
ε	Under-relaxation parameter in the predictor-corrector scheme
ρ	Density of a fluid

Continued on the next page.

Continued from previous page.

Symbol	Description
	Weights of GLL quadrature
ρ_f	Density of a fluid
ρ_b	Density of a body
λ	Constant in the Helmholtz equations
μ	Absolute or dynamic viscosity of a fluid
ν	Kinematic viscosity of a fluid, $\nu = \mu/\rho$
ω	Angular frequency, $2\pi f$
Ω	Computational domain
ϕ	Inclination (azimuthal) angle measured from y axis in yz plane
Φ	Test function of MWR
Ψ	Weighting function of MWR
φ	Phase difference or Phase angle
ϑ	Layover angle or Angle measured from y axis
θ	Tether angle or Angle measured from x axis
ξ	GLL quadrature points
A	Amplitude of oscillation
	Frontal area of a body
A^*	Nondimensionalised amplitude of oscillation
$\mathbf{A}(\mathbf{x}_B, \mathbf{u}, p)$	Acceleration term in the coupled Navier-Stokes equations
B	Buoyancy
C1	Cylinder mesh 1
C2	Cylinder mesh 2
C3	Cylinder mesh 3
C4	Cylinder mesh 4
C_D	Drag coefficient
C_{PB}	Base pressure coefficient, pressure at the immediate rear of the body normalised by $\frac{1}{2}\rho U^2$
C_T	Force coefficient in the tangential direction to the tether

Continued on the next page.

Continued from previous page.

Symbol	Description
C_x	Force coefficient in x direction or Drag coefficient
C_y	Force coefficient in y direction or Lift coefficient
C_z	Force coefficient in z direction
D	Diameter of a circular cylinder or a sphere
D_{circle}	Diameter of the quasi-circular area of the oscillating sphere in the yz plane
f	Body oscillation frequency
f_{Drag}	Oscillation frequency of drag
f_n	Natural frequency of the system in vacuum
f_{vo}	Vortex shedding frequency of a fixed body
f_v	Vortex shedding frequency of a moving body
f_{ex}	Body excitation frequency
f^*	Nondimensionalised frequency of oscillation, f/f_n
f_n^*	Nondimensionalised natural frequency, $f_n D/U$
F_{total}	Total force, $F_P + F_V$
F_P	Pressure component of force
F_V	Viscous component of force
F_x	Force in x direction or Drag
F_y	Force in y direction or Lift
F_z	Force in z direction
Fr	Froude number, U/\sqrt{gD}
Fr'	Reduced Froude number, $U/\sqrt{g(1-m^*)D}$
F_{tol}	Tolerance of force convergence
g	Acceleration of gravity
	Function to be solved in the Helmholtz equations
i	Imaginary part of complex numbers
	Specific macro element in Spectral-element methods
J	Jacobian of the coordinate transformation
k	Spring constant for linear spring (restoring) force for the tether
k_t	Elasticity parameter, $\frac{2\pi U}{D} \sqrt{\frac{m_b}{k}}$

Continued on the next page.

Continued from previous page.

Symbol	Description
L	Tether length
L_0	Initial tether length
L^*	Nondimensionalised tether length, L/D
L_N	Legendre polynomial of order N
$\mathbf{L}(\mathbf{V})$	Linear operator in the Navier-Stokes equations, $\nabla^2 \mathbf{V}$
m	Body mass
	Wave number in Spectral-element methods
m_b	Body mass
m_f	Displaced fluid mass
m_a	Added mass of an accelerating body in a fluid
m^*	Mass ratio, ρ_b/ρ
$\mathbf{N}(\mathbf{V})$	Nonlinear operator in the Navier-Stokes equations, $(\mathbf{V} \cdot \nabla) \mathbf{V}$
N	Number of GLL points
Ma	Mach number, ratio of speed of sound to speed of fluid flow
p	Kinematic pressure, P/ρ_f
	Order of GLL interpolants
P	Pressure
r	Cylindrical or spherical coordinate in the radial direction
R	Radial offset distance for a tethered sphere
Re	Reynolds number, UD/ν
Re_{S1}	Reynolds number of the first transition
Re_{S2}	Reynolds number of the second transition
Re_{S3}	Reynolds number of the third transition
S1	Sphere mesh 1
S2	Sphere mesh 2
S3	Sphere mesh 3
St	Strouhal number, fD/U
t	Time
T	Tether tension

Continued on the next page.

Continued from previous page.

Symbol	Description
	Oscillation period
U	Velocity of a fluid
u	x component of velocity in a non-inertial coordinate
u'	x component of velocity in an inertial coordinate
\mathbf{u}	Fluid velocity in a non-inertial coordinate
\mathbf{u}_B	Velocity of the oscillating body
u_m	Velocity or pressure Fourier mode in the Helmholtz equations
u_{tol}	Tolerance of velocity convergence
U_∞	Fluid velocity at far-field
U^*	Reduced velocity, $U (f_n D)$
v	y component of velocity in a non-inertial coordinate
v'	y component of velocity in an inertial coordinate
\mathcal{V}	Volume of a body
\mathbf{V}	Fluid velocity in an inertial coordinate, $\mathbf{u} + \mathbf{u}_B$
U_∞	Fluid velocity at far-field
w	z component of velocity in a non-inertial coordinate
w'	z component of velocity in an inertial coordinate
W	Weight of a body
x	Non-inertial Cartesian coordinate in the streamwise direction
x'	Inertial Cartesian coordinate in the streamwise direction
\mathbf{x}_B	Position vector of the oscillating body
y	Non-inertial Cartesian coordinate in the direction transverse to the flow
y'	Inertial Cartesian coordinate in the direction transverse to the flow
z	Non-inertial Cartesian coordinate in the direction lateral to the flow
z'	Inertial Cartesian coordinate in the direction lateral to the flow

Contents

1	Introduction	1
2	Literature Review	5
2.1	Flow past a Stationary Circular Cylinder	5
2.1.1	Two-dimensional steady flows	5
2.1.2	Two-dimensional unsteady flows	7
2.1.3	Three-dimensional unsteady flows	9
2.1.4	High Reynolds number flows	11
2.2	Flow past a Stationary Sphere	12
2.2.1	Steady axisymmetric flow	12
2.2.2	Steady asymmetric flow	15
2.2.3	Unsteady flow	18
2.2.4	High Reynolds number flow	20
2.3	Dynamics of Bubbles	22
2.4	VIV of Elastically Mounted Circular Cylinders	25
2.4.1	Cylinder oscillating in transverse direction	26
2.4.2	Cylinder oscillating in streamwise direction	28
2.4.3	Cylinder oscillating in transverse and streamwise direction	29
2.5	VIV of a Tethered Circular Cylinder	30
2.6	VIV of a Tethered Sphere	33
2.6.1	Tethered spheres in oscillatory flow	33
2.6.2	Tethered spheres in uniform flow	33
2.7	Chapter Summary and Points of the Present Study	38
3	Methodology and Validation	41
3.1	Problem Formulation: Tethered Circular Cylinder	41
3.2	Problem Formulation: Tethered Sphere	43
3.3	Coordinate Transformation to a Tethered Body	45
3.4	Numerical Method	46
3.4.1	Time-advancement of governing equations	47
3.4.2	Spatial discretisation: Spectral-element/Fourier-spectral method	50
3.4.3	Boundary Conditions and Convergence	53

3.5	Definition of Controlling Parameters	54
3.6	Validation: Tethered Cylinder Case	55
3.6.1	Mesh Independence	56
3.6.2	Grid Resolution Study	58
3.7	Validation: Tethered Sphere Case	60
3.7.1	Mesh Independence	60
3.7.2	Grid Resolution Study	63
3.8	Experimental Method: Tethered Sphere Case	64
3.9	Chapter Summary	66
4	VIV of a Tethered Circular Cylinder	67
4.1	Introduction	67
4.2	VIV of a Neutrally Buoyant Cylinder: $m^* = 1$	67
4.2.1	Time-mean position: Layover angle ϑ	68
4.2.2	Amplitude of oscillation	69
4.2.3	Frequency of oscillation	70
4.2.4	Trajectory and forcing of the oscillating cylinder	71
4.2.5	Vortex structure around the oscillating cylinder	74
4.2.6	History and phase of the displacements and forces	76
4.2.7	Power spectrum of the displacements and forces	80
4.3	VIV of Non-Neutrally Buoyant Cylinders: $m^* \neq 1$	82
4.3.1	Layover angle	83
4.3.2	Amplitude of oscillation	84
4.3.3	Frequency of oscillation	86
4.3.4	Trajectory and forcing of the oscillating cylinder	87
4.3.5	History and phase of displacements and forces	89
4.3.6	Comparison to VIV of the neutrally buoyant tethered cylinder	94
4.4	VIV of a Vertically Tethered Cylinder	97
4.4.1	Response of the cylinder	98
4.4.2	Comparison to VIV of the neutrally buoyant tethered cylinder	101
4.5	Chapter Conclusions	103
5	VIV of a Tethered Sphere	105
5.1	Introduction	105
5.2	VIV of a Neutrally Buoyant Sphere: $m^* = 1$	105
5.2.1	Time-mean position: Layover angle ϑ	106
5.2.2	Amplitude of oscillation	107
5.2.3	Frequency of oscillation	108
5.2.4	Trajectory of the oscillating sphere	110
5.2.5	Vortex structure around the sphere	115

5.2.6	Phase between forces and displacements	120
5.3	VIV of a Buoyant Tethered Sphere: $m^* < 1$	125
5.3.1	Response of oscillation	125
5.4	Effect of the Reynolds number on the response	127
5.5	VIV of a Vertically Tethered Sphere	130
5.5.1	Response of oscillation	131
5.5.2	Comparison to VIV of the neutrally buoyant tethered sphere . .	136
5.6	Chapter Conclusions	141
6	Effect of Tether Elasticity on VIV of a Tethered Bluff Body	145
6.1	Introduction	145
6.2	VIV of an Elastically Tethered Cylinder	146
6.2.1	Response of the tethered cylinder	147
6.2.2	Trajectory, forcing and phase of the oscillating cylinder	150
6.2.3	Vortex structure around the oscillating cylinder	154
6.3	VIV of an Elastically Tethered Sphere	156
6.3.1	Response of the tethered sphere	157
6.3.2	Trajectory, forcing and phase of the oscillating sphere	160
6.3.3	Vortex structure around the oscillating sphere	164
6.4	Chapter Conclusions	166
7	Conclusions and Future Work	169

Chapter 1

Introduction

It is well known that a body in a fluid flow can extract energy from the fluid stream and sustain oscillations of the body itself. These oscillations occur as a result of changes in the low pressure zone of the fluid at the rear of the body. The shedding of vortices formed in the wake at high enough flow speed provide an oscillating lift and drag that lead to vibration of the body, which is known as vortex-induced vibration (VIV).

If the shedding of vortices from the body is of a frequency that is close or equal to the natural frequency of the body, a resonance condition occurs. Especially for bluff bodies, this results in large scale oscillations of the structure, and can result in catastrophic failure. Thus, to overcome these problems, there has been much research activity in the field of vortex-induced vibration and its controlling mechanisms over the last few decades, particularly in relation to applications for marine structures and underwater pipelines, as well as for buildings and bridges. A large number of fundamental studies of VIV are discussed in the comprehensive reviews of Sarpkaya (1979), Griffin & Ramberg (1982), and Williamson & Govardhan (2004).

Due to intrinsic instability in the wake of bluff bodies, the vortices begin to periodically shed from alternate sides of the body. As vortices represent a region of low pressure with respect to the surrounding fluid, this periodic vortex shedding generates a force on the bluff body, with a periodically fluctuating component that is predominantly transverse to the free stream direction. This transverse vortex force, together with any other transverse forces, are often referred to as the lift force experienced by the bluff body. In this sense, knowledge of the instantaneous fluid forces, i.e. drag and lift, is crucial in understanding vortex-induced vibration phenomena, and much research has been devoted to deducing the unsteady fluid forces on oscillating bluff bodies.

Most studies of VIV have focused on a transversely vibrating cylinder. Only a

few studies have examined other types of VIV and body shapes: such as VIV of a cylinder with 2 degree-of-freedom (DOF), and VIV of a tethered cylinder and a tethered sphere. Previous studies on the transversely vibrating cylinder have shown that there are several physical parameters affecting the amplitude and frequency of the vibration. Two important parameters are the flow speed and relative body mass to fluid. At low flow speeds, the wake of a bluff body is steady. Beyond a critical flow speed, the wake becomes unsteady and vortex shedding commences, resulting in body vibration and the possibility of a resonance, which is the main concern of VIV. The relative body mass (so called mass ratio) is related to the range of resonance. It has been identified that the smaller the mass ratio is, the larger the resonance region becomes. Moreover, the number of response branches within the resonance is dependent on the mass ratio. A body that is heavier than fluid exhibits two responsive branches, whereas a light body shows three branches including a higher amplitude branch.

Two other parameters used in previous studies are the structural damping of the body in fluid and the Reynolds number. The damping affects the maximum amplitude of VIV; the lower the damping, the larger the amplitude. However, researchers do not agree whether the damping combined with the mass ratio (so called mass-damping ratio) is a suitable parameter to determine the maximum amplitude of VIV. In spite of this, this parameter has been adopted in some marine engineering studies to determine the maximum amplitude. The effect of Reynolds number on the amplitude is not clear due to the technical difficulty, especially in experiments, in isolating its effect from the effects of several other parameters. However, a few studies have shown that the Reynolds number does have an effect on the maximum amplitude, and also on the number of response branches at a given mass ratio. Most VIV studies have focused on the effect of these parameters on VIV of a transversely vibrating cylinder. However, the influence of body geometry and method of constraint means that the results for a transversely vibrating cylinder is not necessarily extendible to the VIV of other cases.

The present study investigates the VIV of neutrally buoyant tethered bodies as a different type of VIV by varying the mass ratio and the Reynolds number. Although it is common to see this type of body constraint (i.e., tether) in marine applications, not many aspects of the motion of a tethered body is understood. Neutrally buoyant bodies are chosen firstly due to the recent studies of vertically tethered sphere, which indicated that this body may develop a different type of motion in a fluid flow. Secondly, it may

represent a special case due to the disappearance of the gravity effect on their motion. By analysing the responses at various Reynolds number, we first hope to determine whether the VIV of neutrally buoyant bodies can be explained with the knowledge having compiled so far, or need to uncover new aspects of this type of VIV, if any. To focus on the fundamental mechanisms of the VIV of neutrally buoyant bodies and to relate them to the results of previous studies, two generic bluff bodies are chosen for the research: a circular cylinder and a sphere.

The other aim of the current dissertation is to study the effect of tether elasticity on the VIV of a tethered cylinder and sphere. This is inspired by some previous experimental studies on the VIV of a cylinder freely oscillating in both the streamwise and transverse directions, which reported a new responsive branch characterised by a very large amplitude. Moreover, there has been no study (to the author's knowledge) on the VIV of elastically tethered bodies which might be the case closer to some realistic engineering applications. It is anticipated that the introduction of elasticity to the tether, which introduces one more DOF to the motion, will have a considerable effect on the body response, as occurred in the case of cylinder VIV with 2 DOFs. The body dynamics and flow structures of the inelastically tethered body and elastically tethered one will be compared. An additional parameter representing tether elasticity is suggested and used to interpret the results.

The thesis consists of 6 chapters in addition to the Introduction. In chapter 2, a critical review of studies of the flow past a fixed bluff body and of VIV of an oscillating body is presented. Chapter 3 provides details of the numerical method, its validation, and the experimental method adopted in the study. Three results chapters, comprising the main part of the thesis, follow. Chapter 4 deals with the VIV of a neutrally buoyant tethered cylinder. Chapter 5 presents detailed results for a neutrally buoyant sphere and discusses the effects of mass ratio and the Reynolds number on its VIV. In chapter 6, a parameter for the tether elasticity is introduced and its effect on the dynamics of the tethered cylinder and sphere is discussed. Finally, the conclusions and recommended future work are presented in chapter 7.

Chapter 2

Literature Review

As the flow structures and the vortex shedding patterns of bluff bodies are closely related to vortex-induced vibration (VIV), the literature on the flow past bluff bodies at rest is reviewed here first. The generic bluff bodies of a circular cylinder and a sphere are chosen as they have been extensively studied owing to their geometric simplicity and broad application in engineering. Studies on the motion of bubbles in a fluid flow will be reviewed due to the possible link to the motion of a sphere, followed by a review of vortex-induced vibration of cylinders and spheres.

2.1 Flow past a Stationary Circular Cylinder

Flow structures shed from fixed two-dimensional bluff bodies and wake transitions have been of interest to researchers for many decades. The geometrical simplicity of a circular cylinder led to a highly studied two-dimensional body which depends on a simple parameter, its diameter D . When a cylinder is immersed in an incompressible Newtonian fluid, the Reynolds number, $Re = UD/\nu$, is the sole governing parameter on which the flow regimes are dependent. Here, U is the flow velocity, D is the cylinder diameter, and ν is the kinematic viscosity of the fluid. The Reynolds number is the ratio of inertial to viscous forces. As Re is increased from zero towards infinity, the flow undergoes a series of transitions from steady two-dimensional flow, through unsteady and three-dimensional flow, to fully turbulent flow. A comprehensive review of the work on the circular cylinder is provided by Williamson (1996a).

2.1.1 Two-dimensional steady flows

For very low Reynolds numbers (where $Re < 1$), viscous forces dominate the flow. The flow does not separate from the surface of the cylinder, but remains completely attached,

and the flow streamlines appear identical upstream and downstream of the cylinder. This flow is sometimes called *creeping flow*. An example of such a flow is shown in figure 2.1(a). This symmetrical pattern is also observed in analytical solutions of the flow past a cylinder with potential flow theory. While the flow pattern of potential flow looks very similar to that obtained with creeping flow, the solution leads to the conclusion that the cylinder should experience no drag force, a conclusion known as d’Alambert’s paradox (Roshko 1993). This zero drag conclusion is wrong, as the drag coefficient, C_D , is at its highest when Re goes to zero. This problem was overcome by Stokes, whose equations considered viscous effects. Stokes’ treatment of the flow around a sphere analytically obtained the forces on a pendulum ball in creeping flow (Stokes 1851). For this reason, such creeping flow is often referred to as Stokes flow. Stokes flows, being governed by a set of linear equations, have the property of being reversible, so that if the flow and external forces are reversed, the flow returns exactly to its original state.

Stokes flow around a circular cylinder persists only at very small values of Re , until the first of a series of transitions occurs. This is the transition to separated flow, when a recirculation region forms at the rear of the cylinder. An example of this steady, separated flow is shown in figure 2.1(b). This separation occurs at $Re = 5$ (Taneda 1956; Noack & Eckelmann 1994). The flow is no longer reversible, and convection effects cannot be ignored. With increasing Re , the length of this recirculation region increases (Taneda 1956; Roshko 1993). This trend continues until $Re = 46$ (Taneda 1956; Roshko 1993; Dušek *et al.* 1994; Williamson 1996*b*; Thompson & Le Gal 2004). At this limit, the flow undergoes its second major transition to an unsteady, time-periodic flow. This type of transition, from a steady flow to a time-periodic flow, is known as

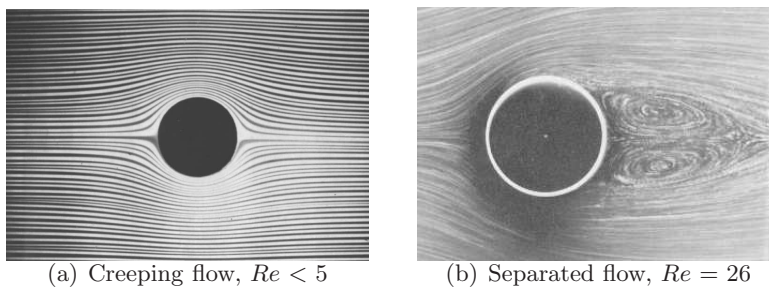


FIGURE 2.1: Flow regimes around a fixed circular cylinder where the flow is steady and two-dimensional. Images taken from Van Dyke (1982).

a Hopf bifurcation (Hopf 1942). Analysis shows that this transition obeys very closely the Stuart-Landau model (Stuart 1958, 1960), and that this transition is supercritical, having no hysteresis (Provansal *et al.* 1987).

2.1.2 Two-dimensional unsteady flows

The transition from a steady flow to a time-periodic one is probably the most important transition in cylinder wakes with respect to vortex-induced vibration because of the inception of laminar vortex shedding. The vortices are shed in turn from alternate sides of the cylinder. This periodic shedding causes a periodic force on the cylinder, the transverse component of which is responsible for exciting crossflow oscillation of elastically-mounted cylinders. The shed vortices organise themselves into a two-row configuration, known as the Kármán or Bénard-von Kármán vortex street, so called because of the early observation of this street by Benard (1908) and the observation and analysis of the configuration by von Kármán (1911). A classic example of the Kármán vortex street is shown in figure 2.2.

The frequency of the vortex shedding, where the flow remains laminar and two-dimensional, is a function of the Reynolds number. Further, this frequency can be expressed as a non-dimensional quantity known as the Strouhal number $St = f_{vo}D/U$, where f_{vo} is the frequency of vortex shedding, D is the cylinder diameter, and U is the freestream velocity. This dimensionless group was first suggested by Rayleigh (1879), to collapse the data presented by Strouhal (1878) in a study of Aeolian tones from cylindrical strings.

Roshko (1954) proposed a functional fit of St versus Re for $Re < 1000$. However, there was considerable spread in the data, especially for Re in the range of



FIGURE 2.2: The Bénard-von Kármán vortex street behind a circular cylinder at $Re = 65$ (taken from Provansal *et al.* (2004)).

$90 < Re < 350$, and it was suggested by Tritton (1970) that there was a “low-speed” mode of shedding for $Re < 105$, and a “high-speed” mode for $Re > 80$. This suggestion was because of an apparent discontinuity in the $St-Re$ curve at $Re \approx 100$. This discrepancy was effectively resolved by the discovery of oblique shedding modes by Williamson (1989), where vortices are shed with their axes not parallel to the axis of the cylinder. Williamson (1989, 1992) showed that if the Strouhal number was corrected according to the angle of the oblique shedding, the Strouhal number data collapsed to a single curve.

This work on oblique shedding modes showed that careful manipulation of the flow at the ends of the cylinder (such as with end plates or base suction) could induce parallel shedding. Effectively, this was through decreasing the local stability in the near wake at the ends of the cylinder (Monkewitz 1996). With the ability to induce parallel vortex shedding, and methods to correct the Strouhal number for oblique shedding effects, a new curve fit was suggested by Williamson & Brown (1998) based upon a series in $1/\sqrt{Re}$ extending up to at least $Re = 1000$. Very close fits could be obtained to the data, except over the range $190 < Re < 260$, which was attributable to the introduction of the three-dimensional mode A into the wake dynamics, described in section 2.1.3.

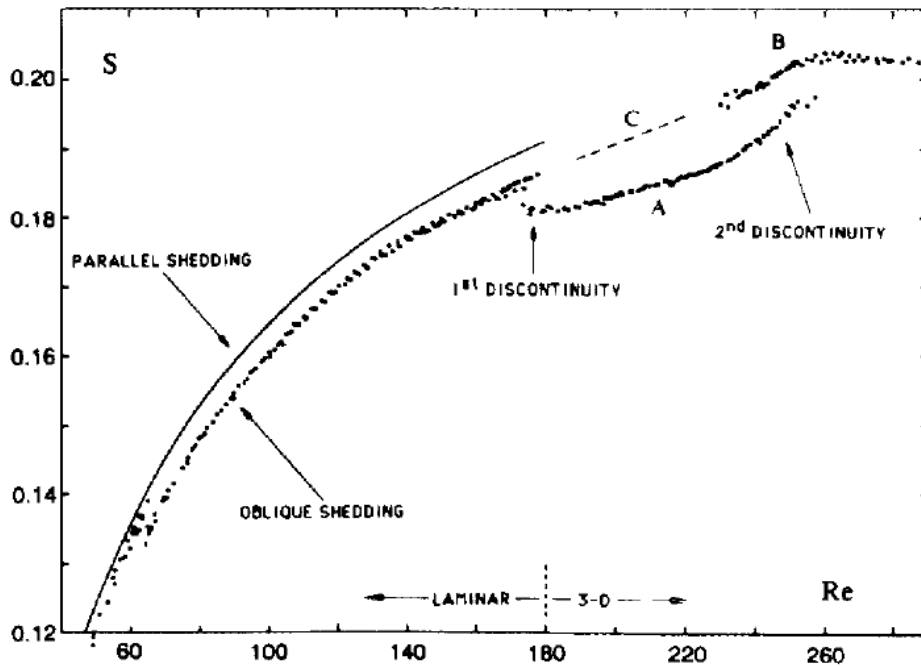


FIGURE 2.3: $St-Re$ curve, taken from Williamson (1988b).

This discontinuity has long been documented, but has only relatively recently been attributed to the transition to three-dimensionality (Williamson & Roshko 1988). The transition marks the start of the path to turbulence in the wake. An example of such a $St-Re$ plot is shown in figure 2.3.

Vortex shedding is also very robust. While the shed vortices, and the shear and boundary layers, eventually become turbulent with increasing Re , evidence of vortex shedding persists up to values of at least $Re = 10^7$. This, of course, has ramifications for vortex-induced vibration, and reinforces continuing importance of the initial transition to unsteady flow in the cylinder wake.

2.1.3 Three-dimensional unsteady flows

Experiments have shown that the parallel periodic vortex shedding street becomes unstable to three-dimensional instabilities for $Re > 178$ (Williamson 1988*a*, 1996*a*). This transition, known as mode A, was studied using linear Floquet stability analysis (Barkley & Henderson 1996), and it was found that at $Re = 188.5$, the cylinder wake becomes unstable to three-dimensional perturbations with a spanwise wavelength of $3.96D$, where D is the cylinder diameter (see figure 2.4(a)).

A second instability on the two-dimensional base flow was found at $Re = 259$, with a spanwise wavelength of $0.822D$ (see figure 2.4(b)). These instabilities and their respective spanwise wavelengths agree well with experimental observations of the saturated wake structures of the mode A and B instabilities made by Williamson (1988*b*). Three-dimensional simulations by Thompson *et al.* (1995, 1996), amongst others captured detailed images of the saturated three-dimensional streamwise vortical structures corresponding to these two different bifurcations. Henderson (1997) numerically studied the wake of the circular cylinder by three-dimensional simulations through the mode A and mode B instabilities. The span of the simulations was varied up to 4 times the spanwise wavelength of the mode A instability. The interaction between the mode A and mode B instabilities was studied by monitoring the energy present in the various spanwise Fourier modes of the simulations. The coexistence of both mode A and mode B wake structures at $Re = 265$ was shown by the wake visualisations. This spontaneous switching between one mode and the other may explain the presence of two distinct Strouhal frequencies in the wake in the range of $Re = 230-260$, as shown in Williamson (1988*b*).

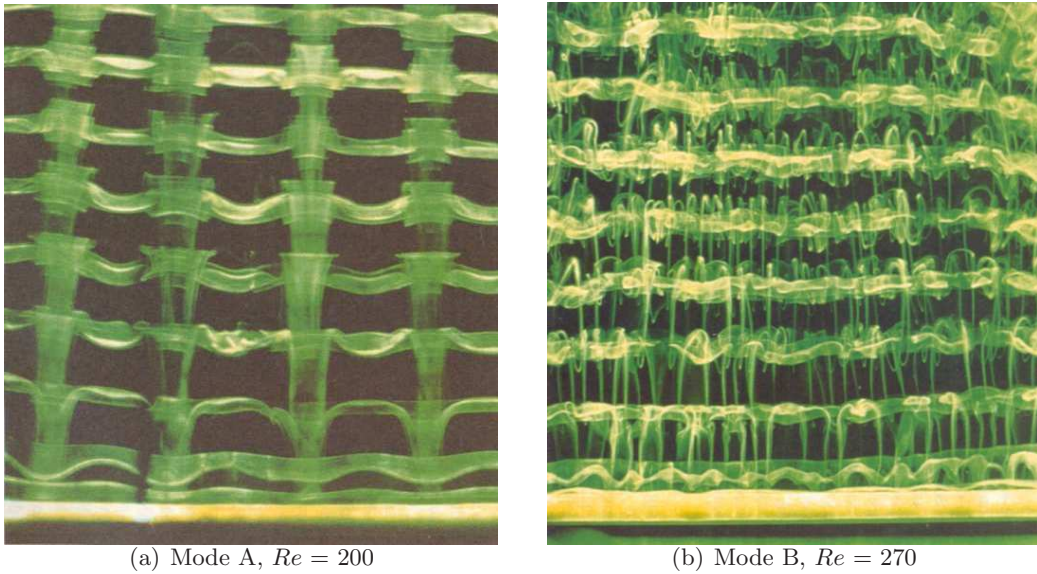


FIGURE 2.4: Wake modes of the flow around a fixed circular cylinder where the flow is unsteady and three-dimensional, taken from Williamson (1996a).

Following the discovery of modes A and B, and their involvement on the path to turbulence, it seems natural to investigate what other types of modes are possible. As well as modes A and B, other modes have been shown to be theoretically possible. Marques *et al.* (2004) and Blackburn *et al.* (2005) showed that for flows possessing the symmetries of the Kármán wake, only three generic bifurcations can arise from the two-dimensional base flow: the first breaks only the spanwise translational symmetry, and corresponds to mode A; the second breaks the “space” part of the spatio-temporal symmetry in the original plane of the flow, and corresponds to mode B; and the third, and last, breaks the “time” part of the spatio-temporal symmetry, and is represented by a quasi-periodic mode (mode QP), or a mode that has a different period to the two-dimensional base flow.

Such a quasi-periodic mode can be found numerically in the fixed cylinder wake (Blackburn & Lopez 2003). It is predicted to occur around $Re = 377$, and so is not observed in experiments, as the base flow is far from two-dimensional by this stage. However, experiments by Zhang *et al.* (1995) with an upstream tripping wire excited a mode with a similar wavelength to this quasi-periodic mode, in the Reynolds number range $170 \leq Re \leq 270$. The experiments of Zhang *et al.* (1995) and the restricted-domain simulations of Karniadakis & Triantafyllou (1992) demonstrated that relatively passive

measures could be used to act on the inception order of the three-dimensional modes, even if there is only a small number of possible transition types involved (Marques *et al.* 2004; Blackburn *et al.* 2005). It is therefore plausible that an oscillating cylinder, such as that which occurs during vortex-induced vibration, will have a different mode inception order and different path to wake turbulence than a fixed cylinder.

2.1.4 High Reynolds number flows

As the Reynolds number is increased further, the disorder of the wake increases as full turbulence is approached. This occurs because of the presence of a series of fundamental instabilities of the shear flow. The first of these is an instability of the free shear layer, which is a Kelvin-Helmholtz instability, that causes the shear layers to become wavy. The transition point from laminar to turbulent flow in the shear layer moves upstream toward the cylinder with increasing Re . The shear layers can also develop some three-dimensionality.

At $Re > 2 \times 10^5$, the so-called drag crisis is encountered, where the average drag force is suddenly reduced. This occurs due to the fact that a separation-reattachment bubble is formed by the shear layer. The reattached boundary layer then finally separates much further towards the rear of the cylinder, resulting in a narrow wake, hence lower

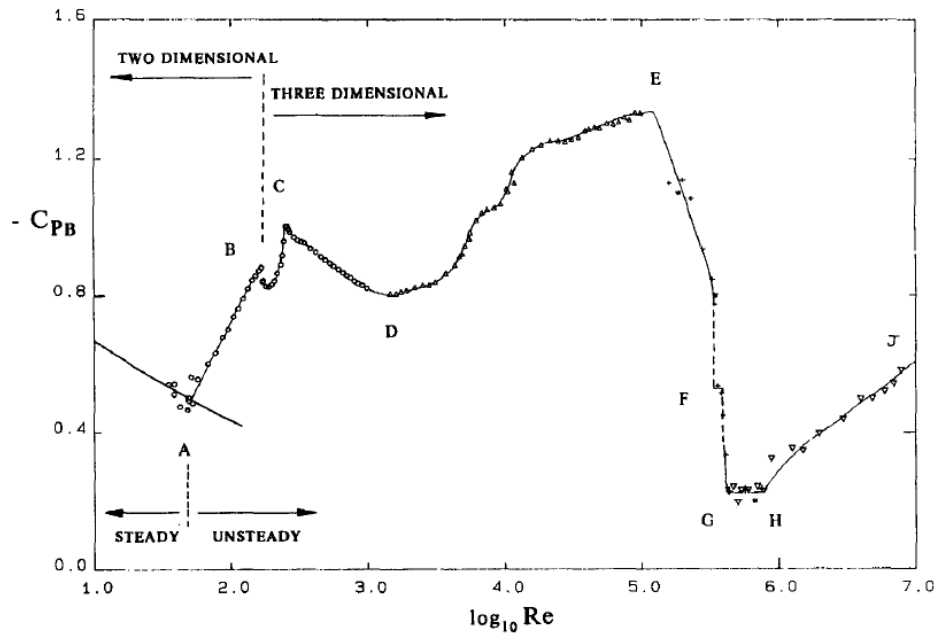


FIGURE 2.5: C_{PB} - Re curve, taken from Williamson (1996b).

form drag (Williamson 1996*b*) and a significantly lower base suction coefficient. The sudden drop in base suction is well-illustrated in figure 2.5. The Re at which this occurs is classically referred to as critical, with subcritical flow comprising no separation and reattachment, and supercritical flow occurring at Re higher than that where the separation-reattachment bubble is formed. However, vortex shedding is still present. An example is shown in figure 2.6.

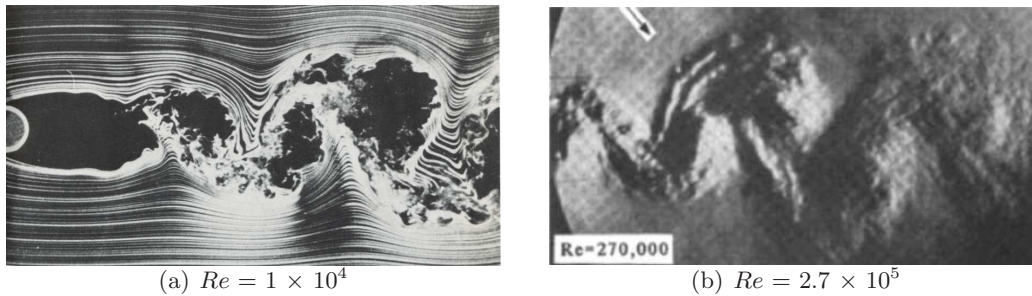


FIGURE 2.6: Vortex streets behind a fixed circular cylinder where the flow is turbulent, taken from Williamson (1996*b*).

As Re is further increased, the forming boundary layers themselves become fully turbulent. It was originally envisaged that this would mark the end of any periodicity in the wake, as vortex shedding gave way to a completely turbulent wake fed by turbulent boundary layers. However, periodicity has been detected at Reynolds numbers above this limit, further emphasising the importance of this initial transition.

2.2 Flow past a Stationary Sphere

The flows around another widely studied bluff body, the sphere, are remarkably different to those of the circular cylinder, as the Reynolds number is increased. A major difference is in the wake transition behaviour. The wake of a sphere becomes asymmetrical prior to a transition to unsteady flow, whereas the cylinder wake becomes unsteady before asymmetric structures appear in the wake (Williamson 1988*b*).

2.2.1 Steady axisymmetric flow

Attached flow

One of the earliest analytical studies of the flow past a sphere was performed by Stokes (1851) as part of a study into the resistance on the motion of a pendulum. Stokes solved equations of motion which excluded advection, but included viscous diffusion,

and assumed a no-slip condition at the sphere surface. The solution of this problem represents the low velocity limit of the flow of a viscous incompressible fluid past a sphere as Re approaches zero. Stokes flows exhibit a remarkable property known as reversibility, as mentioned in section 2.1.1. For reversible flow past a symmetrical body such as a sphere, the flow streamlines are symmetrical both upstream and downstream of the body, as shown in figure 2.7(a). Despite efforts to gain a better analytical description of the far wake of the flow past a sphere over the century following the work of Stokes, it has only been since the middle of the twentieth century that many advancements have been made in the study of the flow past a sphere.

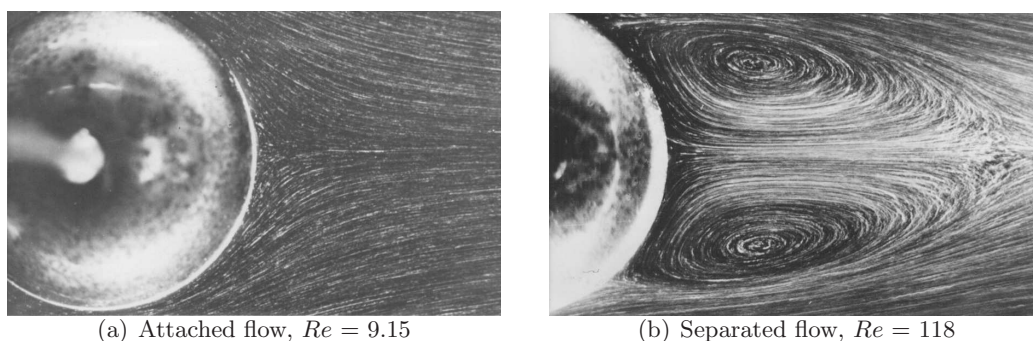


FIGURE 2.7: Steady flow around a fixed sphere where the flow is axisymmetric, taken from Taneda (1956).

Proudman & Pearson (1957) sought to extend the solution of Stokes to higher Reynolds numbers. They developed separate locally valid stream function equations for the flow fields near to and far from the body. This formulation reduced the problem to a single set of boundary conditions for each expansion; a no-slip boundary at the sphere surface for Stokes flow, and a uniform stream condition in the far flow field for Oseen flow.

Further efforts were made to extend this analytical description of the flow past a sphere by Chester & Breach (1969). They extended the analysis of Proudman & Pearson (1957) from an expansion of order $Re^2 \log Re$, to an order $Re^3 \log Re$. Consistent with the previous study, they employed expansions for the inner flow which satisfied the no-slip condition of Stokes flow, and expansions for the outer flow field which satisfied the uniform stream condition of Oseen flow.

Chester & Breach (1969) reported that their solution only agrees with experimental measurements over a Reynolds number range $Re = 0-0.5$. The limited range over which

their solution was accurate suggested that an inappropriate form of the expansions was used, however a more fundamental problem existed: the governing Navier-Stokes equations provide an often insurmountable obstacle when an analytical solution to a fluid flow problem is sought. Their method, which divided the flow field into a near field dominated by viscous diffusion, and a far field dominated by advection, provided an inadequate description of the flow, as flow features such as separation, asymmetry, and unsteady flow were suppressed.

The technological revolution of the latter half of the twentieth century brought about a revolutionary analysis technique known as computational fluid dynamics. Instead of deriving solutions to the Navier-Stokes equations with analytical methods, approximate solutions are obtained with numerical methods. An early computational study of the flow past a sphere was performed by Rimon & Cheng (1969). Their study employed a time-dependent axisymmetric stream function/vorticity formulation, with a finite-difference method used for the spatial discretisation of the vorticity transport equation, and a second-order central-difference scheme used for space and time integration. Their work provides early treatment of the difficulties in constructing a pressure field from vorticity when the velocity field is unknown. Although the computations were undertaken in an era in which computing power was limited, a relatively small sphere-to-domain diameter ratio of approximately 1:8.2 (blockage of about 1.5%) was employed.

Separated flow

The computations of Rimon & Cheng (1969) predicted that the flow past the sphere remained steady and attached for $Re \lesssim 25$, and for $Re \gtrsim 25$, the flow separated from the rear of the sphere, forming a recirculation bubble, as shown in figure 2.7(b). They computed a linear relationship between the bubble length and $\log Re$ for $Re \lesssim 150$. They reported a secondary separation of flow for $Re \approx 1000$, but earlier experimental flow visualisations of the flow past a sphere (Magarvey & Bishop 1961*a,b*; Magarvey & MacLachy 1965) suggested that the computational assumption of axisymmetric flow was nonphysical at these higher Reynolds numbers. Despite this, a good correlation between the computed drag coefficient C_D , and experimentally measured values of C_D was found for $0 \lesssim Re \lesssim 1000$.

A semi-analytical numerical study was conducted by Dennis & Walker (1971) for

the wake around a sphere. They employed Legendre functions to reduce the governing equations to a series of ordinary differential equations, which were then solved numerically. Only a steady axisymmetric flow was considered, with solutions being sought for the vorticity and stream-function equations. By assuming that at separation, the change in vorticity in the tangential direction at the rear of the sphere would be zero, they interpolated a value for the separation transition Reynolds number of $Re_{S1} \approx 20.5$, between flows computed at $Re = 20$ and $Re = 40$.

Taneda (1956) performed an experimental study of the flow past a sphere being towed through a tank, for Reynolds numbers $Re = 5 - 300$. By extrapolating the linear relationship between the measured recirculation bubble length and $\log Re$ to zero, he obtained a transition Reynolds number for flow separation from the sphere of $Re_{S1} = 24$. He commented on the potential for discrepancies when measuring the transition Reynolds number for flow separation in the wake. He noted that attempts to identify the initial formation of the recirculation bubble visually was difficult, as the bubble was initially very small and formed near to a stagnation in the flow where the velocities were very small. Extrapolation of the recirculation bubble length against Reynolds number was the preferred method for calculating the separation transition Reynolds number, as the length of the bubble could be measured easily at higher Reynolds numbers.

Recent numerical computations have allowed the separation transition Reynolds number to be accurately determined. By extrapolating the variation in length of the recirculation bubble with Reynolds number to zero from direct numerical computations, a value of $Re_{S1} = 20$ was determined from several studies (Tomboulides *et al.* 1993; Johnson & Patel 1999; Tomboulides & Orszag 2000). This value is remarkably consistent with the value obtained from the early study by Dennis & Walker (1971). Studies have also observed that at a critical Reynolds number Re_{S2} , the recirculation bubble becomes unstable to asymmetric flow.

2.2.2 Steady asymmetric flow

In the experimental study by Taneda (1956), it was observed that the axisymmetric recirculation bubble became unstable with an increase of Reynolds number. The stability of the axisymmetric wake of a sphere to axisymmetric and asymmetric disturbances has been studied numerically with varied success by Kim & Pearlstein (1990) and Natarajan

& Acrivos (1993).

The numerical stability analysis of Kim & Pearlstein (1990) employed a spectral method to solve the axisymmetric stream function form of the governing equations for the base flow. An axisymmetric stability analysis was performed, which employed the same method, and a non-axisymmetric stability analysis was performed, which employed a modified primitive variables form. Their computations predicted that the axisymmetric wake undergoes a non-axisymmetric Hopf bifurcation at $Re = 175.1$, with an azimuthal mode number $m = 1$. The instability that they predicted had an imaginary component giving a predicted linear oscillation frequency of $St = 0.0955$ at the onset of the instability. These predictions were at odds with the observations from experimental studies, as unsteady flow was generally only observed for $Re \gtrsim 300$ (Taneda 1956; Magarvey & Bishop 1961*a,b*; Magarvey & MacLachy 1965).

The more recent numerical study performed by Natarajan & Acrivos (1993) proved to be more successful. They employed a robust finite-element method for spatial discretisation of the flow past a sphere and the flow past a disc. They verified that a high grid convergence was obtained in their computations by monitoring various wake parameters, and an excellent agreement was obtained between the computed drag coefficients of spheres and discs, and the previous experiments of Roos & Willmarth (1971), up to $Re = 200$. Natarajan & Acrivos (1993) based their Reynolds number length scale on the radius of the sphere and disc, whereas here they are converted to Reynolds numbers based on the diameter for consistency with other reported results. They predicted that the first bifurcation of the steady axisymmetric wake of a sphere occurred at $Re = 210$, with an azimuthal mode number $m = 1$. This instability was predicted to occur through a regular (steady to steady flow) transition. They predicted that a secondary mode occurs at $Re \approx 277.5$. This secondary instability was predicted to occur through a Hopf bifurcation to unsteady flow, with an azimuthal symmetry of $m = 1$. Despite the axisymmetric base flow not providing a physical representation of the wake beyond the primary non-axisymmetric instability, the predicted Hopf mode was still qualitatively consistent with the experimental observations of the onset of unsteady flow in the wake ($270 < Re_{S3} < 300$). The predicted azimuthal symmetries of the primary and secondary non-axisymmetric instabilities were in excellent agreement with experimental observations of the non-axisymmetric wakes over similar Reynolds numbers (Magarvey & Bishop 1961*a,b*).

Stability of the sphere wake was studied using the complex wave amplitude Landau equation (Ghidiersa & Dušek 2000; Thompson *et al.* 2001). The coefficients of the linear and cubic terms of the Landau model were estimated from non-axisymmetric numerical computations close to the transition Reynolds numbers. The initial asymmetric transition was found to be a regular type transition, occurring at Re_{S2} , and the subsequent transition was identified as being a Hopf transition at $Re_{S3} = 272$. The critical Reynolds numbers of the transitions are in excellent agreement with previous studies. The analysis demonstrates that both transitions are predicted to occur through continuous supercritical bifurcations, and hence no hysteresis is expected in the vicinity of either transition. The Hopf transition in the wake of a sphere was the subject of a recent study by Schouveiler & Provansal (2002). They verified the supercritical nature of the transition, and through experimental measurements of the wake of a sphere, they determined coefficients of the Landau model to test the suitability of the model in describing the wake dynamics.

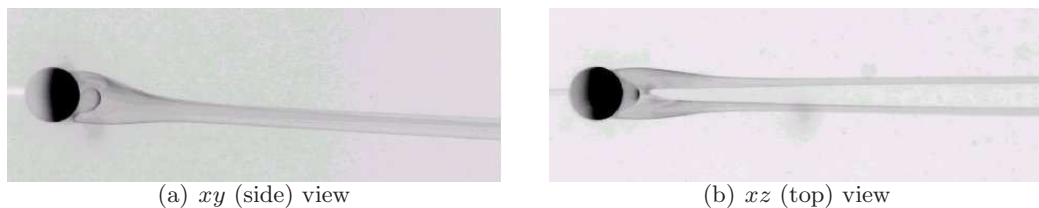


FIGURE 2.8: Steady asymmetric flow around a fixed sphere at $Re = 250$, taken from Ormières & Provansal (1999).

Experiments and numerical computations performed by Johnson & Patel (1999) found the axisymmetric wake to undergo a regular bifurcation through a shift of the steady recirculating bubble behind the sphere from the axis at $Re_{S2} \approx 211$. They observed the double-threaded wake, consistent with previous experimental observations (Magarvey & Bishop 1961*a,b*). The numerical studies of Tomboulides *et al.* (1993) and Tomboulides & Orszag (2000) find a similar value, $Re_{S2} = 212$. The flow visualisations in figure 2.8 provide a detailed representation of the asymmetric wake beyond the transition. The shift of the recirculation bubble from the axis is evident, and to the far right of the images, the pair of streamwise vortices which form the double-threaded wake may be observed.

2.2.3 Unsteady flow

Taneda (1956) perceived a small periodic *pulsing* with a long period at the rear of the recirculation bubble for $Re \gtrsim 130$. However, the far wake was observed to be completely laminar up to $Re \approx 200$, and the vortex ring was attached to the sphere up to $Re \approx 300$. In light of the more recent results reported here, it is reasonable to assume that the observed pulsing was the result of an extrinsic instability associated with the towing apparatus, as it was localised to the tail of the recirculation bubble. This observed pulsing does suggest, however, that the recirculation bubble is sensitive to perturbations in the vicinity of the transition.

Striking flow visualisations of the wakes behind spherical liquid droplets descending through a tank were presented by Magarvey & Bishop (1961*a*). The liquid droplets remained relatively uniform in size and shape, and provided a useful approximation to the flow past a fixed solid sphere. They controlled the Reynolds number by judicious selection of appropriate droplet size and liquid phases, as the Reynolds number depended on the terminal velocity of a given droplet. They presented visualisations of various wake states, including a steady, axisymmetric wake at $Re = 200$, and several images of unsteady wakes at Reynolds numbers $350 \leq Re \leq 500$. In all cases, the unsteady wakes that they observed consisted of vortex loops being shed into the wake from the alternate sides of the sphere. A plane of reflective symmetry was observed in the wake up to approximately $Re \approx 500$, and they observed that the wake at $Re \approx 600$ no longer exhibited periodic shedding, and had lost its planar symmetry.

In their following paper, Magarvey & Bishop (1961*b*) reported similar experiments over a wider Reynolds number range $0 < Re < 2500$. Their experimental rig enabled detailed images of the trailing wakes to be obtained, as the droplets were motionless in the reference frame of the camera. Attention was paid to classifying the observed wakes, which were summarised as follows: Class I ($0 < Re < 210$) exhibit a single thread wake, Class II ($210 < Re < 270$) exhibit a double thread wake, Class III to V ($270 < Re < 700$) exhibit planar-symmetric unsteady wakes, and Class VI ($Re > 700$) exhibit asymmetrical aperiodic wakes.

Detailed photographs presented in Magarvey & Bishop (1961*b*) illustrate examples of an axisymmetric Class I wake observed at $Re = 170$. Images of the Class II double-threaded wake show a steady non-axisymmetric wake caused by a loss of axisymmetry of the recirculation bubble. A distinction is drawn between the Class III wakes

($270 < Re < 290$), in which a waviness evolves downstream of the double-threaded wake, and the Class IV and V wakes, which display a well-defined shedding of vortex loops. The effect of having no transverse restraint on the free-falling droplets on the observed wakes remained an open question from their work. They estimated a linear $St-Re$ relationship for the single-loop shedding observed for $290 < Re < 410$, which varied between $0.05 < St < 0.065$; the $St-Re$ profile represents data obtained from the double-loop shedding observed for Class V wakes.

A later work by Magarvey & MacLatchy (1965) analysed the formation and evolution of the unsteady wake of a sphere with a careful image-acquisition technique. They proposed a “sheet involution” mechanism for the shedding process, whereby instead of vorticity convecting directly into the axisymmetric wake for $Re \lesssim 200$, vorticity is first transferred to the region behind the sphere, where a loop is formed. They described that below the critical Reynolds number for unsteady flow ($Re_{S3} \approx 300$), sufficient vorticity was transported into the wake via the double-threaded tails to maintain a steady wake, and beyond the critical Reynolds number the wake becomes unstable, and a periodic shedding of vortex loops ensues. A series of photographs capturing the evolution of the initial vortex loop following the destruction of symmetry in the wake was presented, representing a Class III wake at $Re = 340$.

The flow visualisations from various numerical computations (Tomboulides *et al.* 1993; Johnson & Patel 1999; Tomboulides & Orszag 2000) support the bifurcation sce-

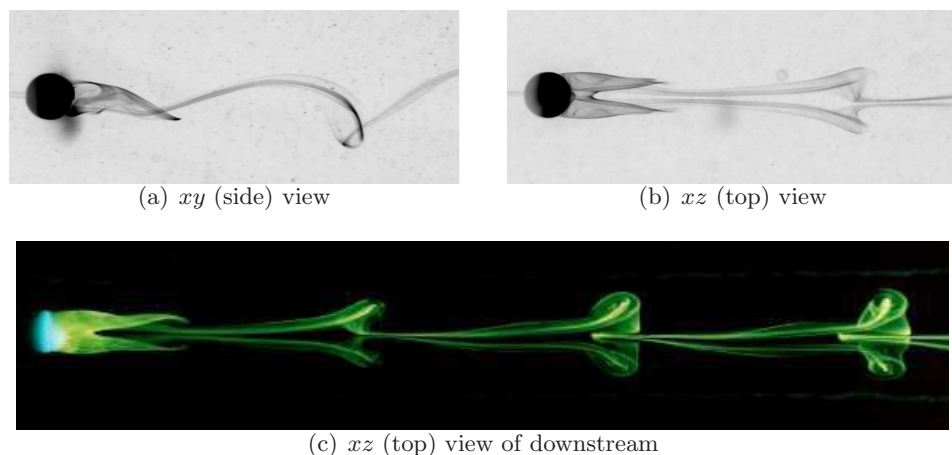


FIGURE 2.9: Unsteady flow around a fixed sphere. $Re = 340$ for (a) and (b), $Re = 320$ for (c). The pictures are taken from Ormières & Provansal (1999) for (a) and (b), and from Leweke *et al.* (1999) for (c).

nario predicted by Natarajan & Acrivos (1993), with unsteady wakes being observed for $Re \gtrsim 280$. Each of these studies found that the unsteady wake consisted of vortex loops or hairpins that shed downstream from the sphere, in the same plane as that of the steady double-threaded wake. The observed wake structures are in good agreement with the experimental observations of Magarvey & Bishop (1961*a,b*); Magarvey & MacLatchy (1965); Ormières & Provansal (1999) and Leweke *et al.* (1999), pertaining to the shedding of vortex-loops into the wake (see figure 2.9).

2.2.4 High Reynolds number flow

Computations by Mittal (1999*a,b*) verified both the earlier computations (Tomboulides *et al.* 1993; Johnson & Patel 1999) and experimental observations (Magarvey & Bishop 1961*b*; Magarvey & MacLatchy 1965) of the periodic wake of a sphere. They showed that the wake remained planar-symmetric up to a Reynolds number of $Re \approx 375$, beyond which the symmetry was lost. Combining a Digital Particle-Image-Velocimetry technique with a spatio-temporal reconstruction technique, the asymmetric structure of the wake of a sphere was analysed by Brücker (2001), who observed a similar loss of symmetry occurring within the Reynolds number range $400 < Re < 500$.

Tomboulides *et al.* (1993) observed fine scale flow structures in the wake of a sphere computed with a large-eddy simulation method, for a Reynolds number range of $500 < Re < 1000$. Magarvey & Bishop (1961*b*) observed a breakdown in periodicity of the hairpin shedding for $Re > 600$ also. These results are considered to mark the onset of turbulence. Measurements indicating the development of similar fine-scale structures are reported by Chomaz *et al.* (1993) and Tomboulides & Orszag (2000), who speculated that these structures developed from a Kelvin-Helmholtz instability of the shear layer separating from the sphere. The smoke-wire visualisations presented by Kim & Durbin (1988) show fine-scale wake structures behind a sphere for $Re = 32000$, consistent with a Kelvin-Helmholtz instability of the separating shear layer.

Achenbach (1972) performed wind-tunnel experiments over a range of Reynolds numbers $5 \times 10^4 < Re < 6 \times 10^6$. At these Reynolds numbers, the wake was observed to be highly turbulent. However, the flow could be considered incompressible, as the Mach number (fluid flow speed/speed of sound) of $Ma \approx 0.1$ was far lower than the critical Mach number requiring consideration of compressible flow ($Ma \approx 0.3$). To overcome skin friction effects, the sphere was highly polished, and measurements of

both pressure drag and skin friction were made. He also reported a massive reduction in drag from $C_D \approx 0.5$ at $Re = 3 \times 10^5$, to $C_D \approx 0.06$ at $Re \approx 3.7 \times 10^5$, and identified four flow regimes over the Reynolds number range he investigated. These flow regimes included a subcritical regime for $4 \times 10^4 < Re \lesssim 3 \times 10^5$, a critical regime for $3 \times 10^5 \lesssim Re \lesssim 3.7 \times 10^5$, a supercritical regime for $3.7 \times 10^5 \lesssim Re \lesssim 1.5 \times 10^6$, and a transcritical regime for $1.5 \times 10^6 < Re \lesssim 6 \times 10^6$.

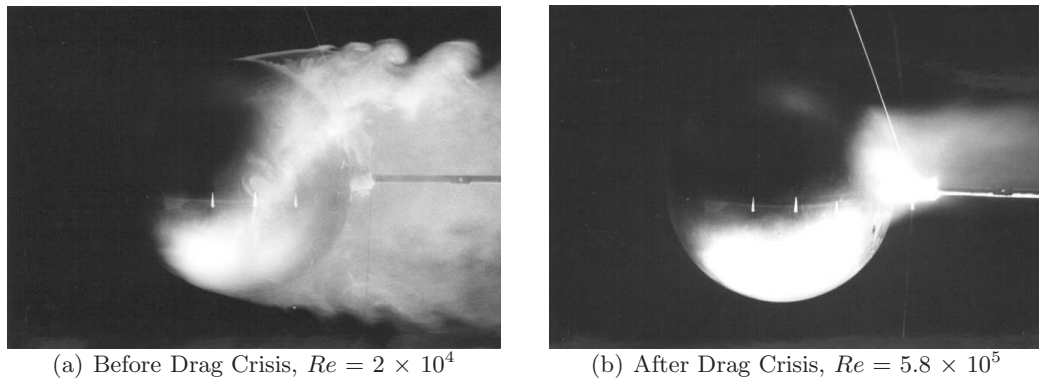


FIGURE 2.10: Turbulent flow around a fixed sphere at high Reynolds numbers, taken from Taneda (1978).

The wake dynamics over this high-Reynolds-number range was investigated by Taneda (1978), employing surface oil-flow visualisation and smoke visualisation to gain an understanding of the wake dynamics and structure. The experimental setup enabled Reynolds numbers to be studied over the range $10^4 < Re < 10^6$. He observed evidence of a progressive wave motion in the wake for $10^4 < Re < 3 \times 10^5$, and a streamwise pair of vortices for $3.8 \times 10^5 < Re < 10^6$. Consistent with Achenbach (1972), a sharp drag decrease (drag crisis) was found over the critical Reynolds number regime to $Re \approx 3.8 \times 10^5$. Further observations confirmed that the critical regime comprised a laminar separation at 100° , and a turbulent reattachment at 117° , followed by a turbulent separation at 135° (see figure 2.10). In addition, he observed a slow irregular rotation of both the subcritical wavy planar wake, and the supercritical turbulent double-threaded wake.

In a subsequent work, Achenbach (1974) studied the vortex shedding in the wake of a sphere for Reynolds numbers $400 < Re < 5 \times 10^6$. Water channel measurements were taken for $Re < 3 \times 10^3$, and from flow visualisation, his famous schematic representation of the vortex-loop configuration of the unsteady wake of a sphere at $Re = 1000$ was

sketched. Visualisations of the wake for $Re \approx 400$ showed a steady, asymmetric wake. Useful Strouhal-Reynolds number measurements were made, illustrating, among other points, the large discrepancy between the measured shedding frequency of the wake of a fixed sphere, and the liquid droplets from Magarvey & Bishop (1961*a,b*).

2.3 Dynamics of Bubbles

The flow around bubbles, in particular spherical bubbles, has many characteristics in common with that around solid spheres, for example the transitions with increasing Re . Among many of the characteristics, the path instability of the spherical bubbles is chosen to be reviewed here because of its close links to the wake dynamics and its resemblance to the trajectory of the vertically tethered sphere (Provansal *et al.* 2004), which is reviewed in section 2.6.2.

Path instability of the bubbles occurs essentially in the intermediate range of bubble size where bubbles are roughly ellipsoidal; nearly spherical bubbles and large, spherical capped bubbles (Wegener & Parlange 1973) do not exhibit path instability. Two types of motion are typically observed when path instability occurs: a *zigzag* motion where bubbles spend a long time in the same vertical plane and a *helical* motion with circular or elliptical horizontal displacements (Mercier *et al.* 1973). A transition from helical to zigzag path is often observed by increasing the size of the bubble (Lunde & Perkins 1997). It was also noticed consistently that the path of a given bubble may be first zigzag and then helical (Saffman 1956; Lunde & Perkins 1997; Wu & Gharib 2002; Shew *et al.* 2006), whereas the reverse transition has never been reported (see figure 2.11).

A theoretical analysis of path instability was developed by Saffman (1956) and Hartunian & Sears (1957). Both studies focused on the coupled action of inertia, surface tension, and interface deformation. Saffman (1956) addressed the conditions under which the bubble can follow a zigzag or helical path and examined the stability of the flow near the front stagnation point, assuming that the liquid motion is irrotational in that region (but not necessarily all around the bubble). It was concluded that the helical motion can exist only if the bubble aspect ratio lies between 1.2 and 2.2, which corresponds to bubble diameters between 1.4 mm and 7.3 mm in pure water. It was also demonstrated that any zigzag deviation from the rectilinear path is amplified when the bubble aspect ratio is larger than 1.2, and he conjectured that the zigzag instability arises from a coupled interaction between this instability and the oscillations of the

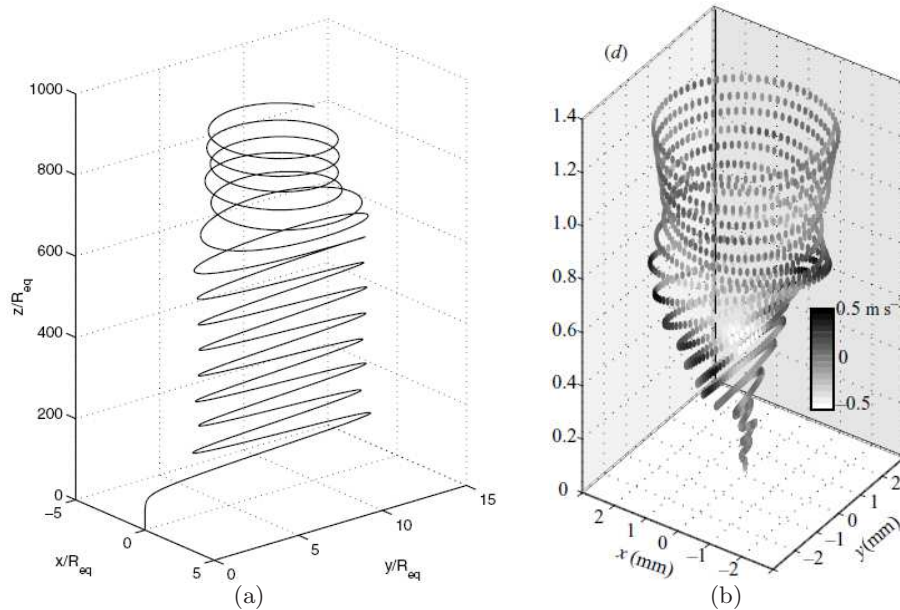


FIGURE 2.11: Examples of the bubble path rising in still fluid, (a) is taken from Wu & Gharib (2002) and (b) from Shew *et al.* (2006). The bubble begins rising straight, followed by zigzag motion with oscillating velocity, followed by a three-dimensional spiral motion with steady velocity. Note that the bubble is an ellipsoid where the aspect ratio is dependent on its equivalent radius.

wake.

In contrast, Hartunian & Sears (1957) assumed that the flow is irrotational everywhere around the bubble and that, prior to the onset of the instability, the bubble is spherical. Based on a linear perturbation analysis of shape, velocity, and pressure, they concluded that shape oscillations lead to a path instability beyond a critical Weber number (the ratio of inertia force to surface tension) of 5.45. By introducing a posteriori the effect of a nonspherical unperturbed shape, they corrected this value and obtained a lower critical Weber number of 3.03 in better agreement with their experiments. Their analysis was repeated by Meiron (1989), who first calculated numerically the unperturbed bubble shape for fixed values of the Weber number and studied the evolution of three-dimensional perturbations around this state. It was verified that path instability requires the flow to be rotational somewhere around the bubble, a condition consistent with the assumptions used by Saffman (1956).

Even though the possible role of the wake was evoked by Saffman (1956), the dynamics of a bubble wake have only recently been illuminated through flow visualisation

studies (Lunde & Perkins 1997; Mougin & Magnaudet 2002). There is now strong support that path instability is intimately coupled to the instability of the wake; however, not many specific theoretical or numerical investigations of the stability of an axisymmetric bubble wake have been reported. In contrast, the stability of the wake structure behind a solid sphere has been studied in detail (Natarajan & Acrivos 1993; Ormières & Provansal 1999; Tomboulides & Orszag 2000; Johnson & Patel 1999). It has been shown, as reviewed in section 2.2, that the flow behind a solid sphere loses its axisymmetry through a regular bifurcation that occurs around $Re_{S1} \approx 210$. Beyond this value, two vortex filaments, in which streamwise vorticity is concentrated, appear. No unsteadiness occurs until a second critical value $Re_{S2} \approx 280$ is reached, when a supercritical Hopf bifurcation takes place, and hairpin-like vortices are shed. Because a fully contaminated bubble behaves like a solid spheroid, it could be anticipated that the axisymmetry of the bubble wake breaks down at Re_{S1} ; this value is in agreement with the experimental criterion given by Hartunian & Sears (1957) for contaminated bubbles.

The relationship between the wake structure and trajectory of clean bubbles (helical or zigzag) has been notably clarified by the flow visualisations of Lunde & Perkins (1997) and Mougin & Magnaudet (2002). They showed that the helical path is associated with a steady wake made of two vortex threads (analogous to the wake of a solid sphere in the range $Re_{S1} \leq Re \leq Re_{S2}$), whereas the zigzag path is observed when hairpin vortices are shed in the wake (as for $Re \geq Re_{S2}$ with a solid sphere).

An integral component to predict the motion of zigzagging or spiralling bubbles is to quantify the force and torque acting on them. In all (both spiralling and zigzagging) cases, experiments show that the minor axis of the bubble is always directed along the local tangent to the path (Lunde & Perkins 1998). Recently, Shew *et al.* (2006) studied the dynamics of millimetre-sized air bubbles rising through still water using ultrasound Velocimetry combined with high-speed video. Drag and lift on the bubble were calculated from their measurements of speed and three-dimensional trajectories of planar zigzag or spiralling motion. The importance of the wake vortices (found in previous studies) was again emphasised by temporal correlations of forces and the oscillatory bubble motions, particularly the lift force.

2.4 VIV of Elastically Mounted Circular Cylinders

Fluid forces acting on a body may be directly related to the vortex structures in the surrounding fluid. For the case of a bluff body, the vortices in the wake form periodic fluid structures referred to collectively as the Kármán vortex street (discussed in section 2.1.2). These structures induce periodic forcing on the body. Depending on the mass of the body, its mechanical damping and its spring stiffness, the periodic forcing can induce vibrations of the body.

Studies of vortex-induced vibration of cylinders generally consider either the motion of an elastically mounted cylinder which has the same motion along the entire length of the span, in which vortex-induced vibration creates travelling modes along the span. An elastically mounted cylinder generally exhibits vortex-induced vibration along part of the span which subsequently forces oscillations at different spanwise locations. Variations in the inlet velocity are quantified by the reduced velocity $U^* = U_\infty / f_n D$, where U_∞ is the inlet velocity, D is the cylinder diameter and f_n is the natural frequency of the elastically mounted cylinder.

Elastically mounted bluff bodies generally exhibit vortex-induced vibrations with components streamwise and transverse to the flow field. Across a wide range of U^* , the largest amplitude of the transverse component of oscillations is typically an order of magnitude greater than the largest amplitude of the streamwise component (Bearman 1984). It could be anticipated that large amplitude transverse oscillations, excited by the lift force, occur when the shedding frequency, f_v , approaches the natural frequency of the system, f_n (i.e., a peak in the transverse component of oscillation occurs as $U^* \rightarrow 1/St$).

As the Strouhal number for a fixed circular cylinder can be assumed to be roughly equal to 0.2 over a wide range of Reynolds number, a peak amplitude in transverse oscillations should occur as $U^* \rightarrow 5$; this phenomenon has been widely reported (Sarpkaya 1979; Griffin & Ramberg 1982; Williamson & Govardhan 2004). Similarly for streamwise oscillations, it may be anticipated that a peak in the amplitude will occur as $f_{Drag} = 2 f_v \rightarrow f_n$, as the drag force is now driving the oscillation. Appreciable streamwise oscillations have been reported in the range $U^* = 1.5 - 4$ by King (1974).

2.4.1 Cylinder oscillating in transverse direction

The general set-up used to study vortex-induced vibration is that of an elastically mounted circular cylinder, in which the cylinder is made to vibrate only transversely to the freestream. This limits the degrees of freedom of the mechanical system, and also allows the results gained to be as general as possible. While generic and simplified, this system can still be difficult to study due to the interaction between the fluid flow and the cylinder movement. The lift force on the cylinder that drives its vibration is flow induced, yet that flow is partially governed by the resulting movement of the cylinder. Still, many studies have been performed in this way, and have observed that the cylinder motion, when periodic, appears sinusoidal over time.

As the flow speed U increases, a condition is reached when the vortex shedding frequency f_v is close enough to the body's natural frequency f_n such that the unsteady pressures from the wake vortices induce the body to respond and to reach *lock-in*, or *synchronisation*. The phenomenon of lock-in, or synchronisation, traditionally means that the body oscillation frequency f is close to the body's natural frequency f_n ; in other words, the ratio f^* remains close to unity.

Feng (1968) found that, for the body with high mass ratio ($m^* \gg 1$), f^* is close

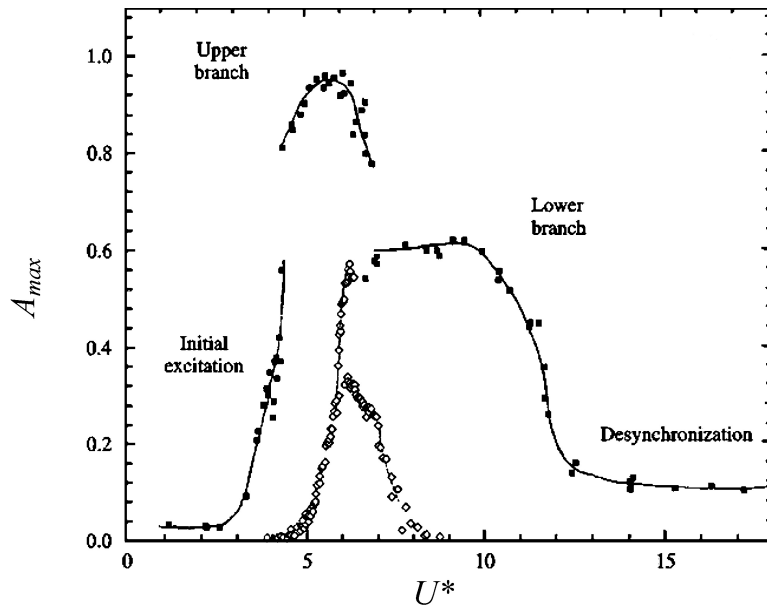


FIGURE 2.12: Amplitude responses of elastically mounted cylinders (Khalak & Williamson 1997). ■ represents the low mass ratio data and ◊ represents the high mass ratio data from Feng (1968).

to unity (see figure 2.12). However, for lighter bodies in water, for instance, $m^* = 2.4$ in figure 2.13(a), the body oscillates at a distinctly higher frequency ($f^* = 1.4$). The experiments by Angrilli *et al.* (1974) found that for cylinders with a low mass ratio ($m^* \approx 1.5$), the body oscillation frequency tended toward the vortex shedding frequency of the flow. The departure of f^* from unity through the lock-in regime was shown in the experimental study of Khalak & Williamson (1999). Therefore, one might define lock-in as the matching of the frequency of vortex shedding f_v with the body oscillation frequency f . Within this lock-in regime, three distinct branches of cylinder oscillation were observed as the flow speed was increased: an initial, upper and lower branch of oscillation as in figure 2.12. These three branches of oscillation have also been found for circular cylinders with low mass ratio (Govardhan & Williamson 2000; Blackburn *et al.* 2001; Shiels *et al.* 2001). The lock-in regime ($f = f_v$) has been observed for higher m^* circular cylinders; however, only two of the observed branches appear to exist, which are the initial and lower branch (Bearman 1984). Govardhan & Williamson (2000) found that the upper branch exhibited significantly higher amplitude oscillations than either of the other two branches.

Certain wake patterns can be induced by body motion, such as the 2S mode (2 single vortices per cycle) and the 2P mode (comprising 2 vortex pairs formed in each cycle) following the terminology in Williamson & Roshko (1988). Interestingly, a forced vibration can also lead to other vortex modes including a P+S mode, which is not able

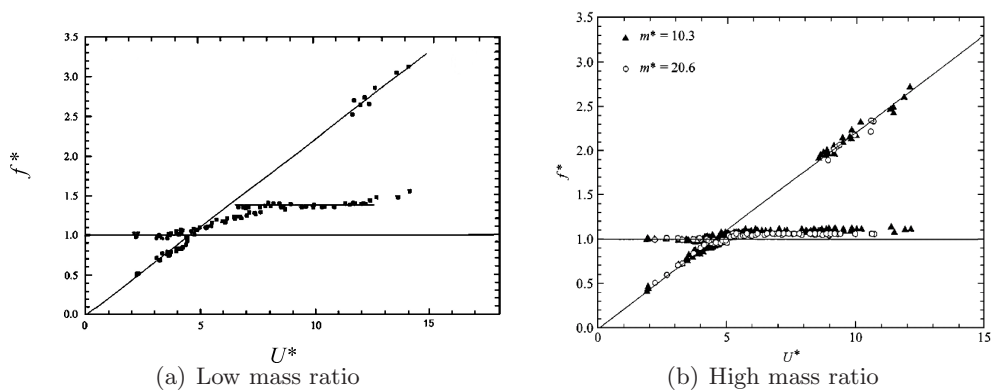


FIGURE 2.13: Frequency response of elastically mounted cylinder from Khalak & Williamson (1999). Note that the oscillating frequency of body with low mass ratio ($m^* = 2.4$) in (a) is higher than its natural frequency f_n . In contrast, the oscillating frequency of body with high mass ratio ($m^* = 10.3$ and 20.6) in (b) is close to f_n

to excite a body into free vibration. Generally, a periodic vibration ensues if the energy transfer, or work done by the fluid on the body, over a cycle is positive. This net energy transfer is influenced significantly by the phase of induced side force relative to body motion, which in turn is associated with the timing of the vortex dynamics. Feng (1968) found a hysteresis between the initial and lower branches, while the upper to lower transition involves an intermittent switching. He also noted that the jump in response amplitude was reflected by a significant jump in the phase of the pressure fluctuations relative to body motion. Zdravkovich (1982), for the first time, showed that a jump in phase angle (between transverse force and displacement) through resonance is matched by a switch in the timing of vortex shedding using visualisations from previous studies.

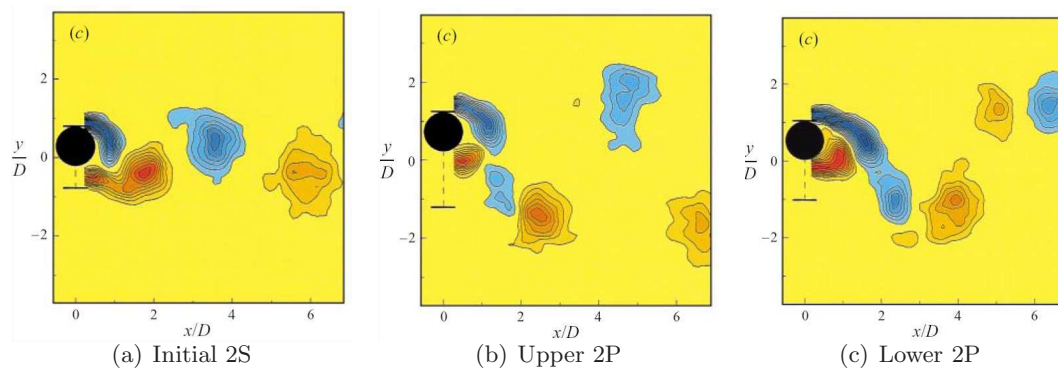


FIGURE 2.14: Wakes of transversely oscillating cylinder from Govardhan & Williamson (2000).

Govardhan & Williamson (2000) found that the upper and lower branches exhibit a 2P wake structure as shown in figure 2.14. They also found that transition from the upper to the lower branch results in a change of the phase between the total lift force and the cylinder displacement; the upper branch exhibiting in-phase oscillation, the lower branch of oscillation exhibiting 180° out-of-phase oscillation. Further, they found that when oscillation amplitude was plotted against reduced velocity U^* , the transition point from the upper to the lower branch of shedding was inversely proportional to the mass ratio of the cylinder.

2.4.2 Cylinder oscillating in streamwise direction

King (1974), by restricting the cylinder to only oscillate streamwise with the flow, observed oscillations up to 0.15 diameters in amplitude in the Reynolds number range

of $6 \times 10^4 \leq Re \leq 6 \times 10^5$. He observed two modes of shedding. The first is a symmetric mode, where both positive and negative vortices are shed from the cylinder for each oscillation cycle and convect downstream symmetrically (see figure 2.15). Further downstream, the symmetric structure becomes unstable and the wake reverts to the staggered Kármán type. The symmetric mode was found to occur in the range, $U^* = 1 - 2.5$. A local minimum in the streamwise oscillation amplitude was noted at $U^* = 2.5$; however, in the range $U^* = 2.5 - 4$, a second mode of shedding was observed (see figure 1.14). In this mode, a single vortex is shed per oscillation cycle, and the wake resembles the traditional Kármán arrangement. King (1974) further speculated that a critical Reynolds number existed, in the range $Re = 1200 - 1500$, below which streamwise oscillations were not observed.

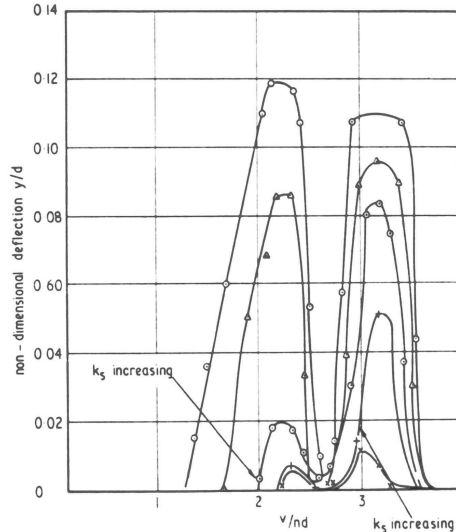


FIGURE 2.15: Amplitude response of a cylinder free to oscillate in the streamwise direction as a function of U^* , taken from (King 1974).

2.4.3 Cylinder oscillating in transverse and streamwise direction

Two distinct areas of research have involved cylinders with oscillation components in both the streamwise and transverse directions. The first area restricts the cylinder to oscillate at an angle inclined to the free stream. Ongoren & Rockwell (1988) investigated the forced oscillation of a cylinder at an angle to the free-stream. They found that phase locking between the cylinder oscillations and the cylinder wake was possible for all oscillation angles investigated ($\alpha = 0 - 90^\circ$).

The second area of the research allows the cylinder to freely oscillate with components in the streamwise and transverse directions. Moe & Wu (1990) studied this case; however, due to their experimental setup, the streamwise mass ratio was different to the transverse mass ratio. The experimental setup also gave distinct streamwise and transverse natural frequencies. They found a broad range of reduced velocity over which large peak to peak oscillations were observed. However, they did not find any evidence of the distinct branches of oscillation discussed previously. Sarpkaya (1995), using a similar experimental setup, found that the response of a cylinder allowed to oscillate with components in both the streamwise and transverse directions could, in certain circumstances, behave substantially differently to the freely oscillating cylinder, restricted to transverse oscillations discussed in section 2.4.1.

Jauvtis & Williamson (2003) investigated the case of a cylinder allowed to freely oscillate in both the streamwise and transverse directions, where the mass ratio and natural frequency was the same in both the streamwise and transverse directions. They investigated the mass ratio range, $m^* = 5 - 25$ and the reduced velocity range, $U^* = 2 - 12$. For $U^* = 5$, they found remarkably little difference in the results between their experimental setup and the transverse oscillating cylinder discussed in the previous section. For low reduced velocities the cylinder oscillated similarly to that described by King (1974) for the case of a cylinder oscillating streamwise with the flow field. However, there was a dramatic change in the response of the cylinder when mass ratios are reduced below $m^* = 6$. A new response branch with significant streamwise motion appeared in what they called “super-upper” branch, which yields large amplitudes of three diameters peak-to-peak. They also reported that the super-upper mode comprises a triplet of vortices formed in a half cycle, and named it the “2T” mode.

2.5 VIV of a Tethered Circular Cylinder

One of the simplest extensions to the classical problem of an elastically mounted oscillating cylinder is a circular cylinder whose motion is confined to an arc by a restraining tether. However, little progress has been made regarding the fluid-structure interaction of a tethered body. This system geometry has practical applications in submerged pipelines, offshore spar platforms and light craft tethered in air. It is also of interest because it exhibits flow-induced oscillation where the combined effects of streamwise oscillation and transverse oscillation maybe observed.

Ryan *et al.* (2004a), for the first time, numerically studied the tethered cylinder system with a spectral element method. It was found that, at large mean layover angles, the tethered cylinder would behave in a fashion similar to the elastically mounted cylinder with low mass ratio and oscillate in either the upper or lower branch of shedding depending on U^* and m^* . They noted that the cylinder system to be strongly influenced by the mean layover angle as this parameter determined if the oscillations would be dominated by streamwise oscillations, transverse oscillations or a combination of the two. Three branches of oscillation were noted, an streamwise branch, a transition branch and a transverse branch (see figure 2.16). It was also reported that the streamwise oscillation for small layover angle corresponds to a classic Kármán street wake, and the transverse oscillation for larger layover angle at higher flow speeds corresponds with the formation of vortex pairs. Within the transition branch, the cylinder oscillates at the vortex shedding frequency and modulates the drag force such that the drag signal is dominated by the lift frequency. It was found that the mean amplitude response is greatest at high reduced velocities, i.e., when the cylinder is oscillating predominantly transverse to the fluid flow. Furthermore, the oscillation frequency is synchronised to the vortex shedding frequency of a stationary cylinder, except at very high reduced velocities.

Ryan *et al.* (2004b) reanalysed the same results, and observed a negative mean lift coefficient for a majority of mean layover angles considered. The mean lift coefficient only approached zero as $\vartheta \rightarrow 0^\circ$ or 90° . The minimum C_L recorded was approximately 0.05, corresponding to $\vartheta = 40^\circ$. They related the non-zero mean lift coefficient to an asymmetry in the wake behind the cylinder. Furthermore, they related the wake asymmetry with the mean layover angle about which the cylinder oscillates, noting that the asymmetry (and hence the magnitude of C_L) was most prominent in the transition mode.

Recently, Carberry & Sheridan (2007) experimentally investigated the flow interaction with a tethered cylinder for mass ratios in the range $m^* = 0.54 - 0.98$, for a fixed tether length ($L^* = 4.6$), and $Re = 900 - 7390$. They found a mass ratio, ($m^* = 0.72$), below which large-amplitude oscillations were observed at high mean layover angles. When the results were plotted against the Froude number ($Fr = U_\infty/\sqrt{gD}$, where U_∞ is the free-stream velocity and g is the gravity acceleration), they found that the jump in amplitude occurred as $Fr \rightarrow 1$ for all $m^* < 0.72$. This finding was qualitatively

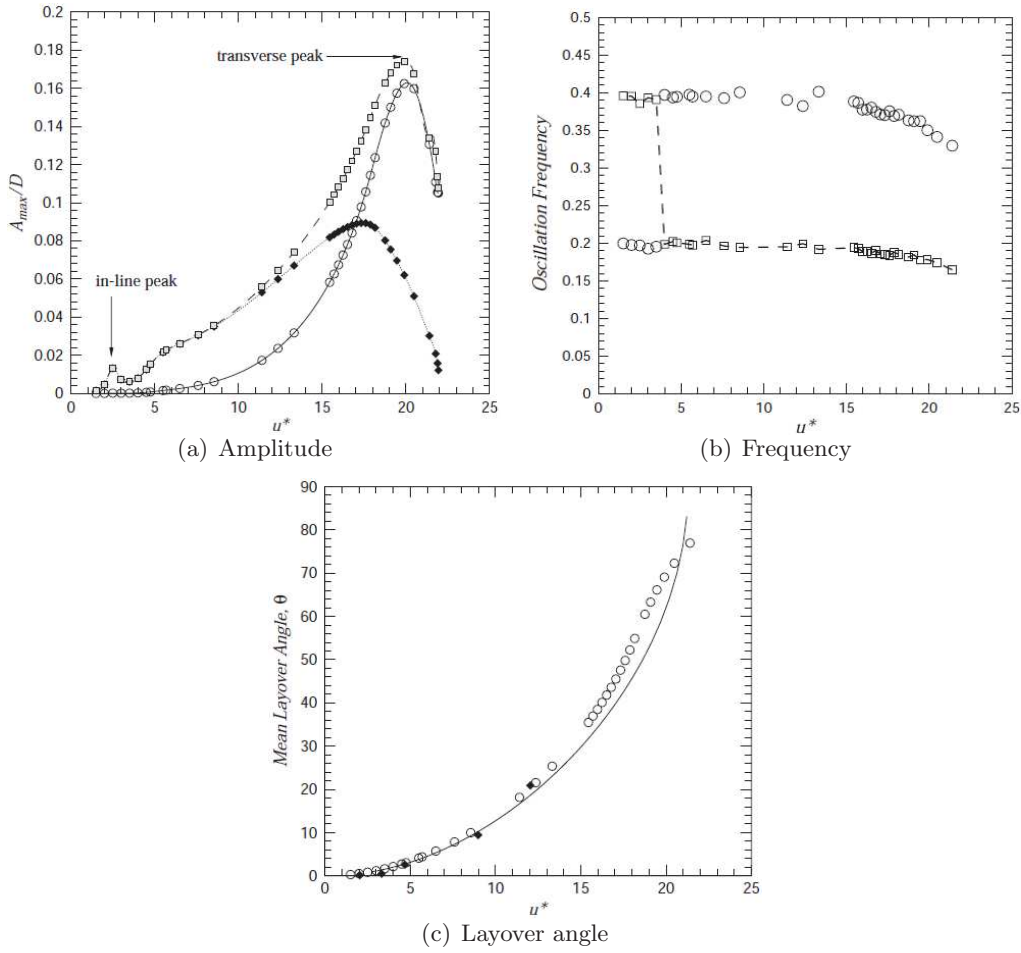


FIGURE 2.16: Response of a buoyant tethered cylinder as a function of the reduced velocity, taken from Ryan *et al.* (2004a). In (a), \square is the amplitude is in the direction of the motion. In (b), \circ corresponds to the principal frequency of the cylinder oscillation and \square corresponds to the secondary frequency. In (c), \circ is from the results of Ryan *et al.* (2004a) compared to the analytical values represented by the solid line.

in agreement with the low-Reynolds-number ($Re = 200$) numerical findings of Ryan (2004), who determined a mass ratio $m^* = 0.38$ below which large-amplitude oscillations were observed with a tether length of $L^* = 5$. Due to their experimental setup, Carberry & Sheridan (2007) could not determine a negative mean lift, and assumed, for their force balance calculations, that it was negligible compared with the other mean forces acting on the cylinder.

2.6 VIV of a Tethered Sphere

2.6.1 Tethered spheres in oscillatory flow

The vast majority of work on tethered spheres were concerned with the action of surface waves on tethered buoyant structures. For example, the investigations of Harlemann & Shapiro (1961) and Shi-Igai & Kono (1969) employed empirically obtained drag and inertia coefficients for use in the so-called *Morison's* equation (Morison *et al.* 1950; Sarpkaya 1986). Consequently, because the waves represented harmonic forcing functions, the tethered sphere was found to vibrate vigorously. However, the coupling of the wave motion and the dynamics of the sphere resulted in complicated equations of motion from which it is difficult to understand the underlying physics.

Gottlieb (1997) investigated a nonlinear, small-body mooring configuration excited by finite-amplitude waves and restrained by a massless elastic tether. A Lagrangian approach was formulated in which the stability of periodic motion was determined numerically using Floquet analysis and revealed a bifurcation structure including ultra-subharmonic and quasi-periodic responses. The hydrodynamic dissipation mechanism was found to control stability thresholds, whereas the convective terms enhanced the onset of secondary resonances culminating in chaotic motion. Consequently, excitation by finite-amplitude waves may generate a complex transfer of energy between the modes of motion for wave frequencies that are integer multiples of the system natural frequencies.

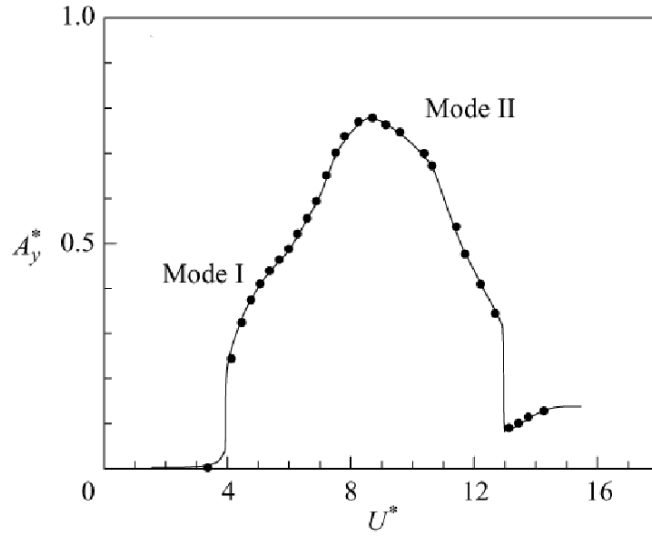
2.6.2 Tethered spheres in uniform flow

Williamson & Govardhan (1997) found that a tethered sphere does indeed vibrate in a uniform flow. In particular, they found that it will oscillate vigorously at a transverse saturation amplitude of close to two diameters peak-to-peak. This transverse oscillation frequency was at half the frequency of the streamwise oscillations, although the natural frequencies of both the streamwise and transverse motions were the same. In the Reynolds number range of their experiments ($Re < 12000$), the response amplitude was a function of the flow velocity. They found that a more suitable parameter on which to gauge the response is the reduced velocity, U^* . However, conclusions regarding the synchronisation of natural and vortex formation frequencies were lacking due to the large scatter in the literature of the vortex formation frequency in the wake of a sphere.

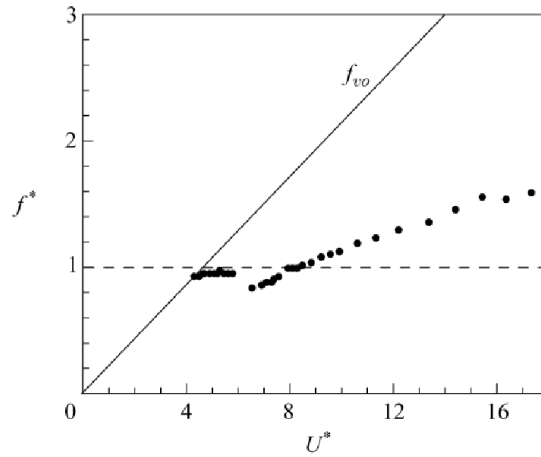
Govardhan & Williamson (1997) noted that the maximum Root-Mean-Square (RMS) amplitude was approximately 1.1 diameters, regardless of the mass ratio. It was further found that the vortex shedding frequency for a fixed sphere matched the natural frequency for the tethered sphere at the same reduced velocity, $U^* \approx 5$, at which the local peak in the RMS response occurred. This suggests that the local peak in the RMS response is caused by a resonance between the natural frequency of the tethered body and the wake vortex shedding frequency, and is known as mode I response (see figure 2.17(a)). For high mass ratios (typically $m^* \gg 1$), the oscillation frequency at large reduced velocity tended toward the natural frequency. However, it is interesting to note that the oscillation frequency for lower mass ratios ($m^* < 1$) at high U^* did not correspond to either the natural frequency or the vortex shedding frequency for a fixed sphere as shown in figure 2.17(b).

Jauvtis *et al.* (2001) focused on mass ratios between $m^* = 80$ and 940 and reduced velocities in the range $U^* = 0 - 300$. For the sphere of mass ratio 80, they found a new mode of vibration (defined as mode III) and which extends over a broad regime of $U^* = 20 - 40$. Because of the high mass ratios involved, the oscillation frequency remained very close to the natural frequency of the tethered sphere, whereas low m^* yielded oscillation frequencies higher than, and depart significantly from, the natural frequency (Govardhan & Williamson 1997). This mode cannot be explained as the classical lock-in effect, since between 3 and 8 cycles of vortex shedding occurs for each cycle of sphere motion. Although no explanation is given here, they note that there must exist vortex dynamics which are repeatable in each cycle, and which give rise to the fluid forcing component that is synchronised with the body motion.

Jauvtis *et al.* (2001) also found that, for reduced velocities beyond the regime for mode III, another vibration mode was discovered that grew in amplitude and persisted to the limit of flow speed in the wind tunnel. The sphere dynamics of this “mode IV” were characterised by intermittent bursts of large-amplitude vibration, in contrast to the periodic vibrations of modes I to III. In addition, despite these intermittent bursts, the vibration frequency of this mode remained very close to the natural frequency throughout the range of up to at least $U^* = 300$. With the vortex shedding frequency between 40 and 50 times the oscillation frequency, the vortex shedding cannot be responsible for these large vibrations, and the origin of these transient bursts remains unknown.



(a) Amplitude



(b) Frequency

FIGURE 2.17: Response of a tethered sphere from Govardhan & Williamson (2005). A_y^* is the transverse amplitude normalised by sphere diameter D , and f^* is the transverse body vibrations frequency normalised by its natural frequency. $m^* = 2.83$ in (a) and $m^* = 0.76$ in (b). The maximum Re for peak amplitude is about 3500.

Govardhan & Williamson (2005) extended their previous study on sphere vortex-induced vibration and found that the body oscillation frequency f is of the order of the vortex shedding frequency of fixed body f_{vo} and there exist two modes of periodic large-amplitude oscillation, defined as modes I and II (Govardhan & Williamson 1997; Williamson & Govardhan 1997), separated by a transition regime exhibiting non-periodic vibration. In the case of the very light tethered body, the transition between modes is quite distinct, especially when the response amplitude is plotted versus the parameter $(U^*/f^*) St$ which is equivalent to f_{vo}/f , where a jump between modes is

clearly exhibited (see figure 2.18).

Govardhan & Williamson (2005) noted that the phase of the vortex force relative to sphere dynamics is quite different between the modes I and II. This difference in the phase of the vortex force is consistent with the large difference in the timing of the vortex formation between modes, which was observed from the vorticity measurements for the light sphere vibrations (see figure 2.19). This mode cannot be explained as the classical lock-in effect, since between 3 and 8 cycles of vortex shedding occurs for each cycle of sphere motion. For reduced velocities beyond the regime for mode III, another vibration mode was discovered that grew in amplitude and persisted to the limit of flow speed in the wind tunnel (Jauvtis *et al.* 2001). The sphere dynamics of this mode IV were characterised by intermittent bursts of large-amplitude vibration, in contrast to the periodic vibrations of modes I, II and III. In addition, despite these intermittent bursts, the vibration frequency of this mode remained very close to the natural frequency throughout the range up to at least $U^* = 300$. With the vortex shedding frequency between 40 and 50 times the oscillation frequency, the vortex shedding was presumably not responsible for these large vibrations, and the origin of these transient bursts remains unknown.

Recently, Provansal *et al.* (2004) reported interesting results regarding the response of a tethered sphere where the tether is parallel to the stream. Their experiments

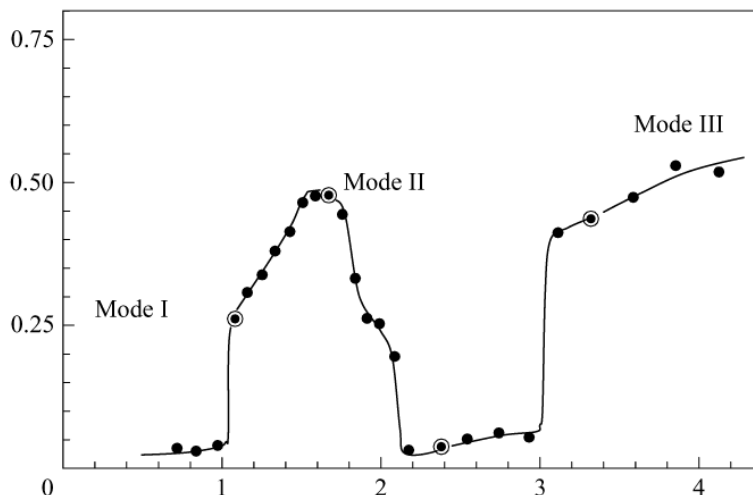


FIGURE 2.18: Amplitude response of a tethered sphere from Govardhan & Williamson (2005). $m^* = 11.7$ and the maximum $Re = 3000$. The ordinate is transverse amplitude normalised by sphere diameter, and the abscissa is the f_{vo}/f .

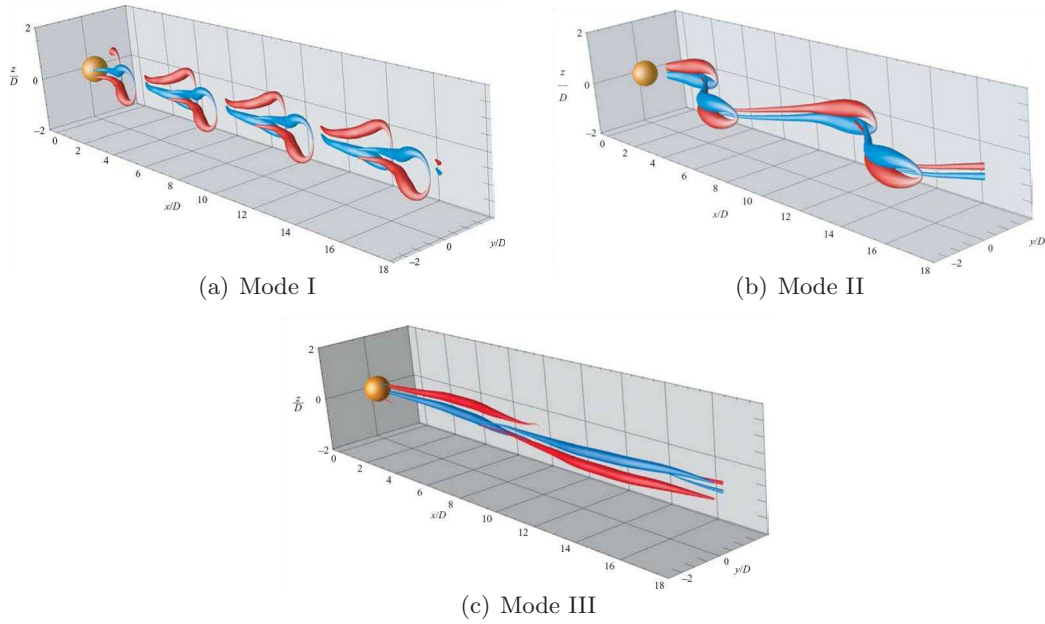


FIGURE 2.19: Reconstructed wakes from Particle-Image-Velocimetry data behind a tethered sphere, taken from Govardhan & Williamson (2005).

were performed in a vertical water tank with a sphere of $m^* = 2.433$ and a tether of 9-diameter long, and found a quasi-circular motion or an elliptic motion in the cross-section normal to the flow when the reduced velocity is $U^* \geq 4$. The Re range was $Re = 600 - 800$. The oscillating frequency was close to its natural frequency, i.e., $f^* = f/f_n = 1$, because the mass ratio $m^* > 1$. Due to this different response of the vertically tethered sphere to the results of Govardhan & Williamson (1997); Williamson & Govardhan (1997); Govardhan & Williamson (2005), it is indicated that the direction of gravity acting on a tethered sphere has considerable effect as well as the gravity magnitude, which is reflected in the mass ratio.

Pregalato (2003) numerically investigated the case of a tethered sphere for the much lower Reynolds number range, $Re = 200 - 500$. In his investigation, the first mode of oscillation, mode I, found by Govardhan & Williamson (2005), was not found. However, the numerical results compared well with experiments performed in the same Reynolds number range.

2.7 Chapter Summary and Points of the Present Study

The preceding review of literature has shown that, while some very useful findings have been made in the field of bluff body flows, and vortex-induced vibration of the body (in particular the cylinder) in general, it is not clear whether the knowledge compiled mainly for the vortex-induced vibration of cylinders is applicable to other types of vortex-induced vibration. Among others, not many aspects of the motion of a tethered body is understood although it is common to see this type of body constraint in marine applications. With a hope to uncover new aspects of the vortex-induced vibrations of tethered bodies using the pre-compiled knowledge, previous studies in the related field have been reviewed.

From the literature, a summary of the wake characteristics of the flow around a fixed cylinder is presented in table 2.1. The Reynolds numbers considered in the present study range from 10 to 300, and this covers the range over which the flow varies from two-dimensional and steady to unsteady and three-dimensional.

Reynolds number	Wake Characteristics
$Re < 6$	Two-dimensional, steady, symmetric, attached to cylinder.
$Re = 6 - 46$	Two-dimensional, steady, symmetric, separated.
$Re = 46 - 180$	Two-dimensional, unsteady periodic, Kàrmàn vortex street.
$Re = 180 - 260$	Three-dimensional, unsteady, Mode A.
$Re = 260 - 300$	Three-dimensional, unsteady, Mode B.

TABLE 2.1: Wake characteristics of the flow around fixed cylinders for the Reynolds number up to $Re = 300$.

The characteristics of the wake for a fixed sphere are summarised in table 2.2 up to $Re = 3000$. It should be noted that the sphere wake becomes asymmetric first prior to being unsteady.

For bubbles rising in fluid, two types of motion have been observed when path instability occurs: a zigzag motion where bubbles spend a long time in the same vertical plane, and a helical motion with circular or elliptical horizontal displacements. A transition from helical to zigzag path is often observed by increasing the size of the bubble. It was also noticed consistently that the path of a given bubble may be first zigzag and then helical (Lunde & Perkins 1997; Mougin & Magnaudet 2002). The relationship between the wake structure and trajectory of bubbles (helical or zigzag)

Reynolds number	Wake Characteristics
$Re < 24$	Laminar, axisymmetric, attached to sphere.
$Re = 24 - 212$	Axisymmetric, steady, separated.
$Re = 212 - 275$	Non-axisymmetric, steady, planar-symmetric, “double thread” wake vortex formation.
$Re = 275 - 420$	Non-axisymmetric, unsteady, planar-symmetric, periodic vortex shedding in the form of vortex loops or hairpin vortices.
$Re = 420 - 480$	Planar symmetry is lost, shedding direction oscillates intermittently.
$Re = 480 - 650$	Vortex shedding pattern becomes irregular.
$Re = 650 - 800$	Separated cylindrical vortex sheet pulsates, vortex tubes begin to be periodically shed in accordance with the pulsation.
$Re = 800 - 3000$	Hairpin vortices become turbulent with alternate fluctuations, both high- and low-mode Strouhal numbers coexist.

TABLE 2.2: Wake characteristics of the flow around fixed spheres for the Reynolds number up to $Re = 3000$.

has been notably clarified by the flow visualisations. It has been shown that the helical path is associated with a steady wake made of two vortex threads (analogous to the wake of a solid sphere in the range $210 \leq Re \leq 270$), whereas the zigzag path is observed when hairpin vortices are shed in the wake (as for $Re \geq 270$ with a solid sphere).

Most studies of vortex-induced vibration that have focused on an elastically-mounted circular cylinder vibrating transversely have originated from the marine engineering sector. Previous studies of this vortex-induced vibration have shown that the (non-dimensional) flow speed and the relative body to fluid mass are two important parameters affecting the vortex-induced vibration of the body. The body is found to vibrate when the value of the flow speed reaches the point where vortex shedding commences. Further increase of the flow speed can result in a resonance occurring, a major concern of VIV. The range of resonance is a function of the relative body mass to the displaced fluid mass (the so-called *mass ratio*). It has been identified that the smaller the mass ratio is, the larger the resonance region becomes. The response branches within the resonance region are also dependent on the mass ratio. A body that is denser than the fluid exhibits two response branches (Feng 1968), whereas a lighter body results in three branches, including a higher amplitude branch (Khalak & Williamson 1999). Several other parameters affecting the response of the cylinder have also been identified

through vortex-induced vibration research. They are the Reynolds number and the mechanical damping of the body in the fluid. Their effects on VIV, however, are not as clear as the effects due to the flow speed and the mass ratio.

In contrast to the amount of research on a transversely oscillating cylinder, only a few studies have examined other types of vortex-induced vibration, such as vortex-induced vibration of a tethered cylinder (Ryan *et al.* 2007; Carberry & Sheridan 2007) or a tethered sphere (Govardhan & Williamson 1997; Pregalato 2003). These studies have shown some similarities to the response of a transversely vibrating cylinder. However, these vortex-induced vibrations have been also shown to have significant differences in their response, and have introduced new parameters to consider. For instance, the tether angle and its length are found to have a large effect on the vortex-induced vibration of a tethered body.

Based on the considerable knowledge reviewed here, the present study investigates the vortex-induced vibration of a tethered body as a different type of vortex-induced vibration using several parameters, such as the flow speed, the mass ratio, the Reynolds number and the tether elasticity. A particular mass ratio of unity, which corresponds to the case of neutrally buoyant body, will be considered due to the disappearance of the gravity effect on its motion. For the first time, to the author's knowledge, the effect of elastic tether on the vortex-induced vibration of a tethered body in uniform flow is also studied. The generic geometries of a cylinder and a sphere are chosen for the research to focus on fundamental mechanisms behind, and to interconnect previous findings of general vortex-induced vibrations.

Chapter 3

Methodology and Validation

This chapter starts with the problem formulations of the tethered cylinder and the sphere cases, resulting in sets of equations of motion. Following this, the implementation of the adopted numerical method, featuring the coupled equations of motion for the fluid and the body, is provided, and the determination of the controlling parameters for the two types of tethered body ensues. The numerical method is explained mainly for the tethered sphere (three-dimensional), as its reduction to the cylinder (two-dimensional) can be easily achieved.

Validation of the numerical results for some selected parts of parameter space are presented for both bodies. Finally, the experimental set-up and its details for the sphere system are provided.

3.1 Problem Formulation: Tethered Circular Cylinder

The tethered cylinder system is shown in figure 3.1. For this system, the forces acting on the body are tether tension T , buoyancy force B , body weight W , streamwise fluid force F_x and transverse fluid force F_y . In the first instance, the tether is assumed to be inextensible, i.e. there is no movement along the tether. However, in the subsequent studies of an elastically tethered cylinder, this restriction is removed. It is also assumed that the tether is attached to the centre of mass of the body. Negligible effect of the precise form of this attachment has been shown as long as the tether length L is long enough compared to the diameter D of the body, e.g. $L \geq 5D$. (Pregalato 2003; Ryan *et al.* 2004a).

The tension acting along the tether of the cylinder is related to the other forces by the equation 3.1

$$T = F_x \cos \theta + (F_y + B - W) \sin \theta, \quad (3.1)$$

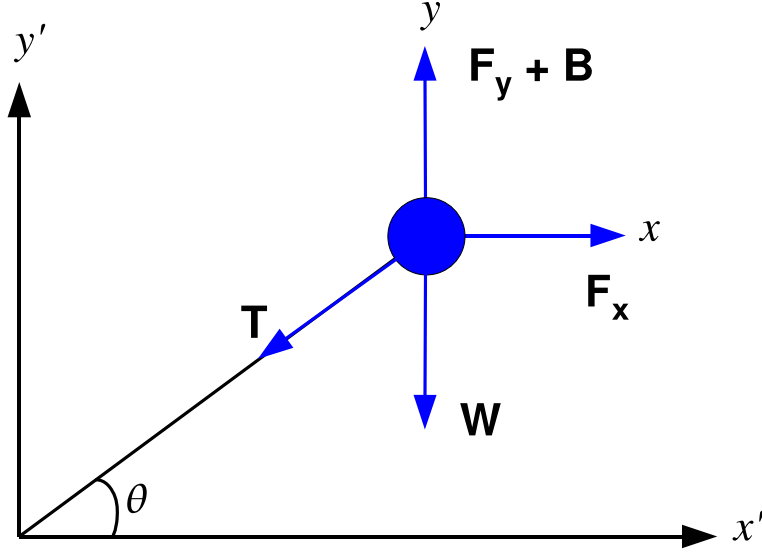


FIGURE 3.1: Coordinate system and forces on a tethered cylinder.

where θ is the tether angle measured from the streamwise (x) axis to the cylinder centre. For reference, $\theta + \vartheta = 90^\circ$ where ϑ is the layover angle of Ryan *et al.* (2004a).

The motion of the cylinder in a Cartesian coordinate system is described by the equations 3.2 and 3.3

$$m\ddot{x} = F_x - T \cos \theta, \quad (3.2)$$

$$m\ddot{y} = (F_y + B - W) - T \sin \theta. \quad (3.3)$$

After substituting equation 3.1 into equations 3.2 and 3.3 and nondimensionalising, the equations of motion can be rewritten as

$$\frac{\ddot{x}}{\gamma} = \frac{1}{m^*} \left[\left(1 - \left(\frac{x}{L} \right)^2 \right) C_x - \left(C_y + (1 - m^*)\alpha \right) \frac{y}{L} \frac{x}{L} \right], \quad (3.4)$$

$$\frac{\ddot{y}}{\gamma} = \frac{1}{m^*} \left[\left(1 - \left(\frac{y}{L} \right)^2 \right) \left(C_y + (1 - m^*)\alpha \right) - C_x \frac{x}{L} \frac{y}{L} \right], \quad (3.5)$$

The parameters used in equations 3.4 and 3.5 are given in table 3.1.

The details of the derivation of the dimensionless form of the equations of motion and the meaning of parameters used will be provided in the section 3.2 dealing with sphere motions, because the derivation for the sphere system is more complicated than for the cylinder system and its reduction to the cylinder system is straightforward. For

Expression	Definition
x/L	$\cos \theta$
y/L	$\sin \theta$
C_x	$F_x/(\frac{1}{2}\rho_f AU^2)$
C_y	$F_y/(\frac{1}{2}\rho_f AU^2)$
m^*	ρ_b/ρ_f
α	$\frac{\pi gD}{2U^2}$
γ	$\frac{2U^2}{\pi D}$

TABLE 3.1: Expressions for the equations 3.4 and 3.5. ρ_f and ρ_b are the density of the fluid and the cylinder respectively. The A is the projected area defined by $A = DB$ where D and B are the diameter and the length of the cylinder.

the same reason, the coordinate transformation to a non-inertial frame employed both for the cylinder and the sphere will also be explained only for the sphere system.

3.2 Problem Formulation: Tethered Sphere

The tethered sphere system is described in figure 3.2. As in the cylinder system, forces acting on the sphere are tether tension T , buoyancy force B , body weight W , streamwise fluid force F_x , transverse fluid force F_y . In addition, the lateral fluid force F_z is considered for the sphere case.

The tension is linked to the other force components by

$$T = F_x \cos \theta + (F_y + B - W) \sin \theta \cos \phi + F_z \sin \theta \sin \phi, \quad (3.6)$$

where the tether angle θ is the angle to the sphere from the streamwise (x) axis, and ϕ is the the inclination angle of the sphere in the crossflow plane (yz plane). This is just a statement of radial force balance. Similar to the tethered cylinder system, the tether angle plus the layover angle of Williamson & Govardhan (1997) equals 90° or $\frac{\pi}{2}$.

The equations of motion for the sphere are given by

$$m\ddot{x} = F_x - T \cos \theta, \quad (3.7)$$

$$m\ddot{y} = (F_y + B - W) - T \sin \theta \cos \phi, \quad (3.8)$$

$$m\ddot{z} = F_z - T \sin \theta \sin \phi. \quad (3.9)$$

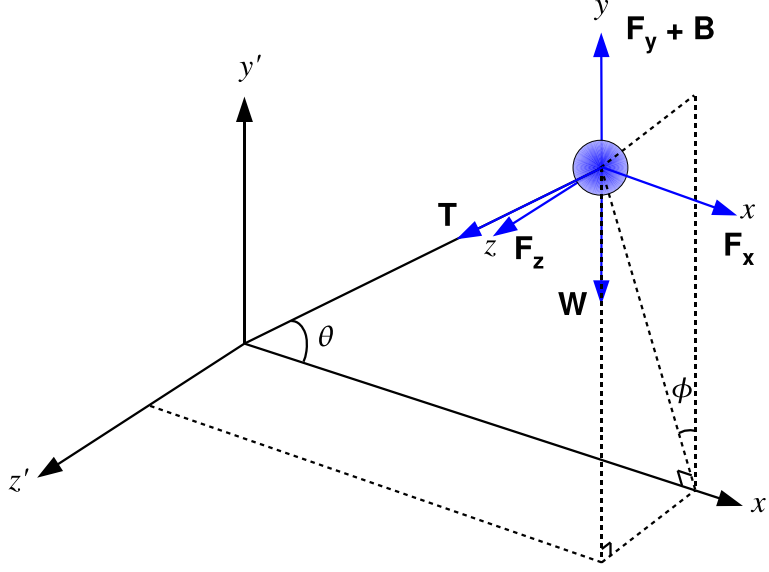


FIGURE 3.2: Coordinate system and forces on a tethered sphere.

In order to avoid repetition, only the x component of the equations of motion is dealt with in detail. Substituting equation 3.6 into equation 3.7 and collecting terms yields

$$m\ddot{x} = F_x \sin^2 \theta - \{(F_y + B - W) \cos \phi + F_z \sin \phi\} \sin \theta \cos \theta. \quad (3.10)$$

Equation 3.10 is in dimensional form, so the dimensionless forms of the fluid forces and buoyancy are used to obtain

$$\ddot{x} = \left(\frac{\rho_f}{\rho_b}\right) \left(\frac{U^2 A}{2\mathcal{V}}\right) \left[C_x \sin^2 \theta - \left\{ \left(C_y + \left(1 - \frac{\rho_f}{\rho_b}\right) \frac{2g\mathcal{V}}{U^2 A} \right) \cos \phi + C_z \sin \phi \right\} \cos \theta \right] \sin \theta. \quad (3.11)$$

where \mathcal{V} is the volume of the sphere and A is the frontal area of the sphere. C_x , C_y and C_z are the force coefficients in the x , y and z directions respectively.

Figure 3.2 is used to relate the polar coordinates in equation 3.11 to Cartesian coordinates. The acceleration of the sphere thus becomes

$$\ddot{x} = \left(\frac{\rho_f}{\rho_b}\right) \left(\frac{U^2 A}{2\mathcal{V}L^2}\right) \left[(L^2 - x^2)C_x - \left\{ \left(C_y + \left(1 - \frac{\rho_f}{\rho_b}\right) \frac{2g\mathcal{V}}{U^2 A} \right) y + C_z z \right\} \right]. \quad (3.12)$$

In equation 3.12, the parameters are defined as follows for the sphere system.

$$\alpha = \frac{2g\mathcal{V}}{U^2 A} = \frac{2g(\pi D^3/6)}{U^2(\pi D^2/4)} = \frac{4gD}{3U^2}, \quad (3.13)$$

$$\gamma = \frac{U^2 A}{2\mathcal{V}} = \frac{U^2(\pi D^2/4)}{2(\pi D^3/6)} = \frac{3U^2}{4D}. \quad (3.14)$$

Due to the difference in \mathcal{V} and A to the cylinder system, the parameters α and γ for the sphere is different to those for the cylinder as shown in equations 3.13 and 3.14. Note that α has no dimension, whereas γ has units of acceleration.

Substitution of the above parameters into equation 3.12 results in the equations of motion for the tethered sphere including the y and z components

$$\frac{\ddot{x}}{\gamma} = \frac{1}{m^*} \left[\left\{ 1 - \left(\frac{x}{L} \right)^2 \right\} C_x - \left(C_y + (1 - m^*)\alpha \right) \frac{y}{L} \frac{x}{L} + C_z \frac{z}{L} \frac{x}{L} \right], \quad (3.15)$$

$$\frac{\ddot{y}}{\gamma} = \frac{1}{m^*} \left[\left\{ 1 - \left(\frac{y}{L} \right)^2 \right\} \left(C_y + (1 - m^*)\alpha \right) - C_x \frac{x}{L} \frac{y}{L} + C_z \frac{z}{L} \frac{y}{L} \right], \quad (3.16)$$

$$\frac{\ddot{z}}{\gamma} = \frac{1}{m^*} \left[\left\{ 1 - \left(\frac{z}{L} \right)^2 \right\} C_z - C_x \frac{x}{L} \frac{z}{L} + \left(C_y + (1 - m^*)\alpha \right) \frac{y}{L} \frac{z}{L} \right]. \quad (3.17)$$

The parameters used in equations 3.15 to 3.17 are presented in table 3.2.

Expression	Definition
x/L	$\cos \theta$
y/L	$\sin \theta \cos \phi$
z/L	$\sin \theta \sin \phi$
C_x	$F_x / (\frac{1}{2} \rho_f A U^2)$
C_y	$F_y / (\frac{1}{2} \rho_f A U^2)$
C_z	$F_z / (\frac{1}{2} \rho_f A U^2)$
m^*	ρ_b / ρ_f
α	$\frac{4}{3} \frac{qD}{U^2}$
γ	$\frac{3}{4} \frac{U^2}{D}$

TABLE 3.2: Expressions for the equations 3.15 to 3.17. ρ_f and ρ_b are the density of the fluid and the cylinder respectively. The A is the projected area defined by $A = \pi D^2/4$ where D is the diameter of the sphere.

3.3 Coordinate Transformation to a Tethered Body

Solving fluid-structure interaction problems generally involves the use of deforming or moving computational domains. The arbitrary Lagrangian-Eulerian (ALE) formulation has been used successfully in the past for spectral discretisation (Warburton & Karniadakis 1996). However, in the present study of the tethered sphere (also of the tethered cylinder), the difficulty of using the deforming mesh is avoided by attaching

the reference frame to the sphere centre. From figure 3.2, this mapping is given by the following transformation:

$$\begin{aligned}x &= x' - x_B(t), \\y &= y' - y_B(t), \\z &= z' - z_B(t)\end{aligned}\tag{3.18}$$

where

$$\begin{aligned}x_B(t) &= L \cos(\theta(t)), \\y_B(t) &= L \sin(\theta(t)) \cos(\phi(t)), \\z_B(t) &= L \sin(\theta(t)) \sin(\phi(t)).\end{aligned}\tag{3.19}$$

Similarly, the velocity and pressure fields are transformed as follows.

$$\begin{aligned}u &= u' - \frac{dx_B}{dt}, \\v &= v' - \frac{dy_B}{dt}, \\w &= w' - \frac{dz_B}{dt}, \\p &= p'.\end{aligned}\tag{3.20}$$

Equation 3.18 provides the relationship between an inertial coordinate system (denoted by a prime) and the non-inertial coordinate system attached to the sphere. These equations for the tethered sphere and the Navier-Stokes equations for fluid (to be discussed in section 3.4.1) are solved in the non-inertial frame.

3.4 Numerical Method

Assumptions are made to simulate the fluid flow. The fluid is assumed to be a continuum, Newtonian, and incompressible. These are standard assumptions and their details can be found in many textbooks (Munson *et al.* (2006) for example). With these assumptions, the Navier-Stokes and continuity equations governing the unsteady viscous motion of the fluid are given by

$$\frac{\partial \mathbf{V}}{\partial t} = -\frac{1}{\rho_f} \nabla P + \nu \mathbf{L}(\mathbf{V}) - \mathbf{N}(\mathbf{V})\tag{3.21}$$

and

$$\nabla \cdot \mathbf{V} = 0,\tag{3.22}$$

where \mathbf{V} and P are the fluid velocity field and the pressure field, respectively. $\mathbf{N}(\mathbf{V})$ represents the nonlinear convection term defined as

$$\mathbf{N}(\mathbf{V}) = (\mathbf{V} \cdot \nabla)\mathbf{V}, \quad (3.23)$$

$\nu\mathbf{L}(\mathbf{V})$ is the linear diffusion term, and the linear operator $\mathbf{L}(\mathbf{V})$ is defined as

$$\mathbf{L}(\mathbf{V}) = \nabla^2\mathbf{V}. \quad (3.24)$$

For the present problem, the displacement of the body (\mathbf{x}_B) and its velocity (\mathbf{u}_B) at the new time instance are unknown. Therefore, the coupled differential equations describing the body motion and flow field have to be solved. If we apply the coordinate transform that $\mathbf{V} = \mathbf{u} + \mathbf{u}_B$ to equations 3.21 and 3.22, these can be rewritten,

$$\frac{\partial \mathbf{u}}{\partial t} = -\nabla p + \frac{1}{Re}\mathbf{L}(\mathbf{u}) - \mathbf{N}(\mathbf{u}) + \mathbf{A}(\mathbf{x}_B, \mathbf{u}, p), \quad (3.25)$$

$$\nabla \cdot \mathbf{u} = 0, \quad (3.26)$$

where $\mathbf{A}(\mathbf{x}_B, \mathbf{u}, p)$ is an additional acceleration term introduced by the transformation and is equivalent to the acceleration of the body. Note p is the kinematic pressure, i.e., P/ρ_f . These equations were solved numerically to simulate the tethered body VIV.

Note that the following subsections focus on the tethered sphere VIV as its reduction to the tethered cylinder VIV is straightforward as mentioned previously.

3.4.1 Time-advancement of governing equations

A three-step time-splitting scheme was employed in the solution of the governing equations in time. The three substeps account for the convection, pressure and diffusion terms of the coupled Navier-Stokes equations. The acceleration term is solved in the convection substep. As a result, the three substeps are provided as follows:

$$\hat{\mathbf{u}} - \mathbf{u}^{(n)} = -\int_t^{t+\Delta t} \mathbf{N}(\mathbf{u}) dt + (\mathbf{u}_B^{(n+1)} - \mathbf{u}_B^{(n)}), \quad (3.27)$$

$$\tilde{\mathbf{u}} - \hat{\mathbf{u}} = -\int_t^{t+\Delta t} \nabla p dt, \quad (3.28)$$

$$\mathbf{u}^{(n+1)} - \tilde{\mathbf{u}} = -\frac{1}{Re}\int_t^{t+\Delta t} \mathbf{L}(\mathbf{u}) dt. \quad (3.29)$$

Here, (n) represents the present timestep, and $\hat{\mathbf{u}}$ and $\tilde{\mathbf{u}}$ are the intermediate velocity fields at the end of convection and pressure substeps, respectively. Each substep uses the solution from the previous substep as the starting condition.

3.4.1.1 Convection substep

To proceed with the solution of the coupled equations 3.25 and 3.26 with unknown displacement of the sphere at $(n + 1)$, a ‘predictor-corrector’ scheme was adopted.

For the first time through the loop, a ‘prediction’ for the velocity and for the displacement ($\mathbf{u}_B^{(n+1)*}$ and $\mathbf{x}_B^{(n+1)*}$) of the sphere are given by

$$\mathbf{u}_B^{(n+1)*} = 3\mathbf{u}_B^{(n)} - 3\mathbf{u}_B^{(n-1)} + \mathbf{u}_B^{(n-2)}, \quad (3.30)$$

$$\mathbf{x}_B^{(n+1)*} = \mathbf{x}_B^{(n)} + \left(\frac{5}{12}\mathbf{u}_B^{(n+1)*} + \frac{8}{12}\mathbf{u}_B^{(n)} - \frac{1}{12}\mathbf{u}_B^{(n-1)} \right) \Delta t. \quad (3.31)$$

Note that equation 3.30 is just a quadratic extrapolation from known values at the previous timesteps.

With these predictions, equation 3.27 is solved explicitly using a third-order Adams-Bashforth scheme given by

$$\begin{aligned} \hat{\mathbf{u}} &= \mathbf{u}^{(n)} \\ &+ \left[\frac{23}{12}\mathbf{N}(\mathbf{u})^{(n)} - \frac{16}{12}\mathbf{N}(\mathbf{u})^{(n-1)} + \frac{5}{12}\mathbf{N}(\mathbf{u})^{(n-2)} \right] \Delta t \\ &- \left(\mathbf{u}_B^{(n+1)*} - \mathbf{u}_B^{(n)} \right). \end{aligned} \quad (3.32)$$

Note that, for subsequent iterations, a semi-implicit method is used instead and is provided later. Following this, the remaining two substeps are solved to obtain the first estimate of the fluid velocity field $\mathbf{u}^{(n+1)}$. These two substeps are explained in section 3.4.1.2 and 3.4.1.3.

Once the velocity field is estimated, a ‘correction’ to $\mathbf{u}_B^{(n+1)}$ and $\mathbf{x}_B^{(n+1)}$ commences. The forces on the sphere are calculated from the estimate of the fluid velocity at the end of the time ($\mathbf{u}^{(n+1)}$), and are used to get the acceleration of the body at that time ($\ddot{\mathbf{x}}_B^{(n+1)}$) with equations 3.15 to 3.17. The equations for this correction scheme are given by

$$\mathbf{u}_B^{(n+1)} = \mathbf{u}_B^{(n)} + \left(\frac{25}{24}\ddot{\mathbf{x}}_B^{(n+1)} - \frac{2}{24}\ddot{\mathbf{x}}_B^{(n)} + \frac{1}{24}\ddot{\mathbf{x}}_B^{(n-1)} \right) \Delta t, \quad (3.33)$$

$$\mathbf{x}_B^{(n+1)} = \mathbf{x}_B^{(n)} + \left(\frac{5}{12}\mathbf{u}_B^{(n+1)} + \frac{8}{12}\mathbf{u}_B^{(n)} - \frac{1}{12}\mathbf{u}_B^{(n-1)} \right) \Delta t. \quad (3.34)$$

This finalises the first iteration of the convection substep.

For subsequent iterations, a semi-implicit, third-order Adams-Moulton method is employed to improve the stability of the numerical scheme, and to utilise the fluid

information obtained from the previous iterations.

$$\begin{aligned}\hat{\mathbf{u}} &= \mathbf{u}^{(n)} \\ &+ \left[\frac{5}{12} \mathbf{N}(\mathbf{u})^{(n+1)} + \frac{8}{12} \mathbf{N}(\mathbf{u})^{(n)} - \frac{1}{12} \mathbf{N}(\mathbf{u})^{(n-1)} \right] \Delta t \\ &- \left(\mathbf{u}_B^{(n+1)} - \mathbf{u}_B^{(n)} \right).\end{aligned}\quad (3.35)$$

As in the first iteration, the two substeps are solved to obtain a new estimate of $\mathbf{u}^{(n+1)}$.

The correction then starts with equation 3.33. However, an under-relaxation parameter ε is introduced to improve stability before updating the sphere displacement. Therefore, the correction procedure from the second iteration is given by

$$\mathbf{u}_B^* = \mathbf{u}_B^{(n)} + \left(\frac{25}{24} \ddot{\mathbf{x}}_B^{(n+1)} - \frac{2}{24} \ddot{\mathbf{x}}_B^{(n)} + \frac{1}{24} \ddot{\mathbf{x}}_B^{(n-1)} \right) \Delta t, \quad (3.36)$$

$$\mathbf{u}_B^{(n+1)} = \mathbf{u}_B^{(n)} + \varepsilon \left(\mathbf{u}_B^* - \mathbf{u}_B^{(n)} \right), \quad (3.37)$$

$$\mathbf{x}_B^{(n+1)} = \mathbf{x}_B^{(n)} + \left(\frac{5}{12} \mathbf{u}_B^{(n+1)} + \frac{8}{12} \mathbf{u}_B^{(n)} - \frac{1}{12} \mathbf{u}_B^{(n-1)} \right) \Delta t. \quad (3.38)$$

3.4.1.2 Pressure substep

The second substep solves equation 3.28 using a second-order Adams-Moulton method, giving

$$\tilde{\mathbf{u}} = \hat{\mathbf{u}} - \Delta t \left(\frac{1}{2} \nabla p^{(n+1)} + \frac{1}{2} \nabla p^{(n)} \right), \quad (3.39)$$

where $\tilde{\mathbf{u}}$ is a second intermediate velocity field. By taking the divergence of equation 3.39 and imposing the continuity constraint for $\tilde{\mathbf{u}}$, a Poisson equation for the pressure is obtained

$$\nabla^2 p^{(n+\frac{1}{2})} = \frac{1}{\Delta t} \nabla \cdot \hat{\mathbf{u}}. \quad (3.40)$$

The pressure field at $(n + \frac{1}{2})$ could be obtained by solving equation 3.40, and this pressure field is then substituted back into equation 3.39 to obtain the second intermediate velocity field $\tilde{\mathbf{u}}$. This equation has to be solved with a Neumann boundary condition for pressure on the boundary surface, reducing splitting errors. This pressure boundary condition is explained in section 3.4.3.

3.4.1.3 Diffusion substep

The third and final substep involves solving equation 3.29 for the diffusion terms as follows:

$$\mathbf{u}^{(n+1)} = \tilde{\mathbf{u}} + \nu \Delta t \mathbf{L}(\mathbf{u}). \quad (3.41)$$

This is performed implicitly using a Crank-Nicolson method that is second-order accurate in both space and time, together with a θ scheme modification (Canuto *et al.* 2006).

Karniadakis *et al.* (1991) demonstrated that the above scheme produces time differencing errors in the velocity field that are one order smaller in Δt than the corresponding error in the boundary divergence. In particular, a time-treatment of first-order for equation 3.41 can be expected to produce second-order results in the velocity field. Note that higher-order accurate treatments are generally less stable and require reduced timesteps.

3.4.2 Spatial discretisation: Spectral-element/Fourier-spectral method

The spatial discretisation of the equations, is implemented using a nodal-based spectral-element method. This is a method from the finite-element class, where the computational domain is divided into a series of macro-elements, and a continuous solution is obtained over each element.

A two-dimensional spectral-element method is used for the tethered cylinder. Its implementation for a freely moving cylinder is described in Leontini (2007), and will not be covered in detail here. An extension of the spectral-element method to three-dimensional space was developed and applied to the geometries of a cylinder (Thompson *et al.* 1996), a sphere (Thompson *et al.* 2001) and a torus (Sheard *et al.* 2003). This is called a spectral-element/Fourier spectral method as a Fourier series expansion is applied in the third dimension. The spectral-element/Fourier spectral method employed for the simulation of tethered sphere is presented briefly in this section.

The method starts by considering the flow past a stationary sphere in cylindrical coordinates z , r and ϕ , with the origin located at the sphere centre. The acceleration term in equation 3.25 is neglected for the following formulation, but could be dealt with in the same way as is explained in this section. In this formulation, the z axis is parallel to the free stream velocity U , r is the distance to the z axis and ϕ is the azimuthal angle. Due to the homogeneity in the azimuthal direction, the velocity and pressure field can be decomposed using a Fourier series expansion in ϕ by

$$u(z, r, \phi, t) = \sum_{m=0}^{M-1} u_m(z, r, t) e^{im\phi}, \quad (3.42)$$

where m is an integer wavenumber. Substituting equation 3.42 into the governing equation (equation 3.25 without the acceleration term), and applying the change of

variables

$$\begin{aligned}\tilde{v}_m &= v_m + iw_m, \\ \tilde{w}_m &= v_m - iw_m\end{aligned}\tag{3.43}$$

gives

$$\begin{aligned}\frac{\partial u_m}{\partial t} + \mathcal{F}_m \left[\mathbf{N}(\mathbf{u}) \right]_z &= -\frac{1}{\rho_f} \frac{\partial p_m}{\partial z} + \nu \left(\nabla_{rz}^2 - \frac{m^2}{r^2} \right) u_m, \\ \frac{\partial \tilde{v}_m}{\partial t} + \tilde{\mathcal{F}}_m \left[\mathbf{N}(\mathbf{u}) \right]_r &= -\frac{1}{\rho_f} \left(\frac{\partial}{\partial r} - \frac{m}{r} \right) p_m + \nu \left(\nabla_{rz}^2 - \frac{(m+1)^2}{r^2} \right) \tilde{v}_m, \\ \frac{\partial \tilde{w}_m}{\partial t} + \tilde{\mathcal{F}}_m \left[\mathbf{N}(\mathbf{u}) \right]_\phi &= -\frac{1}{\rho_f} \left(\frac{\partial}{\partial r} - \frac{m}{r} \right) p_m + \nu \left(\nabla_{rz}^2 - \frac{(m-1)^2}{r^2} \right) \tilde{w}_m,\end{aligned}\tag{3.44}$$

where

$$\begin{aligned}\nabla_m &= \left(\frac{\partial}{\partial z}, \frac{\partial}{\partial r}, i \frac{m}{r} \right), \\ \nabla_m^2 &= \frac{\partial^2}{\partial z^2} + \frac{1}{r} \frac{\partial}{\partial r} \left(r \frac{\partial}{\partial r} \right) - \frac{m^2}{r^2}, \\ &= \nabla_{rz}^2 - \frac{m^2}{r^2},\end{aligned}\tag{3.45}$$

$$\begin{aligned}\tilde{\mathcal{F}}_m \left[\mathbf{N}(\mathbf{u}) \right]_r &= \mathcal{F}_m \left[\mathbf{N}(\mathbf{u}) \right]_r + i \mathcal{F}_m \left[\mathbf{N}(\mathbf{u}) \right]_\phi, \\ \tilde{\mathcal{F}}_m \left[\mathbf{N}(\mathbf{u}) \right]_\phi &= \mathcal{F}_m \left[\mathbf{N}(\mathbf{u}) \right]_r - i \mathcal{F}_m \left[\mathbf{N}(\mathbf{u}) \right]_\phi,\end{aligned}\tag{3.46}$$

and \mathcal{F}_m refers to a Fourier transform in ϕ .

Throughout this process, the time-integration of equation 3.21 results in a set of Helmholtz-like equations for the velocity and pressure modes given by

$$\frac{1}{r} \frac{\partial}{\partial r} \left(r \frac{\partial}{\partial r} u_m \right) - \frac{m^2}{r^2} u_m - \lambda^2 u_m = g,\tag{3.47}$$

where u_m is either a velocity or pressure Fourier mode, and the constant λ^2 is equal to zero for the pressure. To simplify the notation, equation 3.47 may be written as

$$(\nabla^2 - \lambda^2) \Phi = g,\tag{3.48}$$

subject to Dirichlet or Neumann boundary conditions on the boundaries. This completes the reformation of the governing equations.

The solution of the equation 3.48 is obtained by a method of weighted residuals (MWR) with Galerkin projection, choosing the test function and the weighting function from the same family of functions. A variational form of equation 3.48 used to find the solution is given by

$$\int_{\Omega} \nabla \Psi \cdot \nabla \Phi \, d\mathbf{x} + \lambda^2 \int_{\Omega} \Psi \Phi \, d\mathbf{x} = - \int_{\Omega} \Psi g \, d\mathbf{x},\tag{3.49}$$

where Ω represents the computational domain, \mathbf{x} represents the physical coordinate, Ψ is the weighting function, and Φ is the test function.

To calculate the integral of equation 3.49 over the entire computational domain, it is first evaluated over each element separately, and then the elemental contributions are summed together. Each quadrilateral element is mapped to a square defined over the range $[-1, 1]$ in both directions. The computational coordinates are just the orthogonal coordinates of this square. The internal node points in each element are then defined at the Gauss-Lobatto-Legendre (GLL) quadrature points of this unit square, which simplifies the approximation of the integral. The resulting equation is then

$$\begin{aligned} \sum_{k=1}^K \sum_{p=0}^N \sum_{q=0}^N \rho_{pq} J_{pq}^k \left(\nabla \Psi \cdot \nabla \Phi \right)_{\xi_{pq}^k} + \lambda^2 \sum_{k=1}^K \sum_{p=0}^N \sum_{q=0}^N \rho_{pq} J_{pq}^k \left(\Psi \Phi \right)_{\xi_{pq}^k} \\ = - \sum_{k=1}^K \sum_{p=0}^N \sum_{q=0}^N \rho_{pq} J_{pq}^k \left(\Psi g \right)_{\xi_{pq}^k}, \end{aligned} \quad (3.50)$$

where K is the number of macro-elements, $N + 1$ is the number of quadrature points, ξ_{pq}^k are the Gauss-Lobatto points, ρ_{pq} are the corresponding weights, and J_{pq}^k are the Jacobians of the transformation to the computational domain.

Lagrange polynomials of order N are chosen both for test functions and weighting functions, and are defined as

$$\Phi_i(\xi) = \Psi_i(\xi) = -\frac{(1 - \xi^2)L'_N(\xi)}{N(N + 1)L_N(\xi_i)(\xi - \xi_i)}. \quad (3.51)$$

These polynomials are also known as the GLL interpolants. The chosen nodes ξ_i are the solutions of the equation

$$(1 - \xi^2)L'_N(\xi) = 0, \quad (3.52)$$

where $L_N(\xi)$ is the Legendre polynomial of order N .

The GLL interpolants are used in all elements in the entire domain. This departs somewhat from the method employed by Tomboulides & Orszag (2000), who used Lagrange polynomials based on zeroes of Jacobi polynomials for the elements adjacent to the axis of symmetry and GLL interpolants in the rest of the elements. In the present approach, the singular terms in equation 3.48 are set equal to zero at the axis. This is equivalent to assuming that values go toward zero faster than r^2 as r approaches 0. This retains the efficiency of standard spectral-element techniques as well as preserving spectral convergence for typical axisymmetric problems (Gerritsma & Phillips 2000).

3.4.3 Boundary Conditions and Convergence

A no-slip condition is applied at the body surface both for the cylinder and the sphere. The velocity at the upstream boundary of the body, and those to either side, is set to the sum of the freestream velocity plus the negative of the body motion, to account for the accelerating frame of reference attached to the body. The transverse velocity of the body is solved for during the simulation, as explained in the section 3.4.1.1.

Imposed at the boundary downstream of the body is the condition $\frac{\partial \mathbf{u}}{\partial \mathbf{n}} = 0$, where \mathbf{n} is the unit normal vector. While this assumption is not completely physical, as long as the outlet boundary is sufficiently far from the body, and the Reynolds number is low enough so that vortex structures can exit the domain, this does not pose a significant problem. A domain size study was performed to ensure that this did not affect the results.

First-order (in time) boundary conditions are derived for the pressure at the body surface and freestream boundaries. The result of this derivation is a condition on the gradient of the pressure normal to the boundary, and is given by

$$\mathbf{n} \cdot \nabla p^{(n+\frac{1}{2})} = \frac{dp^{(n+\frac{1}{2})}}{dn} = \mathbf{n} \cdot \left[\mathbf{N}(\mathbf{u})^{(n)} + \frac{1}{Re} (\nabla \times (\nabla \times \mathbf{u}^{(n)})) \right] \text{ on } \Omega. \quad (3.53)$$

where Ω is the parts of the domain boundary on which the velocity is defined.

The use of this first-order accurate condition for the pressure resulted in second-order accuracy for the velocity. Details of this scheme and its derivation can be found in (Karniadakis *et al.* 1991). The boundary conditions are completed by imposing a constant pressure across the domain at the outlet boundary.

The convergence characteristics are improved by employing a under-relaxation factor (ε) in equation 3.37. The relaxation parameter was introduced after extensive testing; without it, it was found that for some parameter combinations, the method was unstable except for very small timesteps. This was especially the case for small mass ratios. The introduction of under-relaxation improves the convergence quality considerably. The choice of an optimal value for ε is highly problem-specific, and extensively studied by Ryan (2004); Pregalato (2003) for tethered bodies. This parameter does not affect the accuracy provided the equations are converged at each timestep before moving to the next timestep.

The local truncation errors introduced by the approximations are typically $\mathcal{O}(\Delta t^3)$ both for the third-order Adams-Bashforth predictors and the Adams-Moulton correc-

tors used, although overall the combined problem is second-order accurate in time. Even though the errors are small, the position of the sphere drifts away from the surface defined by the tether, although only marginally over a single time step. However, when considering the long time traces that are needed for accurate determinations of oscillation amplitudes and frequencies for example, this position drifting is no longer insignificant. As a result, the sphere position is projected onto the surface defined by the tether and, for consistency, the velocity of the sphere is also projected. This stabilises the scheme without affecting the accuracy.

Finally, convergence of the system at each timestep is monitored by three convergence criteria. These are represented by the following formulae:

$$\frac{|\Delta \mathbf{u}_B|}{|\mathbf{u}_B|} < u_{tol}, \quad (3.54)$$

$$\frac{|\Delta \mathbf{u}_{max}|}{|\mathbf{u}_{max}|} < u_{tol}, \quad (3.55)$$

$$\frac{|\Delta \mathbf{F}_B|}{|\mathbf{F}_B|} < F_{tol}. \quad (3.56)$$

Equation 3.55 states that the normalised change in the velocity of the sphere between iterations must be less than some tolerance u_{tol} , whereas equation 3.56 asserts that the normalised maximum change in the velocity field between iterations must be less than the tolerance u_{tol} at any point in the entire domain. The last convergence criterion ensures that the normalised change in the force of the body between iterations is less than some tolerance F_{tol} . For all of the simulations, the values of u_{tol} and F_{tol} were kept at 0.001 and 0.001, respectively. If these criteria are not met, then the iteration continues. However, if equations 3.55 to 3.56 are satisfied, then we continue to the next step.

3.5 Definition of Controlling Parameters

There have been a number of suggestions of the most appropriate parameters to use to characterise VIV of bluff bodies. The reduced velocity U^* has been extensively used, and most studies in VIV have adopted it as a controlling parameter to present results. To define U^* , the natural frequency of the body f_n is used. A reason why f_n is chosen as a normalising factor is that it is independent of the flow condition for a transversely vibrating circular cylinder, which is the target body of much VIV research. However, the adoption of f_n is a shortcoming for tethered body VIV due to its dependence

on the flow condition. As alternatives, the Fr and its modified version, the reduced Froude number Fr' , have been suggested for the tethered body VIV (Ryan *et al.* 2007; Carberry & Sheridan 2007). The appropriateness of Fr related parameters, however, has not been sufficiently verified for a wide range of body mass.

In the current study, the Re and the U^* are used to present the results for a couple of reasons. Firstly, the Re is chosen because of the focus on neutral buoyancy of the tethered bodies. When $m^* = 1$, there is no buoyancy (gravity) effect, thus the modified Froude number (Fr'), suggested in recent studies of the tethered cylinder, and the conventional U^* are of no use. For example, the Fr' has the value of ∞ , and there is virtually no restoring force for long tethers so U^* has a very large value. Therefore, the Re is used as a parameter to characterise the system behaviour. for bodies with neutral buoyancy in the present results.

Secondly, U^* is adopted in order to compare the results of buoyant tethered bodies with those of previous research. Only a few studies have dealt with the VIV of tethered bodies, and most of these, particularly for the tethered sphere case, have used U^* to present the results, in spite of its inadequacy to tethered body VIV at high U^* . For this reason, U^* is used for the results of buoyant tethered bodies, but its dependence on the flow condition is considered simultaneously.

3.6 Validation: Tethered Cylinder Case

A detailed study to validate the numerical results has been performed. This was done by comparing key properties of simulation results with different domain sizes and the grid resolutions. The latter can be done using h -refinement (i.e., adding more elements) and p -refinement (i.e., increasing the polynomial order within each element) (Karniadakis & Sherwin 2005) in the spectral-element context.

Firstly, a mass ratio was fixed at unity to consider the neutrally buoyant case, and the results using four different meshes were compared at selected Reynolds numbers. Having determined a suitable mesh, a grid resolution study was performed by varying the order of the tensor-product polynomials employed in the spectral-element method. To check the validity for the cases of $m^* \neq 1$, a grid resolution study for the $m^* = 0.833$ case was also carried out.

For the validation of the elastic tether results, the mass ratio was kept at $m^* = 0.833$, and the polynomial order was changed. One supercritical value and one subcritical value

of parameter k_t (see section 6.1) were chosen.

3.6.1 Mesh Independence

Four meshes were used to check their suitability for tethered cylinder VIV. As shown in figure 3.3, C1 is the smallest mesh, and C2 is the second smallest with longer outlet length than C1. C3 is the largest mesh. C4 is a similar mesh used in Ryan *et al.* (2004a), having similar dimension to C3. It should be noted that the C3 mesh was made after an extensive review of previous studies. Its domain size, the number of macro-elements, and the size of the macro-element in the near wake were determined based on the meshes used in many studies of fixed cylinders (Barkley & Henderson 1996; Thompson *et al.* 1996) and oscillating cylinders (Blackburn & Henderson 1999; Blackburn *et al.* 2001; Leontini *et al.* 2007). The domain size of each mesh is summarised in table 3.3.

Mesh	Inlet	Side	Outlet	M
C1	$5D$	$5D$	$10D$	356
C2	$5D$	$5D$	$15D$	476
C3	$15D$	$15D$	$20D$	652
C4	$15D$	$15D$	$25D$	518

TABLE 3.3: Domain size of meshes where D is the diameter of the cylinder.

The key properties that were chosen to be compared are the root-mean-square (RMS) of the displacement and the oscillation frequency in the x and y directions.

The mass ratio m^* was set to unity, and the tether length was set to $10D$. Two Reynolds numbers of 100 and 200 were selected. $Re = 100$ is chosen as it represents the increasing St range in the $St-Re$ chart (Williamson 1988a). The $Re = 200$ is selected as the highest Re for two-dimensional simulations. The sixth-order tensor-product polynomials were used for the domain study.

Table 3.4 shows the key properties when $Re = 100$ and $m^* = 1$. The frequencies and the force coefficients in both directions show values different to those of C3, whereas C4 shows similar values of these properties. Based on these, C1 and C2 meshes have a significant blockage effect.

Table 3.5 shows the results when $Re = 200$. Similar to the $Re = 100$ case, C1 and C2 produce quite different results to those for C3 and C4.

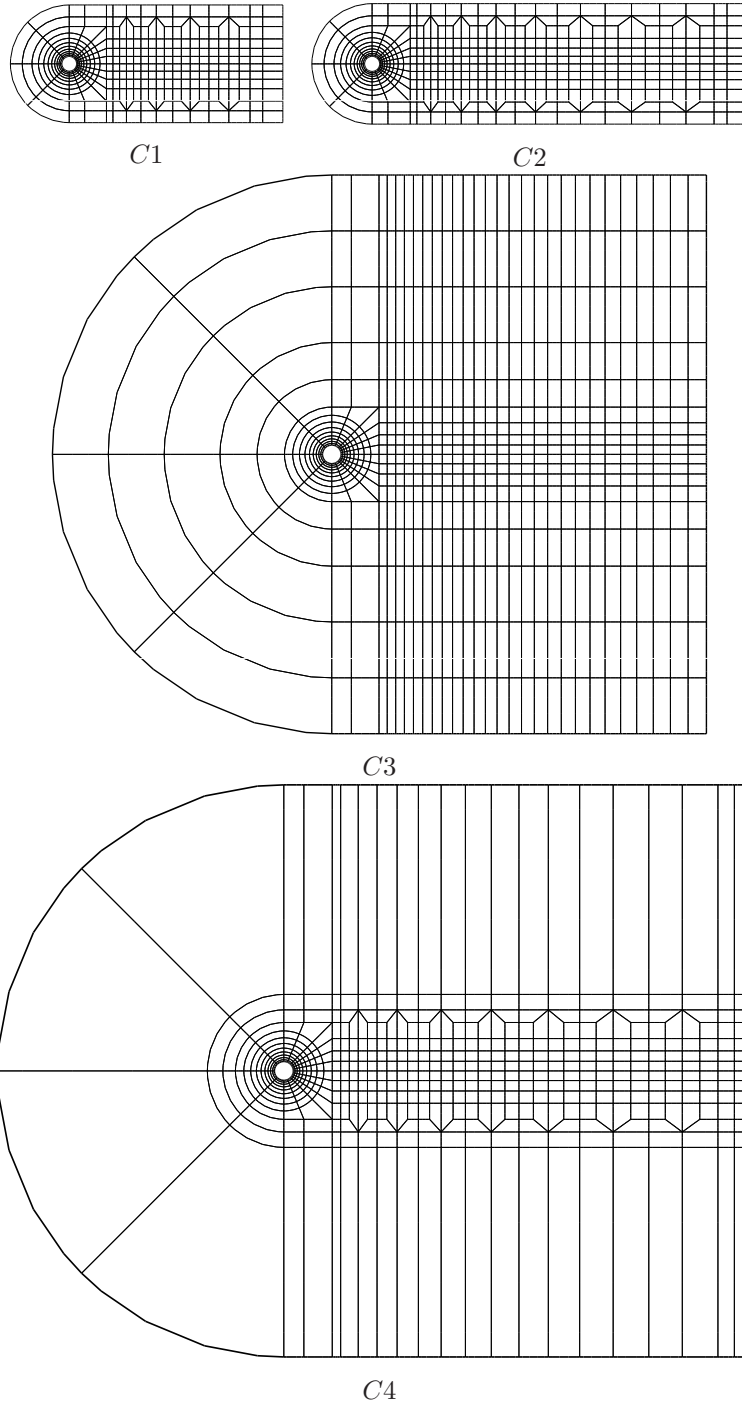


FIGURE 3.3: Meshes for tethered cylinder.

Therefore, it is determined that $C1$ and $C2$ have a significant blockage effect. The blockage ratio for meshes $C3$ and $C4$ is $1/30$. The domain size of these two meshes is also consistent with many previous studies of oscillating cylinder using various meshes.

Considering the elastic tether cases which may exhibit large oscillations, C3 is chosen for the all simulations of tethered cylinder VIV in this thesis.

Mesh	x_{RMS}^*	f_x^*	y_{RMS}^*	f_y^*	C_x	C_y
C1	0.0004	0.1678	0.0413	0.1678	1.5201	0.0132
C2	0.0004	0.1678	0.0411	0.1678	1.5199	0.0131
C3	0.0005	0.1465	0.0483	0.1465	1.2897	0.0125
C4	0.0005	0.1465	0.0478	0.1465	1.2893	0.0123

TABLE 3.4: Result using different meshes when $Re = 100$ and $m^* = 1$. x_{RMS}^* , f_x^* and C_x are root-mean-square value of the displacement, frequency of the oscillation and force coefficient in the x direction respectively. y_{RMS}^* , f_y^* and C_y correspond to those in the y direction.

Mesh	x_{RMS}^*	f_x^*	y_{RMS}^*	f_y^*	C_x	C_y
C1	0.0002	0.1831	0.0693	0.1831	1.3820	0.0006
C2	0.0002	0.1831	0.0692	0.1831	1.3815	0.0005
C3	0.0002	0.1709	0.0701	0.1709	1.2069	0.0006
C4	0.0002	0.1709	0.0709	0.1709	1.2076	0.0006

TABLE 3.5: Result using different meshes when $Re = 200$ and $m^* = 1$. The properties are the same as in table 3.4.

3.6.2 Grid Resolution Study

Using the C3 mesh, the order of Lagrange polynomials was changed to study grid resolution for the tethered cylinder VIV. As the polynomial order is raised, the grid resolution increases. The polynomial order, p , was varied from 4 to 9. Note that $N \times N$ internal points within each macro-element corresponds to a polynomial order of $N - 1$.

Firstly, the inelastic tethered cylinder case is tested. The properties chosen for comparison are the same as those used in the domain size studies. Tables 3.6 and 3.9 show the results for $Re = 100$ and $Re = 200$. The values for the x direction show no difference to the number of decimal places shown in the tables. The values for the y direction show a small difference, but all the values are well within 1%, except for C_y of 5×5 at $Re = 100$. Based on this, the polynomial of order $p = 6$ (7×7 internal node

points) is selected, and should give an accurate solution for this study without huge computational cost.

$\mathbf{N} \times \mathbf{N}$	x_{RMS}^*	f_x^*	y_{RMS}^*	f_y^*	C_x	C_y
5×5	0.0005	0.1465	0.0486	0.1465	1.2897	0.0130
6×6	0.0005	0.1465	0.0485	0.1465	1.2896	0.0116
7×7	0.0005	0.1465	0.0482	0.1465	1.2898	0.0126
8×8	0.0005	0.1465	0.0484	0.1465	1.2899	0.0117
9×9	0.0005	0.1465	0.0482	0.1465	1.2899	0.0126
10×10	0.0005	0.1465	0.0482	0.1465	1.2899	0.0122

TABLE 3.6: Result using different polynomial orders when $Re = 100$ and $m^* = 1$ with inelastic tether. The properties are the same as in table 3.4.

$\mathbf{N} \times \mathbf{N}$	x_{RMS}^*	f_x^*	y_{RMS}^*	f_y^*	C_x	C_y
5×5	0.0002	0.1678	0.0701	0.1678	1.2077	0.0007
6×6	0.0002	0.1709	0.0701	0.1709	1.2069	0.0006
7×7	0.0002	0.1709	0.0702	0.1709	1.2071	0.0005
8×8	0.0002	0.1709	0.0703	0.1709	1.2074	0.0005
9×9	0.0002	0.1709	0.0703	0.1709	1.2075	0.0005
10×10	0.0002	0.1709	0.0704	0.1709	1.2076	0.0005

TABLE 3.7: Result using different polynomial orders when $Re = 200$ and $m^* = 1$ with inelastic tether. The properties are the same as in table 3.4.

Secondly, grid resolution is checked for the VIV of an elastically tethered sphere. The Reynolds number was fixed at $Re = 200$ and the tether length was set to $L = 10D$. As the effect of elasticity is prominent in the $m^* \neq 1$ cases, the mass ratios were chosen to be $m^* = 0.833$. Two elastic cases were selected: one ($k_t = 0.1$) below the critical value of the parameter k_t , and the other ($k_t = 5$) above the critical value. The parameter k_t and its critical value are introduced and explained detail in chapter 6.

Tables 3.8 and 3.9 show the results. Regardless of the k_t values, there is little dependence on the polynomial order, p , when the $p \geq 5$. Considering the computational cost and the accuracy of the converged solution, the polynomial order of $p = 5$ is chosen for the VIVs of elastically tethered cylinder. Note that this p value, which is lower than $p = 6$ for the inelastic case, is chosen because of the longer time to reach the asymptotic state for the elastic case than that for the inelastic case.

$\mathbf{N} \times \mathbf{N}$	x_{RMS}^*	f_x^*	y_{RMS}^*	f_y^*	C_x	C_y
5×5	0.0104	0.1678	0.0733	0.1678	1.1979	0.0011
6×6	0.0104	0.1678	0.0733	0.1678	1.1971	0.0013
7×7	0.0104	0.1678	0.0733	0.1678	1.1975	0.0015
8×8	0.0104	0.1678	0.0734	0.1678	1.1978	0.0016
9×9	0.0104	0.1678	0.0734	0.1678	1.1979	0.0016
10×10	0.0104	0.1678	0.0735	0.1678	1.1980	0.0016

TABLE 3.8: Result using different polynomial orders when the tether is elastic ($k_t = 0.1$) and $m^* = 1$. The properties are the same as in table 3.4.

$\mathbf{N} \times \mathbf{N}$	x_{RMS}^*	f_x^*	y_{RMS}^*	f_y^*	C_x	C_y
5×5	0.0076	0.1678	0.0701	0.1678	1.1944	-0.0067
6×6	0.0076	0.1678	0.0701	0.1678	1.1937	-0.0070
7×7	0.0076	0.1678	0.0701	0.1678	1.1940	-0.0071
8×8	0.0076	0.1678	0.0702	0.1678	1.1943	-0.0071
9×9	0.0076	0.1678	0.0702	0.1678	1.1944	-0.0071
10×10	0.0076	0.1678	0.0703	0.1678	1.1945	-0.0071

TABLE 3.9: Result using different polynomial orders when the tether is elastic ($k_t = 5$) and $m^* = 1$. The properties are the same as in table 3.4.

3.7 Validation: Tethered Sphere Case

A validation study for tethered sphere VIV has also been performed. Similar to the tethered cylinder case, a nearly optimal mesh was first constructed based on meshes from the previous studies for fixed and oscillating spheres. The key fluid properties and sphere motions for different domain sizes and the grid resolutions were compared to determine the grid, which generates accurate and computationally practical solutions.

3.7.1 Mesh Independence

Three meshes shown in figure 3.4 were used to validate the numerical results. In particular, S1 is constructed after an extensive search of the literature dealing with the flow simulations around a sphere. From the literature, it was reported that for a fixed sphere in a freestream, the inlet extent and radial extent of $5D$ and $10D$ show little difference in terms of fluid properties (Tomboulides & Orszag 2000; Pregalato 2003). In addition, it was also reported that the result of the outlet extent of $20D$ exhibits

little difference to that of $40D$ (Tomboulides & Orszag 2000; Ghidersa & Dušek 2000). With these findings, the radial and inlet extent of the mesh S1 was set to $5D$, and the outlet extent set to $20D$, for computational efficiency with marginal error in the solutions relative to the unconfined case.

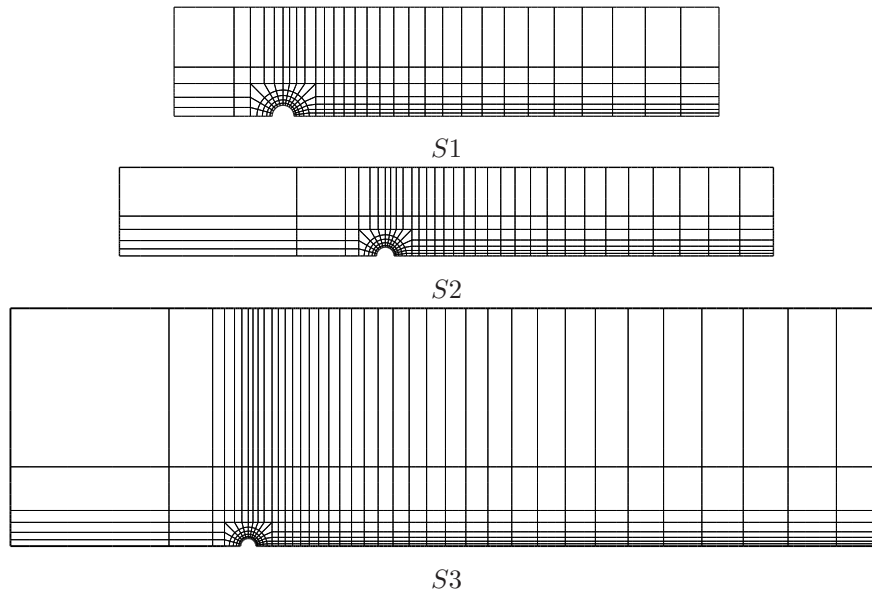


FIGURE 3.4: Meshes for tethered sphere.

Care was taken to decide the element size close to the sphere. The size of the elements adjacent to the sphere was chosen according to the boundary layer thickness for axisymmetric laminar boundary layers. From estimates of the boundary layer thickness, the required size of the elements was derived following (Tomboulides & Orszag 2000; Gottlieb & Orszag 1977) for spectral methods. According to this requirement, the element thickness of all meshes was set to $0.1D$, which allows polynomial order down to 4 for $Re = 1000$. A quick calculation shows that polynomials of order 5 can be used for accurate resolution of the boundary layer, even for a Reynolds number of $Re = 1000$.

S2 and S3 meshes were used to test whether the S1 mesh has an excessive blockage effect. These meshes were extended from the S1 mesh to have the longer inlet and the longer radial extent. The domain size of each mesh is presented in table 3.10.

The three-dimensional mesh generated by rotating the S1 mesh around the axis of symmetry is shown in figure 3.5, with all its internal node points. This gives a better understanding of the size and the resolution of the mesh used for the tethered sphere

Mesh	Inlet	Side	Outlet	M
S1	$5D$	$5D$	$20D$	239
S2	$15D$	$5D$	$20D$	251
S3	$15D$	$15D$	$40D$	338

TABLE 3.10: Domain size of meshes.

simulations.

At $Re = 300$, the flow past a stationary sphere is known to be unsteady and characterised by the presence of periodically shed vortices. In addition, the tethered sphere shows a periodic oscillation around its mean radial position with amplitude around $0.8D$ at this Reynolds number. Note that this oscillation and radial mean position are some of the largest values (even though it is small in magnitude) from the tethered sphere simulations at various Reynolds numbers within periodic regimes. Based on this, the Reynolds number of 300 was selected, then mean values of the tether angle, and the radial oscillation amplitude were computed to compare the results.

Table 3.11 indicates that S1 is large enough for the tethered sphere simulation.

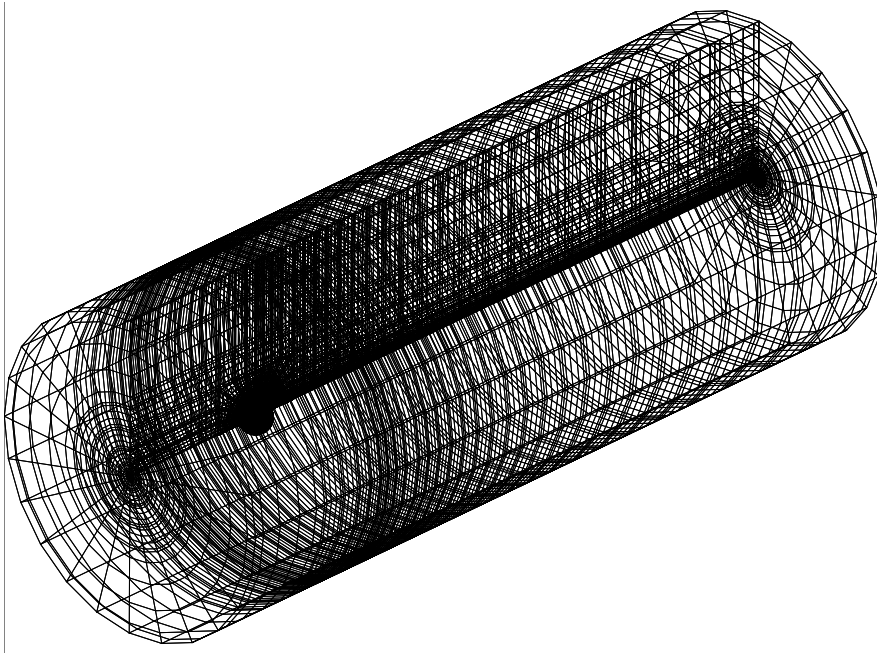


FIGURE 3.5: Three-dimensional mesh using the S1 mesh ($p = 5$) for the tethered sphere. This is the full mesh used for the tethered sphere simulations. Only surface nodes are shown.

Thus, the S1 mesh was used for all the simulations for the tethered sphere.

Mesh	θ°	A_{tot}^*
S1	4.12	0.0346
S2	3.98	0.0351
S3	4.11	0.0348

TABLE 3.11: θ is the tether angle, and A_{tot}^* is the sum of the normalised amplitude in all three directions. The results are for the tethered sphere with $m^* = 1.0$ and $10D$ tether length at $Re = 300$. All the values are the time-mean values.

3.7.2 Grid Resolution Study

Having checked the validity of the S1 mesh, the resolution of the mesh required to fully resolve the flow was studied by changing the order of the Lagrange polynomial interpolants as in the tethered cylinder case. Due to the need for considerably increased computational resources than for the cylinder case (because the flow is three-dimensional not two-dimensional), the study was carried out at a Reynolds number of $Re = 300$ for inelastically-tethered sphere. For comparison, the mean values of force coefficients in each direction are calculated

$\mathbf{N} \times \mathbf{N}$	C_x	C_y	C_z
5×5	0.679	-0.0207	0.057
6×6	0.677	0.0025	0.062
7×7	0.677	0.0027	0.061
8×8	0.677	0.0027	0.061
9×9	0.678	0.0028	0.061

TABLE 3.12: Streamwise fluid force coefficient C_x , transverse fluid force coefficient C_y and lateral fluid force coefficient C_z with the increase of polynomial interpolant p . The results are for the tethered sphere with $m^* = 1.0$ and $10D$ tether length at $Re = 300$. All coefficients are the time-mean values.

Table 3.12 indicates that the most cost-effective simulations are obtained when $\mathbf{N} \times \mathbf{N} = 6 \times 6$ (the polynomial order, $p = 5$). This is cost-effective in the sense that all scales observed in the flow for the Reynolds numbers considered (less than 1000) are clearly resolved, and running the simulations using $p = 5$ is much more efficient than corresponding simulations using $p = 8$, which only marginally increases the solution

quality. For these reasons, all simulations for the tethered sphere were performed using fifth-order ($p = 5$) tensor-product Lagrange polynomial interpolants. For the Reynolds numbers higher than 300, however, p value is increased from 6 ($Re = 500$) to 8 ($Re = 800$) to resolve the flow.

Having undertaken the intensive process of achieving an accurate mesh in the streamwise-radial plane, another issue remains concerning the accuracy of the results with respect to the azimuthal resolution. This was examined by altering the number of Fourier planes in the azimuthal direction. Ghidersa & Dušek (2000) showed that 6 Fourier modes, i.e., 12 Fourier planes, were sufficient in capturing the secondary instability for $Re = 275$. However, the breaking of planar symmetry for $Re \geq 350$ means that more modes are required to accurately resolve the shed vortices not only because they shed asymmetrically but also because they are coupled with the motion of the sphere. Therefore, together with the need for additional resolution to handle an increase of Re up to 800, 24 Fourier planes were selected. Other studies have shown this resolution to be sufficient (Tomboulides & Orszag 2000). Nevertheless, to confirm the validity of this number (24) of Fourier planes, force coefficients were calculated for the values of 24 and 32 at a higher Reynolds number of $Re = 500$. The difference of the coefficients for each number of Fourier planes was less than 1%, and hence is not depicted here.

3.8 Experimental Method: Tethered Sphere Case

The experimental study to validate the numerical findings for the tethered sphere and investigate the high Reynolds number cases were carried out in a recirculating free surface water channel. Upstream of the working section, water flows through a honeycomb and a thin wire mesh before going through a 9:1 contraction to the working section. The combination of the screens and contraction yield a turbulence level of less than 1.0%. The schematic of the experimental set-up is shown in figure 3.6(a) (see Lee *et al.* (2008) for the details).

Spheres of diameters of 16 mm and 9 mm made with Perspex were used for the experiments. The spheres were manufactured to be separated in half and hollowed out to adjust their buoyancy and mass distribution by putting some types of material inside. In every experiment, a piece of sponge was weighted and inserted to set the mass ratio to a specified value. A thin string with the diameter of 0.1 mm was connected to the sphere as a tether, and then the tether was attached to a 0.315 mm wire which was

vertically tensioned between the bottom of the working section and the ceiling right above it as a support. The wire tension required to suppress vibration was calculated and applied. To minimise the effect of vortex shedding of the wire, visual observations and preliminary video analysis of moving sphere with a thicker wire of 0.5 mm and a thinner wire of 0.15 mm were performed. Based on this observation, it was expected that the effect of wire vortex shedding on the sphere movement is negligible although a part of experiments ($Re > 5000$) were above the threshold of vortex shedding for the support wire.

For the 16 mm sphere experiments, a series of images of 8-bits grayscale were captured to locate the centre of the sphere. Each image had 1360×1024 pixels and a size of 1.4 megabytes. 2 fps(frame per second), 4 fps and 8 fps were tested to record the images, and 4 fps was used in most cases. For the 9 mm sphere, a normal video camera with MiniDV tape was used to capture the sphere motion at a higher frequency of 25 fps. The recorded videos were converted to uncompressed avi files, and then each frame in an avi file was exported to an image of 720×576 pixels. Sample images are shown in figure 3.6(b).

To extract the position of the sphere recorded in the images, bitmap information was used without filtering techniques. This postprocessing procedure consists of three steps. In the first step, the diameter of the sphere in an image (usually the first of the images) and the position of its centre were identified and saved. In the second step, the number of bright bitmaps within a circle of the sphere diameter using the previously

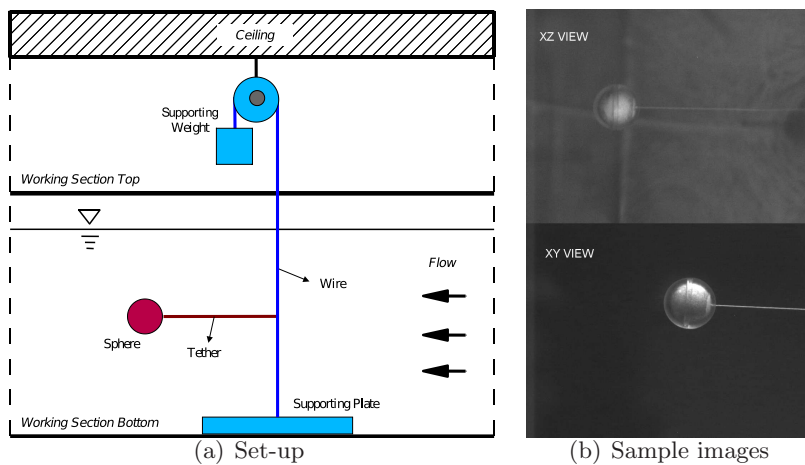


FIGURE 3.6: Schematics of the experimental set-up and sample images from the experiment.

calculated position of the sphere centre is calculated. In the third step, an optimisation function is used to find the updated and actual position of the sphere centre which maximises the number of bright bitmaps within the circle.

This method is valid only when the image has a simple background and circular object in it. To make the images better for processing, two or three spot lights were set up to focus the moving sphere during the experiments. As a result, this method was found to extract the sphere centre correctly, and was applied to process the images from the sphere experiments. This procedure was performed using specially written Matlab code using its image processing and optimisation libraries. The whole procedure was tested for a set of bitmap image data by comparing the calculated centre and boundary of the sphere with those through visual identification for all the images of the set.

3.9 Chapter Summary

In this chapter, theoretical and numerical formulations of the tethered cylinder and the tethered sphere problems were presented. Note the equations of motion are not nondimensional.

A spectral element method was used for the two dimensional simulations of the tethered cylinder system. For the tethered sphere system, fully three-dimensional simulations were performed using a spectral-element/Fourier-spectral method with a global Fourier spectral discretisation in the azimuthal (ϕ) direction.

Time advancement of the coupled equations of motion for the fluid and the cylinder/sphere was achieved using a time-splitting method with first-order pressure boundary conditions, leading to second-order time accuracy for the velocity field.

For the neutrally buoyant tethered body, the Reynolds number was put forward as the main parameter to characterise the behaviour. Since for this case the traditional characterisation parameter, the reduced velocity, is effectively infinite.

Following this, numerical validation and resolution studies were presented which allowed suitable mesh sizes and internal resolutions to be selected for the main studies presented in the following chapters.

Finally, the set-up for the experimental studies of the tethered sphere was given and the method to calculate the position of the sphere was briefly described.

Chapter 4

VIV of a Tethered Circular Cylinder

4.1 Introduction

This chapter presents the results of numerical simulations for a flow past tethered cylinder, initially focusing on a neutrally buoyant cylinder ($m^* = 1$). Next, numerical predictions for non-neutrally buoyant tethered cylinders are presented to identify differences with the neutrally buoyant case.

4.2 VIV of a Neutrally Buoyant Cylinder: $m^* = 1$

A schematic of the neutrally buoyant tethered cylinder is shown in figure 4.1. The simulations were performed using high performance computers in the range of $Re = 10 - 300$. The tether length was set to $10D$ for all cases in order to restrict the parameter space covered. For all the simulations herein, the initial tether angle was set to 1° after testing the same asymptotic states occurred with values of 0.2, 0.5, 1, 5 and 10° . As

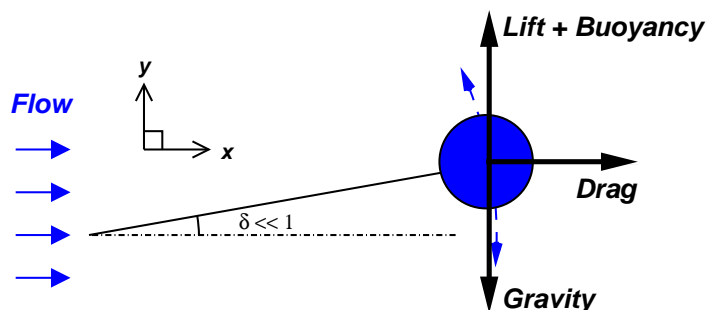


FIGURE 4.1: Schematic of a neutrally buoyant tethered cylinder.

the oscillation occurs predominantly in the transverse (y) direction, determination of the different regimes was based on the amplitude and frequency of oscillation in this direction, and layover angle measured from the y axis. The layover angle was adopted to represent the time-mean position of the body, as it has been used in previous studies on VIV of tethered bodies (Williamson & Govardhan 1997; Ryan *et al.* 2004a; Carberry & Sheridan 2007; Ryan *et al.* 2007).

4.2.1 Time-mean position: Layover angle ϑ

Three regimes have been found as the Reynolds number increases. The first regime, designated Regime I, covers the range of $Re = 10 - 30$. Regime II ranges from $Re = 40$ to 150, and Regime III from $Re = 200$ to 300. The boundaries separating these regimes are indicated in figure 4.2. In Regime I, the mean position of the cylinder is very close to, but not on, the x axis. Of note is that the layover angle $\vartheta = 90^\circ$ indicates when the cylinder is on the x axis. In Regime II, the cylinder offsets from the x axis and moves away from this axis as Re increases. As the Re further increases and exceeds 150, the approximate boundary between Regimes II and III, the cylinder returns close to the x axis but not as close as in Regime I. Of interest is that the simulations starting from the same absolute value of the initial tether angle (or layover angle), but with opposite sign, attain the same absolute value of mean position but with opposite sign.

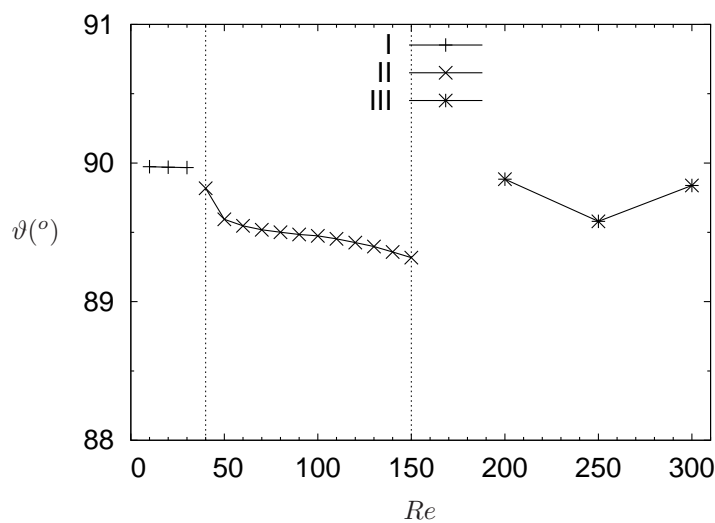


FIGURE 4.2: Layover angle ϑ of a neutrally buoyant cylinder, where $m^* = 1$. Note that the layover angles are close to 90° although there is a variation in their values.

This evidently results from the symmetry about the x axis for the neutrally buoyant ($m^* = 1$) cylinder.

4.2.2 Amplitude of oscillation

Although steady in Regime I, the cylinder oscillates in Regime II and III. Figure 4.3 shows the Root-Mean-Square (RMS) value of the dimensionless y amplitude designated as A_y^* . The RMS value was used to indicate the size of oscillation as it is appropriate both for sinusoidal and non-sinusoidal oscillations. In Regime II, the oscillation amplitude becomes larger as Re increases, counter to the trend of decreasing layover angle in this regime shown in figure 4.2. The case of $Re = 40$ was determined to be in this regime by considering both the amplitude and frequency of the oscillation. In Regime III, the amplitude jumps significantly up to about $0.2D$, and is not purely sinusoidal, contrary to that of Regime II. The time histories of the x and y positions show slowly varying behaviour superimposed on shorter period sinusoidal oscillations. The details of the time histories are shown later. This behaviour of the histories of x and y positions in Regime III for the neutrally buoyant case is different from that for the cylinder when $m^* \neq 1$.

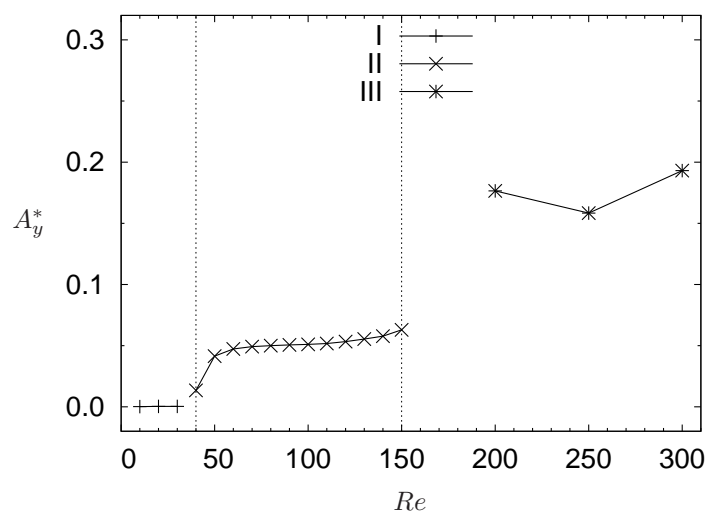


FIGURE 4.3: Amplitude of oscillation in the y direction versus Reynolds number Re for a neutrally buoyant cylinder.

4.2.3 Frequency of oscillation

The oscillation frequency is presented in dimensionless form of $St = fD/U_\infty$ in figure 4.4, where f is the oscillation frequency, D is the cylinder diameter, and U_∞ is the incoming flow speed. $St = 0$ for Regime I as there is no oscillation. In Regime II, the frequency increases as Re is increased. This increase in frequency is comparable to that of vortex shedding for a fixed cylinder within the same Re range. The St of the tethered cylinder at each Re is close to (but less than) that for a fixed cylinder. Contrary to the case of Regime II, the oscillation frequency in Regime III is virtually constant even though Re changes from 200 to 300. The saturated value is $St = 0.178$, also less than the value of 0.2 for a fixed cylinder.

The nondimensionalised natural frequency f_n^* was calculated using equation 4.1 and is in the range of $f_n^* = 0.0316 - 0.0352$. It is clear that the cylinder oscillates at a frequency higher than its natural frequency (f_n^*) but lower than the vortex shedding frequency of a fixed cylinder (f_{vo}).

$$f_n^* = \frac{f_n D}{U} = \frac{1}{2\pi} \sqrt{\frac{2}{\pi} \frac{\sqrt{C_x^2 + \{(1 - m^*)\alpha + C_y\}^2}}{(C_A + m^*)L^*}} \quad (4.1)$$

In equation 4.1, U is the inflow velocity, m^* is the mass ratio, L^* is the nondimensionalised tether length, α is the parameter defined in section 3.1 and C_A is the added

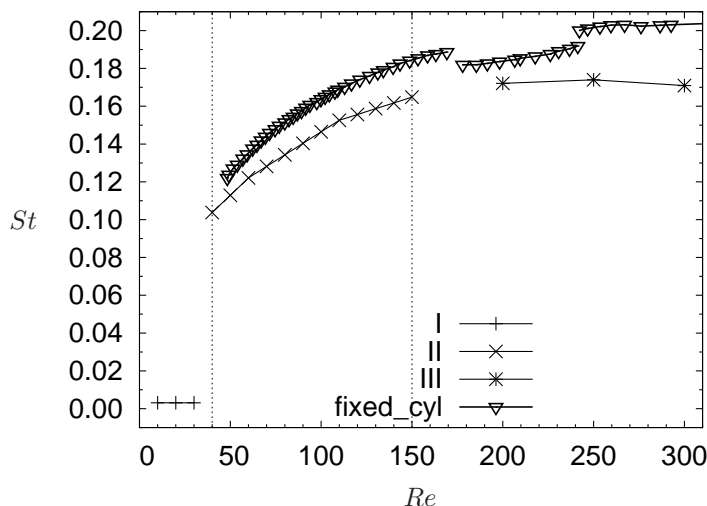


FIGURE 4.4: Frequency of oscillation in the y direction versus Reynolds number Re for a neutrally buoyant cylinder. The frequency for a fixed cylinder is the vortex shedding frequency.

mass coefficient ($C_A = 1.0$ for cylinder) of an ideal flow. Derivation of equation 4.1 is explained in detail for a sphere in section 5.2.3.

Figure 4.5 shows the results of spectral analysis of the y displacement. It is clear that the secondary and tertiary frequencies appear at the higher Reynolds numbers of $Re = 100$ and 150 within Regime II. These secondary frequencies are observable in the histories of the y displacements and are given in section 4.2.7. In Regime III, the subharmonic frequencies disappear and a range of low frequencies appears. This indicates an irregular nature to the y displacement, and is a principal difference from the response of non-neutrally buoyant cylinders.

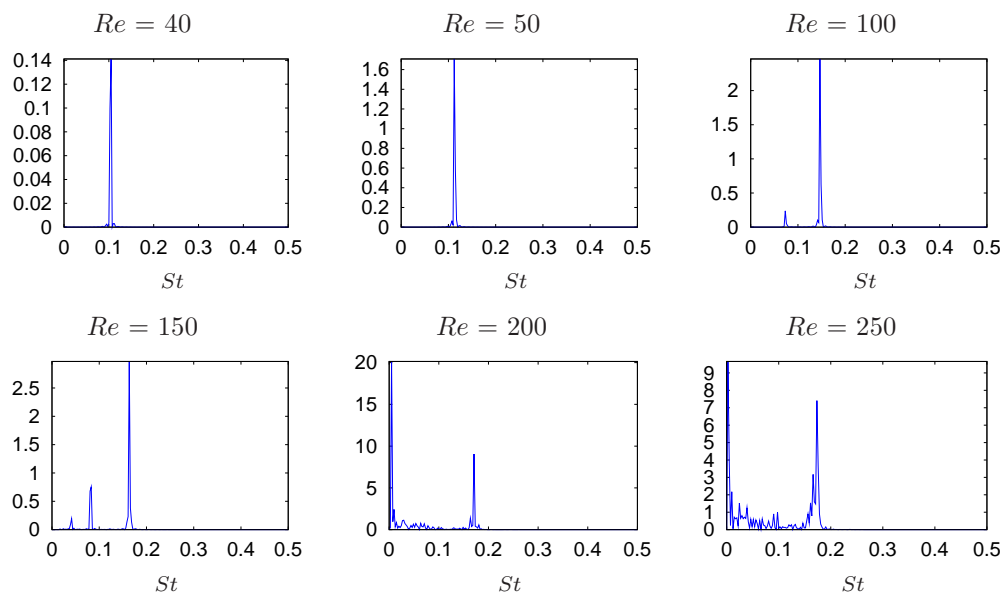


FIGURE 4.5: Power Spectra of the y oscillation. The unit of power is arbitrary. Subharmonic frequencies appear in Regime II ($Re = 100$ and 150). In Regime III ($Re = 200$ and 250), a range of low frequencies is observable below $St < 0.2$.

4.2.4 Trajectory and forcing of the oscillating cylinder

Figure 4.6 presents the trajectories of the cylinder for two oscillating regimes. Within Regime II, the y amplitude grows as Re increases, as expected from figure 4.3. In Regime III, the amplitude is greater than that of Regime II, but the growth rate of the amplitude is not as evident as in Regime II when Re is increased. Due to the neutral buoyancy and the resulting layover angle of $\vartheta \approx 90^\circ$, the trajectory for both regimes is virtually parallel to the y axis, and the trajectory keeps its symmetry about the y axis within Regime II. However, the symmetry about the y axis is lost in Regime III

because of the irregular nature of the displacement history.

Figure 4.7 shows the phase plots of C_y versus C_x . In general, the plots are in the form of a figure-of-eight, but not exactly in symmetric form about the y axis. This asymmetry is due to the fact that the layover angle ϑ is not exactly 90° for each Re and that there is a minute restoring force where $m^* = 1$.

Figures 4.8 and 4.9 show the trajectory and the phase plots of total forces in the (r, θ) coordinate system, where r and θ represent the radial and circumferential components respectively. Only the cases for higher Reynolds numbers of $Re = 150 - 250$ are presented because of their discernible patterns. As expected from the similar plots in the xy coordinates, it is obvious from figure 4.8 that the oscillation amplitude (in the φ direction) grows as Re increases in Regime II, and is saturated in Regime III. Because the radial position of the cylinder is fixed at $10D$, no variation appears in the r displacement in figure 4.8. As the layover angle $\vartheta \approx 90^\circ$, there is little difference in the phase plots of the forces between the (r, θ) coordinates and the (x, y) coordinates when $m^* = 1$.

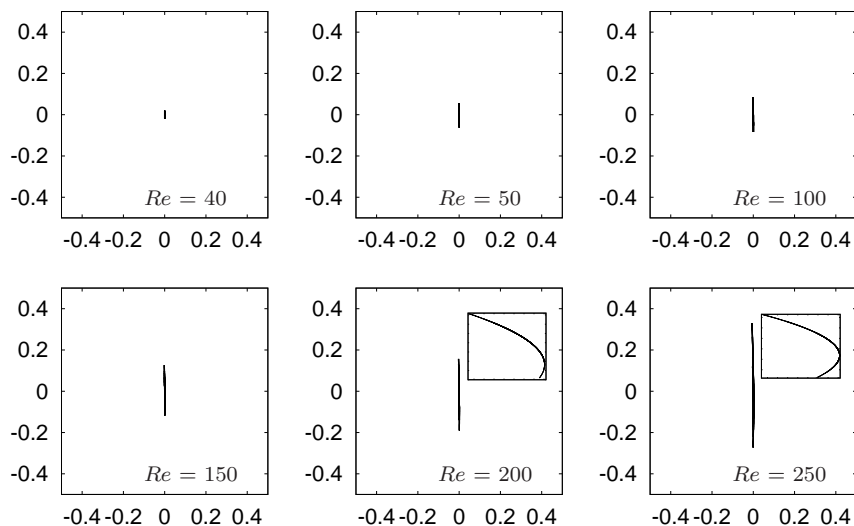


FIGURE 4.6: Trajectories of the oscillating cylinder in the xy coordinates when $m^* = 1$. The abscissa is the x displacement and the ordinate is the y displacement. The displacements are normalised by the cylinder diameter D . For $Re = 200$ and 250 , magnified and autoscaled inset are added to show their asymmetry.

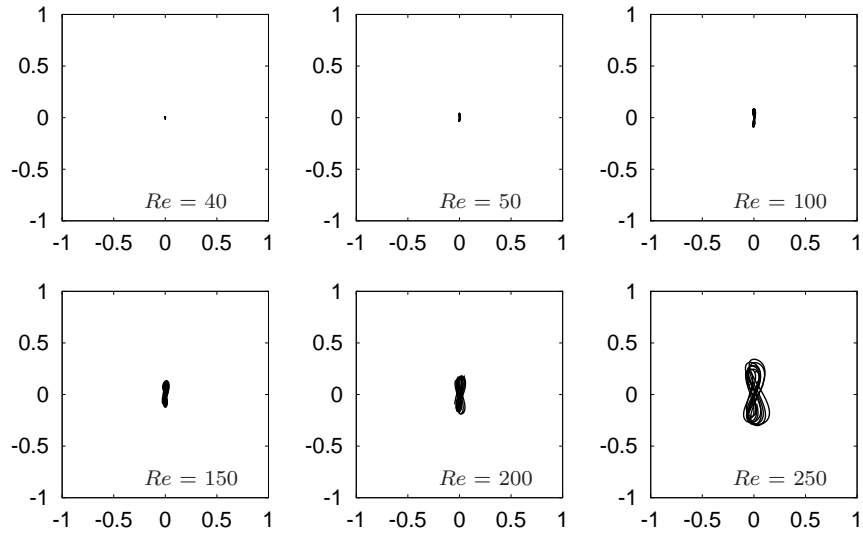


FIGURE 4.7: Phase plot of the total force coefficients in the xy coordinates when $m^* = 1$. The abscissa is C_x and the ordinate is C_y .

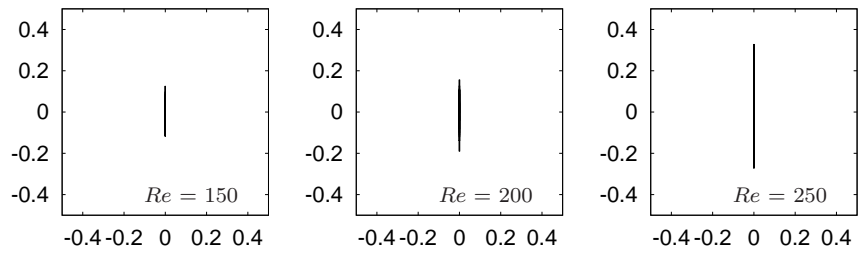


FIGURE 4.8: Trajectories of the oscillating cylinder in the $r\theta$ coordinates when $m^* = 1$. The abscissa is the r displacement normalised by the cylinder diameter D and the ordinate is the θ in radian.

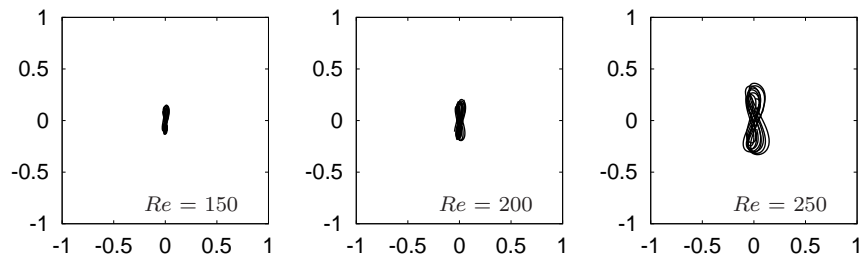


FIGURE 4.9: Phase plot of the total force coefficients in the $r\theta$ coordinates when $m^* = 1$. The abscissa is C_r and the ordinate is C_θ .

4.2.5 Vortex structure around the oscillating cylinder

Figures 4.10 to 4.14 show spanwise vorticity at selected Reynolds numbers. The flow of $Re = 20$, which is in Regime I, is steady, and the others are periodic.

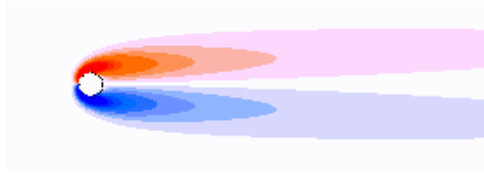


FIGURE 4.10: Spanwise vorticities at $Re = 20$ (Regime I). Red denotes clockwise vorticity, blue denotes counterclockwise vorticity. The flow is from left to right, and is steady.

All of the periodic flows are basically ‘2S’ wake modes, following the terminology of Williamson & Roshko (1988). For this wake state, two single vortices are shed per oscillation period. The spacing between the vortices gets narrower as Re increases from 50 to 150, but does not change much between 150 and 250. This is consistent with the frequency response in figure 4.4 showing an increase of the y oscillation frequency. It is also apparent that the vortex formation length at the rear of the cylinder decreases as the oscillating frequency increases, and that the vortex concentrations at high shedding frequency occupy a smaller region in the wake than at low shedding frequency.

For all the Reynolds numbers investigated, the streamwise vorticity is nearly symmetric about the x axis even though the displacements in Regime III show an additional low frequency oscillation. Note that the vorticity is asymmetric in a strict sense as the layover angle ϑ is not exactly zero. It is expected that the the principal frequency of

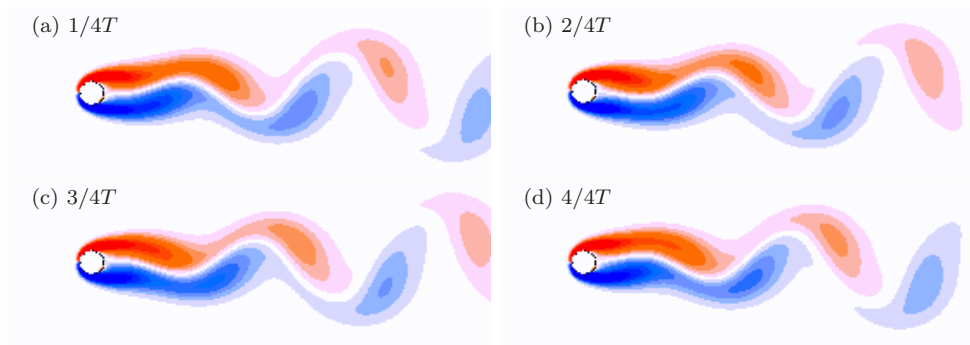


FIGURE 4.11: Spanwise vorticities when $Re = 50$ (Regime II) at each quarter cycle of the cylinder oscillation starting from the top of the oscillation. Flow is from left to right.

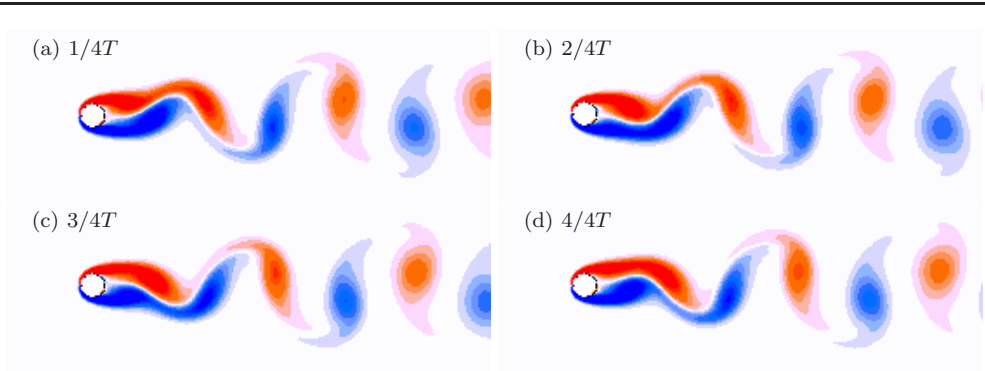


FIGURE 4.12: Spanwise vorticities when $Re = 100$ (Regime II). Descriptions are the same as figure 4.11.

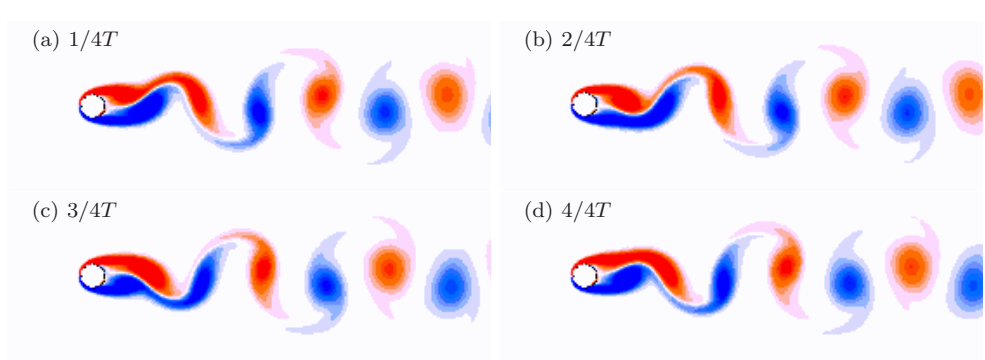


FIGURE 4.13: Spanwise vorticities when $Re = 150$ (Regime II). Descriptions are the same as figure 4.11.

cylinder oscillation is due to the periodic nature of the vortex shedding.

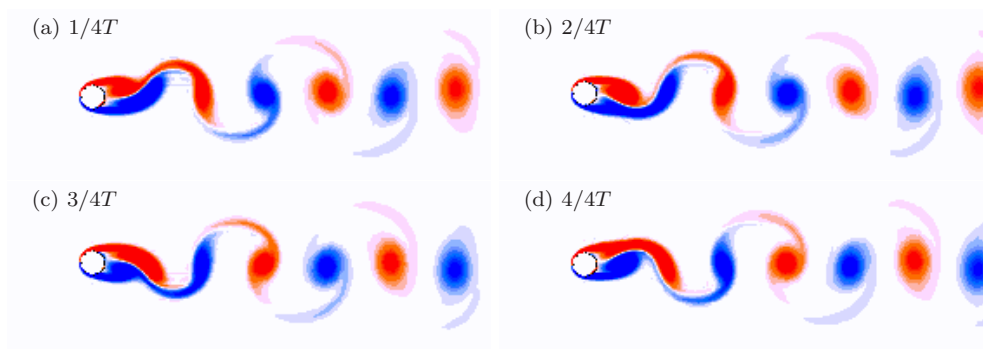


FIGURE 4.14: Spanwise vorticities when $Re = 250$ (Regime III). Descriptions are the same as figure 4.11.

4.2.6 History and phase of the displacements and forces

In Regimes II and III, the pressure component of the force dominates the total force in both the x and y directions. This is due to the fact that the cylinder is a bluff body and the flow separates, leading to the pressure varying considerably and not recovering at the rear of the cylinder. In Regime II, where a gradual change in the oscillation amplitude and frequency is observed, there is a considerable difference in the phase observed as Re increases. As the main oscillation occurs in the y (transverse) direction, the history and phase in the y direction are presented first, followed by those in the x direction.

Figure 4.15 shows the histories of the y displacement and the phases to the forces when $Re = 50$ and 100 corresponding Regime II. The total force F_y in the y direction is nondimensionalised according to the equation $C_y = F_y / (\frac{1}{2}\rho_f A U_\infty^2)$. The pressure force F_P and the viscous force F_V are the two components of the total force, i.e., $F_{Py} + F_{Vy} = F_y = \frac{1}{2}C_y$. The last term only holds because of the non-dimensionalisation used to set up the problem, i.e., $A = \rho_f = U_\infty = 1$.

At $Re = 50$, the total force, pressure force, and the displacement exhibit sinusoidal oscillations. However, the viscous force shows non-sinusoidal oscillation although it is not very distinct. The total and pressure forces in y lead the y displacement by $\varphi \approx 90^\circ$, thus they are out of phase. In contrast, the viscous force leads the y displacement by $\varphi \approx 270^\circ$. The phase difference for the total force is different to that for the pressure force alone although the pressure dominates the total force in magnitude. Comparing the magnitude of the pressure and viscous forces (the thin dashed lines), it is clear that the pressure force fluctuation is greater than that of the viscous force.

When the Reynolds number is increased to $Re = 100$, a secondary frequency appears in the y displacement. This secondary frequency is also observable in the total force and the pressure force, but not in the viscous force. The phase plots for the total, pressure, and viscous forces are greatly different to those of the $Re = 50$ case due to the appearance of the secondary frequency. Similar to the $Re = 50$ case, only the viscous force leads the displacement by $\varphi \approx 270^\circ$, whereas the other forces lead the displacement by $\varphi \approx 90^\circ$.

Figure 4.16 shows the histories and the phase when $Re = 150$ and 250 . The case of $Re = 150$ shares most of the features with the $Re = 100$ case, except the appearance of the lower frequency oscillation resulting in a drift of the lines of the phase plots. Based

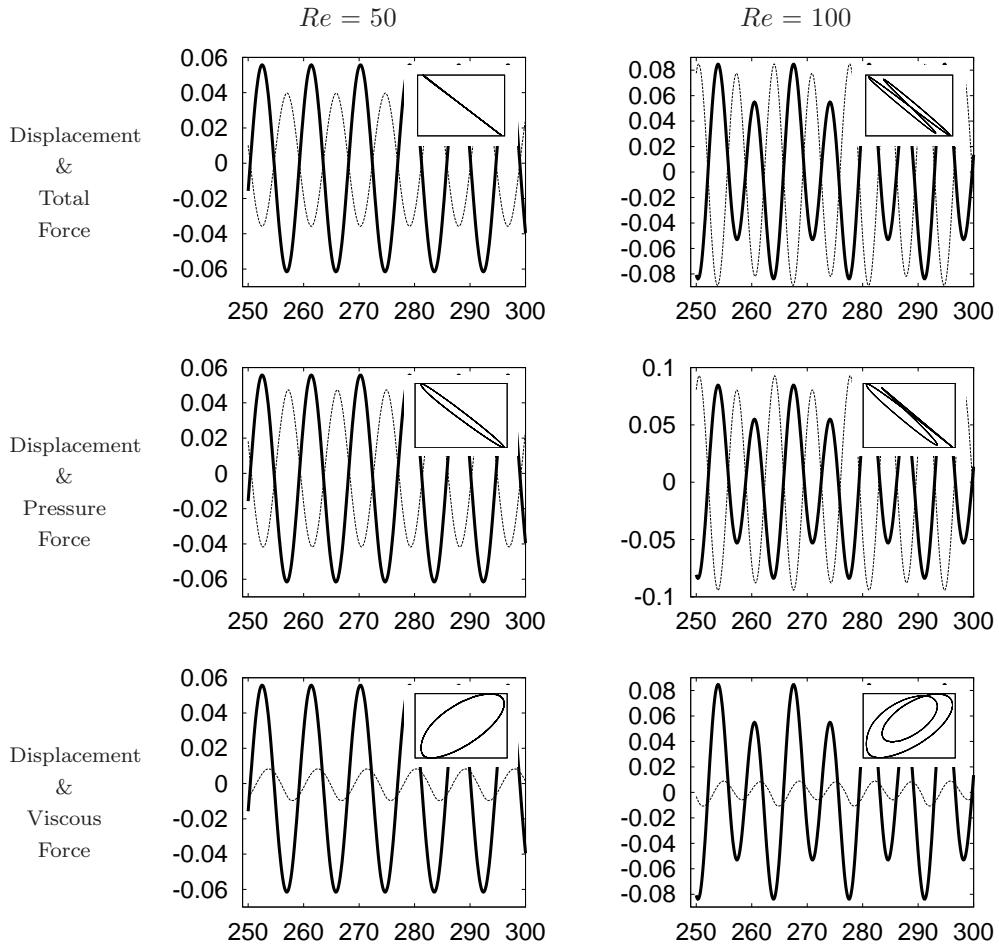


FIGURE 4.15: History and phase of the force and the displacement in the y direction at $Re = 50$ and 100 . The thick solid line in the history is the displacement, and the thin dashed line is the force. The inset is the phase where the ordinate is the force. The axes in the phase plot are autoscaled to see the pattern more clearly.

on the results for $Re = 100$ and 150 , the lower frequency oscillation is considered as a precursor to the regime change. At $Re = 250$ (Regime III), the y oscillation amplitude increases more than twice the amplitude for $Re = 150$, and also shows more irregularity. A significant difference to Regime II ($Re = 50, 100, \text{ and } 150$) is the viscous phase plot, demonstrating the different nature of the oscillation between the two regimes.

It is of interest to analyse the history of the cylinder displacement and the phase in the x direction, as the oscillation of a tethered cylinder is basically two-dimensional in the xy plane, which is one of the main differences from the previous studies of VIV of an elastically mounted cylinder.

Figure 4.17 shows that the x oscillation is not sinusoidal when $Re = 50$. Moreover,

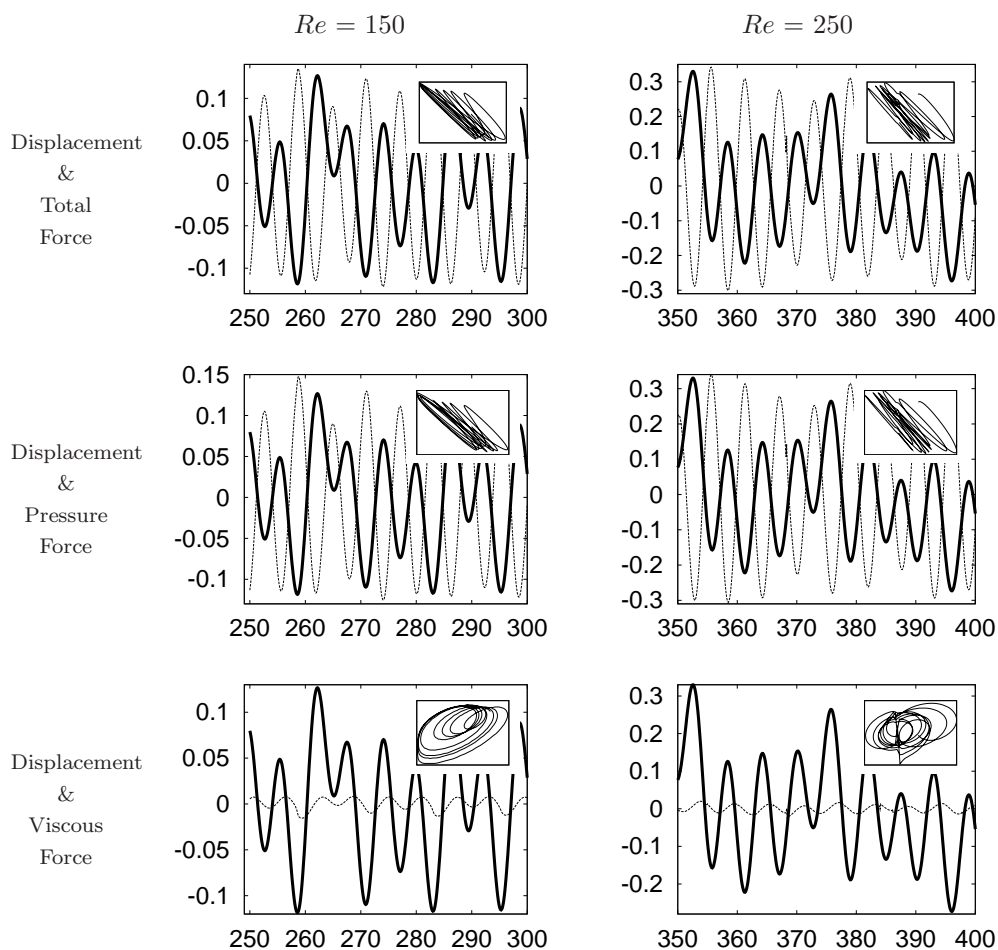


FIGURE 4.16: History and phase of the force and the displacement in the y direction at $Re = 150$ and 250 . Note that $Re = 250$ corresponds to Regime III. Descriptions for the figures are the same as figure 4.15.

the total fluid force in the x direction as well as the dominating pressure force exhibit two peaks a cycle, which indicates a secondary frequency. This is different to the y oscillation, in which the oscillation is sinusoidal and the force fluctuation has a single frequency. However, the secondary frequency is not apparent for the viscous force, with the magnitude about 20% of the pressure force. Because of the secondary frequency, the phase plots, except for the viscous force, portray a limit cycle in the form of a figure of eight. The large peaks in the total, pressure and viscous forces lead the x displacements by $\varphi \approx 270^\circ$.

At $Re = 100$, the x oscillation history is not sinusoidal as is the case at $Re = 50$; a secondary frequency emerges in the x oscillation. The number of peaks per cycle in the force histories is doubled that for $Re = 50$. The viscous force is about 20% of the

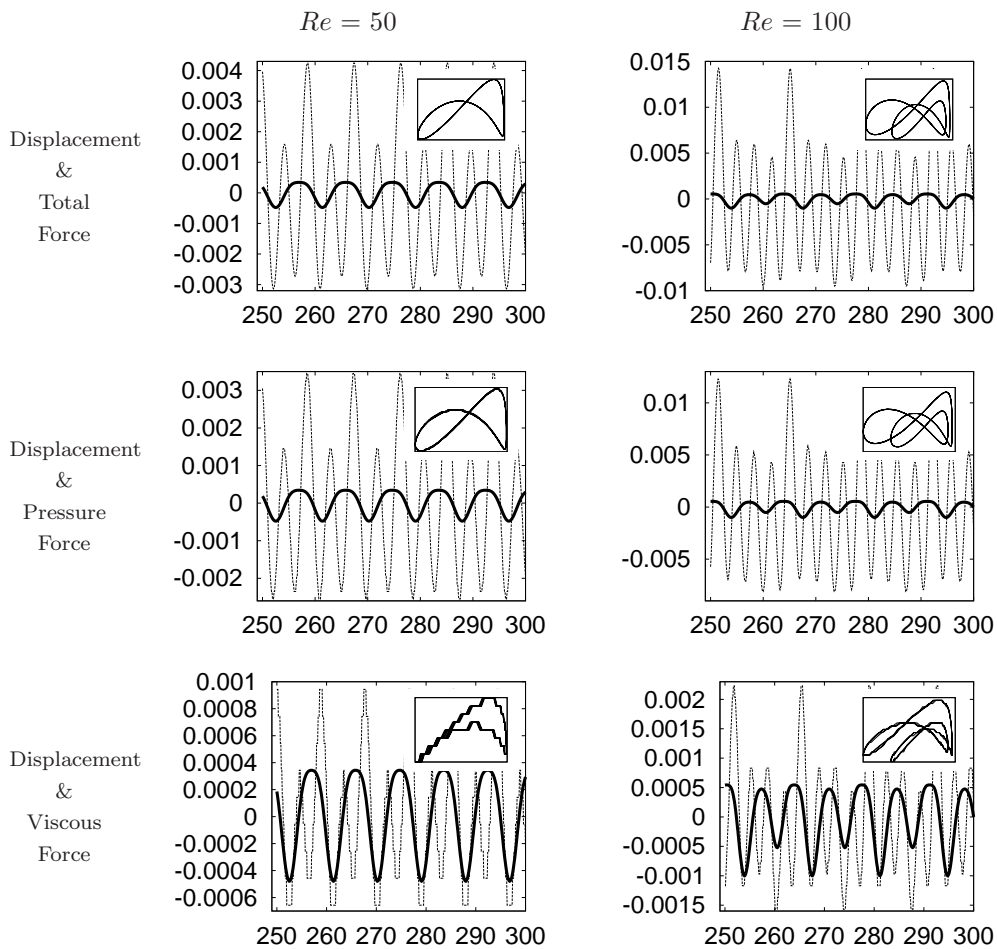


FIGURE 4.17: History and phase of the force and the displacement in the x direction at $Re = 50$ and 100 . The thick solid line in the history is the displacement, and the thin dashed line is the force. The inset is the phase where the ordinate is the force. The axes in the phase plot are autoscaled to see the pattern more clearly.

pressure force, similar to the $Re = 50$ case, but exhibits a secondary frequency in its history. Due to the appearance of secondary frequencies both in the oscillation and the force fluctuation, the phase plot portrays a double figure-of-eight.

The phase pattern at $Re = 150$ depicted in figure 4.18 shows additional doubling of the figure-of-eight with a drift of the lines due to slowing varying oscillations in the history of the force and the displacement. Except for the doubling in the phase, the principal phase value is consistent with the $Re = 100$ case for all the forces. Note that the tether constrains especially the x motion because the trajectory is on a circular arc. When Re is increased to 250 , the magnitude of the fluctuating forces increases considerably, but the oscillation amplitude varies little. There is no doubling of the

phase pattern like the cases of $Re = 100$ and 150 , and irregular oscillation is enhanced.

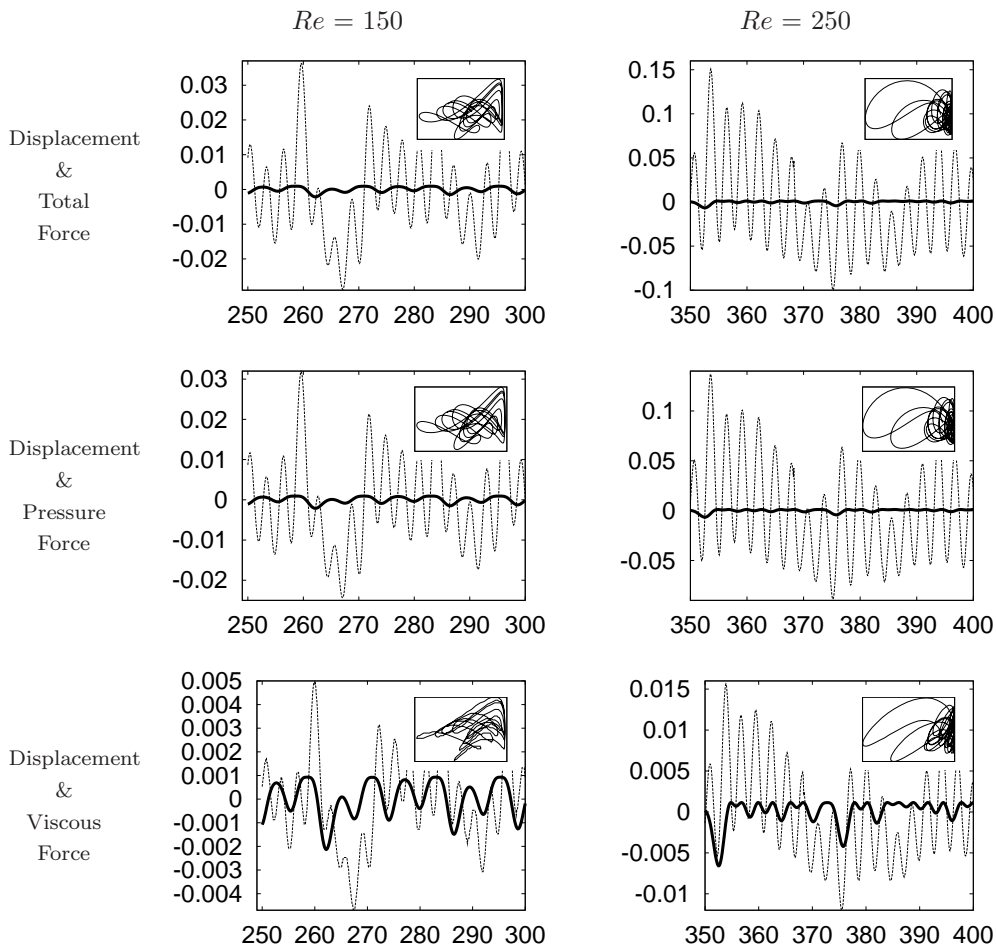


FIGURE 4.18: History and phase of the force and the displacement in the x direction at $Re = 150$ and 250 . Descriptions for the figures are the same as figure 4.17.

4.2.7 Power spectrum of the displacements and forces

Figures 4.19 and 4.20 show the spectra of the oscillation for x , y , C_x and C_y . Both in the x and y oscillations, subharmonic frequencies appear at $Re = 100$ and 150 in Regime II. In Regime III, represented by $Re = 250$, a range of low frequencies below $St < 0.2$ appears, which is an indication of the irregular motion of the cylinder in y within this regime.

Contrary to the spectra of the x and y oscillations, those for the C_x and C_y are different. Only one frequency appears for the y force C_y . This demonstrates that there are other forces having an effect on the y oscillation besides the fluctuating y force. However, several subharmonic frequencies appear for Regime II. In Regime III, a range

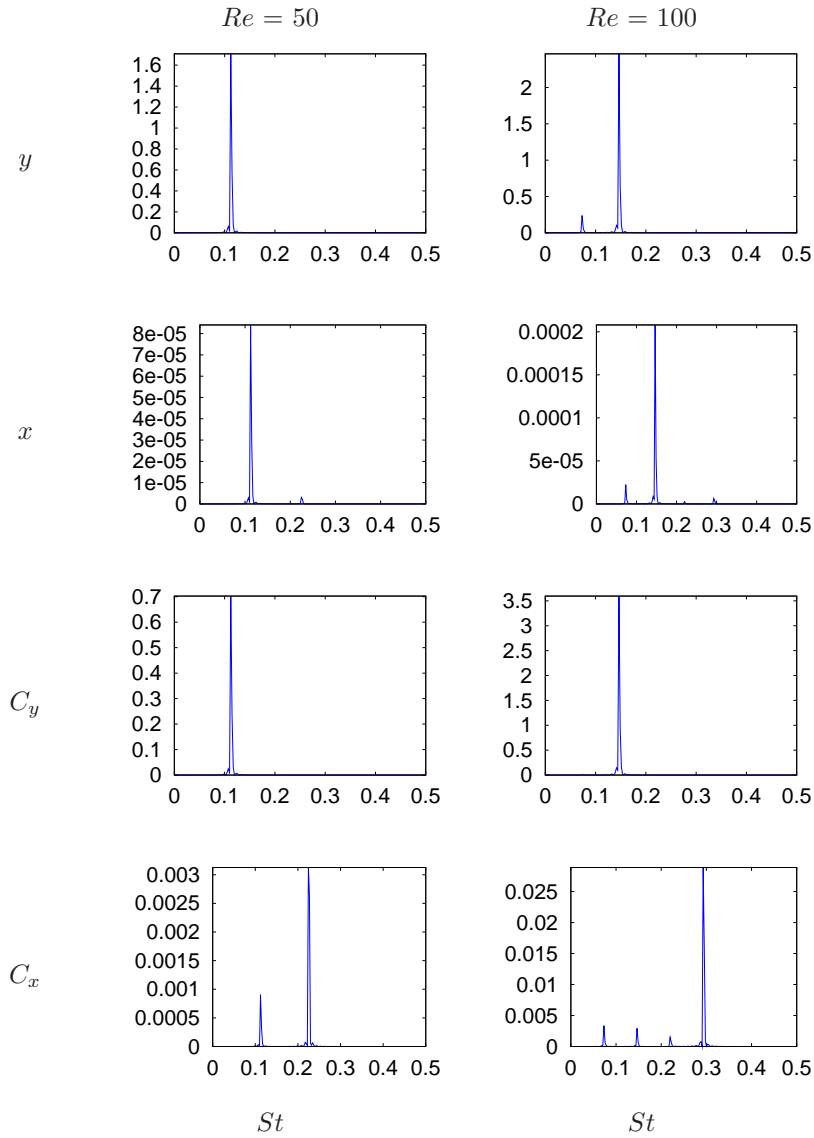


FIGURE 4.19: Power spectrum for the displacements and the total forces in x and y . The unit of the power is arbitrary.

of low frequencies below $St < 0.4$ appears. Note that the principal frequency is twice of that of the x displacement. The subharmonic frequencies of C_x and x explain the shape of the phase plots presented in section 4.2.7.

Considering the principal frequency of C_y , it is clear that the C_y fluctuation is the main cause of the x oscillation as well as of the y oscillation, and the secondary frequencies of the C_x are the cause of the secondary motions in the x and y oscillation histories. The effect of C_x on the y oscillation is due to the layover angle ϑ being $\approx 90^\circ$ when $m^* = 1$.

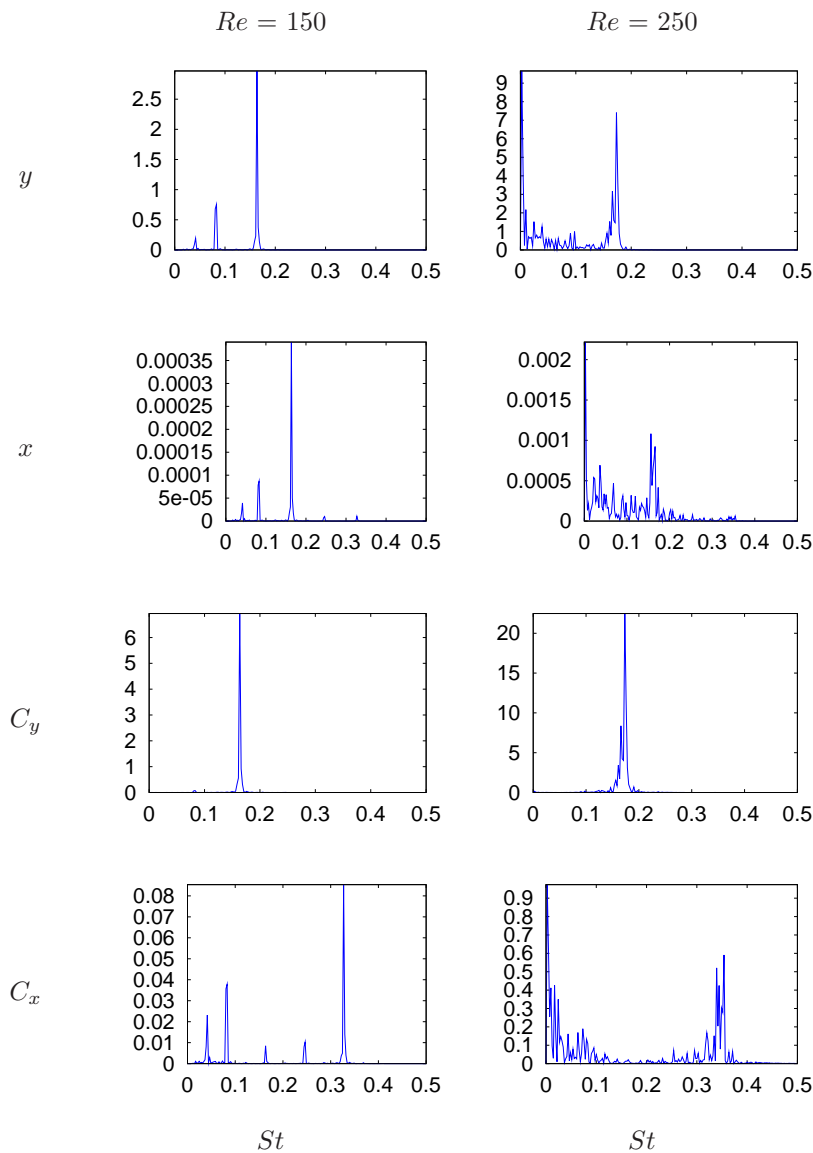


FIGURE 4.20: Power spectrum for the displacements and the total forces in x and y . The unit of the power is arbitrary.

4.3 VIV of Non-Neutrally Buoyant Cylinders: $m^* \neq 1$

Previous studies of VIV of tethered bodies have focused on the case of $m^* \neq 1$, where the buoyancy plays an important role in the equations of the body motion. In this section, the some simulation results for non-neutrally buoyant cylinders are provided to investigate any similarities or dissimilarity to the neutrally buoyant case where the buoyancy term in the equations of motion disappears. The simulations were performed over the same range of $Re = 20 - 300$ for the neutrally buoyant ($m^* = 1$) cylinder, with

other conditions the same as those for the $m^* = 1$ case. The range of m^* covered was $m^* = 0.1 - 1.11$.

Of these investigated, the mass ratios considered to be close to the neutrally buoyant case are $m^* = 1.11$, 0.909 and 0.833, with the cases of $m^* = 1.11$ and 0.833 chosen to be presented as the $m^* = 0.909$ case showed similar response to the $m^* = 0.833$ case. Further deviation from neutral buoyancy is also investigated by choosing mass ratio of $m^* = 0.5$, 0.2 and 0.1, with the case of $m^* = 0.2$ chosen to be highlighted in the following discussions. The selection of these three mass ratios is based on the similar results for the neighbouring mass ratios. By decreasing m^* , it is found that the response of a buoyant tethered cylinder changes as the mass ratio passes through $m^* = 0.5$. Note that this study is limited to the case of a fixed tether length of $10D$ and the range of $Re = 10 - 300$, as it is reported that the tether length and Re have an effect on the response of the tethered body (Ryan *et al.* 2007). It is also found that the tether length $L \geq 5D$ is regarded as long tethers, where the effect of neglecting the rotational motion of the body is minimal (Ryan *et al.* 2004a, 2007).

Three response regimes are identified based on the layover angle and the amplitude and frequency of oscillation for all the mass ratios considered. The Re range for each regime is found to be the same as that for the neutrally buoyant cylinder. The responses of the cylinders with different mass ratios are presented together to highlight any differences among them, as well as to identify any differences from the case of a neutrally buoyant cylinder.

4.3.1 Layover angle

Not surprisingly, the layover angle, for all three regimes, becomes smaller as the mass ratio decreases, as depicted in figure 4.21. The trend of the layover angle is dependent on the mass ratio. The case of $m^* = 1.11$ is a slightly heavier-than-fluid case compared with the $m^* = 1$ case. Other cases deviating from the $m^* = 1$ case such as the lighter-than-fluid $m^* = 0.909$ case, are also considered. Notice that the change of m^* by 10% is a priori a very small change in terms of the buoyancy force. When $m^* = 1.11$, the layover angle gradually increases over all three regimes as the Reynolds number is increased, and is greater than 90° as the cylinder is heavier than the displaced fluid. Unlike the $m^* = 1$ case, the layover angle increases within Regime I due to buoyancy. In Regime II, the layover angle grows more slowly than in Regime I. When $Re \geq 200$,

defined as Regime III, it grows faster than in Regime II.

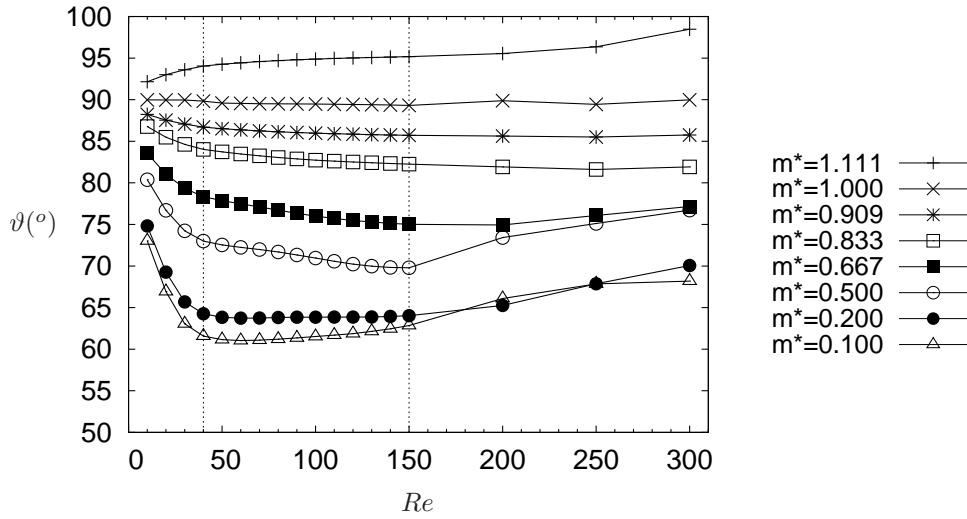


FIGURE 4.21: Effect of m^* on layover angle.

When m^* is between 0.909 and 0.5, the layover angle decreases as Re increases in Regimes I and II, then increases or remains constant in Regime III. The rate of decrease of the layover angle is greater in Regime I than in Regime II for these mass ratios. However, when $m^* \leq 0.2$, the layover angle decreases rapidly in Regime I, then increases gradually over Regimes II and III. The layover angle in Regime III shows little difference at these mass ratios ($m^* = 0.2$ and 0.1).

Due to the high buoyancy when $m^* = 0.2$, the layover angle within Regime I changes greatly. In Regime II, the layover angle does not decrease any more ($m^* = 0.2$) or slightly increases ($m^* = 0.1$), which is different to the $m^* \geq 0.667$ cases. Additionally, the layover angle increases considerably within Regime III, while it remains unchanged for the mass ratios of $m^* = 1$ to 0.667 .

4.3.2 Amplitude of oscillation

The oscillation amplitude, in general, increases as the mass ratio decreases, and the cylinder oscillates in Regimes II and III for all the mass ratios considered, as shown in figure 4.22. The behaviour of the oscillation amplitude, however, within the regimes is dependent on the mass ratio. When $m^* = 1.11$, the amplitude changes little in Regime II except at the beginning of the regime, then it grows gradually in Regime III.

When m^* is between 0.909 and 0.5, two noticeable differences exist compared with

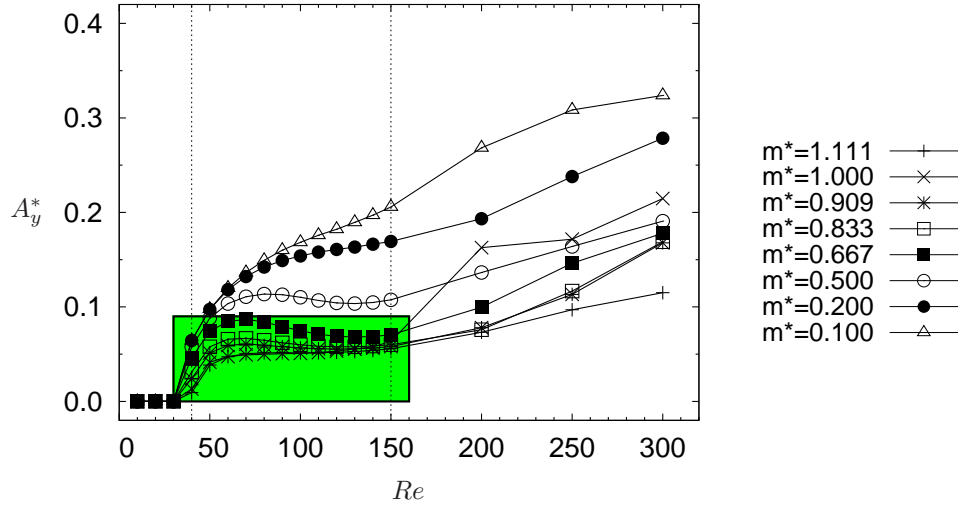


FIGURE 4.22: Effect of m^* on oscillation amplitude.

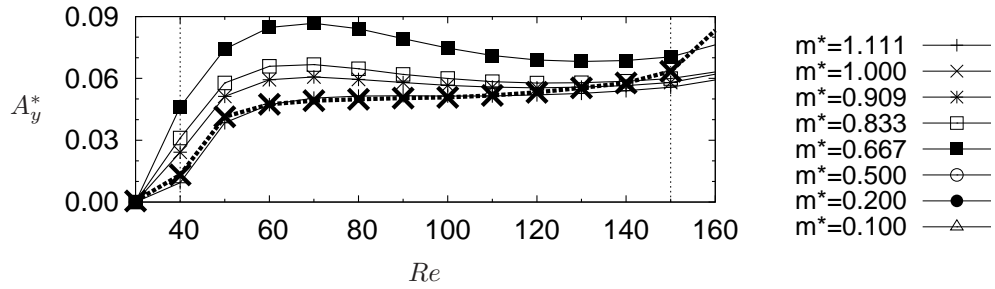


FIGURE 4.23: Effect of m^* on oscillation amplitude within Regime II. The dashed line corresponds to the neutrally buoyant case. Contrary to other cases, it follows neither the trend of lighter-than-fluid cylinder nor that of heavier-than-fluid one.

the $m^* = 1.11$ case. The first is that the amplitude does not grow monotonically within Regime II. It increases rapidly within the range of $Re = 40 - 60$, and slightly decreases within $Re = 70 - 120$, then increases again for $Re = 130 - 150$. Secondly, the amplitude grows faster than for the $m^* = 1.11$ case within Regime III. Additionally, no jump is observed between $Re = 150$ and 200 .

When $m^* \leq 0.2$, continuous growth in amplitude is clear in Regime II as well as in Regime III, contrary to the trend when $m^* = 0.5 - 0.909$. As for the other mass ratio cases, the cylinder oscillates from $Re = 40$ when $m^* = 0.2$. There exists a principal difference in Regime II compared to the less buoyant cases. The amplitude grows fast and continuously throughout Regime II without any local decrease as was observed

when $m^* = 0.833$. However, the amplitude grows faster in Regime III than in Regime II, similar to the $m^* = 0.833$ case.

If we consider the amplitude response within Regime II, which is indicated by a rectangular box in figure 4.22 and shown in figure 4.23, it is observed that the neutrally buoyant cylinder follows neither the trend of a lighter-than-fluid cylinder nor that of a heavier-than-fluid one. Together with the jump in the amplitude between $Re = 150$ and 200, this suggests that the response of a tethered cylinder with neutral buoyancy is different in nature to that of the non-neutrally buoyant cylinder.

4.3.3 Frequency of oscillation

The oscillation frequency in y given in figure 4.24 shows little dependence on the mass ratio. Particularly in Regime II, the frequency gradually increases as Re increases, similar to the variation for a fixed cylinder (Williamson 1988a), but has a value lower than that for a fixed cylinder at a given Re . The rate of increase reduces as Re approaches 150. In Regime III, the frequency reaches a saturated value of about $St = 0.17$ and remains unchanged. When $m^* \geq 0.5$, a small but obvious increase of the frequency is observed.

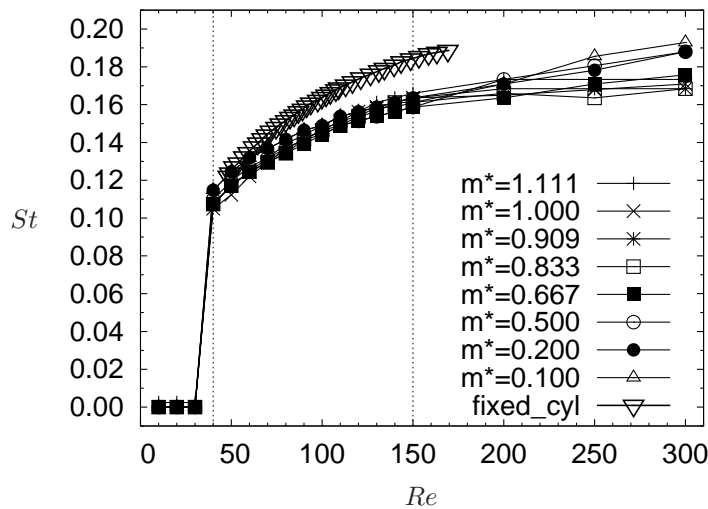


FIGURE 4.24: Effect of m^* on oscillation frequency versus Reynolds number.

4.3.4 Trajectory and forcing of the oscillating cylinder

In figure 4.25, the xy trajectories of the oscillating cylinder at different mass ratios are shown. Firstly, it is found that, for all the mass ratios, an inclination of the trajectory is apparent, due to the buoyancy. The inclination angle for $m^* = 1.11$ is opposite to the other two mass ratios, as it is a heavier-than-fluid case. For the other two lighter-than-fluid cases of $m^* = 0.833$ and 0.2 , the inclination angle grows as the mass ratio decreases. Secondly, the amplitude grows as Re increases, mainly in the y direction at a given mass ratio. Of note is that the amplitude for $m^* = 0.2$ is considerably greater than for the other two mass ratios of $m^* = 1.11$ and 0.833 .

Figure 4.26 presents phase plots of the total force coefficients ($C_x - C_y$) in the x and y directions. These forces are the cause of the oscillatory motion of the cylinder in the xy plane. When $m^* = 1.11$, both force components grow in magnitude as Re increases. The effect of buoyancy appears clearly at higher Reynolds numbers of $Re > 150$, being characterised by asymmetry about zero of the ordinate. The minimum value of the y force coefficient C_y is larger than the maximum value because of the neg-

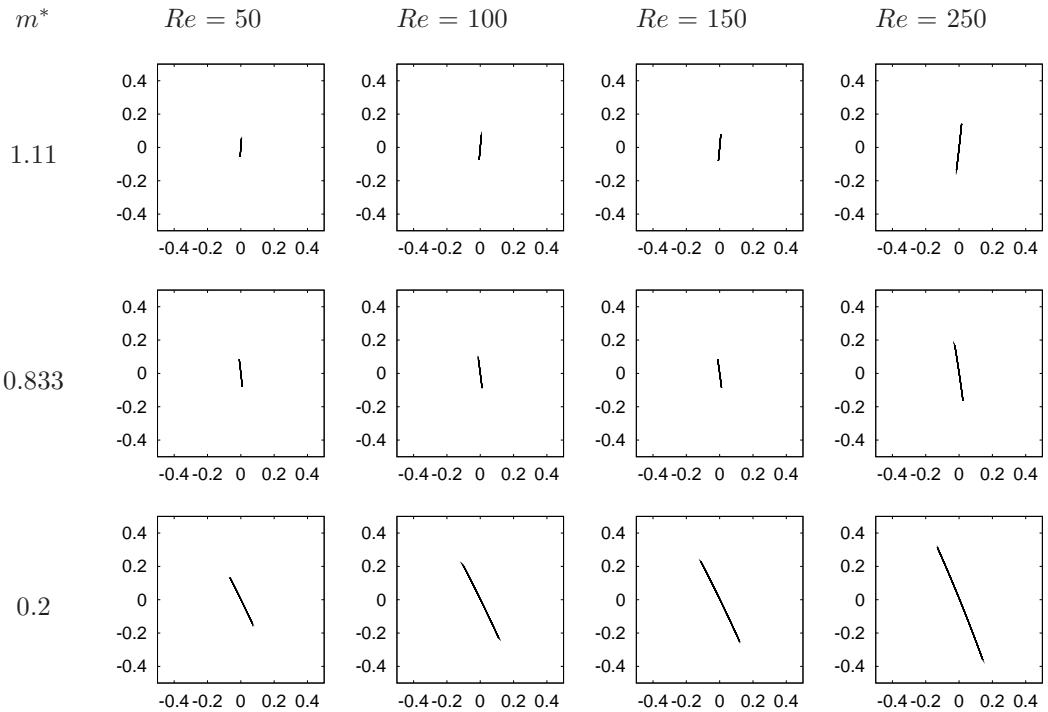


FIGURE 4.25: Trajectories of the oscillating cylinder at various mass ratios in the xy coordinate. Flow is from left to right. The abscissa is x^* and the ordinate is y^* , where the $*$ denotes the dimensionless value.

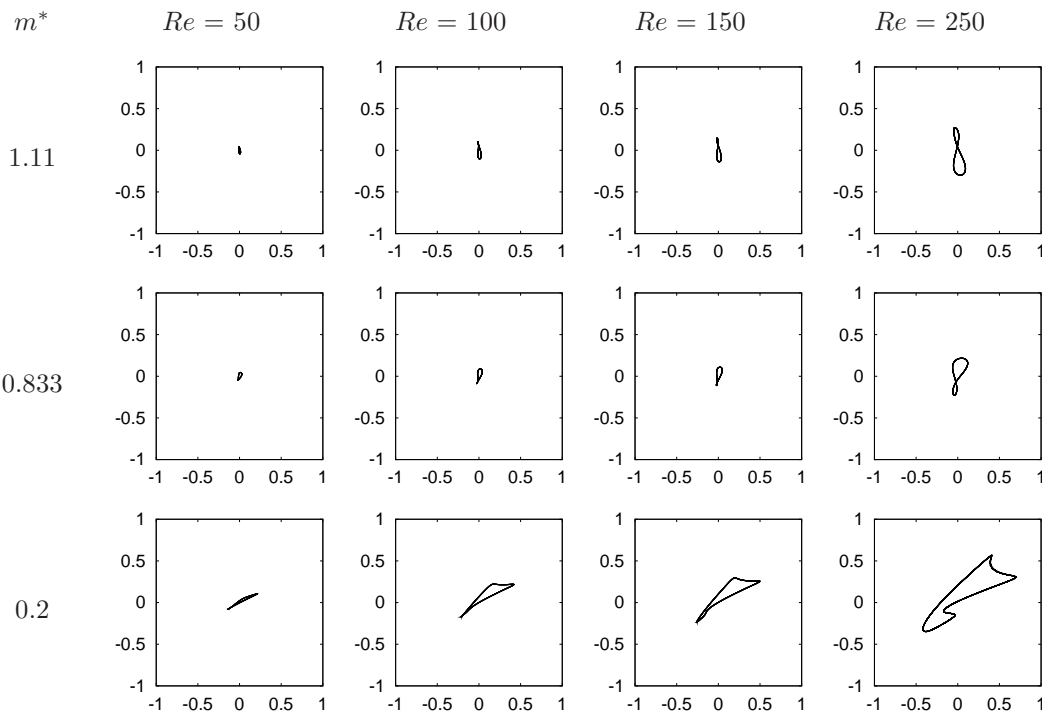


FIGURE 4.26: Phase of the total forces in x and y , $C_x - C_y$, at various mass ratios. The abscissa is C_x and the ordinate is C_y .

ative buoyancy when $m^* < 1$, but the phase plot still shows a figure-of-eight pattern. When $m^* = 0.8333$, the total forces in the x and y directions are different from those for the $m^* = 1.11$ case because of the positive buoyancy. Despite this, the phase of the total forces still exhibits a figure-of-eight pattern for both mass ratios of $m^* = 1.11$ and 0.833 . Moreover, the phase pattern shows a single line of the figure-of-eight, indicating no secondary oscillation of low frequencies.

When $m^* = 0.2$, a remarkable difference from the other two mass ratios is found. At the discrete Reynolds numbers considered, the phase plots of the force components exhibit completely different patterns, as depicted in figure 4.26, and the magnitudes of the forces are much larger than those of $m^* = 1.11$ and 0.833 . Combined with the difference found in the layover angle and oscillation amplitude for the mass ratios considered, it is found that the buoyant tethered cylinder shows a different response when the mass ratio is raised above a critical value. More precisely, it is expected that this critical mass ratio is located close to $m^* = 0.5$, based on the mass ratios considered with the tether length of $10D$. The phase of the force when $m^* = 0.5$ showed a transitional pattern and is presented in section 4.3.5. Another view of the

phase between the forces $C_r - C_\theta$ between the $r\theta$ coordinate shows little difference to the behaviour in terms of $C_x - C_y$. Thus, it appears sufficient to investigate the phasing of the force components in the xy coordinate without considering the $r\theta$ counterparts.

4.3.5 History and phase of displacements and forces

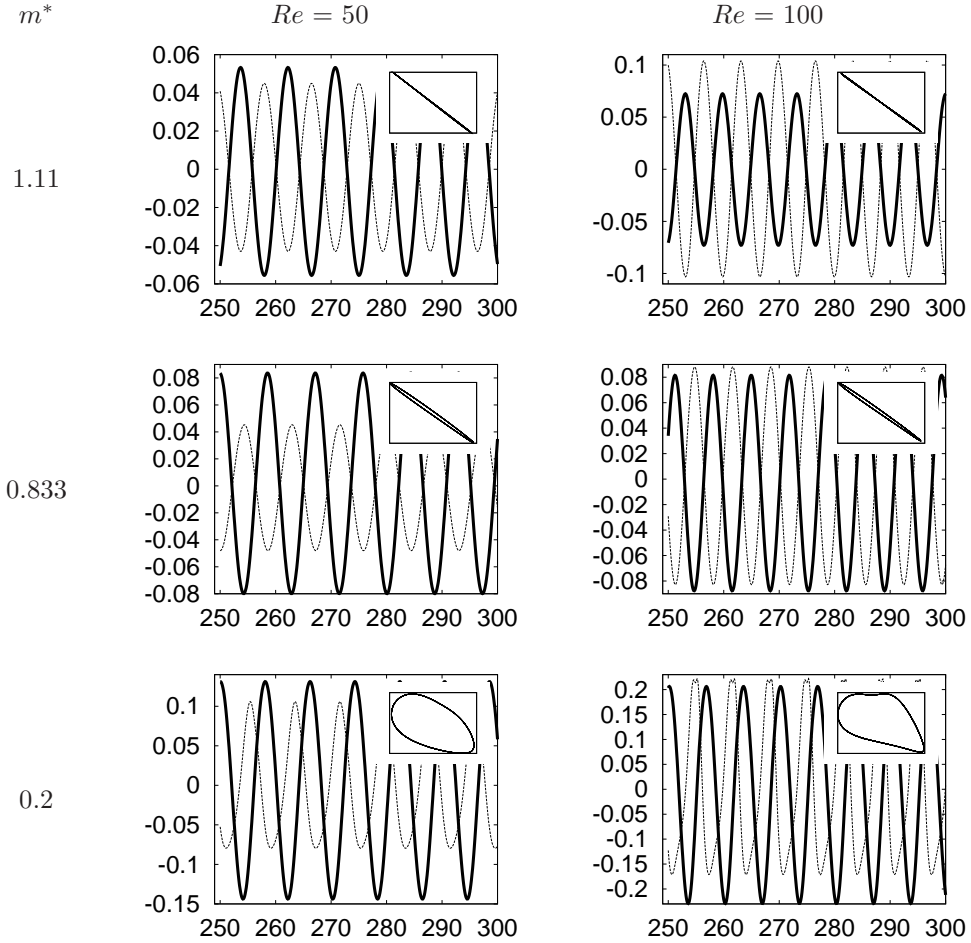


FIGURE 4.27: History and phase of the total force and the displacement in the y direction at $Re = 50$ and 100 . The thick solid line is the displacement, and the thin dashed line is the force. The inset is the phase where the ordinate is the force. The axes in the phase plot are autoscaled to see the pattern more clearly.

As the mass ratio varies, changes to the y displacement history and its phase relationship to the different types of forces is observed. Figures 4.27 and 4.28 show the histories of the displacement and their phase difference relative to the total force in the y direction.

For all the mass ratios and Reynolds numbers considered, the y displacement ap-

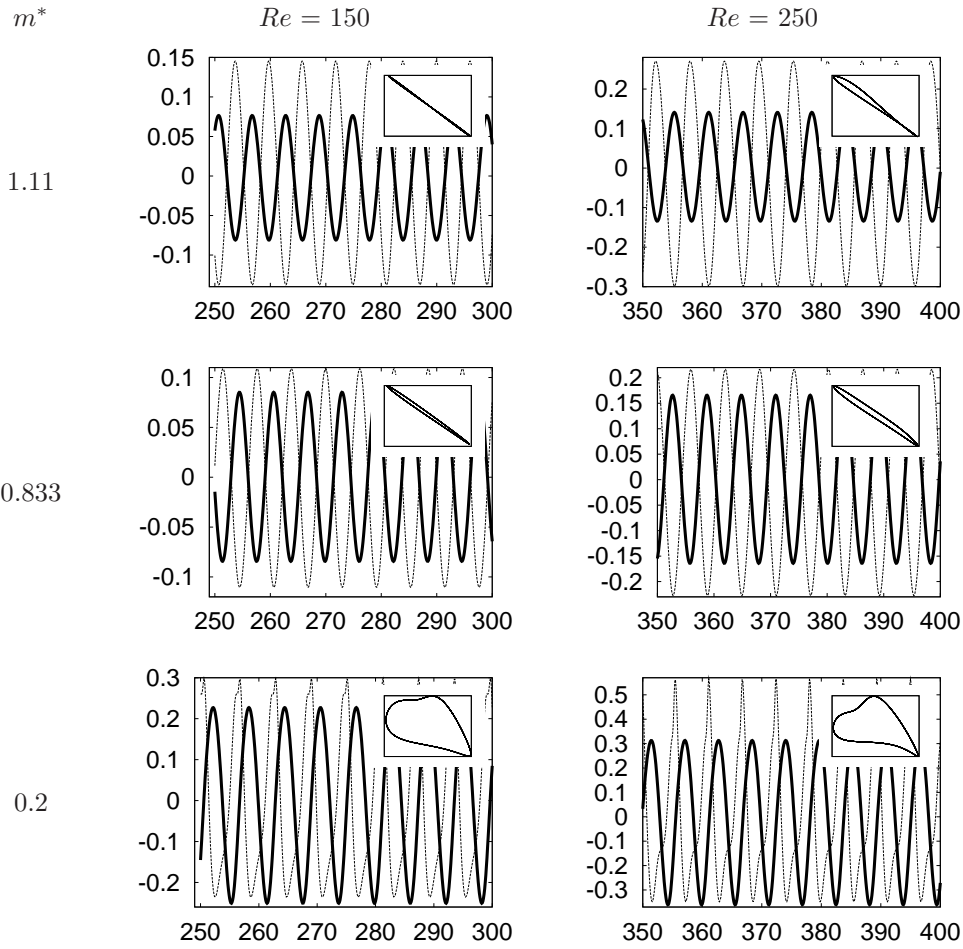


FIGURE 4.28: History and phase of the total force and the displacement in the y direction at $Re = 150$ and 250 . Descriptions for the figures are the same as figure 4.27.

pears sinusoidal, and the amplitude of oscillation grows as Re increases. For $m^* = 1.11$ and 0.833 , the total force is also sinusoidal and is out of phase with the y displacement ($\varphi \approx 180^\circ$) resulting in the phase plots of a line or a flat oval as shown in the insets of figures 4.27 and 4.28. When $m^* = 0.2$, however, the total force is not sinusoidal, particularly at $Re \geq 100$. In addition, the phase difference is $\varphi \approx 90^\circ$ and exhibits a pattern of a wide oval with increasing distortion around top-left and bottom-right corners. This is another indication of the existence of a critical mass ratio mentioned previously.

Of interest is that the mean value of the total force in y is not zero. This is indicated clearly by a slight distortion of the oval in the phase plots at $Re = 250$. As the pressure force contributes about 80% to the total force, and shows history and phase patterns similar to the total force, it is not presented here.

However, the viscous force, which contributes only about 20% to the total force,

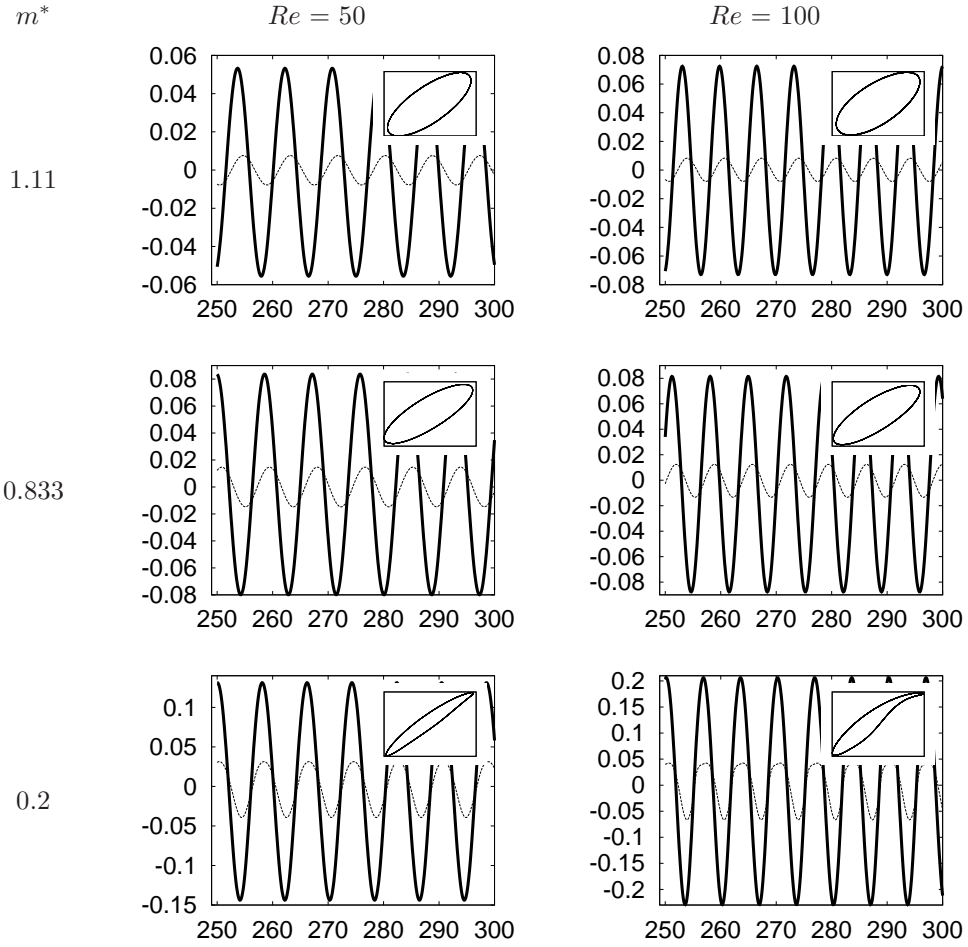


FIGURE 4.29: History and phase of the viscous force and the displacement in the y direction at $Re = 50$ and 100 . Descriptions for the figures are the same as figure 4.27.

leads the y displacement by $\varphi \approx 270^\circ$ for all the mass ratios and Reynolds numbers considered. As a result, the phase plot has a pattern in the form of a wide oval with different inclination angle. This is depicted in figures 4.29 and 4.30. In contrast to the pressure and total forces, the magnitude of the viscous force remains almost unchanged as Re increases. The phase plot for $Re = 250$ and $m^* = 1.11$ showing a wider oval with a flat part in its top-right corner is due to the negative buoyancy for the heavier-than-fluid cylinder. An obvious pattern change to a hook shape around its top-right corner appears when $m^* = 0.2$, particularly at $Re \geq 100$. This is due to a non-sinusoidal oscillation of the force as presented in figures 4.29 and 4.30.

The effect of changing the mass ratio on the VIV of tethered cylinders emerges clearly when we look into the motion and the forces in the x direction. This is mainly due to the appearance of the buoyancy (or gravity) in the equations of motion, which

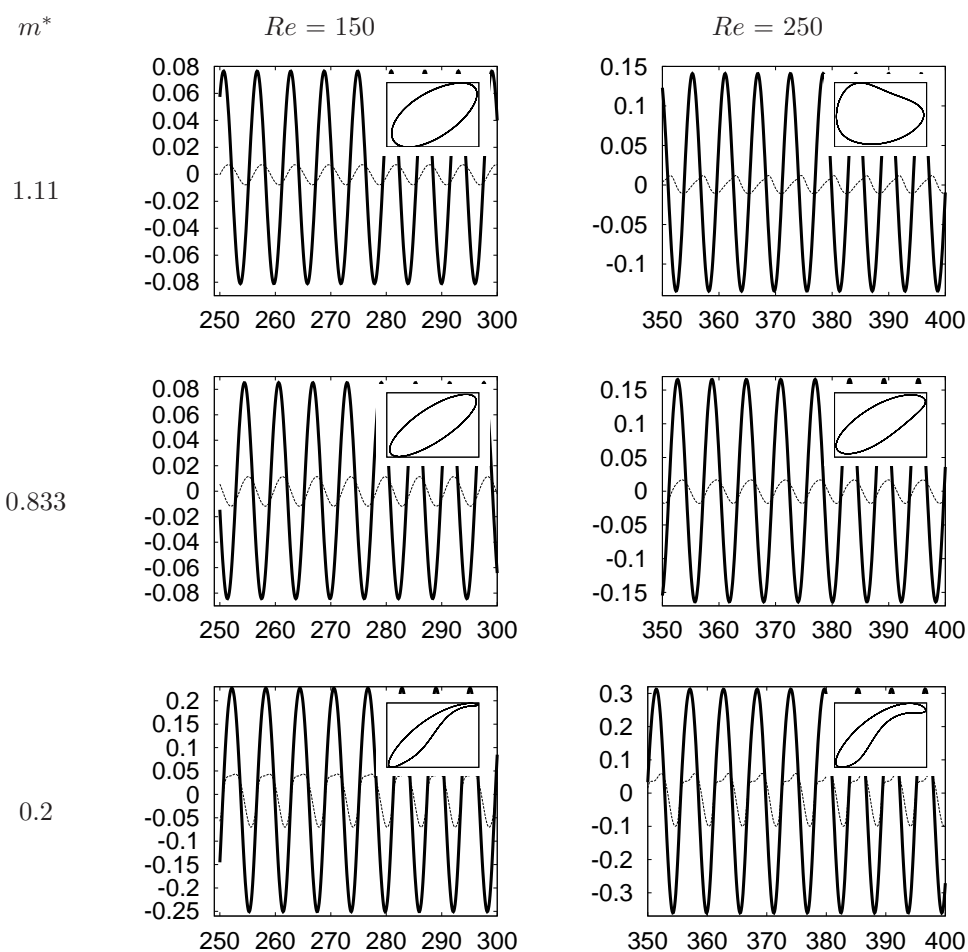


FIGURE 4.30: History and phase of the viscous force and the displacement in the y direction at $Re = 150$ and 250 . Descriptions for the figures are the same as figure 4.27.

in turn changes the layover angle of the cylinder, which also depends on the flow speed. As the layover angle ϑ departs from 90° , the amplitude of oscillation in the x direction is allowed to grow.

As is the case for the y displacement, the x displacement is sinusoidal for all mass ratios and Reynolds numbers investigated. However, a great difference is found as the mass ratio and Re vary. At a given Re , small peaks on the history of the x total force (C_x) get bigger as m^* is increased to 1.11. This results in a distorted oval with a narrow tip at its top right corner or a figure-of-eight pattern in the phase plots when $m^* = 1.11$ and 0.833 at $Re \geq 150$ (see figures 4.31 and 4.32). Once again, the phase for $m^* = 0.2$ shows a difference to that for the other two mass ratios. An additional change at the top of the cycle of the C_x history appears at $m^* = 0.2$ and results in the pattern shown in figures 4.31 and 4.32. This is clearly shown at $Re = 250$. Even though the pattern

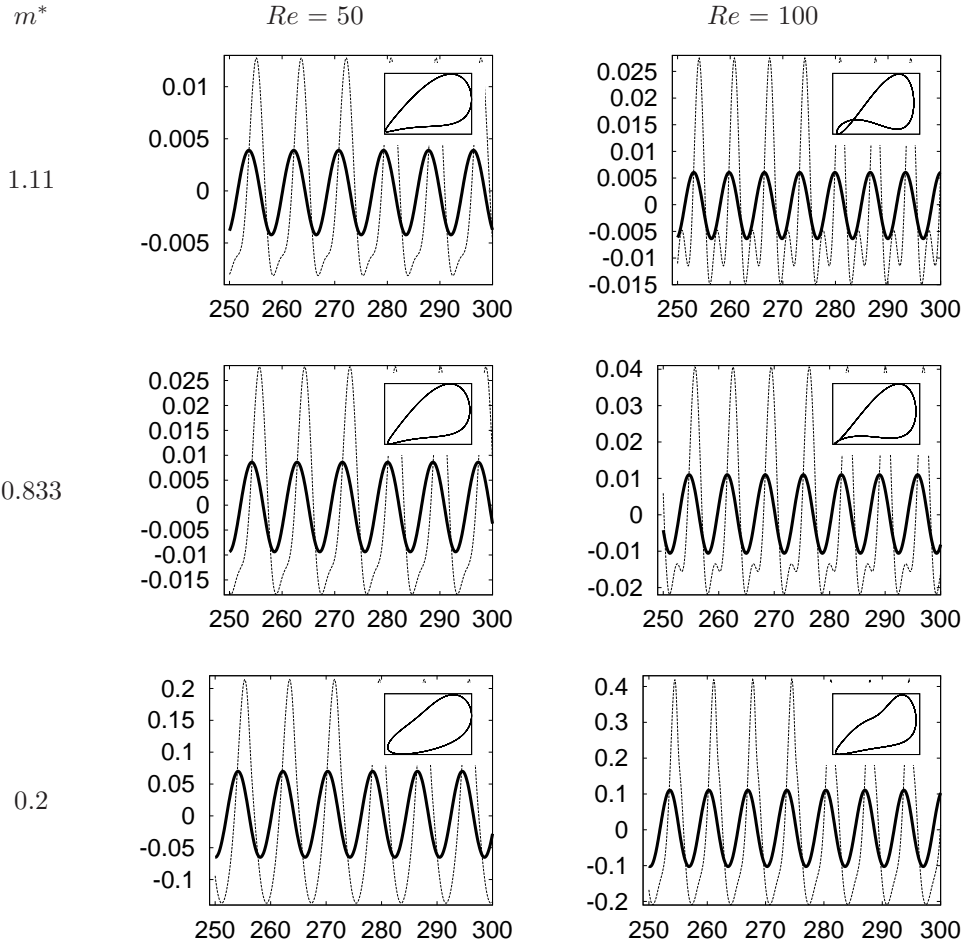


FIGURE 4.31: History and phase of the total force and the displacement in the x direction at $Re = 50$ and 100 . The thick solid line in the history is the displacement, and the thin dashed line is the force. The inset is the phase where the ordinate is the force. The axes in the phase plot are autoscaled to see the pattern more clearly.

is different, the phase difference for all the mass ratios has a similar value of $\varphi \approx 270$.

Irrespective of the differences found between $m^* = 1.11$, 0.833 and 0.2 , there is a fundamental difference of the behaviour of the neutrally buoyant cylinder to that of the non-neutrally buoyant cylinder, which is highlighted by the power spectra, histories, and phase plots of the displacements and forces. The neutrally buoyant tethered cylinder exhibits low frequency motions in the history of the displacement and force when Re increases beyond 100 , whereas the non-neutrally buoyant cylinder does not, even at high Re corresponding to Regime III. More detailed comparisons between the neutrally buoyant and others are discussed in section 4.3.6. Interestingly, the simulation results for a vertically tethered heavier cylinder have shown that its response behaviour is very

similar to that of the neutrally buoyant cylinder.

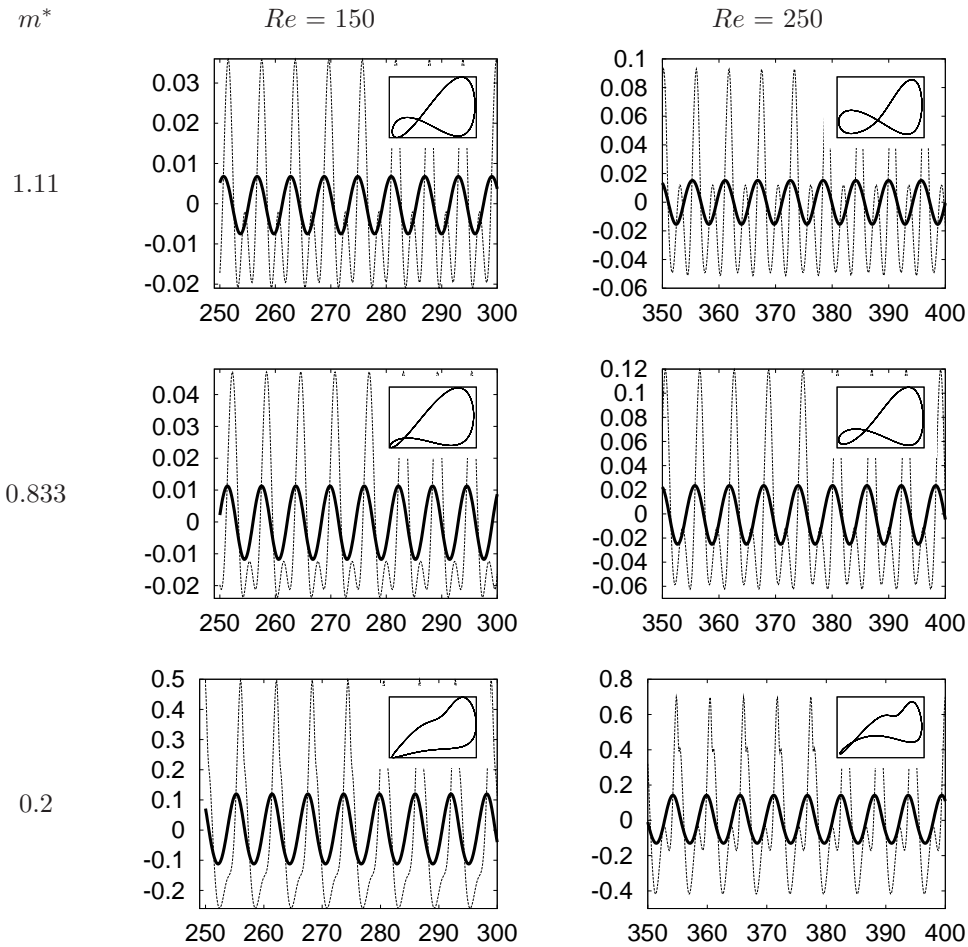


FIGURE 4.32: History and phase of the total force and the displacement in the x direction at $Re = 150$ and 250 . Descriptions for the figures are the same as figure 4.31.

4.3.6 Comparison to VIV of the neutrally buoyant tethered cylinder

As there is little difference in the xy trajectory with varying mass ratios, the phase between the force and the displacement is used to compare the response of the tethered cylinders with various mass ratios.

Figure 4.33 shows magnified and autoscaled phase plots in the x direction, i.e. $x - C_x$. For each Re , only the neutrally buoyant cylinder ($m^* = 1$) exhibits a different pattern. Considering the smooth variation of the pattern at a given Re for other mass ratios, it is clear that the response of the neutrally buoyant cylinder is quite different to that of the other tethered cylinders of $m^* \neq 1$. This is also clear in the phase plot in the y direction as depicted in figure 4.34. As is the case for the phase in x , the neutrally

buoyant cylinder exhibits a different shape to those for other mass ratios.

There are two main differences in the phase between the neutrally buoyant cylinder and the non-neutrally buoyant ones. The first is that the neutrally buoyant cylinder shows a non-periodic response at $Re \geq 150$. In contrast, non-neutrally buoyant cylinders, where the buoyancy is acting parallel to the y direction, show periodic oscillations even at $Re = 250$. This is due to the magnitude of the restoring force. In general, the drag (the x force) is primarily restoring force in both cases. For the neutrally buoyant one, however, the restoring force is very small as there is no contribution of the buoyancy to the restoring force as shown in figure 4.35. Thus, the neutrally buoyant cylinder is more sensitive to small disturbances than the non-neutrally buoyant tethered cylinder, where the buoyancy significantly contributes to the restoring force.

The second difference is the *doubling* of the figure-of-eight pattern in the $x - C_x$ phase plot for Regime II (see figure 4.33). The figure-of-eight pattern also appears when $m^* \neq 1$ at $Re > 100$, but the *doubling* of the patterns does not happen in those cases as it does for the neutrally buoyant case. This doubling of the pattern is closely related to the contribution of the buoyancy to the restoring force as depicted in figure 4.35. For the neutrally buoyant cylinder, where the buoyancy or lift is zero and $\vartheta \approx 90^\circ$, the drag (the x force) acts pretty much at right angle to the allowed motion (see figure 4.35(a)). However, when $m^* \neq 1$, the layover angle $\vartheta \neq 90^\circ$ and some component of the drag is

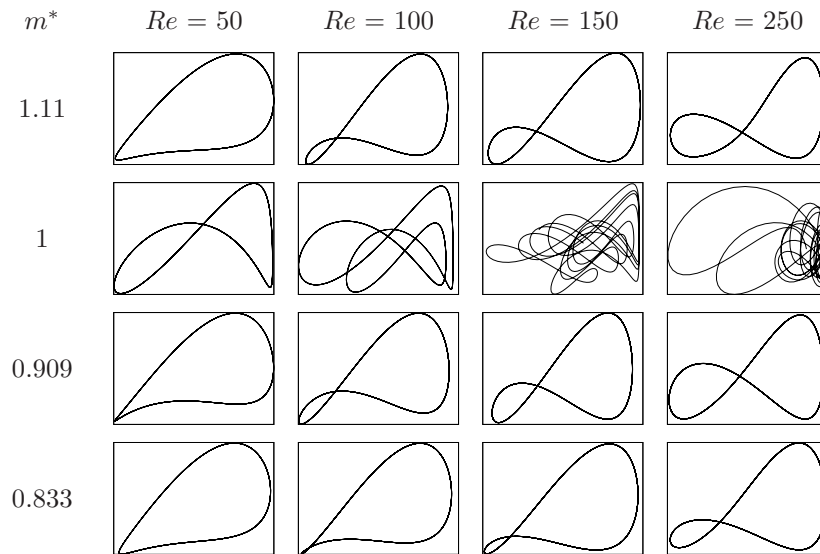


FIGURE 4.33: Phase between the displacement and the force in x . The abscissa is x and the ordinate is C_x . The axes are autoscaled to show the pattern more clearly.

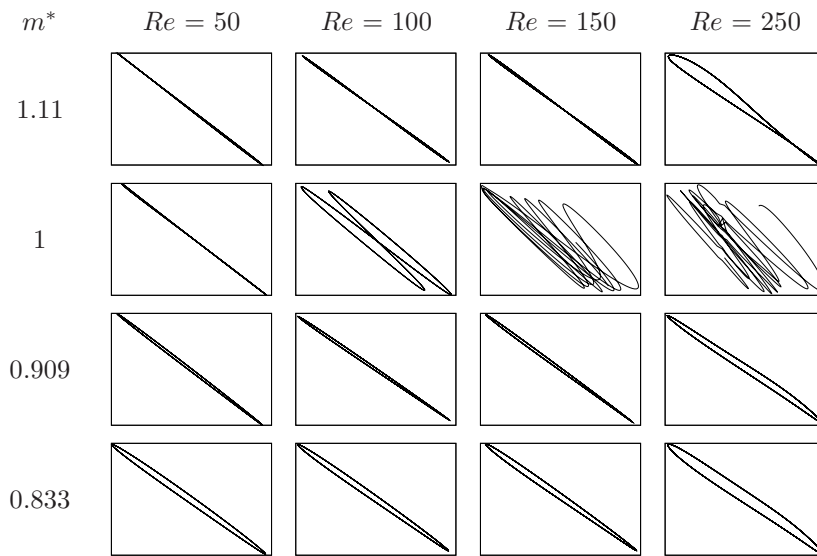


FIGURE 4.34: Phase between the displacement and the force in y . The abscissa is y and the ordinate is C_y . The axes are autoscaled to show the pattern more clearly.

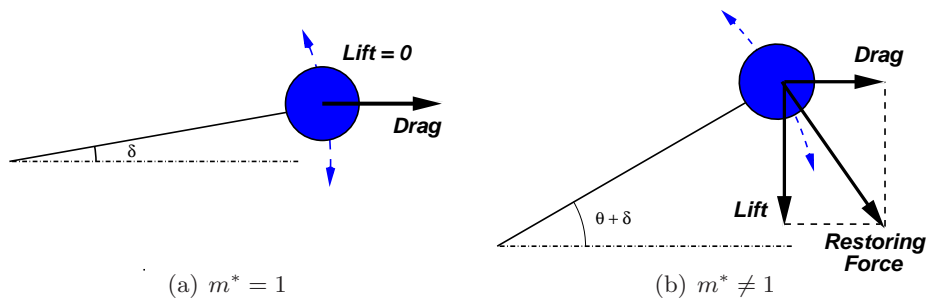


FIGURE 4.35: Restoring force for the neutrally buoyant ($m^* = 1$) tethered cylinder (a) and the non-neutrally buoyant $m^* \neq 1$ cylinder. Lift is equivalent to buoyancy. The oscillation angle δ varies in time and $\delta \ll 1$. The time-mean of the tether angle for the non-neutrally buoyant cylinder is denoted as θ in (b). The mean tether angle is omitted in (a) as $\theta \approx 0^\circ$ when $m^* = 1$.

allowed to act to restore the mean position (see figure 4.35(b)). Because of this, the fluctuation of the drag has a larger effect on the y oscillation than for the case of $\vartheta \neq 90^\circ$ although the fluctuating x force is not the largest effect on the y oscillation. This is verified in the previous spectral analysis for the neutrally buoyant cylinder showing the matching of the subharmonic frequency of C_x to the secondary frequency of the y oscillation.

4.4 VIV of a Vertically Tethered Cylinder

Based on the findings of the different response of the neutrally buoyant cylinder to the non-neutrally buoyant one, a question that arises is what makes the difference in the results for that relatively narrow range of the mass ratio of $m^* = 0.833 - 1.11$. It appears that the direction of the buoyancy (or gravity) force acting on the cylinder can make a difference. As for the tethered sphere case, which will be discussed in chapter 5, the idea of performing simulations for a vertically tethered cylinder originated from the work of (Provansal *et al.* 2004), who experimentally found a different oscillation mode for a vertically tethered sphere.

It is not hard to find a similarity between the neutrally buoyant and the vertically tethered non-neutrally buoyant cylinders in terms of the force balance. A schematic of the vertically tethered cylinder is shown in figure 4.36. Unlike the horizontal tethering configuration used for the previous sections, the buoyancy acts parallel to the flow (in the x direction) for the vertical tethering. This causes the layover angle to be close to 90° as is the case for the neutrally buoyant case. As the layover angle $\vartheta = 90^\circ$ results in the x force having an effect on the y oscillation, the vertically tethered cylinder will exhibit a response different to that for the horizontally tethered cylinder, and possibly a similar response to that for the neutrally buoyant one.

Simulations for a vertically tethered cylinder were performed by modifying the numerical code adopted from the neutrally buoyant tethered cylinder with the horizontal tethering configuration. The modification was performed on the equations of motion

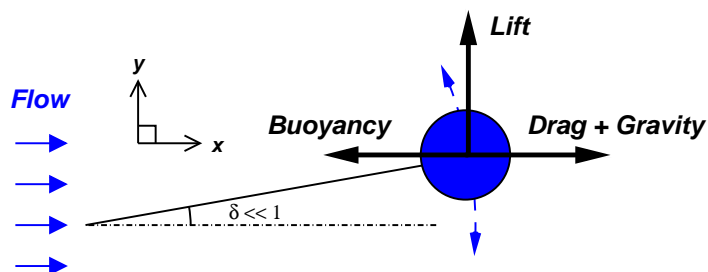


FIGURE 4.36: Schematic of a vertically tethered cylinder.

of the cylinder. The tension, T , is described by

$$T = (F_x - B + W) \cos \theta + F_y \sin \theta. \quad (4.2)$$

The mass ratio is assumed to have the value of $m^* \geq 1$, but the cases of $m^* < 1$ can be solved easily by simply changing the signs of the buoyancy (B) and the cylinder weight (W).

Accordingly, the resulting equations of motion are:

$$m\ddot{x} = (F_x - B + W) - T \cos \theta, \quad (4.3)$$

$$m\ddot{y} = F_y - T \sin \theta. \quad (4.4)$$

4.4.1 Response of the cylinder

Simulations for a vertically tethered cylinder with $m^* = 1.25$ were carried out over the range of $Re = 10 - 300$, as for the previous tethered cylinders. The α value describing the magnitude of the gravity was set to unity to be consistent with the neutrally buoyant case. Note that, for this vertically tethered cylinder, the solutions diverged for $Re \geq 200$, where the history of the x and y oscillations showed irregularity. Some other mass ratios of $m^* = 1.1, 2.0$ and 4.0 were tested and showed the similar diverged solutions when the oscillations became irregular. As the mass ratio increases, the Reynolds number at which the irregular oscillation initially appears to decrease. Lowering the timestep of the simulations had been tried and showed the same results for the three mass ratios. Unfortunately, there has been no experimental results to which the current simulation results to be compared. Thus, a comparison of the vertically tethered cylinder to the neutrally buoyant cylinder is focused on Regime II, where the oscillation is initiated and is periodic.

Figure 4.37 compares the mean layover angle for the vertically tethered cylinder and that for the neutrally buoyant cylinder. The main difference is the Reynolds number at which Regime II starts. Here, it is found to occur between $Re = 40$ and 50 , whereas it was between $Re = 30$ and 40 for the neutrally buoyant cylinder. This is also apparent in the amplitude and frequency response shown in figures 4.38 and 4.39. The difference is suspected to be due to the difference in the magnitude of the restoring force. For the neutrally buoyant cylinder where the restoring force is very small, the cylinder reacts to small fluctuations resident in surrounding fluid, whether they are regular or irregular. Therefore, it is believed that this results in the early start of Regime II at $Re = 40$

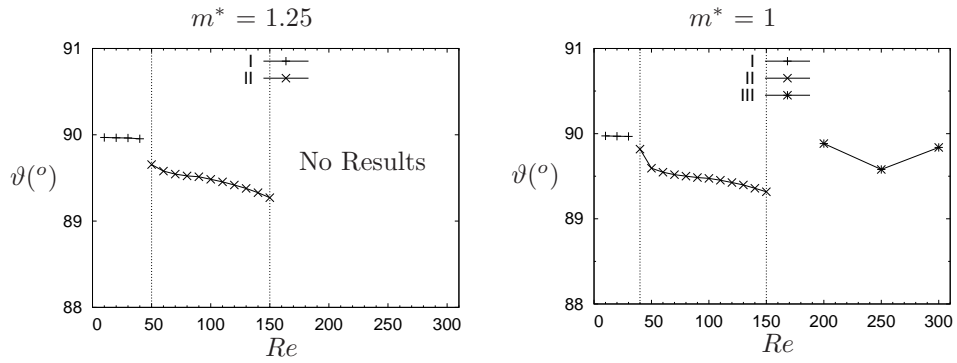


FIGURE 4.37: Layover angle ϑ of a vertically tethered cylinder (left) and of a neutrally buoyant tethered cylinder (right). Note that ϑ s are close to 90° .

compared to the vertically tethered cylinder case. Besides this difference in the Re range, both cylinders exhibit virtually identical responses in Regime II, as shown in figures 4.37 to 4.39.

Figure 4.40 shows the xy trajectories for $Re = 50, 100$ and 150 . The trajectories for all the Reynolds numbers are perpendicular to the flow because $\vartheta \approx 90^\circ$, and their amplitude grows with increasing Re , as anticipated from the amplitude response depicted in figure 4.38.

The forces responsible for the trajectory are presented in figure 4.41. As is the case for the trajectory, the magnitude of the x and y forces grow as Re increases. If we look at the insets, it is also clear that there is a doubling of the figure-of-eight pattern of the phase between the two forces. This indicates that subharmonic frequencies exist in the history of the two forces.

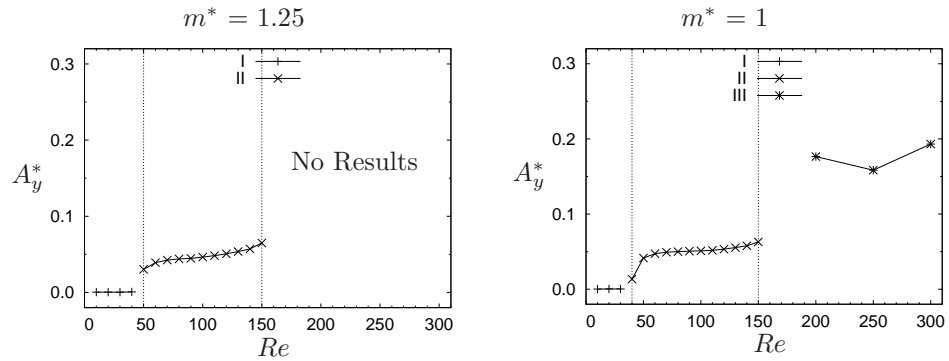


FIGURE 4.38: Amplitude of oscillation in the y direction for a vertically tethered (left) and a neutrally buoyant tethered (right) cylinder.

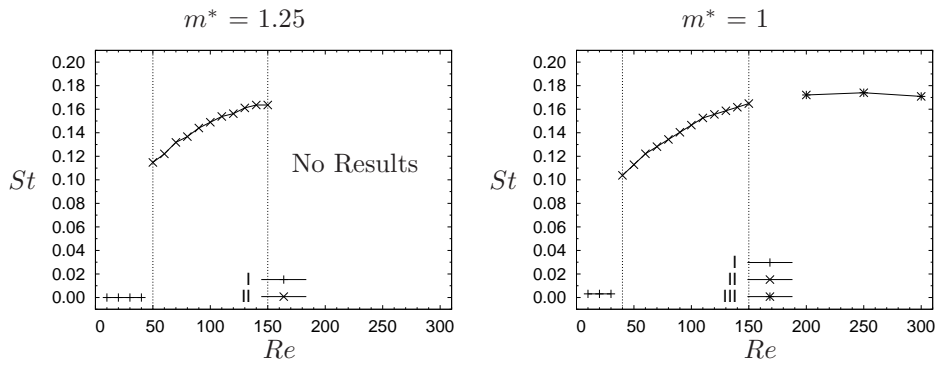


FIGURE 4.39: Frequency of oscillation in the y direction for a vertically tethered (left) and a neutrally buoyant tethered (right) cylinder.

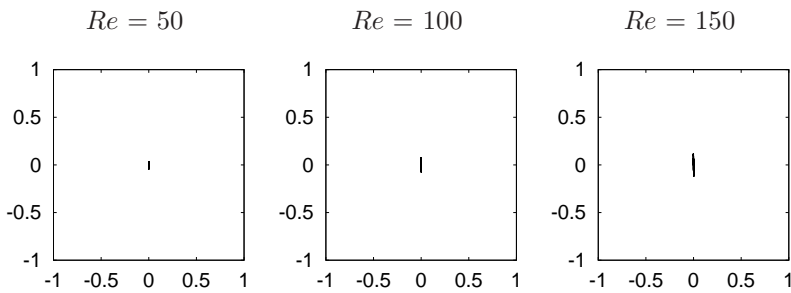


FIGURE 4.40: Trajectories of the oscillating cylinder in the xy coordinates when $m^* = 1.25$. Flow is coming from left. The abscissa is the x displacement and the ordinate is the y displacement. The displacements are normalised by the cylinder diameter D .

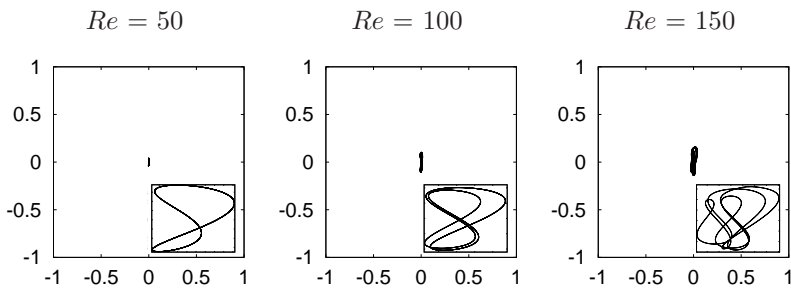


FIGURE 4.41: Phase plot of the total force coefficients in the xy coordinates when $m^* = 1.25$. The abscissa is C_x and the ordinate is C_y . The inset is magnified and autoscaled.

4.4.2 Comparison to VIV of the neutrally buoyant tethered cylinder

The results presented in section 4.4.1 indicate that the vertically tethered cylinder exhibits a response similar to that of the neutrally buoyant one at least in terms of phase plots of force coefficients. It is also possible to investigate other aspects of the response, such as the power spectrum of the oscillation for the vertically tethered cylinder, and compare these to the horizontally tethered cylinder case. To undertake this comparison, the power spectra of the x , y , C_x and C_y , and the phase between displacement and force in the x and y directions, are investigated for the following three cases: a horizontally tethered cylinder; a neutrally buoyant tethered cylinder; and a vertically tethered cylinder.

Figure 4.42 presents the power spectra of the displacements and the forces in the

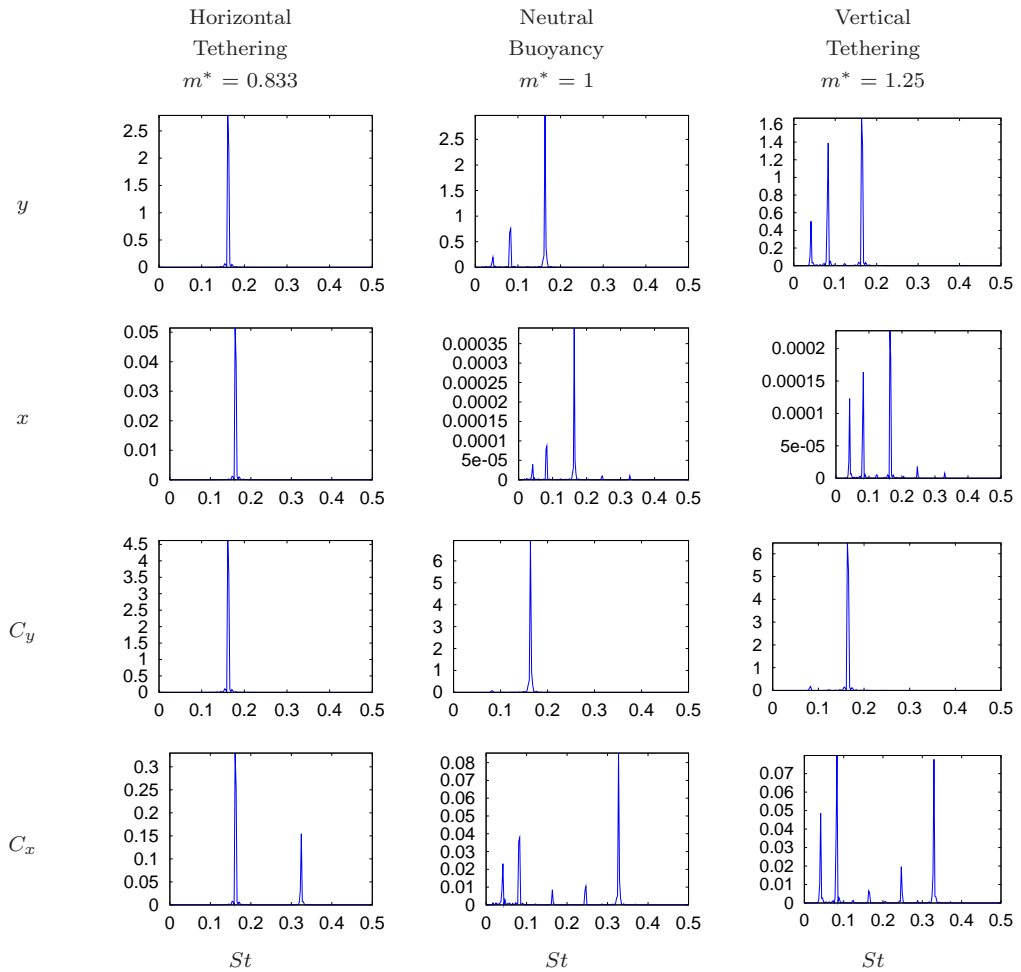


FIGURE 4.42: Power spectrum for the displacements and the total forces in x and y at $Re = 150$. The unit of the power is arbitrary.

x and y directions. Only the power spectra at $Re = 150$ are given because other Reynolds numbers showed similar characteristics but less clearly. Note that the right two columns correspond to the neutrally buoyant cylinder and the vertically tethered cylinder, respectively. First of all, subharmonic frequencies are present in the y direction as well as in the x direction for the neutrally buoyant and the vertically tethered cylinder. However, this is not the case for the horizontally tethered cylinder, which shows one frequency only in each direction.

Secondly, several discrete subharmonic frequencies appear in the power spectrum of C_x for the neutrally buoyant and the vertically tethered cylinder, whereas the horizontally buoyant tethered cylinder exhibits one additional superharmonic frequency. Of interest is that the power at the subharmonic frequencies for the vertically tethered cylinder is larger than those for the neutrally buoyant cylinder, due to larger restoring force. It is also clear, for the neutrally buoyant cylinder and the vertically tethered one, that the C_x affects the y oscillation as well as the x oscillation, based on the matching of the subharmonic frequencies of C_x and y . In contrast, the fluctuating C_y is the only force contributing to the x and y oscillations for the horizontally tethered cylinder.

The phase between the displacements and the forces depicted in figure 4.43 also reveals the close resemblance of the behaviour of the neutrally buoyant cylinder and the vertically tethered cylinder. Note that the bottom two rows correspond to the neutrally buoyant cylinder and the vertically tethered cylinder, respectively. The phase in the x direction for the two cases is characterised by a figure-of-eight pattern at $Re =$

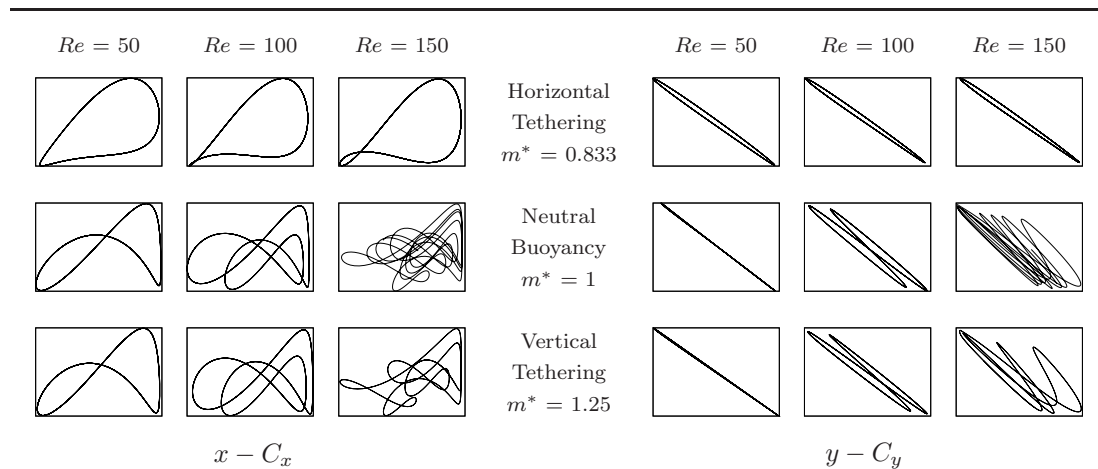


FIGURE 4.43: Phase plot between displacement and force. The abscissa is the displacement and the ordinate is the force. The axes are autoscaled to show the pattern more clearly.

50 and its doubling at higher Reynolds numbers of $Re = 100$ and 150 ; this behaviour is different to that of the horizontally tethered cylinder case. The difference of the horizontally tethered cylinder to the other two cases is clearly shown in the y phase, particularly at $Re = 100$ and 150 . A doubling of the phase pattern is also observable in the y phase as is the case in the x phase. It is of note that the doubling of the phase pattern is closely related to the subharmonic frequencies appearing in the power spectra for the displacements and the forces.

4.5 Chapter Conclusions

Numerical simulations of VIV for a neutrally buoyant tethered cylinder have shown that there exist three flow regimes within the range of Reynolds number $Re = 10 - 300$: Regime I, II and III. The layover angle ϑ , oscillation amplitude and frequency are used to define the regimes.

Regime I covers $10 \leq Re < 40$, and is steady with $\vartheta = 90^\circ$. Regime II exists between $40 \leq Re < 200$, and shows unsteady and periodic oscillation with growing amplitude and frequency as Re increases whereas ϑ decreases with increasing Re . Regime III, starting at $Re = 200$, exhibits much larger amplitude than that of Regime II, with slowly varying components on its principal oscillation. The frequency of this regime is saturated at $St \approx 0.17$, which is lower than that for a fixed cylinder reported in Williamson (1988a). The history and phase of the displacements and forces in the x and y directions, together with the power spectra of those, reveal that the principal oscillation in both displacements is dominated by a fluctuating y force, C_y , with secondary oscillations affected by subharmonic frequencies of the x force, C_x , particularly in Regime II. It is found that this subharmonic oscillation in the displacements is due to the layover angle being close to 90° and presumably dictated by restricting the motion to a circular arc.

Simulations of VIV for tethered cylinders where the buoyancy is acting in the y (crossflow) direction have been carried out to find any similarities or dissimilarities from the neutrally buoyant case, when $m^* = 1$. These are performed by varying the mass ratio from $m^* = 1$, covering the range $0.1 \leq m^* \leq 1.11$. Similar to the neutrally buoyant case, three response regimes are found for all the mass ratios considered, and each regime has the same Re range as from the neutrally buoyant case. The frequency of oscillation shows little difference from the neutrally buoyant cylinder for all three

regimes.

However, remarkable differences are also found to exist, particularly in the two oscillating regimes: Regime II and III. Due to buoyancy, the layover angle is no longer close to 90° even for the steady Regime I, and decreases continuously across Regime I and II for the mass ratios up to 0.5. Unlike the neutrally buoyant case, the oscillation amplitude grows smoothly across Regime II and III and maintains periodicity in Regime III. Moreover, there is no subharmonic oscillation in the displacement signal for Regime II. It is found that the difference in response from the neutrally buoyant case stems from the buoyancy changing the layover angle considerably. Additionally, it is found that there is a critical mass ratio beyond which the response and phase of the forces and displacements change. From the mass ratios considered for the tether length of $10D$, the critical mass ratio exists within $0.5 \leq m^* \leq 0.667$. The dependence of behaviour on mass ratio has been reported in previous studies of transversely oscillating cylinder (Govardhan & Williamson 2003) and (Ryan *et al.* 2005) where there is a distinct change in behaviour as the mass ratio is lowered below a critical mass ratio.

VIV of a vertically tethered cylinder where the buoyancy is acting parallel to the flow is also investigated to identify the resemblance to the neutrally buoyant sphere. The vertically tethered cylinder has the same force balance as the neutrally buoyant cylinder except for the difference of magnitude of the restoring force in the x (parallel) direction, and this was expected to reveal a close link to the neutrally buoyant cylinder. Indeed, the same response, phase and power spectrum are observed for the vertically tethered and neutrally buoyant cylinders featuring the doubling of a figure-of-eight in the phase plots as the Reynolds number is increased. Perhaps of interest if that the period-doubling of the phase plots seen as the Reynolds number is increased is consistent with one of the classical paths to chaos. This could be a topic of further investigation. Due to relatively larger effective drag force of the vertically tethered cylinder, Regime II starts at a higher Re than the neutrally buoyant case, and the cylinder oscillates periodically at the end of Regime II, whereas the cylinder with neutral buoyancy shows less periodic oscillation with a slowly varying low frequency component.

Chapter 5

VIV of a Tethered Sphere

5.1 Introduction

This chapter provides the details of the numerical and experimental results for a tethered sphere with an emphasis on a neutrally buoyant sphere ($m^* = 1$). The results for VIV of a neutrally buoyant tethered sphere are given first. Next, numerical result for a buoyant tethered sphere is presented to highlight any differences from the neutrally buoyant case. In addition, for a buoyant tethered sphere, the effect of the Reynolds number is investigated and the result fill a gap in literature for this type of VIV. Finally, the numerical results for a vertically-tethered sphere are presented, which shows its similarity to the neutrally buoyant case.

5.2 VIV of a Neutrally Buoyant Sphere: $m^* = 1$

This study reveals that the tethered sphere experiences seven different flow regimes as Re increases. The first six regimes were determined by numerical simulations and the seventh regime was found through experiments at high Reynolds numbers. A schematic of the neutrally buoyant tethered sphere is shown in figure 5.1.

Using the spectral-element/Fourier-spectral code, the simulations have been performed on high performance computers, and have been run using a parallel version of the software to reduce the calculation time, for the range of $Re = 50 - 800$. Some simulations have been run over 5000 non-dimensional time units to reach converged solutions. For example, the calculation at $Re = 400$ was run up to 5000 non-dimensional time units, which took about 30 hours. The initial Reynolds numbers were chosen in the range of $Re = 50 - 800$ in steps of 50, and intermediate Reynolds numbers between any two neighbouring Reynolds numbers were selected if any difference in body dynam-

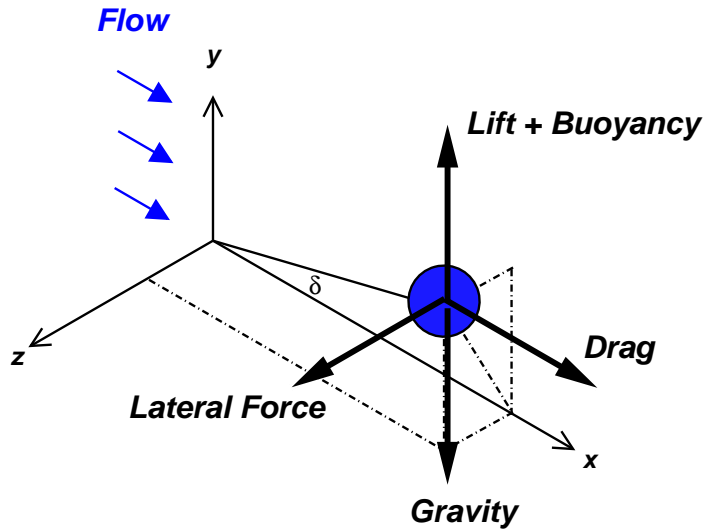


FIGURE 5.1: Schematic of a neutrally buoyant tethered sphere.

ics was observed. $Re = 205, 210, 270, 280$ and 330 are some examples chosen by this process. The tether length was chosen to $10D$ for all cases.

Experiments were carried out to support the numerical findings and to expand the Re range beyond the limit of the numerical simulations. The experiments covered the range of $Re = 700 - 8000$, which is higher than that of the numerical study. Importantly, this Re range overlaps the Re range of the experiments as well.

A parameter R is defined as a position vector in the crossflow (yz) plane (refer figure 3.2). Its magnitude is the distance to the centre of the body from the tether pivot in the crossflow plane. The parameter R is more applicable than y or z for a neutrally buoyant tethered sphere because there is no preferred direction of oscillation in the crossflow plane. For each simulation, the time history of R was used to calculate the time-mean position of the body, its amplitude and frequency, and the regimes were determined based on these three response variables.

5.2.1 Time-mean position: Layover angle ϑ

The angle measured from the transverse axis to the centre of the body is used to represent the time-mean position of the body. This angle ϑ , which is known as the layover angle, has been used in the previous studies of VIV of tethered bodies. The layover angle for the range of $Re = 50 - 800$ is shown in figure 5.2.

In the first regime (Regime I), the sphere remains on the pivot axis without move-

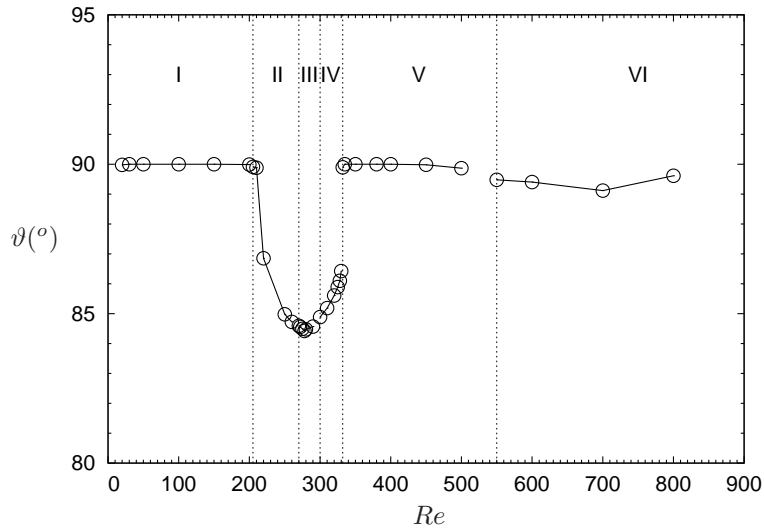


FIGURE 5.2: Layover angle of a neutrally buoyant sphere

ment. Its Reynolds number range is $Re < 200$. The second regime (Regime II), starting at $Re = 210$, is also steady but the axisymmetry is lost. This corresponds to the two-threaded wake of the stationary sphere observed by Johnson & Patel (1999) and Magarvey & Bishop (1961*b*). Thus, the sphere offsets from the symmetry axis and the layover angle decreases as Re increases. This regime exists up to $Re = 250$. As Re is increased further, the sphere starts to vibrate at $Re = 270$, the start of Regime III. Regime IV begins at $Re = 300$. It shows a steep increase of the layover angle indicating the body offsets more from the pivot axis than other regimes. In Regime V ($Re = 335 - 500$), the layover angle comes back to 90° which means the body oscillates around the pivot axis.

5.2.2 Amplitude of oscillation

Figure 5.3 shows the maximum amplitude of the sphere oscillations. The body shows oscillation from Regime III starting at $Re = 270$. The simulations at neighbouring Reynolds numbers of $Re = 265, 268, 272$ and 275 were performed and indeed the body oscillation was observed from $Re = 270$. Regime IV begins at $Re = 300$. It shows suppressed body oscillation and a steep decrease of the layover angle (see figure 5.2). The amplitude of oscillation in Regime V gradually increases as Re is increased. In Regime VI, the vibrations become chaotic and the sphere undertakes chaotic wandering, having no restoring forces. Note that the oscillation amplitude of this regime in figure 5.3 is

represented using the width and height of the wandering area due to its non-periodic nature.

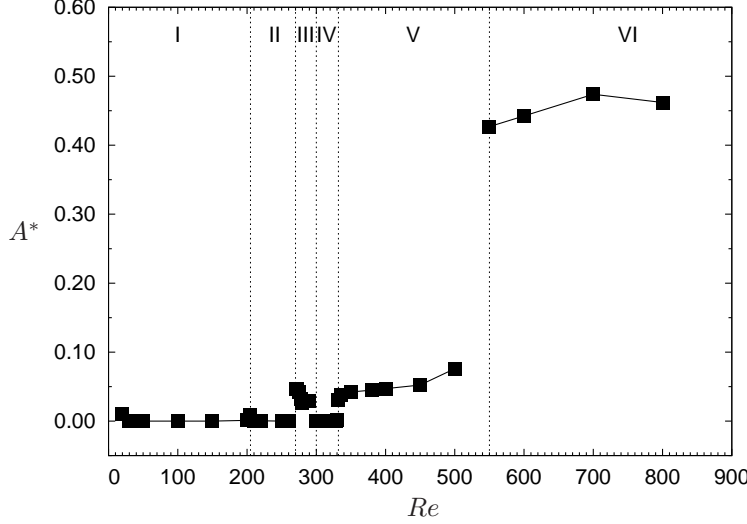


FIGURE 5.3: Amplitude of oscillation using R for a neutrally buoyant sphere.

5.2.3 Frequency of oscillation

In Regime I and II, the sphere does not vibrate. Then, in Regime III, IV and V, it undergoes periodic oscillations. In Regime VI, the oscillations lose their periodicity. The frequency of the sphere oscillation is normalised and expressed by a Strouhal number (St) based on the oscillation frequency (f) in radial direction, the freestream velocity (U), and the sphere diameter (D). Using equation 5.1, the nondimensionalised natural frequency f_n^* with the sphere diameter, D , and the inflow velocity, U , was calculated and is in the range of $f_n^* = 0.0254 - 0.0296$.

$$f_n^* = \frac{f_n D}{U} = \frac{1}{2\pi} \sqrt{\frac{3}{4} \frac{\sqrt{C_x^2 + \{(1 - m^*)\alpha + C_y\}^2 + C_z^2}}{(C_A + m^*)L^*}} \quad (5.1)$$

In equation 5.1, m^* is the mass ratio, L^* is the nondimensionalised tether length, α is the parameter defined in section 3.2 and C_A is the added mass coefficient ($C_A = 0.5$ for sphere) of an ideal flow.

Derivation of equation 5.1 starts from the equations 5.2 to 5.4.

$$(m + m_a)\ddot{x} + \frac{T}{L}x = F_x, \quad (5.2)$$

$$(m + m_a)\ddot{y} + \frac{T}{L}y = F_y + B - W, \quad (5.3)$$

$$(m + m_a)\ddot{z} + \frac{T}{L}z = F_z. \quad (5.4)$$

From these equations, it is obvious that the natural frequency is the same in all three dimensions, and is given by

$$f_n = \frac{1}{2\pi} \sqrt{\frac{T}{(m + m_a)L}}. \quad (5.5)$$

This dimensional natural frequency can be put in non-dimensional form, which is given by

$$f_n^* = \frac{f_n D}{U} = \frac{1}{2\pi} \sqrt{\frac{D^2}{U^2} \frac{T}{(m + m_a)L}}. \quad (5.6)$$

Substituting the expression for the tension in the tether, collecting terms and using the non-dimensional form of the fluid forces results in equation 5.1.

Williamson & Govardhan (1997) used equation 5.7 to calculate f_n^* by assuming the y force, C_y , and the z force, C_z are much smaller than the buoyancy, $(1 - m^*)\alpha$.

$$f_n^* = \frac{f_n D}{U} \approx \frac{1}{2\pi} \sqrt{\frac{3}{4} \frac{\sqrt{C_x^2 + \{(1 - m^*)\alpha\}^2}}{(C_A + m^*)L^*}} \quad (5.7)$$

Figure 5.4 shows that St for Regime III is 0.0671 and is more than two times the calculated f_n^* of the tethered sphere with $m^* = 1$. In this regime, the Strouhal numbers of oscillations in the x , y , z directions have the St value of 0.0671, as for the frequency of R . The fluid forces in all three directions were calculated and also showed the same value of $St = 0.0671$.

The frequency for R in Regime IV is $St = 0.222$, being much higher than its natural frequency of $f_n \approx 0.029$. Note that within this regime, the body predominantly oscillates in the azimuthal direction and the R amplitude is very small (see figure 5.3). The St for this azimuthal oscillation has the value of 0.111, which is the same as that for the oscillation for y and F_y . Only the displacement and force in y direction is mentioned because there is little oscillation in the x and y directions, in contrast to the case of Regime III. The value of $St = 0.111$ is close to that of the stationary sphere ($St = 0.134$) in the same Re range.

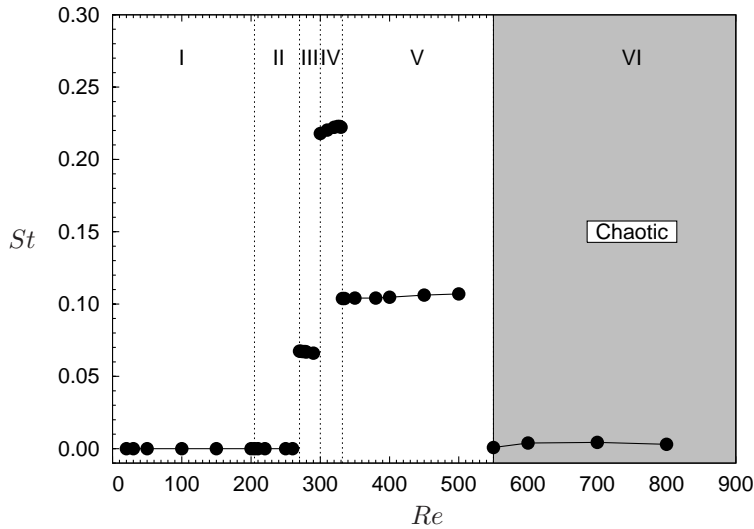


FIGURE 5.4: Frequency of oscillation using R for a neutrally buoyant sphere.

The frequency of R for Regime V is 0.104. In Regime V, St is recalculated considering the mean-position on the pivot axis and its definition as a vector. The St for Regime V ($St = 0.104$) is also close to (but still less than) that of the fixed sphere ($St = 0.134$). Similar to the case of Regime IV, the body predominantly oscillates in the y direction. The frequencies of y and F_y also have the same value of $St = 0.104$ as for the R . Regime VI shows chaotic wandering of the body and the Strouhal number is not meaningful. Hence, the area for this regime is shaded.

It is of interest that the critical Reynolds number separating Regimes II and III is slightly lower than that of a fixed sphere ($Re \approx 280$) found in Tomboulides & Orszag (2000). Other calculations (i.e. Thompson *et al.* (2001) indicate the transition occurs at $Re \approx 272$. This is also the case for the transition to Regime II: the critical value of the Reynolds number is $Re \approx 205$ for the tethered sphere, whereas that for a fixed sphere is $Re = 211$ (Johnson & Patel 1999).

5.2.4 Trajectory of the oscillating sphere

Regime III to VI

The trajectories in xy , yz , and zx planes are shown in figure 5.5. Note that all the trajectories shown correspond to unsteady regimes, i.e., the regimes III to VI, and all determined from the simulations. The trajectories of the other steady regimes are not shown here as the sphere exhibits no oscillation.

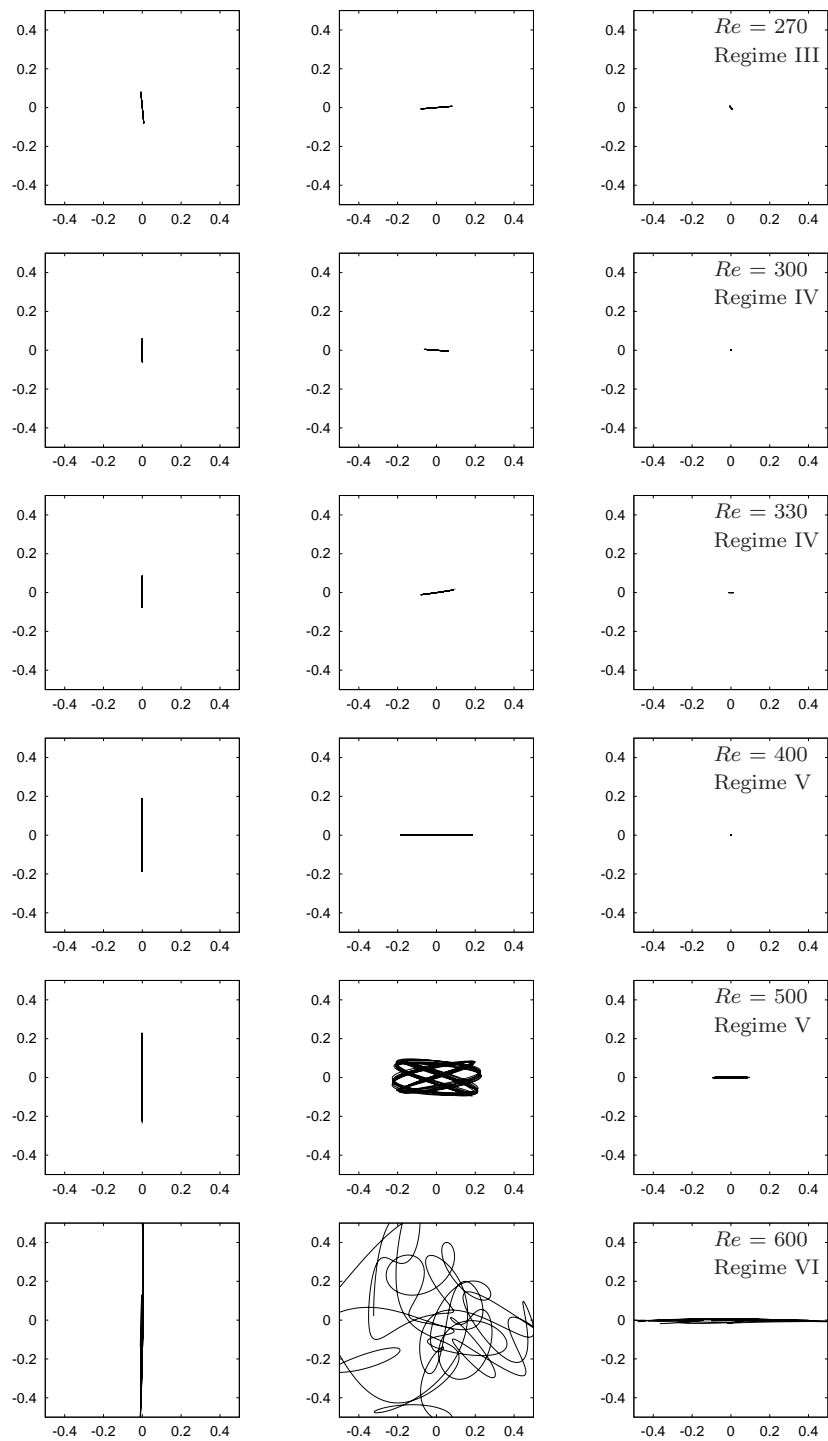


FIGURE 5.5: Trajectories in xy (first column), yz (second column), and zx (third column) planes at various Reynolds numbers. All the axes have the same scale. Each tic represents $0.2D$, and the mean position of the sphere is located to the $(0, 0)$.

Throughout the regimes III to V, the sphere oscillates on a straight line mainly in the y direction. This is in contrast with the previous studies (Govardhan & Williamson 1997; Williamson & Govardhan 1997) showing that a buoyant tethered sphere exhibits an oscillation, mainly in the z direction. This difference is due to the direction of the buoyancy acting on the body ($-y$ for a buoyant body) as well as its relative magnitude as a restoring force. For the case of a neutrally buoyant body, the tethered sphere has no preferred direction of the oscillation, considering its neutral buoyancy. However, for the current simulations, the initial condition of $\phi = 0$ and $\theta = 5$ means an initial displacement of the sphere only in the y direction, and affects the direction of the oscillation. Note that this is only a matter of orientation of the oscillation, not a matter of accuracy of the simulation results.

As the Reynolds number increases, the total amplitude grows gradually in the y direction for the regimes III to V. In the regimes III and IV, the sphere does not oscillate on a straight line parallel to axis. This is due to the fact that the sphere is oscillating at a mean position away from the layover angle of $\vartheta = 90^\circ$ and the fixed-length tether. In contrast, the sphere oscillation trajectories are on a straight line parallel to the axis when the layover angle is $\vartheta \approx 90^\circ$.

The oscillations in the z direction appear at $Re = 500$ (the last Re considered for Regime V) and gets larger at $Re = 600$ with chaotic wandering in the crossflow (yz) plane. The case of $Re = 500$ was determined to be Regime V due to its periodic oscillation, despite having a z oscillation.

The trajectory in yz is of interest not only because the main oscillation of the sphere is observable in that plane but also because the difference between the regimes is clear, for example the inception of the z oscillation. In section 5.2.6, the phase between the forces and the displacement will be provided, focusing on this yz plane for the same reason.

Regime VII

The trajectory in the xy and the yz planes at various Reynolds numbers were recorded and were processed to calculate the position of the tethered sphere. The experimental findings are twofold. Firstly, the existence of Regime VI found from the numerical investigations is verified. In figure 5.6, the sphere shows a chaotic wandering as was observed in the simulations at $Re \geq 600$. The experimental results clearly show chaotic

wandering when $Re < 3000$ with its minimum value of 902. It should be noted that the trajectories in the figure 5.7 are realigned for comparison, as the orientation of the motion is arbitrary for the neutrally buoyant sphere.

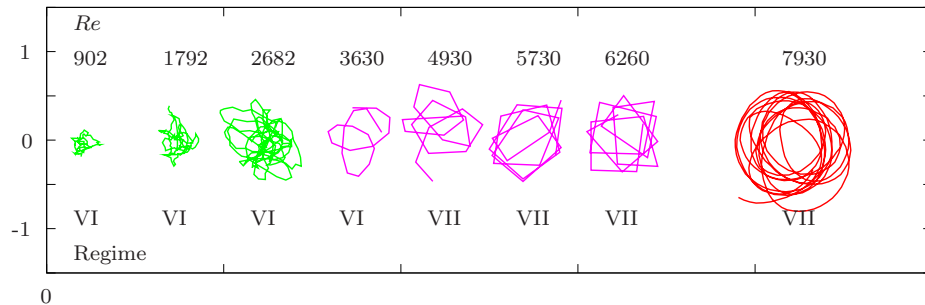


FIGURE 5.6: Trajectories in yz plane. All the results are from the experiments. Both axes are of the same scale and normalised by the sphere diameter D . Note the horizontal axis is the z axis, and the vertical one is the y axis whereas the horizontal axis of yz trajectories in figure 5.5 is the y .

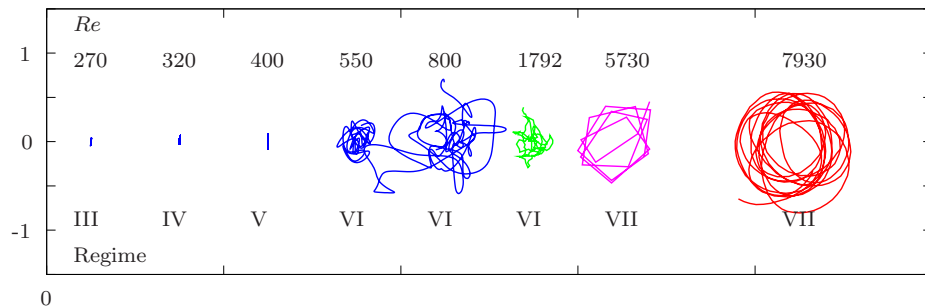


FIGURE 5.7: Trajectories in yz plane for unsteady regimes. The blue lines ($Re = 270$ to 800) are the numerical results. Both axes are of the same scale and normalised by the sphere diameter D . Note the horizontal axis is the z axis, and the vertical one is the y axis whereas the horizontal axis of yz trajectories in figure 5.5 is the y .

Secondly, an additional regime, Regime VII, is found to exist from the experimental study at $Re > 3000$. This regime is characterised by a *quasi-circular* motion in the yz plane, and is observed from $Re = 3630$. As Re is raised further, the sphere motion exhibits more clearly a circular shape. Note that the square-like trajectories for $Re = 5730$ and 6260 are due to the lack of camera speed. The speed of camera was 8 fps up to the $Re = 6260$, and was not suitable to show the full circular shape at those Reynolds numbers. With the aid of a 25 fps video images, the quasi-circular motion shown for a higher Reynolds number of 7930 is much more obvious.

To compare the trajectories and amplitudes of oscillation for each regime, the tra-

jectories in the yz plane of the unsteady regimes are shown in figure 5.7. The variation of the oscillation amplitudes shown in figure 5.3 can be observed in figure 5.7. It indicates that the pattern of the sphere oscillation of the unsteady regimes III to V is close to being a straight line. The sphere shows an irregular pattern in Regime VI, and a quasi-circular motion in Regime VII.

The response variables of the sphere oscillation in Regime VII are given in table 5.1. The diameter of the circle (calculated as $D_{circle} = D_y/2 + D_z/2$) gradually grows as Re increases, and reaches about $0.5D$ at the maximum $Re = 11870$.

The nondimensionalised natural frequency, f_n^* , calculated using equation 5.1, is in the range of $f_n^* = 0.0145 - 0.0214$ for the Re range investigated. Only an estimate of f_n^* was possible due to the lack of force data from the experiments of an oscillating sphere. It is obvious that the sphere oscillates at a frequency higher than its natural frequency in Regime VII. A similar frequency response has been reported in the study of VIV of a transversely oscillating cylinder, that, when $m^* \leq 1$, or of the order unity, the cylinder oscillates at much higher frequency than its natural frequency. This frequency, however, is lower than that of the other regimes.

Interestingly, the quasi-circular motion of sphere was reported for the vertically tethered heavy sphere (Provansal *et al.* 2004). They observed a quasi-circular or an elliptic motion in the plane normal to the flow at the Re range of $Re = 600 - 800$. This contrasts to the sphere response of Regime VII as this motion appeared at much higher $Re > 3000$. Numerical simulations were performed to identify this similarity between

Re	D_{circle}^*	f_y^*	f_z^*
3630	0.22	0.0293	0.0293
4930	0.28	0.0335	0.0335
5730	0.31	0.0352	0.0352
6260	0.29	0.0360	0.0360
6432	0.28	0.0310	0.0310
7418	0.33	0.0347	0.0347
7930	0.34	0.0397	0.0397
11870	0.48	0.0454	0.0454

TABLE 5.1: The diameter of the quasi-circular area and the frequency of oscillation in Regime VII. $D_{circle}^* = D_{circle}/D$, and $f^* = fD/U$. Note that the sphere oscillates at a frequency higher than the estimated range of $f_n^* = 0.0145 - 0.0214$. This is the case for the VIV of a cylinder where $m^* \leq 1$.

the two systems and to investigate the mechanism that induce the quasi-circular motion. The results are detailed in section 5.5.

5.2.5 Vortex structure around the sphere

The vortex structures of the different regimes are shown in figure 5.8 to 5.13. The structures are rendered by isosurfaces of streamwise vorticity (Regime II) and by the field defined in Jeong & Hussain (1995) used to highlight vortical structures in the flow (Regime III to VI). Figure 5.8 shows the vorticity plot of Regime II represented by $Re = 210$. The vorticity plot for Regime I is not presented because the vorticity is virtually zero owing to the steady and axisymmetric flow with a layover angle of $\vartheta = 90$. In contrast, The flow for Regime II is steady but asymmetric for Regime II. Due to this asymmetry of the flow field characterised by the double-threaded vortex loops, the sphere is offset from its pivot axis in the crossflow plane.

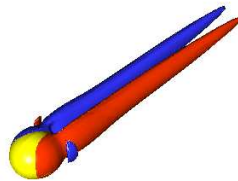


FIGURE 5.8: Streamwise vorticity of Regime II ($Re = 210$). Flow is from the bottom left corner to the top right. Red represents positive streamwise vorticity and blue represents negative streamwise vorticity. The vorticity values are ± 0.1 , and the two trailing vortices are apparent.

Regimes III, IV and V consist of periodic shedding of vortices as shown in figures 5.9 to 5.11. Within Regime III, the body oscillates mainly in the y direction. The streamwise vorticities of opposite signs do not interact much as they shed downstream, and vorticity of each sign always takes one side of the body. As a result, the hairpin-shaped vortex loops do not appear in this regime, as shown in the case of $Re = 270$ by the field defined by (Jeong & Hussain 1995). Dissimilar vortex structures at the bottom and top positions indicate a non-sinusoidal forcing in the y direction. This is verified by comparing the histories of fluid forces, which are shown in section 5.2.6.

Within Regime IV, the body oscillates mainly in the azimuthal direction with a finite mean inclination angle ϕ in the yz plane, whereas the body oscillates predominantly in

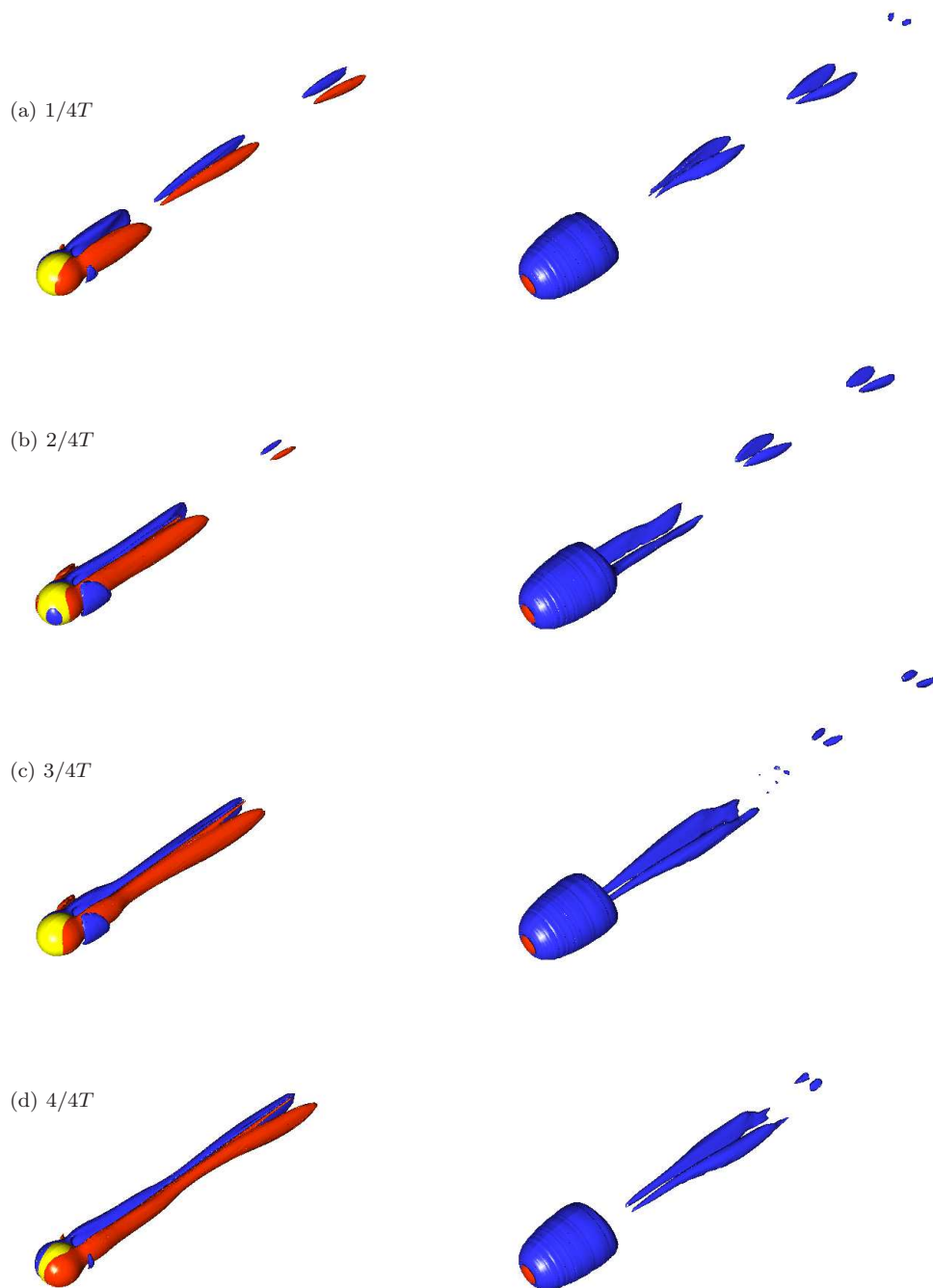


FIGURE 5.9: Vortex structures at $Re = 270$: Regime III. It shows vortex structures for every quarter oscillation period T from the lowest position of the cycle. The first column is the streamwise vorticity, and the second column is the field defined by Jeong & Hussain (1995). The colours for the streamwise vorticity are same as figure 5.8. Periodic shedding of vortices is clear, but no hairpin-shaped vortex loops are shown.

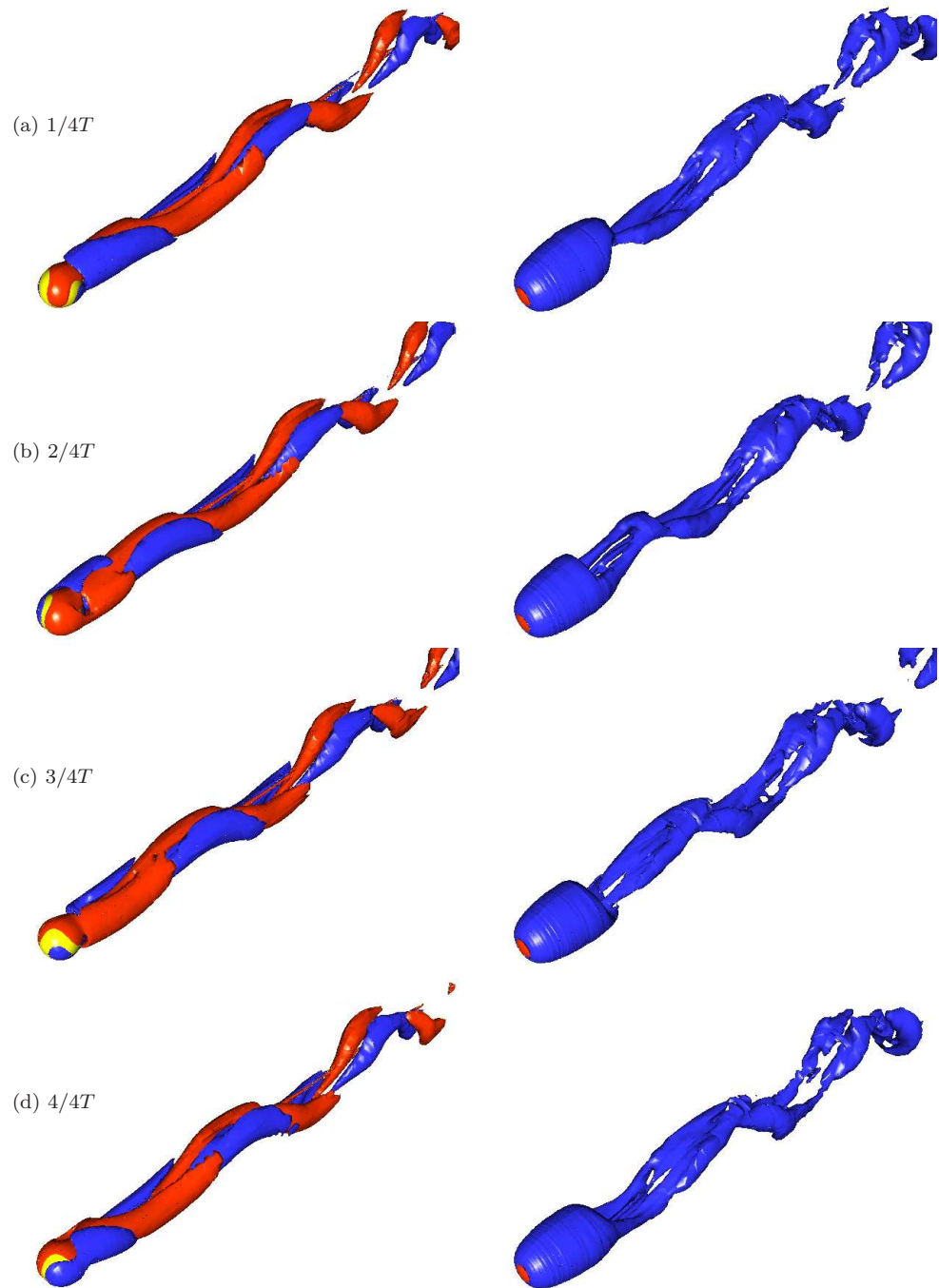


FIGURE 5.10: Vortex structure at $Re = 330$: Regime IV. The details of the plots are the same as figure 5.9. The hairpin-shaped vortices appear.

the y direction. This azimuthal direction of oscillation seems due the vortex structure adjacent to the body shown by the streamwise vortices in figure 5.10. On and around the surface, the forming of the vorticity shows azimuthal variation within one cycle, which is related to the body motion. However, in the far wake downstream, the hairpin

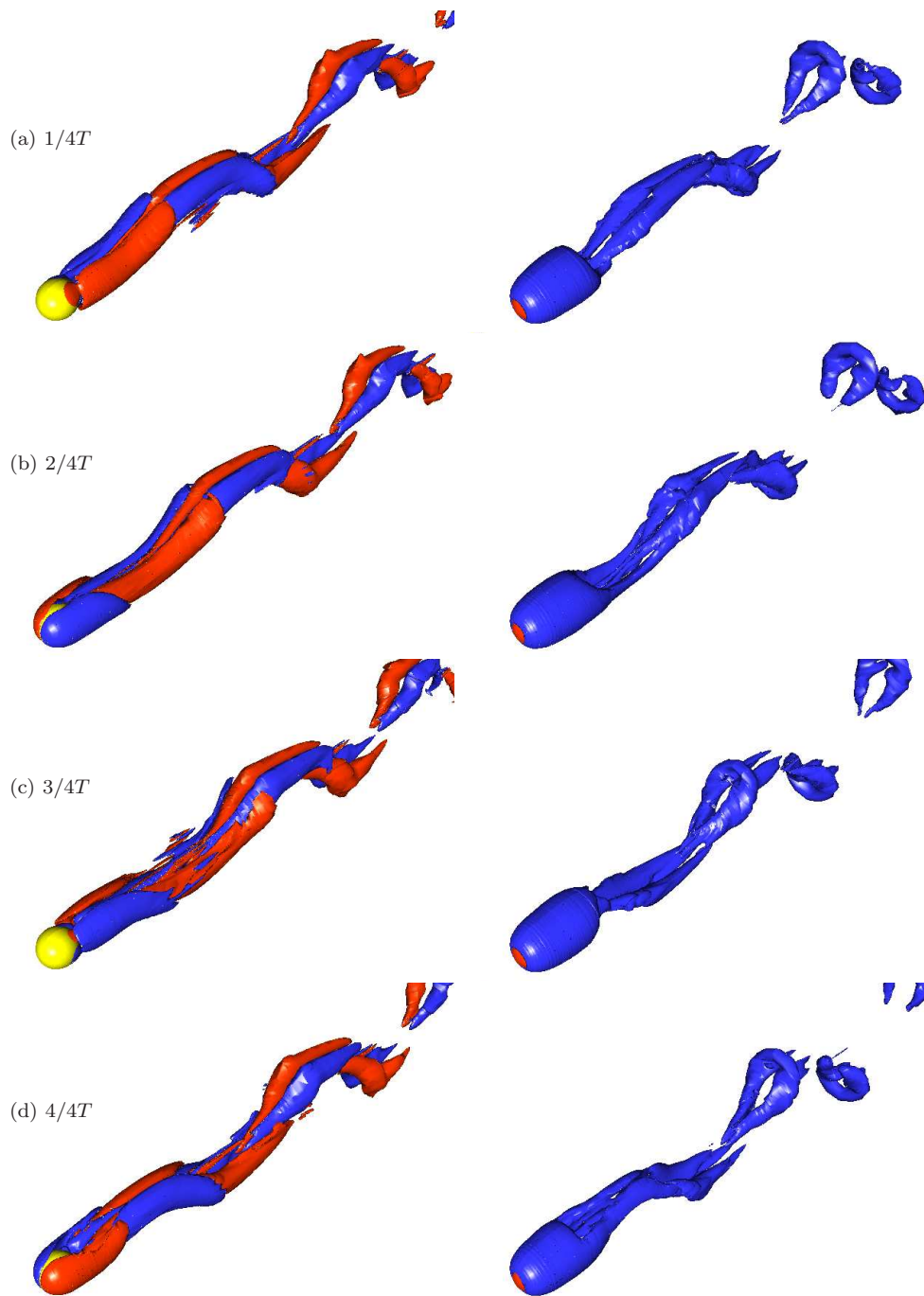


FIGURE 5.11: Vortex structure at $Re = 400$: Regime V. The details of the plots are the same as figure 5.9. The hairpin-shaped vortices is clear and keeps planar symmetry.

vortex loops are formed on both sides ($\pm y$ in this case) from the shed vortices. The two-sided vortex loops were observed for a spherical bubble rising in a fluid (Magarvey & Bishop 1961*b*; Mougin & Magnaudet 2002), whereas the well-known one-sided vortex loops were observed for a fixed sphere.

In contrast, the body oscillates mainly in the radial direction in Regime V with its mean position on the pivot axis, and the vortex structure reflects this difference (figure 5.11). Firstly, the hairpin-shaped vortex loops are formed closer to the body in the far wake region. Secondly, in the near wake, there is no variation of vortex forming as was observed for Regime IV, where the vortices form only at the alternating sides ($\pm z$) over a period in the near wake. The vortex forming period is longer than that for Regime IV, but the vortex loops are formed on both sides ($\pm y$) as was the case for Regime IV.

The motion of the sphere in Regime VI ($Re = 700$) shows irregular behaviour due to the loss of regular shedding of vortices. In figure 5.12, the hairpin vortex loops are visible although they are not as apparent as the cases for Regime IV and V. After the flow becomes irregular, the difference in the vortex structure is difficult to discern.

A point of interest about the vortex structure is that the planar-symmetry is similar to that for a fixed sphere. In figure 5.13, it is obvious that there is a symmetry plane

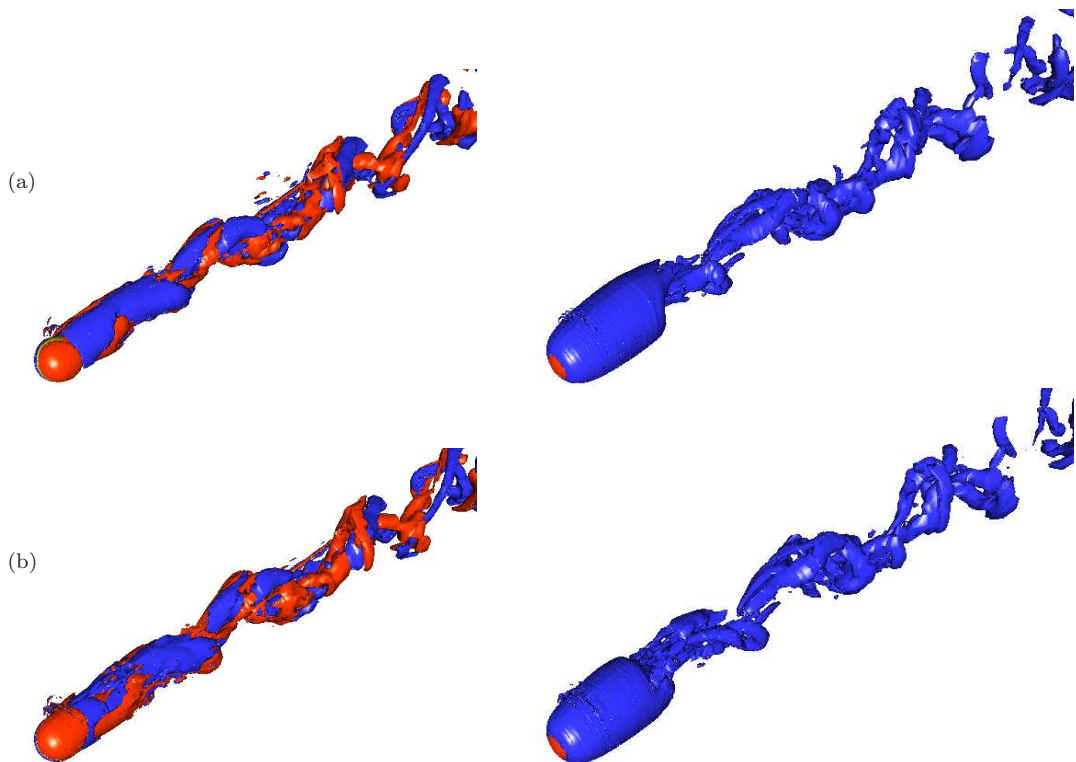


FIGURE 5.12: Vortex structure at $Re = 700$: Regime VI. (a) at $t^* = 510$ and (b) at $t^* = 513$ time units. The sphere motion has no periodicity. The details of the plots are the same as figure 5.9. The hairpin-shaped vortices are visible, but lose their planar symmetry.

for the vortex structure of Regime III and V. However, this planar-symmetry is lost in Regime IV ($Re = 330$), where the body oscillated mainly in the azimuthal direction.

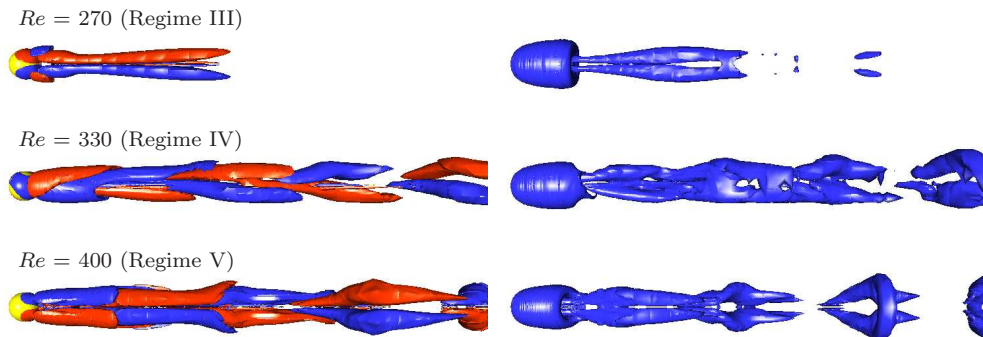


FIGURE 5.13: xy view of the vortex structure at the top position of the cycle in unsteady regimes. It is clear that the structure is planar-symmetric at $Re = 270$ (Regime III) and 400 (Regime V). The planar-symmetry is lost when $Re = 330$ (Regime IV).

5.2.6 Phase between forces and displacements

In general, the fluid forces are the cause of a bluff body movement when the body is free to move. In the problem of VIV, the phase between the fluid force and the displacement is considered to give an explanation for its response, and hence its underlying mechanism can be investigated by looking into these phase plots. Bearman (1984) pointed out the importance of the phase for VIV problem together with other parameters such as the mass ratio and structural damping. Many researchers, such as Blackburn & Henderson (1999); Carberry *et al.* (2004), have interpreted the phase information as the energy being transferred from the fluid flow to the body, and calculated the direction of this energy transfer using the phase plots.

For a bluff body under forced vibrations, the energy transfer may be negative because the body can transfer energy to the fluid flow. However, the energy should be positive for a freely vibrating bluff body or VIV as the body extracts energy from the fluid flow to maintain the vibration. As a result, the phase for the VIV problems will have limited values within the range of $\varphi = 0 - 2\pi$.

The phase information can be used to detect the change of the regimes in the VIV problems. Bishop & Hassan (1964) was the first to mention this relationship. Govardhan & Williamson (2005) found, for VIV of a transversely vibrating cylinder, the phase between the vortex force and the displacement, and the total force and the displace-

ment changes when the body goes through the three response branches; the initial, the upper, and the lower branches. With this in mind, the phase is plotted and analysed for unsteady regimes (Regime III to VI) of the tethered sphere found through numerical simulations. For all three regimes, the total force, pressure force component, viscous force component, and displacement are provided for all three Cartesian directions.

The motions in the x , y and z directions are coupled and not independent due to the constant tether length ($Lstar = 10$). They are related to each other by equation 5.10, and the sphere moves on a spherical surface defined by L^* , θ and ϕ . As L^* is fixed at $L^* = 10$ for all the simulations considered, the motion is actually two-dimensional in θ and ϕ . However, the following discussions are presented in the x , y and z for convenience considering the initial conditions used in the simulations for the neutrally buoyant sphere.

$$x = L \cos \theta \quad (5.8)$$

$$y = L \sin \theta \cos \phi \quad (5.9)$$

$$z = L \sin \theta \sin \phi. \quad (5.10)$$

When $m^* = 1$, there is no preferred direction in the yz plane as buoyancy is zero, whereas the sphere oscillates in the z direction when $m^* \neq 1$. For all the following simulations when $m^* = 1$, the initial conditions put a perturbation in the y direction, thus, the results show the largest oscillation in the y direction. This is one of the reason why the following results is discussed in the xyz coordinate. However, note that the motion of a tethered sphere with a constant-length tether is basically two-dimensional, and there is no preferred direction of oscillation in the crossflow (yz) plane when the sphere is neutrally buoyant.

In Regime III ($Re = 270$), the total fluid force in the x direction as well as its pressure and viscous components lead the x displacement by $\varphi \approx 270^\circ$ as shown in the time histories of the force and the displacement of figure 5.14. At this value of $\varphi = 270^\circ$, the phase plots are characterised by a circle. In the y direction, only the viscous force component shows the phase value of $\varphi = 270^\circ$. The total fluid force in the y direction and its pressure component show a phase value of $\varphi < 90^\circ$. If $\varphi = 90^\circ$, the phase plot will exhibit a straight line from the top left to the bottom right. It should be noted that the body oscillates mainly in this direction. Although the magnitude of the force and the displacement in the z direction are small, they exhibit the same characteristics

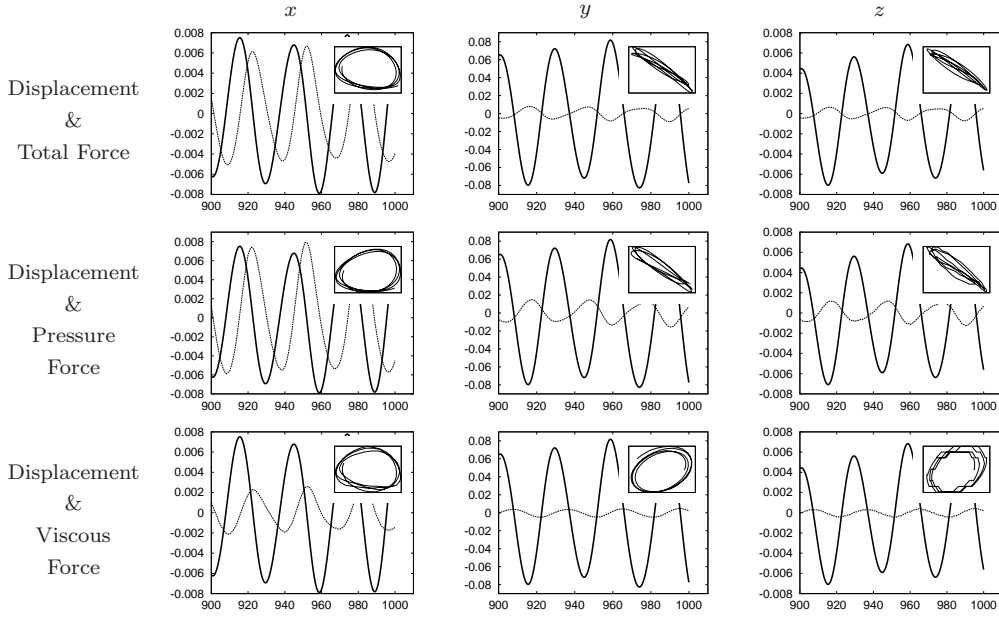


FIGURE 5.14: History of the displacements (thick solid line) and the forces (thin dashed line) forces at $Re = 270$ (Regime III). The abscissa of the history is the nondimensional time unit. The insets of each subfigure are the phase plots between the displacement (abscissa) and the force (ordinate). The axes in the phase plot are autoscaled to show the pattern more clearly.

as in the y direction, i.e., $\varphi_{F_V-z} \approx 180^\circ$, $\varphi_{F_P-z} \approx 90^\circ$, and $\varphi_{F_{total}-z} \approx 90^\circ$.

The histories of the forces and the displacement, and the phase plots for Regime IV ($Re = 330$) are provided in figure 5.15. In the x direction, the total fluid force and all its components have the phase value $\varphi \approx 0^\circ$. In detail, the phase between the viscous force component and the displacement is $\varphi \approx 360^\circ$ (meaning the viscous force is slightly behind the x displacement), and $\varphi_{F_{total}-x}$ is closer to zero than φ_{F_P-x} . In the main oscillation direction of y , these two phase values change to 180° (see figure 5.15). However, $\varphi_{F_V-y} \approx 270^\circ$, similar to that of the x direction as well as that for Regime III. A quick look at the phase plots for the other unsteady regimes shows that φ_{F_V-y} and φ_{F_V-z} have almost the same value of 270° . The z fluid force shows non-sinusoidal history, which makes the phase plots distorted as shown in figure 5.15. As in the y directional force and displacement, $\varphi_{F_{total}-z} \approx 180^\circ$ and $\varphi_{F_P-z} \approx 180^\circ$.

Figure 5.16 shows the histories of the forces and displacement in the x direction for Regime V represented by $Re = 400$. In the x direction, the total force advances the displacement with the phase (φ) less than 45° and close to the condition of in-phase. If we look at the pressure and viscous components of the total, the phase between the

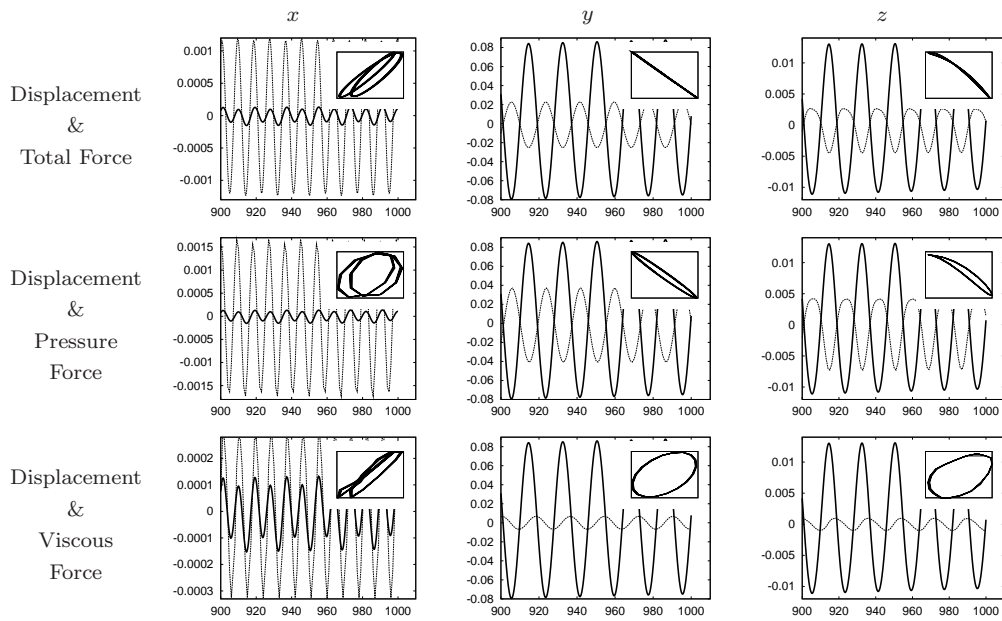


FIGURE 5.15: History of the displacements (thick solid line) and the forces (thin dashed line) forces at $Re = 330$ (Regime III). The abscissa of the history is the nondimensional time unit. The insets of each subfigure are the phase plots between the displacement (abscissa) and the force (ordinate). The axes in the phase plot are autoscaled to show the pattern more clearly.

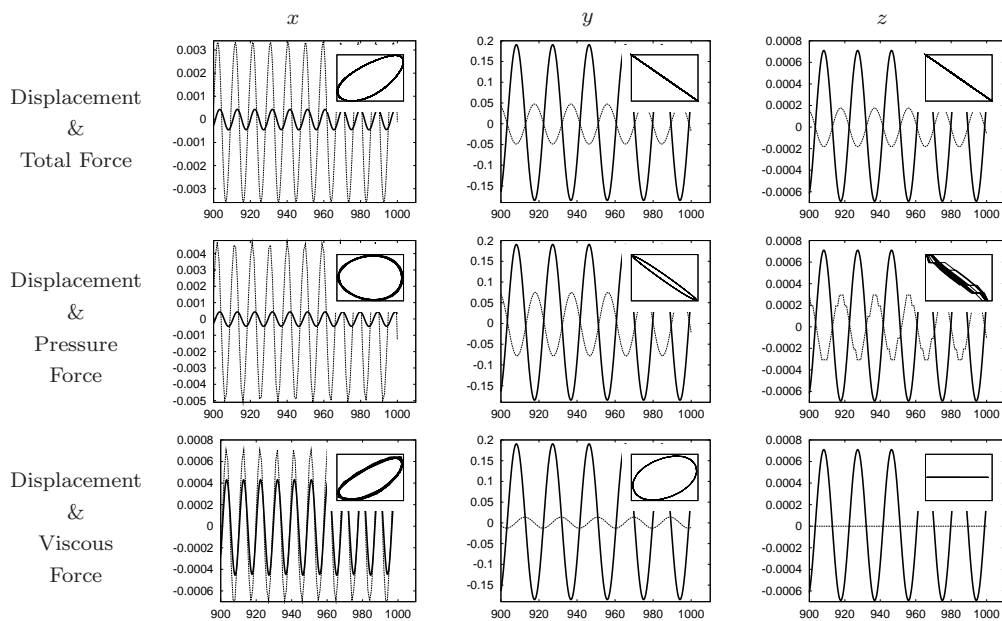


FIGURE 5.16: History of the displacements (thick solid line) and the forces (thin dashed line) forces at $Re = 400$ (Regime III). The abscissa of the history is the nondimensional time unit. The insets of each subfigure are the phase plots between the displacement (abscissa) and the force (ordinate). The axes in the phase plot are autoscaled to show the pattern more clearly.

x and the viscous force components is less than that of the x and the pressure force components. Nevertheless, the difference in the value of the phase is very small and both values are all less than 90° . The pressure force component comprises about 90% of the magnitude of the fluctuating x force. This portion of the force component is similar to the forces in the y and z directions, as the sphere is a bluff body. Actually, the oscillation in x direction is not of interest due to its minute oscillation (since it is highly constrained) compared to that of y and z . The sphere oscillates mainly in the y direction. It is obvious that total force and the displacement are out of phase, i.e. $\varphi_{F_{total}-y} \approx 180^\circ$. This is the same for the pressure component, and $\varphi_{F_P-y} \approx 180^\circ$. However, for the viscous component, $\varphi_{F_V-y} \approx 270^\circ$ as was observed for Regime III and IV.

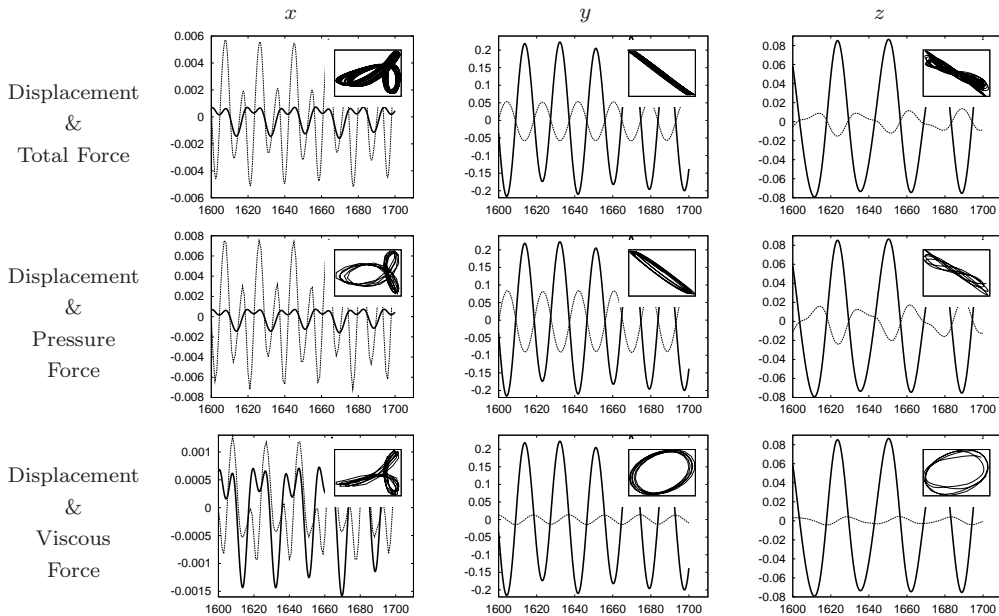


FIGURE 5.17: History of the displacements (thick solid line) and the forces (thin dashed line) forces at $Re = 500$ (Regime III). The abscissa of the history is the nondimensional time unit. The insets of each subfigure are the phase plots between the displacement (abscissa) and the force (ordinate). The axes in the phase plot are autoscaled to show the pattern more clearly.

Figure 5.17 shows the histories of the forces and displacement when $Re = 500$. Even though this Re is categorised in Regime V (the same regime as $Re = 400$), the oscillation in the z direction appears. The y and z oscillations are quite periodic at this $Re = 500$, but their trajectories are very different from those of the $Re = 400$ case. Secondary oscillation is clearly observed in the x force and displacement. As a

result, the phase plots exhibit a particular shape of limit cycle shown in figure 5.17 even though its amplitude is small. This is the case for oscillations in both the y and z directions; their histories of displacement and force exhibit secondary (low frequency) oscillations. Based on the phase plots for the y and z directions, it is indicated that the total force and the corresponding displacement are out-of-phase. This is the case for the pressure force component for both y and z .

5.3 VIV of a Buoyant Tethered Sphere: $m^* < 1$

To examine the effect of mass ratio, the simulations for the mass ratios of $m^* = 0.909$ and $m^* = 0.667$ with selected Reynolds numbers were performed. Unlike the neutrally buoyant case, tension plays a significant role on the VIV of a buoyant tethered sphere. The time needed to reach the converged solution became shorter than that of the $m^* = 1$ case owing to the contribution of buoyancy to a restoring force. A comparison of the response variables (the layover angle, and the amplitude and frequency of body oscillation) with the $m^* = 1$ case is presented.

5.3.1 Response of oscillation

Figures 5.18 to 5.20 shows the oscillation response of a tethered sphere with different mass ratios. Overall, the layover angle decreases as the mass ratio decreases within each flow regime; these regimes are shown divided by vertical dotted lines in the figure. This behaviour is due to the relative buoyancy effect growing as m^* decreases. At a given mass ratio m^* , the layover angle decreases as the Re increases in regimes I ($Re = 50 - 205$), V ($Re = 335 - 500$) and VI ($Re = 550 - 800$), except when $m^* = 1$.

The range of Re for the regimes shows little difference between $m^* = 1$ and 0.909. However, when $m^* = 0.667$, the Re range is shifted toward lower values in regimes II to VI. This is apparent in figure 5.18 and 5.20. As a result, the beginnings of Regime IV and V for $m^* = 0.667$ are shifted relative to those of Regime III and IV for $m^* = 0.909$ and 1, and the range of Regime II for $m^* = 0.667$ is narrower than those of the other mass ratios. Also of note is that the shift for high Re is larger than that of low Re (figure 5.19 and 5.20).

Response characteristics within the regimes, even though the corresponding Re ranges are slightly dependent on the mass ratio, they are very similar to that of a neutrally buoyant tethered sphere for the two mass ratios considered. The sphere remains

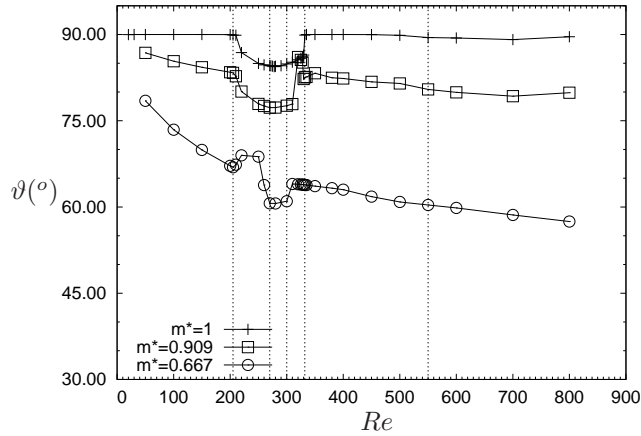


FIGURE 5.18: Effect of m^* on the layover angle

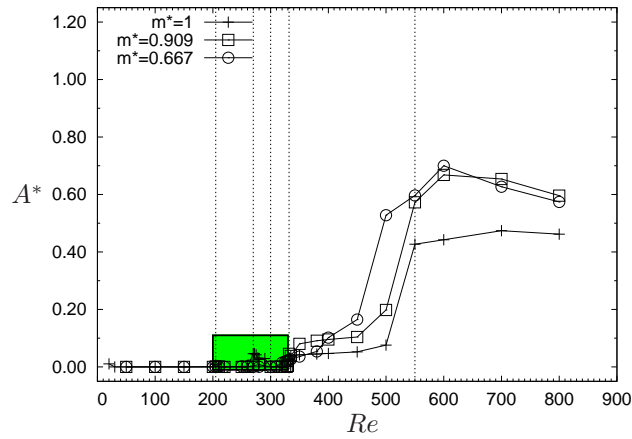


FIGURE 5.19: Effect of m^* on R amplitude

steady in Regime I and II, and shows two-threaded vortex loops trailing downstream in the wake of Regime II. The sphere shows oscillation from Regime III, after which suppressed oscillation of R in Regime IV is observed. In Regime V, the sphere oscillates quite periodically, and finally shows chaotic wandering trajectories in the crossflow plane within Regime VI.

Figure 5.21 demonstrates that a neutrally buoyant tethered sphere exhibits a different amplitude oscillation response to that of a buoyant tethered sphere. This becomes even more evident when the simulations for a vertically tethered sphere in section 5.2 are considered. They show quasi-circular motion that is observed in the experiments for a neutrally buoyant sphere at higher Reynolds numbers. However, considering the

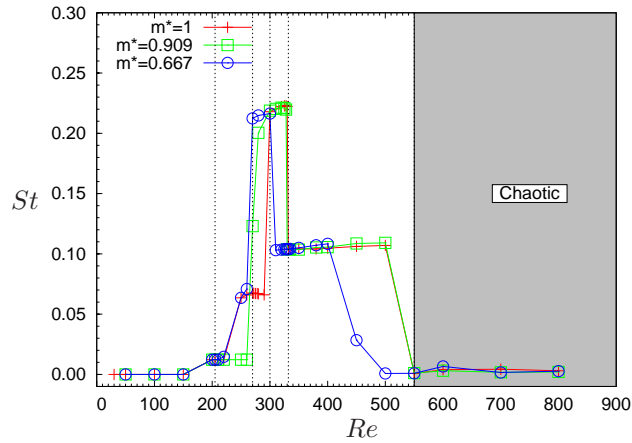


FIGURE 5.20: Effect of m^* on R frequency

departure of layover angle from 90° at high Reynolds numbers, it is not expected that a buoyant tethered sphere would develop such a quasi-circular motion at higher Reynolds numbers.

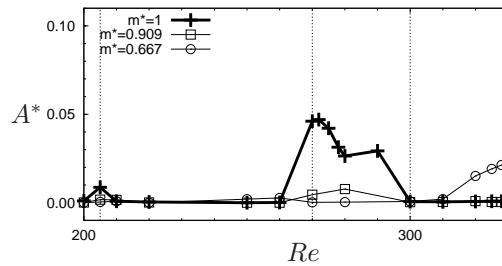


FIGURE 5.21: Effect m^* in Regimes II to IV. This is a magnified figure of the box in figure 5.19. The thickest line corresponds to the $m^* = 1$ case.

5.4 Effect of the Reynolds number on the response

Attempts have been made to find a reason for the difference between the numerical and experimental VIV studies so far. Two of the differences are: Maximum amplitude of oscillation and appearance of the oscillation modes. A few recent studies concerning VIV of an elastically mounted cylinder have suggested that such differences might be due to the Re difference. With this in mind, a series of numerical simulations were carried out for a buoyant tethered sphere. It is found that the Re does have a significant effect on the maximum oscillation amplitude, the range of high-amplitude oscillation and the chaotic oscillation.

The mass ratio and the tether length were set to 0.833 and $10D$, respectively, to match the conditions of previous studies. The reduced velocity was varied from 0.5 to 35 by changing a parameter related to gravity (g). This parameter is termed α , and defined as $\alpha \equiv \frac{4}{3} \frac{gD}{U^2}$ for the sphere. If the parameter α varies, while keeping U and D constant, the gravity will vary. This, in turn, will change the natural frequency of a tethered body as $f_n = \frac{1}{2\pi} \sqrt{\frac{T}{(m+m_a)L}}$ where T is the tether tension, m is the body mass and m_a is the added mass. Recalling the definition of $U^* \equiv \frac{U}{f_n D}$, the change of f_n will change the U^* even when the flow speed is constant. Contrary to the experimental studies, where a range of U^* was obtained by changing the flow speed U , a range of U^* was obtained by changing the gravity term and keeping U constant. By adopting this procedure, Re can be held at one value while U^* varies at a given fluid viscosity. The Reynolds numbers representing the regimes IV to VI found in section 5.2 were chosen for each set of simulations. These Re are 400, 500 and 800.

Figure 5.22 shows the layover angle of the tethered sphere. At a given U^* , the layover angle at low Re is greater than that for higher Reynolds numbers. This trend becomes apparent when $U^* > 14$. The dependence of the maximum attainable U^* on Re is also observed. The U^* corresponding to the layover angle (ϑ) of 45° is of importance because the change of the main oscillation direction from x to y happens once $\vartheta > 45^\circ$. This value of U^* is close to 30 for all the Reynolds numbers investigated.

Figure 5.23 shows the variation of oscillation amplitude as a function of U^* . The

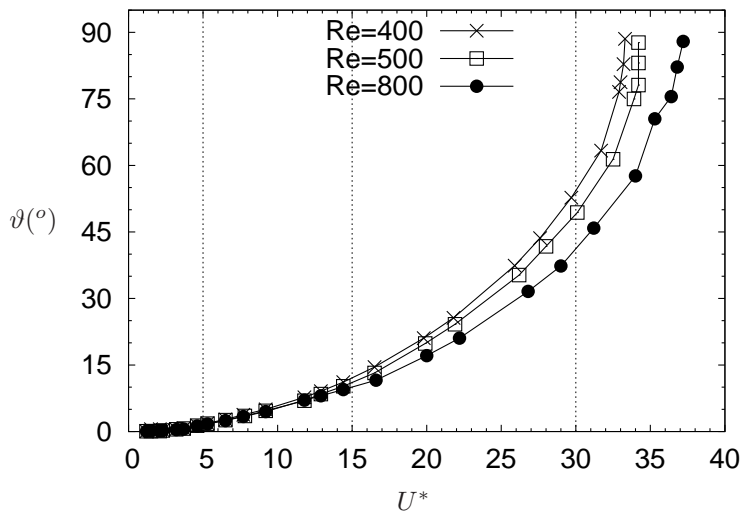


FIGURE 5.22: Re effect on layover angle. $m^* = 0.833$ and $L=10D$.

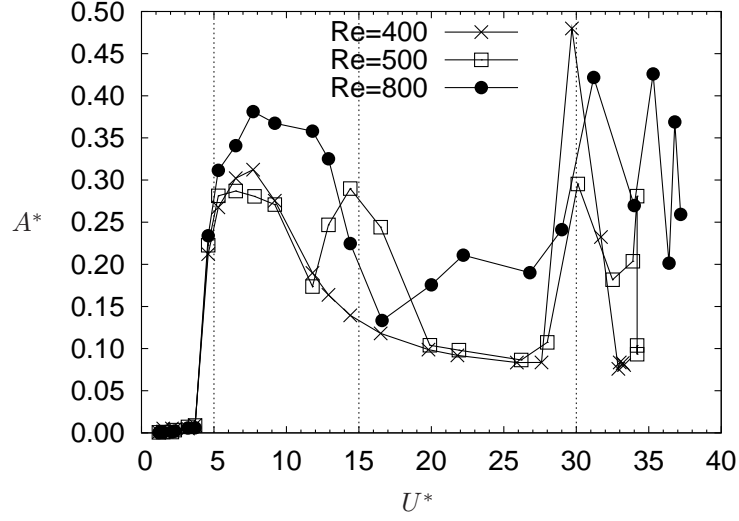


FIGURE 5.23: Re effect on oscillation amplitude. $m^* = 0.833$ and $L = 10D$.

amplitude is the sum of RMS values of the three displacements divided by the sphere diameter. There are two key features in figure 5.23. The first one is that there is a U^* range of high-amplitude oscillation for all Reynolds numbers considered, and the maximum amplitude within this high-amplitude range is dependent on Re . This range covers $U^* = 5 - 12$ for $Re = 400$ and 500 , and $U^* = 5 - 15$ for $Re = 800$. The amplitude peaks at $U^* \approx 8$, and its value increases as Re increases from 400 to 800. Contrary to the case for the two other Reynolds numbers, another peak appears at $U^* \approx 15$ when $Re = 500$. This is due to a quasi-periodic oscillation in the lateral direction (z), and the same type of oscillation is also observed at neighbouring reduced velocities when $Re = 500$. Note that x is the streamwise direction and y is the transverse direction. Despite this z oscillation, $Re = 500$ is classified as the same regime (Regime V) as $Re = 400$ because it is not yet clear whether $Re = 500$ is a transitional regime and, moreover, Regime VI is chaotic.

The second is that the oscillation undergoes a significant change after the high-amplitude range, particularly when U^* passes through the value of $U^* = 30$. When $Re = 400$, the amplitude decreases in the range $U^* = 10 - 28$. However, the amplitude goes through an abrupt jump at $U^* \approx 30$ and then returns to a small value. Similar amplitude response is observed for the $Re = 500$ case, except the peak occurs at $U^* \approx 15$ and the amplitude fluctuation after $U^* = 30$. When $Re = 800$, the decrease of amplitude starts from $U^* = 12$ and ends at $U^* \approx 17$. After this decreases, the time

traces of x and y as well as z exhibit chaotic behaviour. A jump at $U^* \approx 30$ and the amplitude fluctuation are observed as in the previous two Re cases. The jump in amplitude around $U^* = 30$ is due to the change of layover angle over 45° for all the Reynolds numbers considered. For the higher $Re = 500$ and 800 cases, this change of layover angle is expected to have an effect on the fluctuation amplitude when the layover angle is greater than 45° and the displacement history becomes chaotic.

5.5 VIV of a Vertically Tethered Sphere

Simulations for a vertically tethered sphere were performed using a modified numerical code adapted for the neutrally buoyant tethered sphere. The modification was done only for the equations of motion for the sphere as the equations for the fluid flow are the same as previous cases.

In the vertical tethering case, the tension, T , is described by

$$T = (F_x - B + W) \cos \theta + F_y \sin \theta \cos \phi + F_z \sin \theta \sin \phi. \quad (5.11)$$

The mass ratio is assumed to be $m^* \geq 1$ to compare the numerical results with the experimental results of Provansal *et al.* (2004), but the cases of $m^* < 1$ can be solved easily by changing the signs of the buoyancy (B) and the sphere weight (W).

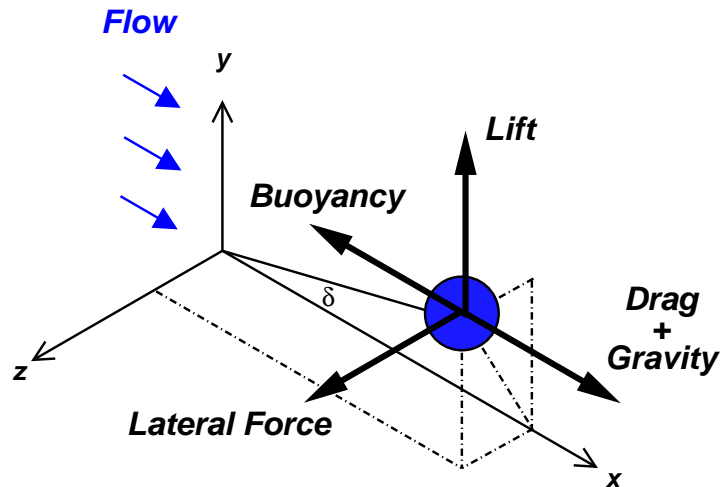


FIGURE 5.24: Schematic of a vertically tethered sphere.

Accordingly, the equations of motion result in

$$m\ddot{x} = (F_x - B + W) - T \cos \theta, \quad (5.12)$$

$$m\ddot{y} = F_y - T \sin \theta \cos \phi, \quad (5.13)$$

$$m\ddot{z} = F_z - T \sin \theta \sin \phi. \quad (5.14)$$

A schematic of the vertically tethered sphere is shown in figure 5.24.

5.5.1 Response of oscillation

The trajectories of the sphere in the xy , yz , and zx planes are shown in figure 5.25. Large oscillations are observed in the yz plane for all the Reynolds numbers considered because gravity is aligned to the flow, resulting in the layover angle $\theta = 90^\circ$. Within

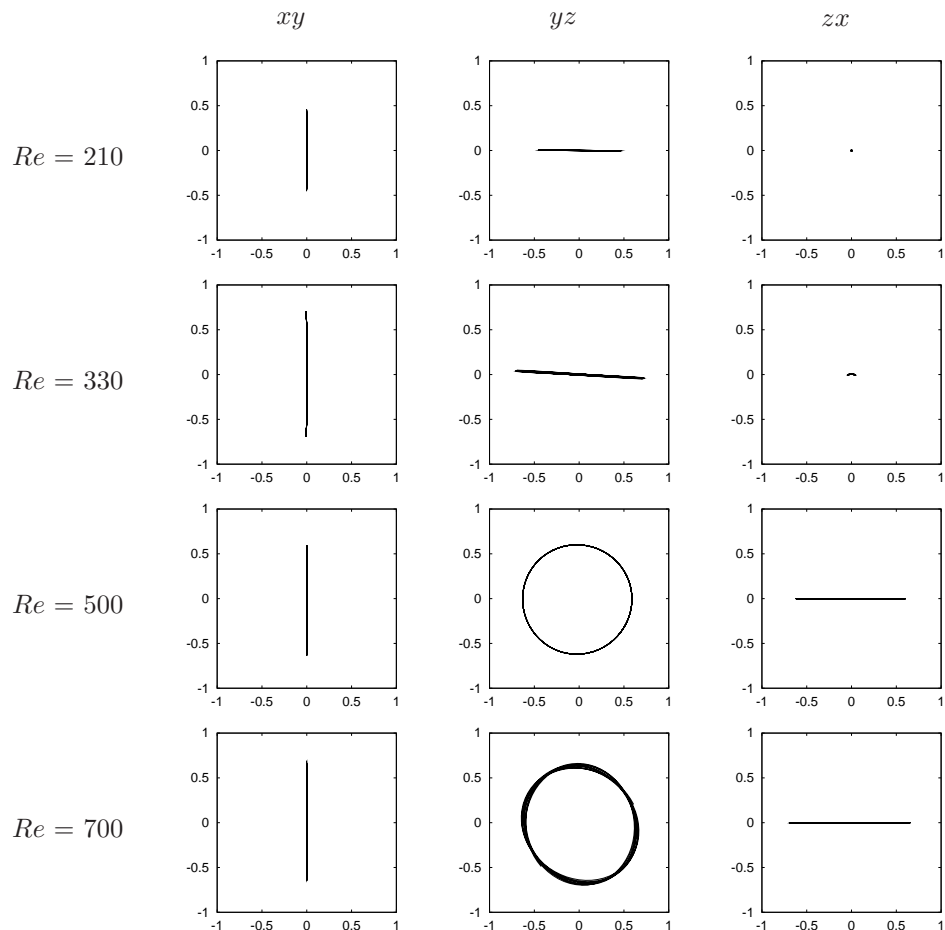


FIGURE 5.25: Trajectories in xy (first column), yz (second column), and zx (third column) planes at various Reynolds numbers. All the axes are in the same scale. Each tic represents $0.5D$, and the mean position of the sphere is allocated to the $(0, 0)$.

the range of $Re = 210 - 400$, the sphere oscillates on a straight line, and its amplitude grows as Re increases. For reference, all the reduced velocities for the Reynolds numbers considered were close to 6.1 due to the layover angle of 90° , thus the natural frequency of this tethered sphere is the inverse of 6.1, or 0.1640. The sphere exhibits the quasi-circular motion when $Re \geq 500$.

The oscillation frequencies in y and z directions are given in table 5.2. It is clear that the oscillation frequency is the same as the natural frequency, as was reported by Provansal *et al.* (2004). This is due to the effect of mass ratio and is well known for the VIV of a cylinder oscillating transversely. Therefore, it is claimed that a vertically tethered cylinder with a mass ratio $m^* > 1$ oscillates at its own natural frequency on a straight line or a circle in the crossflow plane.

The phase plots of the force coefficient and displacement for each direction are shown in figure 5.26. This figure clearly shows that the fluid force and the displacement are in-phase both in the y and z directions. In contrast, a specific phase relation appears for the case of the quasi-circular motions ($Re > 500$) in the x direction. Note that the magnitude of x oscillation is minute compared to that of the other directions.

The forcing affecting the motion of the sphere in a given plane is now considered. As the dominant directions of oscillation are y and z , we focus on the crossflow plane. The trajectory in this plane and the phase plots of $y - C_z$ and $z - C_y$ are given in figure 5.27 to investigate the mechanism responsible for quasi-circular motion of the sphere. They demonstrate that the body motion is controlled by both of the forces in

Re	f_y^*	$f_{C_y}^*$	f_z^*	$f_{C_z}^*$
210	0.1562	0.1562	-	-
270	0.1562	0.1562	-	-
330	0.1660	0.1660	0.1660	0.1660
400	0.1660	0.1660	0.1660	0.1660
500	0.1660	0.1660	0.1660	0.1660
600	0.1660	0.1660	0.1660	0.1660
700	0.1758	0.1758	0.1758	0.1758
800	0.1758	0.1758	0.1660	0.1660

TABLE 5.2: Oscillation frequency at various Reynolds numbers. The dimensionless frequency is $f^* = fD/U$. Note that the natural frequency of the tethered sphere is 0.1640. Thus, the vertically-tethered sphere, where $m^* = 2.43$, oscillates at its natural frequency.

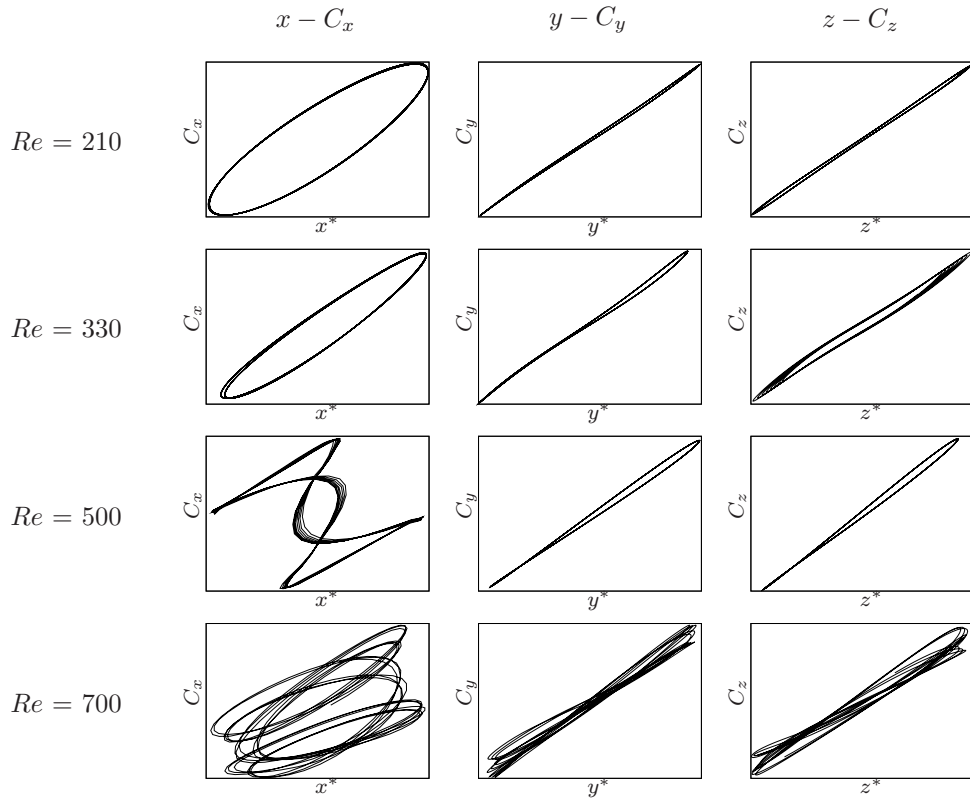


FIGURE 5.26: Phase plots of the force coefficients and the displacements in the same direction at various Reynolds numbers. Each column corresponds to $x - C_x$, $y - C_y$, and $z - C_z$ from the left. The results are from the simulations using the similar condition of Provansal *et al.* (2004), where $m^* = 2.433$, $L = 9D$, and $g = 9.807m^2/s$.

the y and z directions. This becomes clear for the cases of quasi-circular motion, where the magnitude of C_y and C_z are comparable.

Figure 5.28 is given to support the dominant effect of C_z on the body motion in the zx plane. Comparison of the phase plots of $C_z - x$ and $C_x - z$ reveals the motion in this plane is controlled by C_z not by C_x . This is because of the relatively large magnitude of the x directional fluid force in total, which allows little fluctuation of C_x . Contrary to the case where the gravity is acting horizontally, the magnitude of C_y fluctuation is about the same as that of C_z . Interestingly, this balance in magnitude of C_y and C_z fluctuations is truly the case of a neutrally buoyant tethered sphere. This similarity between the vertically tethered sphere and the neutrally buoyant tethered sphere results in the quasi-circular motion. Details of the similarity is discussed in section 5.5.2.

A typical vortex structure of the vertically tethered sphere showing a circular motion

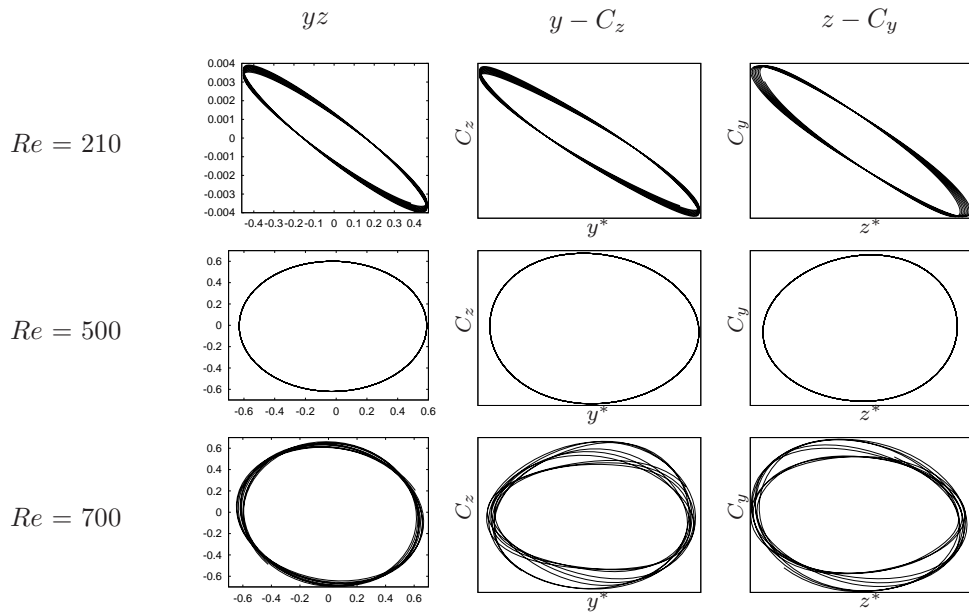


FIGURE 5.27: yz trajectories (the first column), and cross phase plots of the force coefficients and the displacements in this plane at various Reynolds numbers. The second column is $y - C_z$, and the third column is $z - C_y$. All the plots are autoscaled to their extreme values to be easily compared. The order of rows, and the set of data used, are the same as those of figure 5.26.

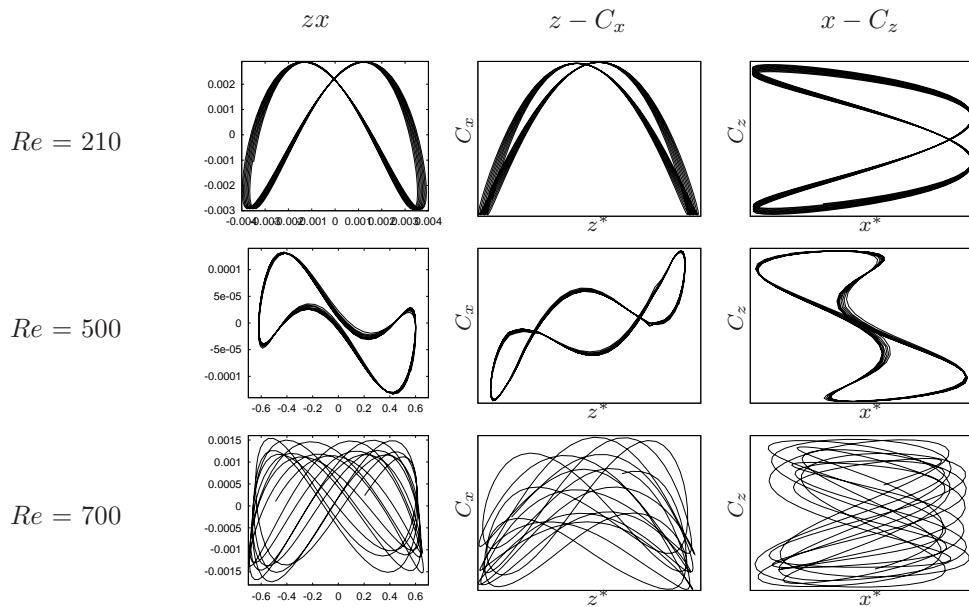


FIGURE 5.28: zx trajectories (the first column), and cross phase plots of the force coefficients and the displacements in this plane at various Reynolds numbers. The second column is $z - C_x$, and the third column is $x - C_z$. Other details of the figure are the same as those of figure 5.27.

is given in figure 5.29. The vortex shows a helical structure as it sheds downstream. This is remarkably different to the vortex structures observed for the oscillation on a straight line, exhibiting hairpin-shaped vortex loops forming on alternating sides. As the vortices shed, they follow the helical path and the negative vorticity grows due to the anticlockwise rotation of the body in the crossflow plane. A low level of asymmetry is observable in the vorticity plots adjacent to the sphere, being also an effect of rotational direction.

Interestingly, the vortex structure seems unchanging when viewed from the non-inertial frame attached to the rotating body. This is deduced from the observation of an animation made of successive images of streamwise vorticities. This phenomenon was reported for a sphere rotating in a streamwise direction at a certain rotational speed (Kim & Choi 2002). They termed this unchanging state of vortex structure the *frozen* state and used the phase plot showing a perfect circle in the crossflow plane to identify this frozen state. This is indeed the case of the vertically tethered sphere because, at the Reynolds number of 600 at which the simulation for figure 5.29 was performed, the phase plot in the crossflow plane clearly shows a circle. It is expected that the frozen

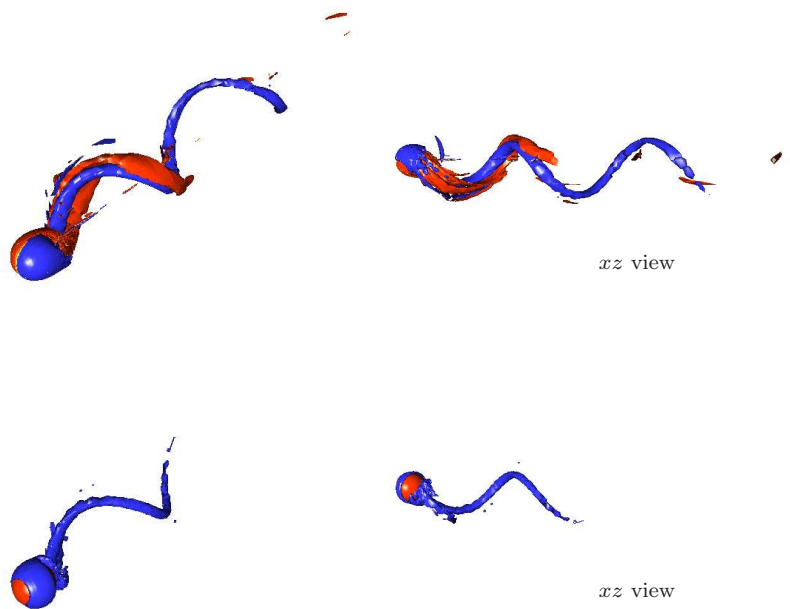


FIGURE 5.29: Vortex structure around the vertically tethered sphere. The first row is the streamwise vorticity and the second row is the field defined in Jeong & Hussain (1995). $Re = 600$, $m^* = 2.63$, $g = 9.807 \text{ m/s}^2$, and $L = 9D$. Helical structure is evident.

state of the vortex structure is closely related to the dimensionless rotational speed ω^* , where $\omega^* = \frac{\omega D}{U}$, of the sphere as is the case for the rotating sphere in the streamwise direction. Kim & Choi (2002) reported that the rotational speeds at which the frozen state occurs increase as Re is raised, being $\omega^* = 0.1$ and 0.3 at $Re = 250$ and $\omega^* = 0.5$ and 0.6 at $Re = 300$. For the vertically tethered sphere at $Re = 600$, $\omega^* = 1.0$. This interesting aspect of the vertically tethered sphere can be considered as a topic of future work.

Due to the inability to visualise the vortex structure in the water channel experiments, it is impossible to directly compare the vortex structure for a neutrally buoyant sphere to that for a vertically tethered sphere, particularly when the body exhibits a circular motion. However, it is reasonable to expect that the vortex structure for a neutrally buoyant sphere would be similar to that shown in figure 5.29 based on the quasi-circular motion observed.

5.5.2 Comparison to VIV of the neutrally buoyant tethered sphere

In this section, a comparison between the body motion and wake structure for the three types of tethering is presented. They are: horizontal tethering, vertical tethering, and the tethering without the influence of gravity which is the case of a neutrally buoyant tethered sphere. An emphasis is on the similarity of the neutrally buoyant tethered sphere to the vertically tethered sphere.

Figure 5.30 shows diagrams of the magnitude of mean forces in the Cartesian coordinate for the three tethering types. In the case of horizontal tethering, all three have different magnitudes due to the fluid flow in the x direction and the buoyancy in the y direction. When $m^* \neq 1$, the body is susceptible to oscillate in the z direction as the mean force $(\overline{F_z})$ in this direction is the smallest. Therefore, it might be expected that the fluctuation of F_z (represented by C'_z) is greatest and dominates the body oscillation. The level of C'_z is dependent on the mass ratio m^* and the Reynolds number Re as they vary the magnitude of the forces in the x and y direction. Of note is that the natural frequency of the body, f_n , is dependent on these two parameters as f_n varies as the layover angle changes. Thus, the suitability of the reduced velocity U^* has to be considered according to m^* and Re .

In contrast, the mean forces in the y and z directions can have the same order of magnitude as for the other two cases because of symmetry. The total magnitude of the

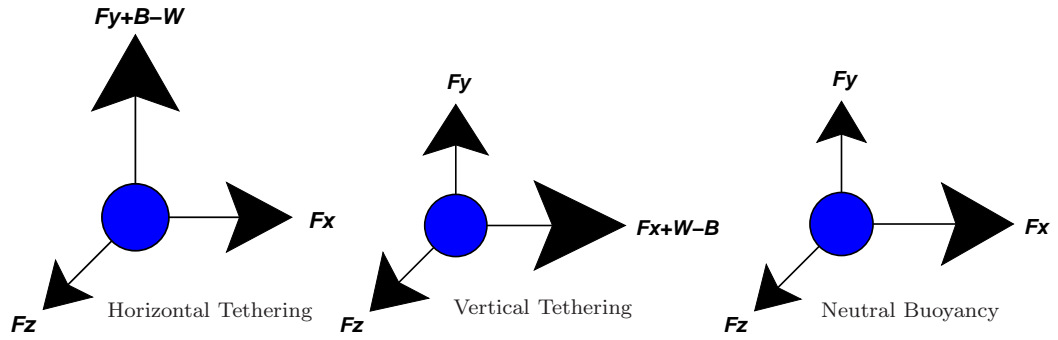


FIGURE 5.30: Magnitude of the mean forces in the Cartesian directions for three different types of tethering. The flow is coming from the left.

x force is the greater than that for the horizontal tethering case because the gravity (buoyancy) is acting parallel to the x direction. This is also the case for the tethered sphere with neutral buoyancy except that the magnitude of F_x is smaller than that for the vertically tethered sphere. Based on this similarity in the relative magnitude of the forces, phase plots in the yz plane and the zx plane are compared.

The phase plots in the yz plane at $Re = 270$ are presented in figure 5.31. The motion in the yz plane is clearly dominated by C'_z for the horizontal tethering, but it is not easy to tell whether it is C'_y or C'_z that dominates the body motion. For the neutrally buoyant case, both phase plots of φ_{y-C_z} and φ_{z-C_y} indicate out-of-phase relation, which is the same as for the vertically tethered case. Note φ_{z-C_y} for the horizontal tethering shows a completely different pattern to the other cases. Figure 5.32 shows the dominating role of C'_z in the zx plane where C'_x is smaller than C'_z . It is obvious, for all types, that the zx motion is controlled by C'_z based on the fact the $x - C_z$ plots resembles the $z - x$ plots when they are rotated 90° counterclockwise. Of course, this is not surprising given the x motion is restricted and dictated by the motion in the zx plane.

At $Re = 330$, the dominating role of C'_z is discernible between the horizontal case and the other two cases (figure 5.33). The yz motion is decided by C'_z for the horizontal tethering, but is decided by C'_y for the neutrally buoyant case as well as for the vertical tethering case. In addition, the forces and the displacements are out-of-phase ($\varphi_{z-C_y} = \varphi_{y-C_z} \approx 180^\circ$) for these two cases, whereas they are in-phase for the horizontal case. However, the zx motion is decided by C'_z for all three types of tethering (see figure 5.34), as is the case for $Re = 270$. This supports the importance of the relative magnitude of the mean fluid forces described in figure 5.30.

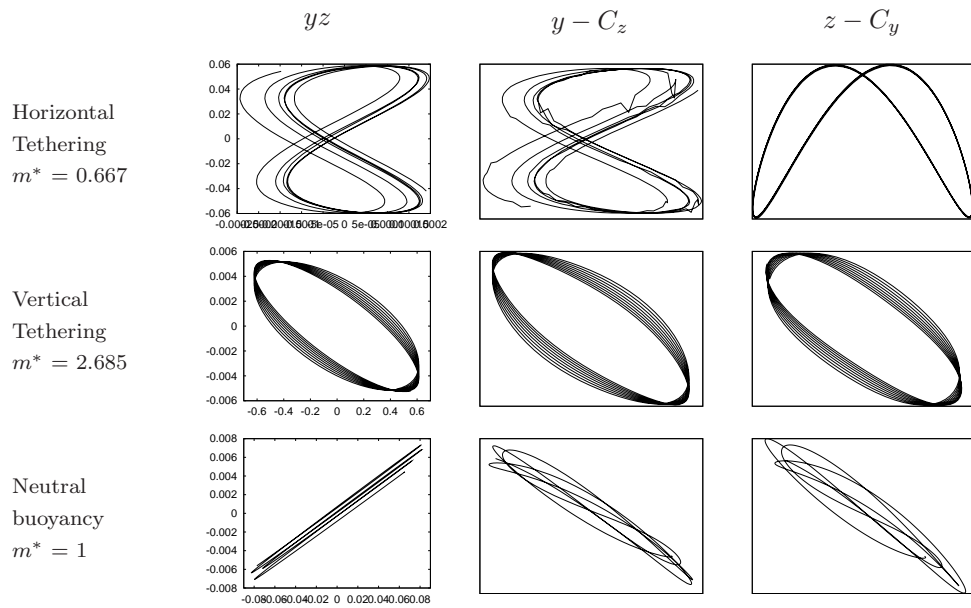


FIGURE 5.31: Trajectories (first column) and phase plots in yz plane at $Re = 270$. The second column is $y - C_z$, and the third column is $z - C_y$. All the plots are autoscaled to its extreme values to be easily compared.

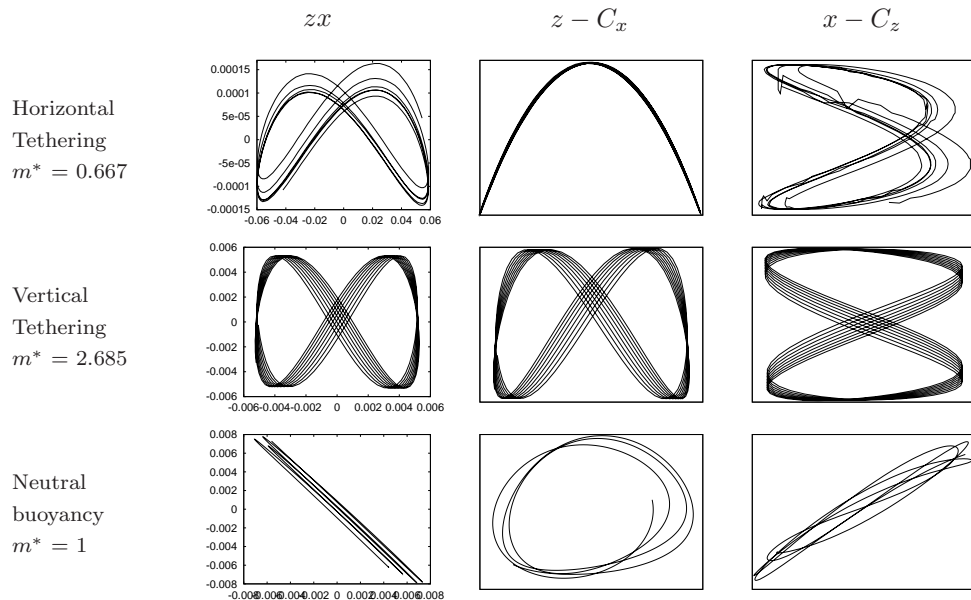


FIGURE 5.32: Trajectories (first column) and phase plots in zx plane at $Re = 270$. The second column is $z - C_x$, and the third column is $x - C_z$. All the plots are autoscaled to its extreme values to be easily compared.

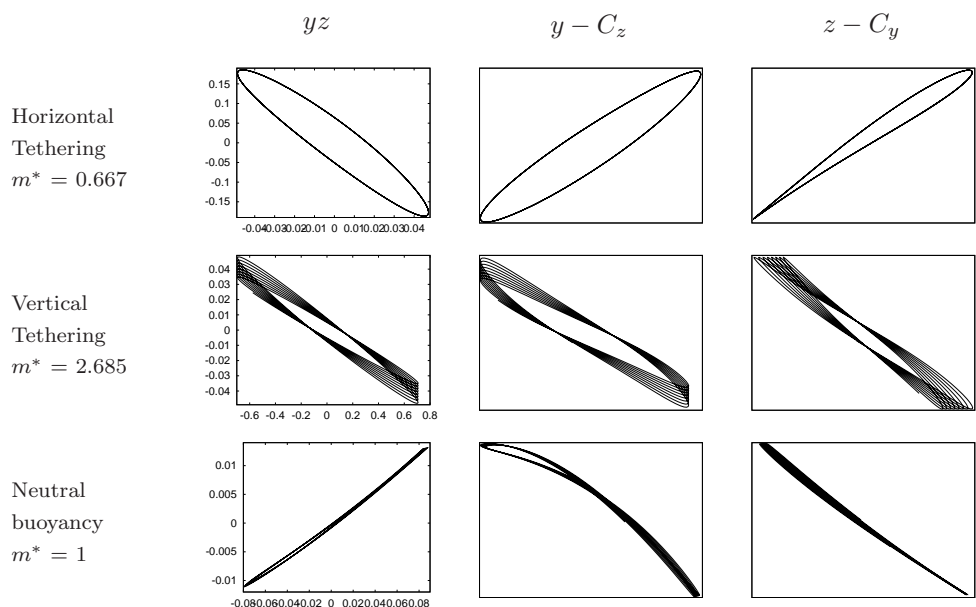


FIGURE 5.33: Trajectories (first column) and phase plots in yz plane at $Re = 330$. The second column is $y - C_z$, and the third column is $z - C_y$. All the plots are autoscaled to its extreme values to be easily compared.

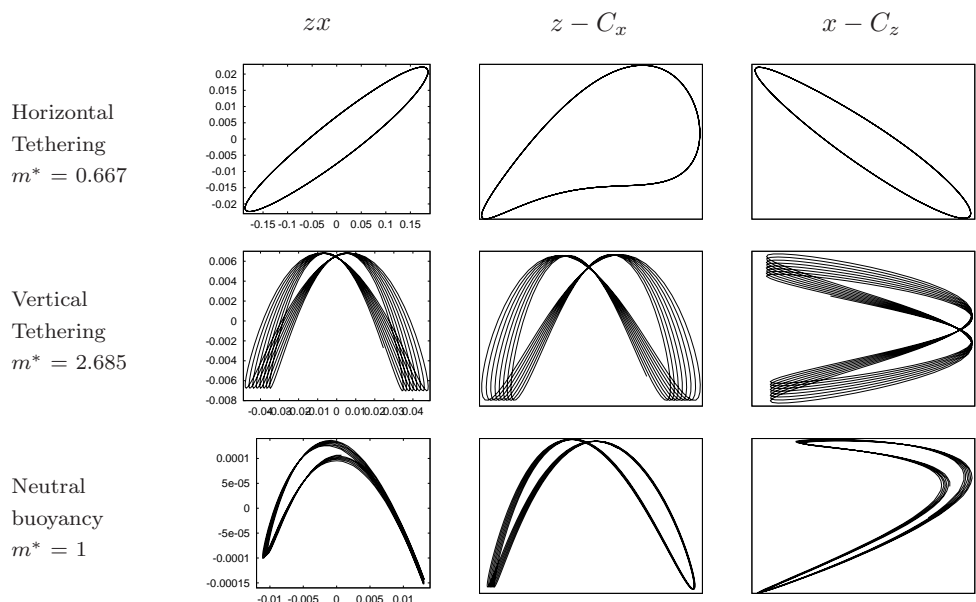


FIGURE 5.34: Trajectories (first column) and phase plots in zx plane at $Re = 330$. The second column is $z - C_x$, and the third column is $x - C_z$. All the plots are autoscaled to its extreme values to be easily compared.

Figures 5.35 and 5.36 are presented to confirm the difference between the horizontal tethering and the neutrally buoyant tethering, and to mention similarities and differences between the cases of vertical tethering and neutrally buoyant tethering. At this Reynolds number of $Re = 500$, the horizontally tethered sphere where $m^* = 0.667$ already shows chaotic wandering in the yz plane, and the phase relationship observed for the lower Reynolds numbers no longer exists. However, the vertically tethered sphere exhibits a circular motion with the same value of C'_y and C'_z , indicating the dominating role of both of them on this circular motion. For the neutrally buoyant tethering, the sphere oscillates on a double or triple figure-of-eight (Lissajous figure of the order more than two). From the phase plots, it is clear that C'_y dominates the yz motion for the neutrally buoyant case. As is the case for the lower Reynolds numbers, C'_z determines the zx motion as shown in figure 5.36. Note that the C'_y values for the vertical and neutrally buoyant tethering are larger than C'_z . This is because the initial condition is given as a perturbation only in the y direction, as there is no preferred direction of oscillation for these two cases at low Reynolds numbers below 500.

The Lissajous figure observed for the neutrally buoyant tethered sphere at $Re = 500$ seems to have a relationship to the inception of a circular motion for the vertically

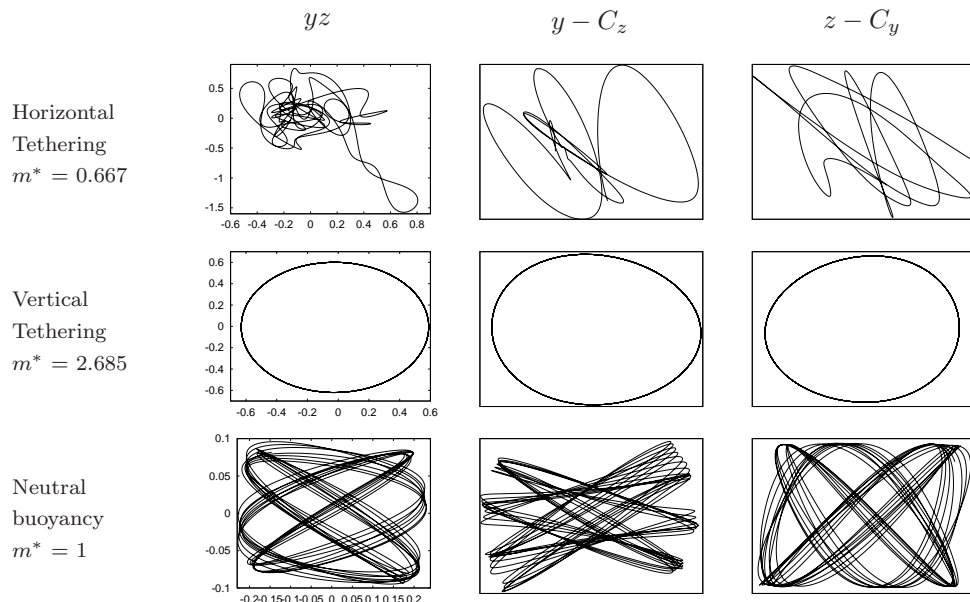


FIGURE 5.35: Trajectories (first column) and phase plots in yz plane at $Re = 500$. The second column is $y - C_z$, and the third column is $z - C_y$. All the plots are autoscaled to their extreme values to be easily compared.

tethered sphere at the same Re . For the neutrally buoyant tethered sphere, chaotic wandering appears at $Re > 550$, thus, it is suspected that the Lissajous figure at $Re = 500$ is a precursor to a chaotic wandering of Regime VI. However, for the vertically tethered sphere, the circular motion appears at $Re = 500$, following the amplitude saturation in the main direction of oscillation at lower Reynolds numbers. At higher Reynolds numbers ($Re > 700$), the vertically tethered sphere shows a motion departing from a perfect circle.

Based on phase plot analysis and the quasi-circular motion being experimentally observed, it is argued that the VIV of a neutrally buoyant tethered sphere is more similar to that of a vertically tethered sphere than that of a horizontally tethered sphere. As these mean forces decide the level of force fluctuations, the oscillation trajectories at high Reynolds numbers are related to the magnitude of the mean forces.

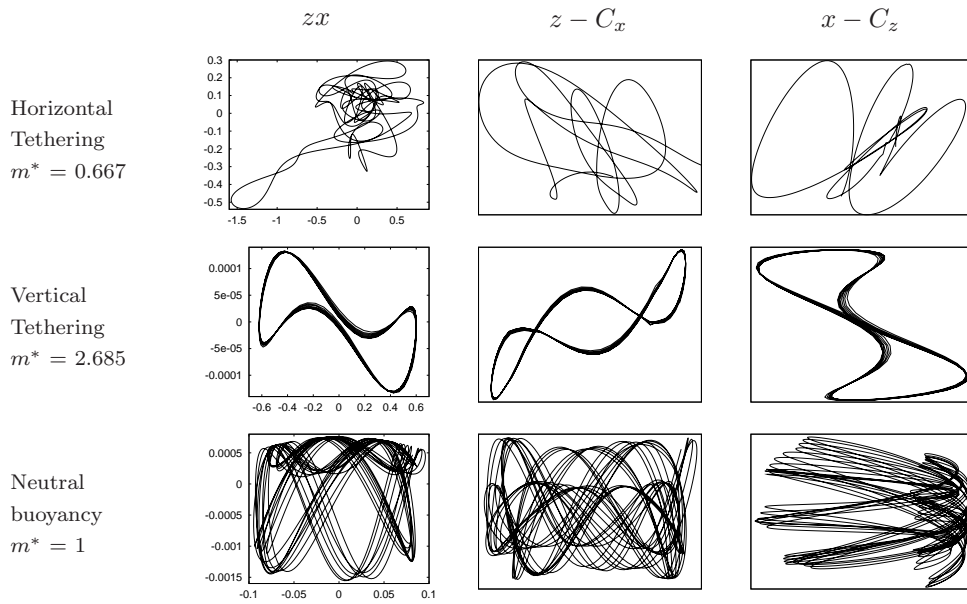


FIGURE 5.36: Trajectories (first column) and phase plots in zx plane at $Re = 500$. The second column is $z - C_x$, and the third column is $x - C_z$. All the plots are autoscaled to their extreme values to be easily compared.

5.6 Chapter Conclusions

For the neutrally buoyant ($m^* = 1$) tethered sphere, it is found that there exist seven different flow regimes in the range of $Re = 50 - 8000$ in terms of the mean layover angle, amplitude of oscillation, frequency of oscillation and trajectory of oscillation in the

crossflow plane. The first six regimes were determined by direct numerical simulations and the seventh regime was found through experiments.

The first regime, Regime I, covers the range of $Re = 50 - 205$, and the sphere remains still with layover angle $\vartheta = 90^\circ$. Regime II starts at $Re = 210$. The flow is steady but asymmetric. Thereafter, the sphere offsets from the symmetry axis and the layover angle decreases as Re increases. This regime exists up to $Re = 250$.

As Re increases further, the sphere starts to vibrate at $Re = 270$, the start of Regime III. Regime IV begins at $Re = 300$. It shows a steep decrease of the layover angle, indicating the body offsets more from the pivot axis than other regimes. The sphere predominantly oscillates in the azimuthal direction with a frequency of $St = 0.111$, which is close to that of the stationary sphere ($St = 0.134$) but much higher than its natural frequency ($St \approx 0.029$).

In Regime V covering $Re = 335 - 500$, the layover angle returns to $\vartheta = 90^\circ$. In contrast to Regime IV, the sphere predominantly in the radial direction. The amplitude of oscillation in Regime V gradually increases as Re is increased. The frequency of the radial displacement for Regime V is 0.104. The St is also close to (but still less than) that of the fixed sphere ($St = 0.134$). In Regime VI, the vibrations become chaotic and the sphere undertakes chaotic wandering, having no restoring forces. The range of Re for Regime VI covers both simulations and experiments, and the existence of the regime is verified by observing the irregular pattern in the experiments.

In Regime VII ($Re \geq 3000$), the oscillation changes to quasi-circular from an irregular pattern. As Re is raised further, the sphere motion exhibits more clearly a circular shape. Table 5.3 summarises the seven regimes found for the neutrally buoyant tethered sphere.

To examine the effect of mass ratio, the simulations for the mass ratios of $m^* = 0.909$ and $m^* = 0.667$ with selected Reynolds numbers have been performed. Response characteristics within the regimes, even though the corresponding Re ranges are dependent on the mass ratio, are very similar to that of a neutrally buoyant tethered sphere for all the mass ratios considered. The sphere remains steady in Regime I and II, and shows two-threaded vortex loops trailing downstream in the wake of Regime II. The sphere shows oscillation from Regime III, after which suppressed oscillation of R in Regime IV is observed. In Regime V, the sphere oscillates quite periodically, and finally shows chaotic wandering trajectories in the crossflow plane within Regime VI. However, a neu-

Regime	Reynolds number	Trajectory	Wake Characteristics
I	$50 \leq Re < 210$	N/A	Steady, axisymmetric.
II	$210 \leq Re < 270$	N/A	Steady, non-axisymmetric, planar-symmetric, “double thread” wake vortex formation.
III	$270 \leq Re < 300$	Line	Unsteady periodic, planar-symmetric, start of periodic vortex shedding.
IV	$300 \leq Re < 335$	Line	Unsteady periodic, no planar-symmetry, periodic vortex shedding in the form of vortex loops.
V	$335 \leq Re < 600$	Line	Unsteady periodic, planar-symmetric, periodic vortex shedding in the form of vortex loops.
VI	$600 \leq Re < 3000$	Irregular	Unsteady non-periodic, vortex shedding pattern becomes irregular.
VII	$3000 \leq Re < 8000$	Quasi-circle	Unsteady periodic, helix-shape vortex formation without shedding.

TABLE 5.3: Regimes of the flow and response of the neutrally buoyant tethered sphere for the range of $Re = 50 - 8000$. The trajectories of the oscillating sphere are on the crossflow (yz) plane.

trally buoyant tethered sphere also exhibits a difference in oscillation response to that of a buoyant tethered sphere, in particular for Regime III ($Re = 270 - 300$) and Regime VII ($Re > 3000$). The difference becomes even more evident when the simulations for a vertically tethered sphere are considered.

The effect of Re on the VIV of buoyant tethered spheres has been numerically examined as an attempt to find a reason for the difference between the numerical and experimental studies on this topic. For a tethered sphere of $m^* = 0.833$ and $L^* = 10$ with varying U^* , it is found that Re does have a significant effect on the oscillation amplitude. The high-amplitude range covers $U^* = 5 - 12$ for $Re = 400$ and 500 , and $U^* = 5 - 15$ for $Re = 800$. The amplitude peaks at $U^* \approx 8$, and its value increases as Re increases from 400 to 800 .

Moreover, the oscillation undergoes a significant change after the high-amplitude range, particularly when U^* passes through the value of $U^* = 30$. At $Re = 400$ and 500 , the amplitude decreases in the range $U^* = 10 - 28$. An abrupt jump follows at $U^* \approx 30$ and then returns to a small value. However, at $Re = 800$, the decrease of amplitude starts from $U^* = 12$ and ends at $U^* \approx 17$. After this decrease, the time

traces of x and y as well as z exhibit chaotic behaviour. Importantly, the amplitude response at the highest $Re = 800$ shows similarity to that of previous experimental studies at much higher Re within $U^* = 1 - 30$. Based on this, it is highly likely that the difference in amplitude response between the simulations and the experiments for the VIV of tethered bodies is due to the difference in the Re ranges.

A comparison between the three types of tethering (horizontal tethering, vertical tethering, and the tethering of a neutrally buoyant sphere) reveals that VIV of a neutrally buoyant tethered sphere is closer to that of a buoyant tethered sphere with vertical tethering. This is confirmed by the discovery of a *quasi-circular* motion both for the neutrally buoyant tethered sphere and the vertically tethered heavy sphere. This results from the similarity of the force balance and the relative magnitude of the forces acting on the sphere. By analysing the phase plots between the force and the displacement, it is also found that the pattern of trajectory depends on the relative magnitude of the mean forces in each direction, as these mean forces decide the level of force fluctuations.

Chapter 6

Effect of Tether Elasticity on VIV of a Tethered Bluff Body

6.1 Introduction

In this chapter, a study to find the effect of making the tether elastic on VIV of a tethered body is presented. The tether elasticity was modelled as a linear spring force allowing the tether tension to be defined, rather than to depend on the constraint of forcing movement on a circle or spherical surface. This corresponds to adding one more degree-of-freedom to the body motion. The tension (T) was calculated using equation 6.1 instead of the equations presented in chapter 3.

$$T = k(L_0 - L). \quad (6.1)$$

The parameter k is the mechanical spring constant, L_0 is the tether length at equilibrium, and L is the tether length at the current instant of time.

A non-dimensional spring parameter k_t is defined using equation 6.2

$$k_t = \frac{2\pi U}{D} \sqrt{\frac{m_b}{k}}. \quad (6.2)$$

This is effectively a reciprocal Strouhal number for the oscillation frequency of the spring-mass system.. Alternatively it can be considered to be a “reduced velocity” or dimensionless oscillation period.

A buoyant body of $m^* = 0.833$ was chosen because, in this case, the effect of elasticity is greater than that for the neutrally buoyant body. A range of the reduced velocity, U^* , is obtained by varying the parameter α . The definition of the parameter α and its relation to the Froude number Fr is given in equation 6.3 for cylinder, and equation 6.4 for sphere.

$$\alpha = \frac{2 gD}{\pi U^2} = \frac{2}{\pi} \frac{1}{Fr^2} \quad (\text{Cylinder}) \quad (6.3)$$

$$\alpha = \frac{4 gD}{3 U^2} = \frac{4}{3} \frac{1}{Fr^2} \quad (\text{Sphere}) \quad (6.4)$$

The initial tether length was set to $10D$ for both bodies, consistent with the previous studies.

6.2 VIV of an Elastically Tethered Cylinder

A schematic of the elastically tethered cylinder is shown in figure 6.1 where a spring force is introduced to the tether.

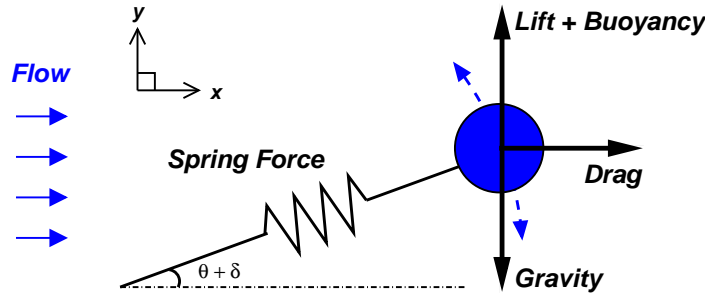


FIGURE 6.1: Schematic of an elastically tethered cylinder.

Before investigating the effect of tether elasticity on the VIV of a buoyant cylinder, a series of simulations at a high value of U^* ($= 28$) and $m^* = 1$ were carried out to locate a critical value of the parameter k_t . Due to its mass ratio being unity, the layover angle will be close to 90° and hence the tether length will change mainly in the streamwise direction. Figure 6.2 shows that the oscillation amplitude undergoes a change around $k_t = 2$ for the three Reynolds numbers considered ($Re = 100, 200$ and 250). The inverse of this k_t value ($1/k_t = 0.5$) is equivalent to the oscillation frequency of the tethered cylinder, and is close to twice the frequency (0.21) for a transversely oscillating cylinder. As the streamwise oscillation for the tethered cylinder is at twice the frequency of the transverse oscillation, it makes sense that the critical value of k_t is around 2.

Following the determination of the critical value of k_t at which inline resonance occurs, simulations were performed at several values of k_t around and beyond the

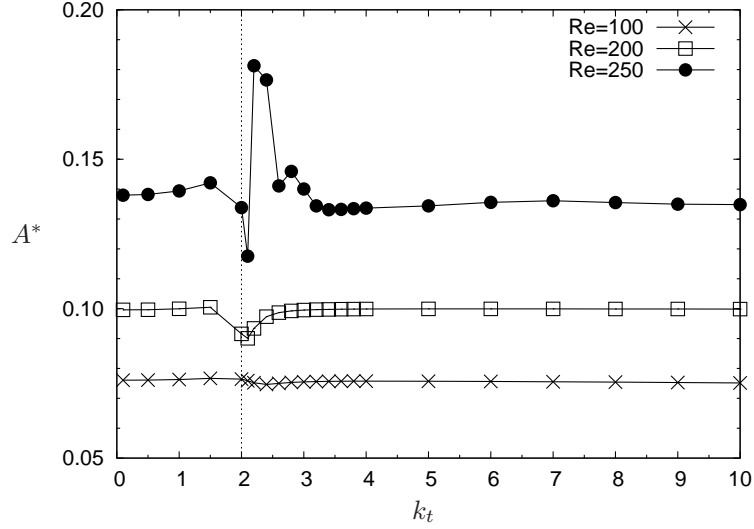


FIGURE 6.2: Total amplitude of oscillation as a function of the parameter k_t . $m^* = 1$, $L_0 = 10D$ and $U^* \approx 28$.

critical value of 2. These k_t values are 0.1, 5, 6 and 8. The Reynolds number was kept constant at 200 to maintain a two dimensional flow field. A range of U^* from 1 to 31 was obtained by changing the parameter α as mentioned before.

6.2.1 Response of the tethered cylinder

Figure 6.3 shows the variation of the mean layover angle ϑ with increasing k_t . The increase of k_t corresponds to the increase of the tether elasticity. The dotted vertical lines indicate the four representative reduced velocities of $U^* = 3.4, 11.6, 28.2$ and 31.8 to be used to compare the details of the response. Two main features are observed. The first is the larger ϑ for the elastically tethered cylinders below a specific U^* . These values are: $U^* = 20$ ($k_t = 8$), 25 ($k_t = 6$) and 27 ($k_t = 5$). The layover angle ϑ grows with increasing k_t at a given U^* below these reduced velocities.

The second feature is the opposite trend of ϑ with increasing k_t when U^* is increased over the specific reduced velocities mentioned above, i.e., when $U^* \geq 20$ ($k_t = 8$), $U^* \geq 25$ ($k_t = 6$) and $U^* \geq 27$ ($k_t = 5$). Within the U^* range, ϑ for the elastically tethered cylinders is smaller than that for the inelastically tethered cylinder. These values of U^* for each k_t correspond to $\vartheta = 40 - 60^\circ$ for the elastically tethered cylinders. This range includes $\vartheta = 45^\circ$, where the switch-over of the main oscillation direction from y to x for the inelastically tethered cylinder occurs; therefore, this switch-over is linked to the change of the ϑ trend. The above two features in the ϑ response are

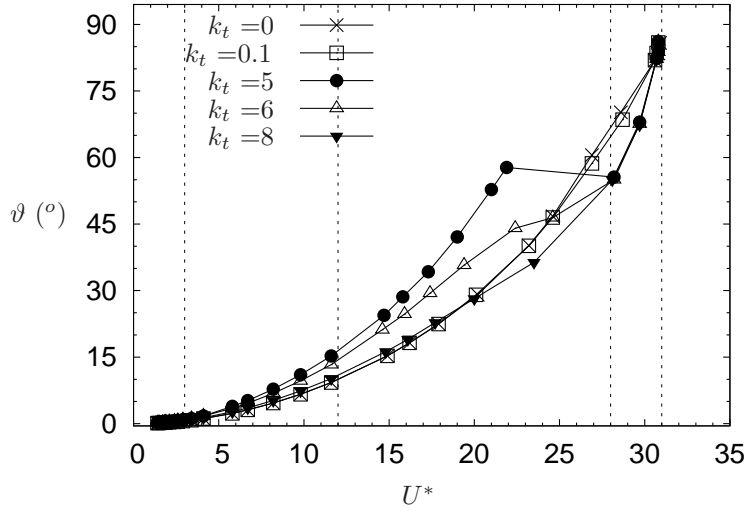


FIGURE 6.3: The effect of k_t on the layover angle. $m^* = 0.833$ and $L_0 = 10D$.

mainly due to the change of the mean force in the x direction (C_x). As is known from the force balance of the tethered cylinder, the cylinder lays over more when the mean x force increases. It is clearly shown in figure 6.4 that the U^* range of larger C_x for elastically tethered cylinders ($k_t \geq 5$) matches well with that of larger layover angle in figure 6.3 for each k_t value.

The amplitude response is also dramatically changed as k_t is increased beyond the

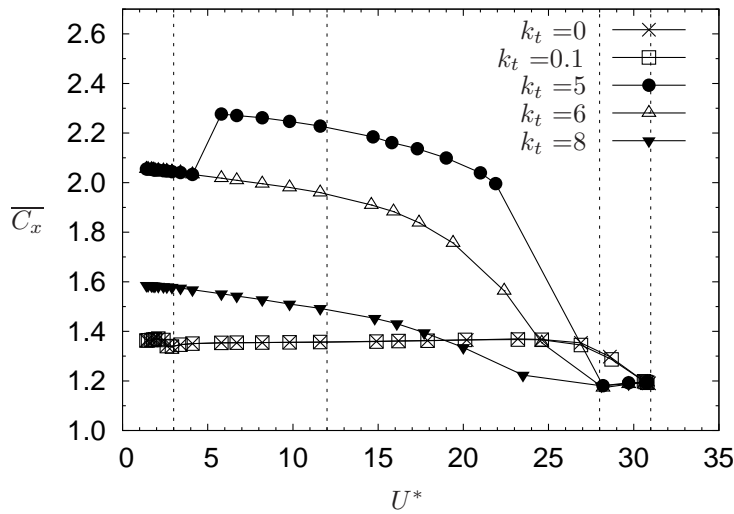


FIGURE 6.4: The effect of k_t on the mean C_x . $m^* = 0.833$ and $L_0 = 10D$.

value of 2. In figure 6.5, the amplitude increases at low U^* for the cases of an inelastic tether and of an elastic tether with a subcritical parameter ($k_t = 0.1$). However, when k_t is raised above the critical value of 2, the amplitude is about $0.7D$ at these low reduced velocities. This amplitude is much higher than the maximum amplitude of inelastic or subcritical elastic cases. This opposite behaviour at low U^* is due to the difference in the degrees of freedom allowed to each system. The tether elasticity gives the body an ability to oscillate in the transverse direction even at low layover angles, and this in turn causes the change in amplitude response. This behaviour is also consistent with the changes in the mean C_x at these low reduced velocities of $U^* < 5$ (see figure 6.4).

The amplitude at different k_t values is closely related to the mean C_y values shown in figure 6.6. It is indicated that, when $U^* = 5 - 25$, the amplitude difference between the k_t values is due to the change of the mean C_y values. It is also clear that the larger amplitude of the inelastically tethered cylinder at the higher $U^* \geq 27$ is due to the smaller mean values of the C_y shown in figure 6.6. Moreover, the maximum amplitude occurs when the mean C_y is the minimum. Note that the mean C_y is negative for entire range of $U^* = 1 - 33$. This is consistent with the work of Ryan *et al.* (2004a) who reported that, for a inelastically tethered cylinder, maximum amplitude occurs when the mean C_y has the minimum value.

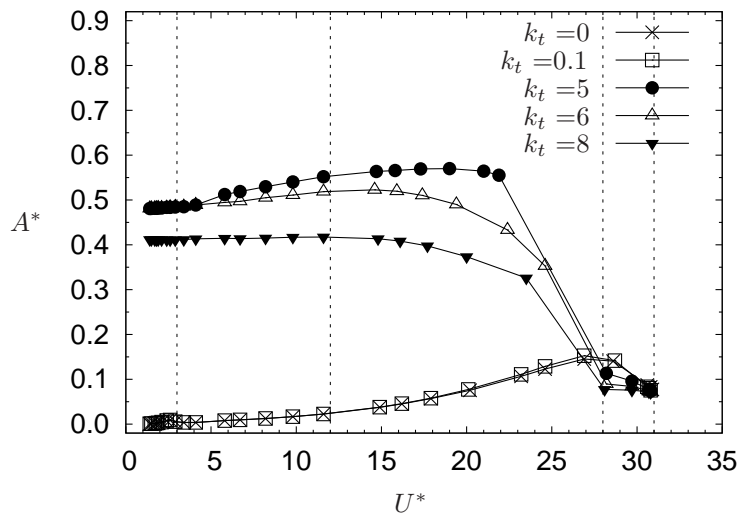


FIGURE 6.5: The effect of k_t on the total RMS values. $A^* = A_x^* + A_y^*$. $m^* = 0.833$ and $L_0 = 10D$.

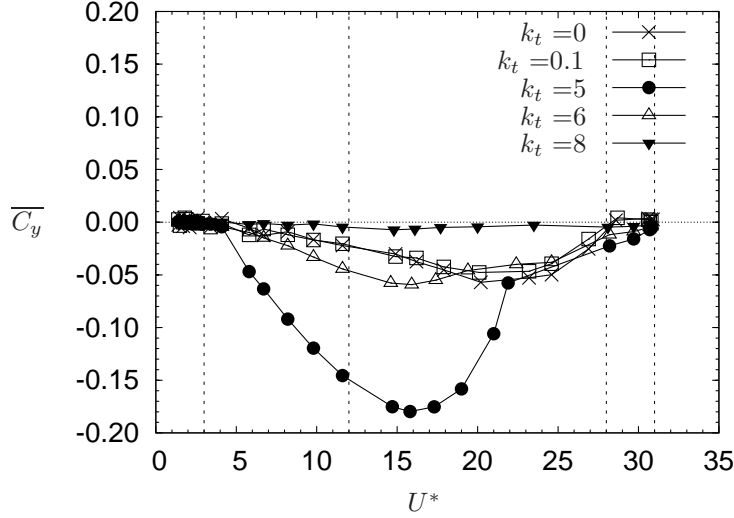


FIGURE 6.6: The effect of k_t on the mean C_y . $m^* = 0.833$ and $L_0 = 10D$.

6.2.2 Trajectory, forcing and phase of the oscillating cylinder

Figure 6.7 shows the xy trajectories of the cylinder at the four reduced velocities indicated by the vertical dotted lines in figures 6.3 and 6.5. As expected from the response of the layover angle and oscillation amplitude, the $k_t = 0.1$ case exhibits little difference to the inelastic tethered ($k_t = 0$) case. The inelastic and $k_t = 0.1$ cases show their maximum oscillation amplitude at $U^* = 28.2$ among the four reduced velocities. At $k_t = 2$, which corresponds to the critical value determined at the beginning of section 6.2, the maximum amplitude of oscillation also appears at $U^* = 28.2$ but exhibits a slowly varying motion, with the principal oscillation contrary to the cases of $k_t = 0$ and 0.1. The $k_t = 2$ case also shows larger and different oscillation patterns at the $U^* = 3.4$ and 11.6 compared with the inelastic case.

The oscillation pattern changes remarkably when $k_t > 2$, i.e., $k_t = 5, 6$ and 8 in figure 6.7. The difference to the inelastic case is highlighted at the two reduced velocities of $U^* = 3.4$ and 11.6. The oscillation amplitude for the elastic case is largest at $U^* = 11.6$, whereas it is largest at $U^* = 28.6$ for the inelastic case among the four reduced velocities. More interestingly, the trajectory at $U^* = 3.4$ and 11.6 shows a figure-of-eight pattern. This oscillation pattern has been reported for the VIV in the case of a cylinder that is free to move in the streamwise (x) direction as well as in the transverse (y) direction (Jauvtis & Williamson 2004; Sanchis *et al.* 2008). The figure-

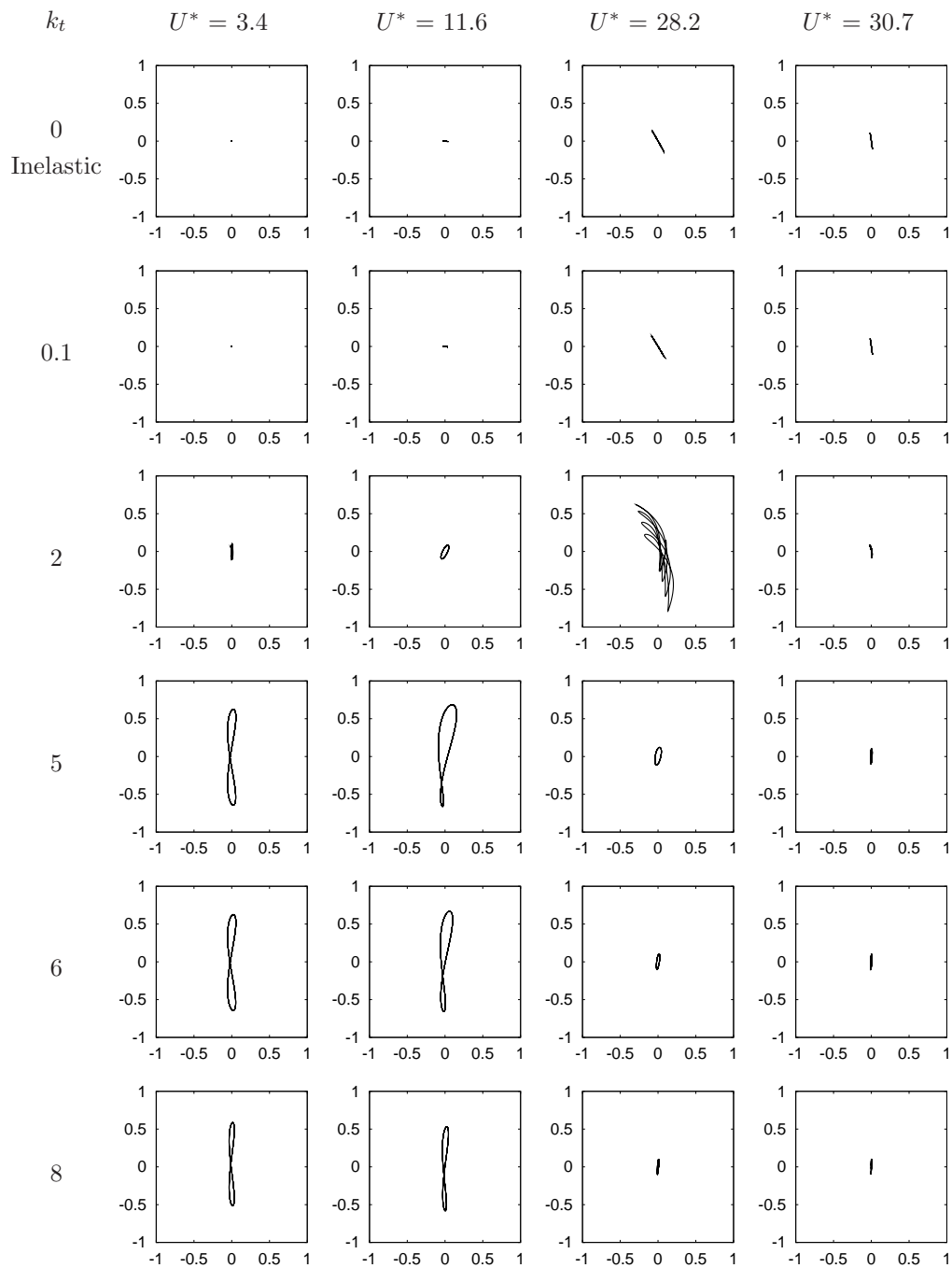


FIGURE 6.7: Trajectory in xy coordinate with varying k_t . The abscissa is x and the ordinate is y for each subfigure.

of-eight pattern is due to the additional freedom allowing the cylinder to move in the direction parallel to the tether, as in the previous studies of VIV of the cylinder with two-degrees-of-freedom. The oscillation amplitude is suddenly reduced as U^* increases beyond 25 as the response plot of the amplitude shows. At the higher U^* , the oscillation

pattern is no longer a figure-of-eight.

The phase plots of the x and y forces ($C_x - C_y$) are given in figure 6.8. They indicate the difference between the cases of an elastically tethered cylinder and an inelastically tethered one by exhibiting entirely different patterns. The pattern of the phase plot of

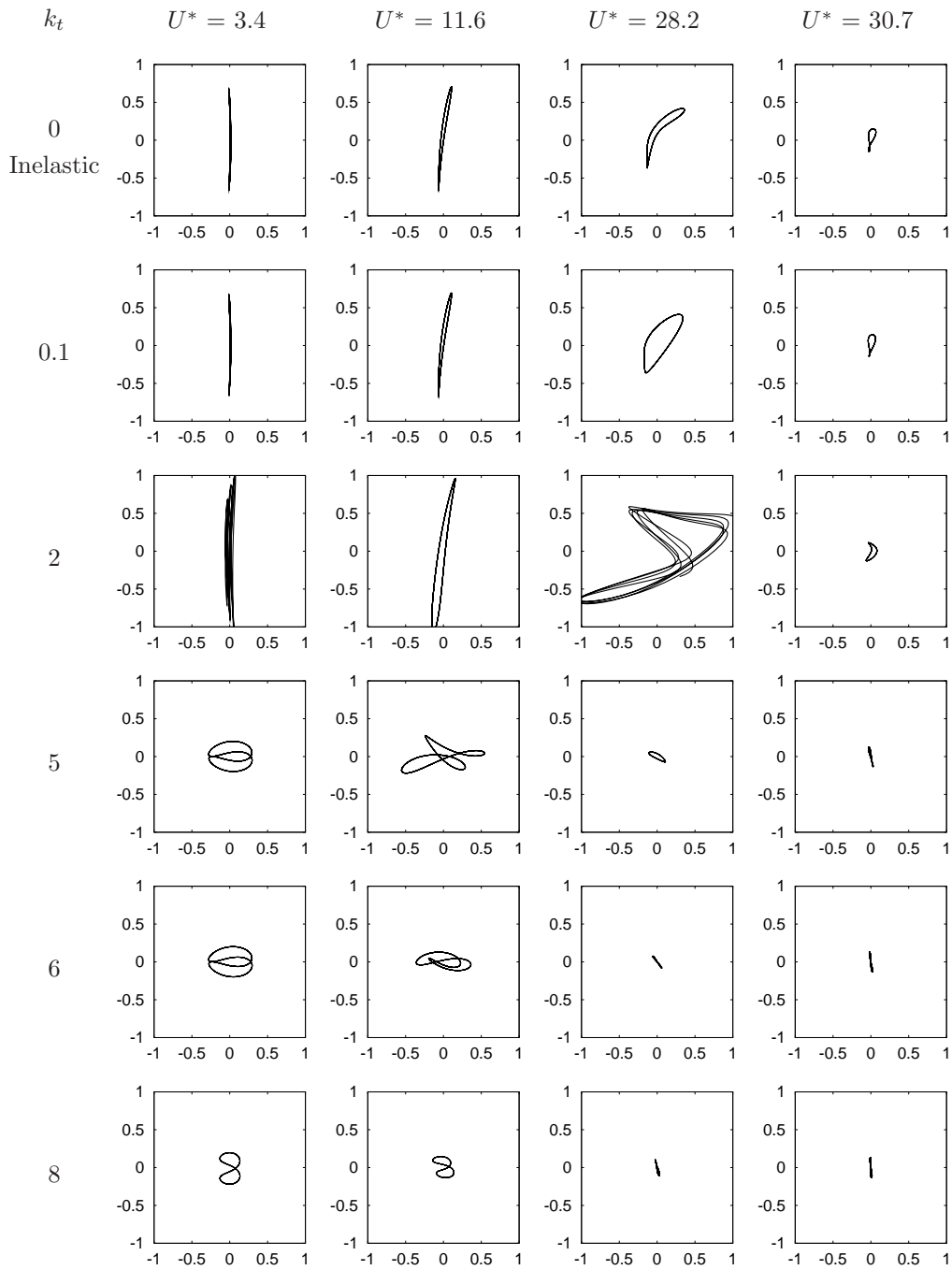


FIGURE 6.8: Phase plot of total forces ($C_x - C_y$) in xy coordinate with varying k_t . The abscissa is C_x and the ordinate is C_y for each subfigure.

$C_x - C_y$ shows magnitudes that are smaller for C_y and larger for C_x compared with those of the discrete values of k_t tested, particularly at the low reduced velocities of $U^* = 3.4$ and 11.6. It is also clear that the $k_t = 2$ case is the critical case distinguishing the VIV response of the tethered cylinder with or without tether elasticity.

Figure 6.9 shows the phase plots between the displacement and the force in both the x ($x - C_x$) and y ($y - C_y$) directions. At each U^* , the inelastic and the $k_t = 0.1$ cases show essentially the same pattern for both $x - C_x$ and $y - C_y$. However, the patterns for $k_t = 5, 6,$ and 8 are distinctly different to those for the inelastic, and the $k_t = 0.1$ cases. At each U^* , the phase plots for $k_t = 5, 6,$ and 8 are similar to each other, or exhibit a gradual change. The $k_t = 2$ case is again identified as the critical case dividing inelastic and elastic tethering cases by showing entirely different phase plots for sets on either side.

In summary, it is found that the elastically tethered cylinder, for which $k_t > 2$, shows different VIV to that of inelastically tethered cylinder. It is also found that, for the elastically tethered cylinder, the trajectory at the low reduced velocities shows a figure-of-eight pattern, similar to the VIV of a cylinder with two degrees-of-freedom (in the x and y directions simultaneously). Note that, at these low reduced velocities, the elastically tethered cylinder oscillates mainly in the y direction whereas the cylinder with an inelastic tether oscillates mainly in the x direction.

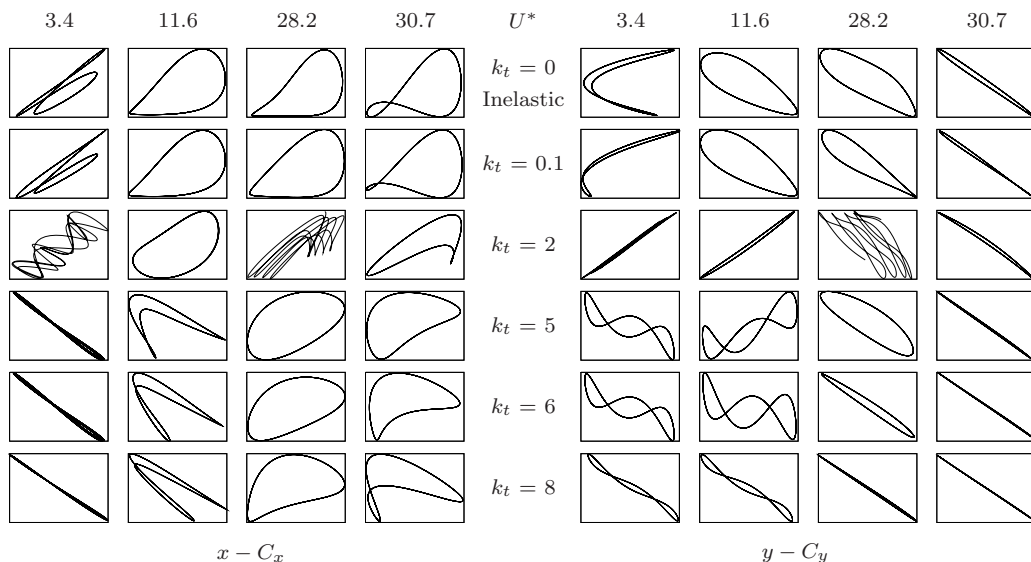


FIGURE 6.9: Phase plot between the displacement and the force. The abscissa is the displacement and the ordinate is the force for each subfigure. The axes are autoscaled to show the pattern easily.

6.2.3 Vortex structure around the oscillating cylinder

Figure 6.10 contrasts the vortex structures (rendered by spanwise vorticity) of the inelastic and elastic cases. Each figure was captured at its top position during one cycle of oscillation. All of the figures show a 2S wake mode, but they are different in terms of wake width and vortex shedding direction, particularly for the elastic case.

Despite the considerable change in the layover angle in this U^* range of $U^* = 1 - 33$, all vortex structures, for the inelastically tethered cylinder, show narrow and well-aligned shedding vortices. The cylinder oscillates mainly in the transverse direction at $U^* = 30.7$, but mainly in streamwise direction at $U^* = 3.4$. At the intermediate values of $U^* = 28.2$ and $U^* = 11.6$, the cylinder oscillates in both directions. The wake width is greatest at $U^* = 28.2$ when the cylinder oscillates at its maximum amplitude, although it is not very distinct from the others. The formation length of the vortex gets shorter as U^* decreases from 30.7 to 11.6. This length, however, becomes slightly longer at $U^* = 2$. This slight increase seems due to the change in oscillation direction

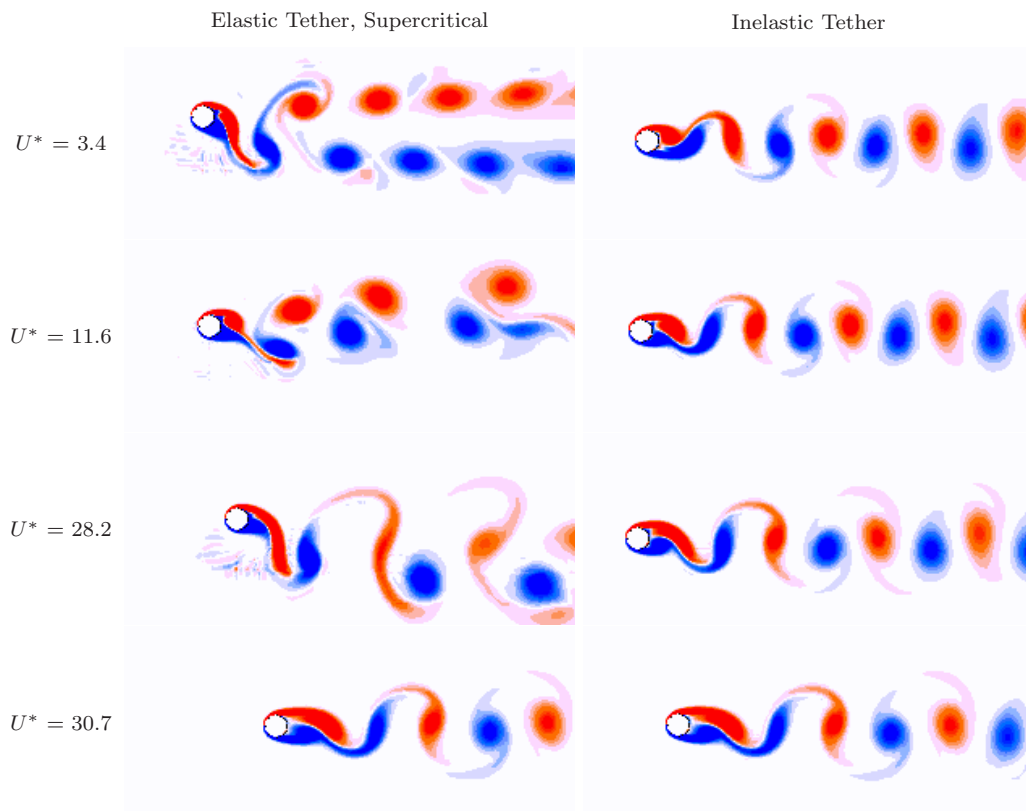


FIGURE 6.10: Spanwise vorticities at the top of the cycle for the elastically ($k_t = 5$) tethered cylinder and inelastically tethered cylinder at various U^* . Flow is coming from left.

when the layover angle surpasses 45° , where the cylinder is more prone to oscillate in the streamwise direction. The spacing of the shed vortices follows the same trend as the vortex formation length.

Vortex structures for the elastically tethered cylinder, where the k_t value is supercritical ($k_t = 5$), show huge differences at the intermediate and low reduced velocities. Vortices are shed downstream with an angle to the flow at the intermediate reduced velocities of 28.2 and 11.6. The shedding orientation is dependent on the oscillation direction of the cylinder. When the cylinder oscillates parallel to the tether ($U^* = 28.2$), the vortex sheds downward (negative y direction). In contrast, the vortex sheds upward when the cylinder oscillates normal to the tether ($U^* = 11.6$). At low $U^* = 3.4$, the cylinder oscillates in the transverse direction with a mean layover angle of 88° . As mentioned above, tether elasticity allows the cylinder to move in the transverse direction, hence it exhibits large amplitudes of oscillation in this direction. Due to this large oscillation, the wake width is considerably wider than that of the inelastically tethered

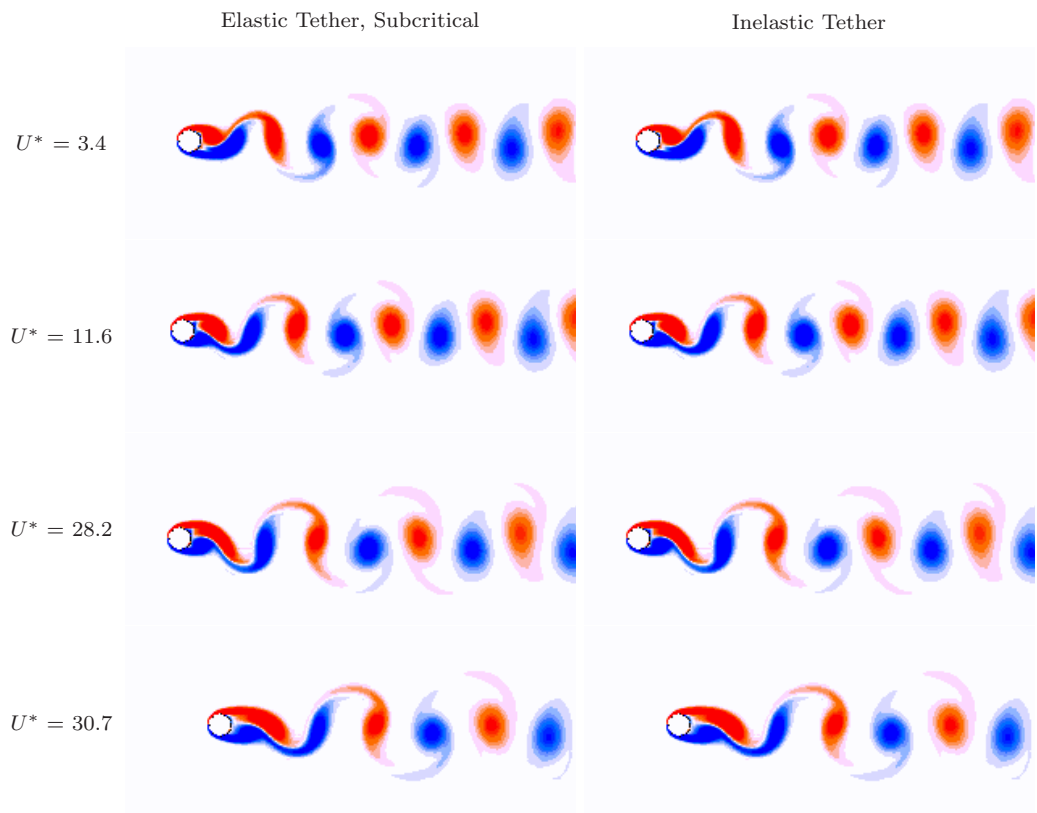


FIGURE 6.11: Spanwise vorticities at the top of the cycle for the elastically ($k_t = 0.1$) tethered cylinder and inelastically tethered cylinder at various U^* . Flow is coming from left.

cylinder. Considering the little difference in the layover angles between the elastic and inelastic cases, it is concluded that the cause of this huge difference in vortex structure is from the change of oscillation direction relative to the tether and from the change of oscillation amplitude. Contrary to the supercritical ($k_t = 5$) case, little difference is observed for a subcritical case of $k_t = 0.1$ as shown in figure 6.11.

6.3 VIV of an Elastically Tethered Sphere

A schematic of the elastically tethered sphere is shown in figure 6.12. The same procedure adopted for the cylinder system was used to locate a critical k_t value for the sphere system. The mass ratio was set to unity, and simulations were performed for a range of $k_t = 0.1 - 40$ at several Reynolds numbers. The selected Re are 270, 330 and 400 representing Regime III, IV and V, respectively, found in the first part of the current study for inelastic tethers.

Similar to the cylinder system, a critical value of the k_t parameter is observed through which the oscillation amplitude undergoes significant change. Figure 6.13 shows the “resonance” response appears to occur at $k_t = 4$ or 8 for the sphere; it was 2 for the cylinder. At higher $k_t = 20$, there appears to be a further change in oscillation behaviour. On the other hand, there are some differences to the cylinder system in the amplitude response. One is that the magnitude of oscillation amplitude increases as Re increases when k_t is over the critical value ($k_t = 20$). For the cylinder

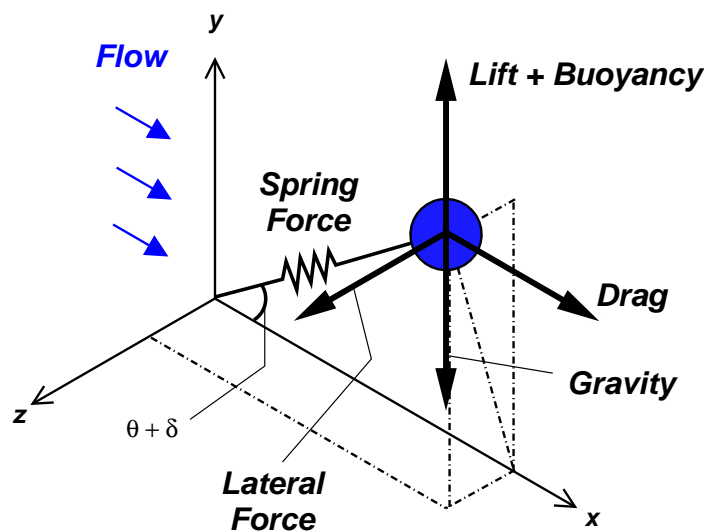


FIGURE 6.12: Schematic of a elastically tethered sphere.

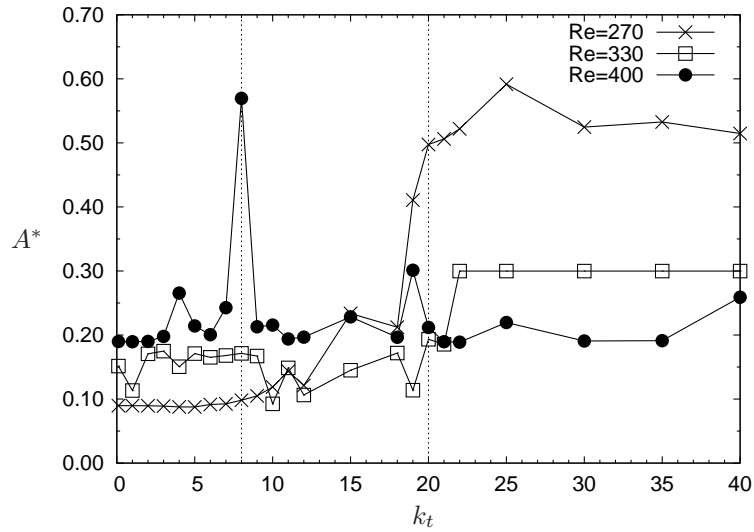


FIGURE 6.13: Total amplitude of oscillation as a function of the parameter k_t . $m^* = 1$, $L_0 = 10D$ and $U^* \approx 32$.

system, the magnitude does not change even when k_t is raised over its critical value. Another is that the critical value of k_t seems to decrease as Re increases. This is based on the appearance of a peak at $k_t = 8$ for $Re = 400$ case, but it is not yet clear that this value of k_t , based on a single point, is a real critical value at $Re = 400$.

6.3.1 Response of the tethered sphere

Following the determination of the effect of varying k_t , simulations were performed at one subcritical point ($k_t = 2$) and one supercritical point ($k_t = 40$), then comparing these with the inelastic case. A range of $U^* = 1 - 34$ was obtained by changing the α parameter as previously mentioned. The Reynolds number was set to 400, as it is the highest Re investigated to determine the variation of the response with k_t .

Figure 6.14 shows the layover angle of the tethered spheres with varying k_t . Three dotted vertical lines correspond to $U^* = 3.2$, 7.7 and 21.8, and these will be used to explain the details of the different responses. Unlike the cylinder case, there is little change of layover angle between the subcritical ($k_t = 2$) and supercritical ($k_t = 40$) cases, over the whole U^* range investigated. For the subcritical case of $k_t = 2$, only a little deviation is observed in the range of $U^* = 27 - 32$ which includes $\vartheta = 45^\circ$. The mean x force, C_x , is investigated as this was closely related to the response of the layover angle for the inelastically tethered cylinder. The mean C_x given for the supercritical case ($k_t = 40$) shown in figure 6.15 exhibits considerable increase in the range of $U^* = 5 - 20$

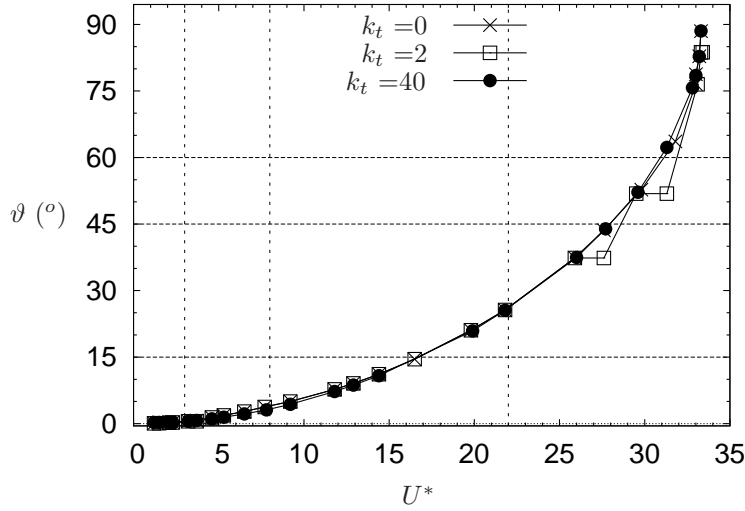


FIGURE 6.14: The effect of k_t on the layover angle. $m^* = 0.833$ and $L_0 = 10D$.

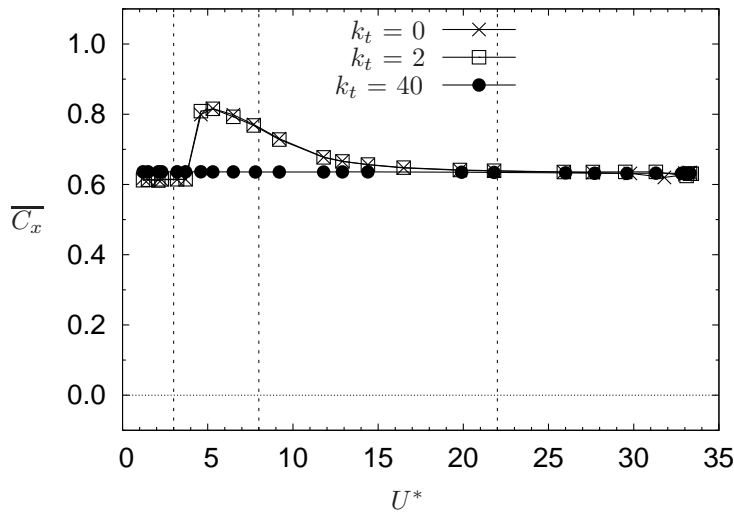


FIGURE 6.15: The effect of k_t on the mean C_x . $m^* = 0.833$ and $L_0 = 10D$.

compared to the subcritical case ($k_t = 2$), despite little difference in the layover angle. This apparent mismatch between the responses of C_x and the layover angle is quite different to the results for the tethered cylinder, where the increase of the mean C_x results in the increase of the layover angle by the same percentage. By investigating the amplitude response, it is revealed that the mean C_x has an effect more on the amplitude than on the layover angle for the tethered sphere.

Different types of response emerge when k_t is supercritical, particularly when $U^* <$

15. The difference is clearly revealed in figure 6.16. Within the range of $U^* = 1 - 4$, the sphere connected to an inelastic or a subcritically elastic tether exhibits minute oscillation. However, when k_t is supercritical, the elastically tethered sphere oscillates at an amplitude of 0.1. This trend changes as the U^* increases further until $U^* = 20$, at which the inelastically tethered sphere oscillates at higher amplitude. Its maximum amplitude is approximately 0.32 whereas the maximum for the elastically tethered sphere ($k_t = 40$) is 0.1. In the range of $U^* = 20 - 34$, the sphere oscillates at the same amplitude, irrespective of the k_t values considered. A peak at $U^* = 29$ for the inelastic case is due to the layover angle surpassing 45° .

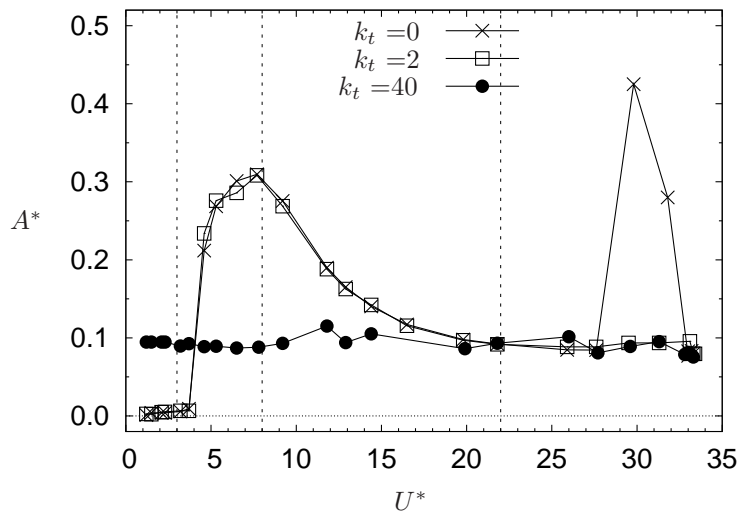


FIGURE 6.16: The effect of k_t on the total RMS values in the x , y and z directions. $m^* = 0.833$ and $L_0 = 10D$.

It is of interest that the overall trend for the oscillation amplitude matches that for the mean C_x for the whole U^* range considered (see figure 6.15). The mean values of C_y and C_z are shown in figure 6.17 as a function of U^* , and reveals that these values vary little for the elastically tethered sphere where k_t is supercritical. In contrast, the mean values of C_y and C_z change considerably, particularly at low and high reduced velocities for the inelastic ($k_t = 0$) or a subcritically elastic ($k_t = 2$) cases. These large mean values of C_y and C_z at low reduced velocities ($U^* = 1 - 4$) are due to the fluctuation of C_y and C_z caused by the inelastic tether. However, the large mean values at high reduced velocities ($U^* = 29 - 34$) is because of the layover angle change through $\vartheta = 45^\circ$ as mentioned above.

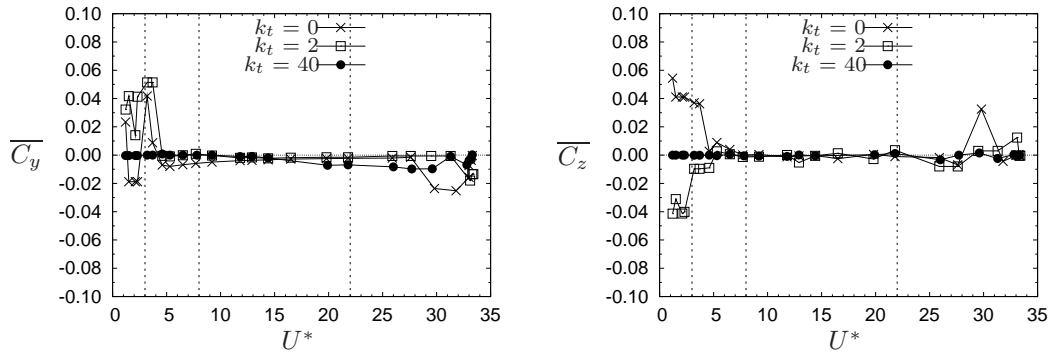


FIGURE 6.17: The effect of k_t on the mean C_y and C_z . $m^* = 0.833$ and $L_0 = 10D$.

6.3.2 Trajectory, forcing and phase of the oscillating sphere

Figure 6.18 shows the xy trajectories of the sphere at the three reduced velocities indicated by the vertical dotted lines in figures 6.14 and 6.16. As expected from the response of layover angle and oscillation amplitude, the trajectory for the $k_t = 2$ case exhibits little difference to inelastic tethered ($k_t = 0$) case. The inelastic and $k_t = 2$ cases show virtually no oscillation in either the x and y directions, except when $U^* = 7.7$. How-

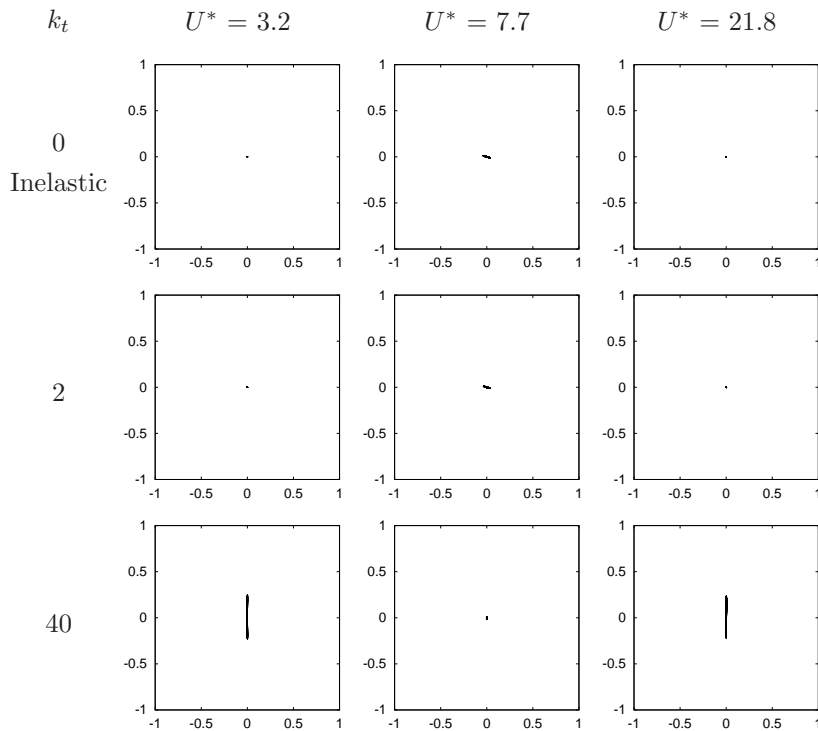


FIGURE 6.18: Trajectory in xy coordinate with varying k_t . The abscissa is x and the ordinate is y for each subfigure. Flow is coming from left.

ever, when the tether is supercritically elastic ($k_t = 40$), the sphere oscillation in the y direction has an amplitude of about $0.25D$ when $U^* = 3.2$ and 21.8 . When $U^* = 7.7$, the sphere with an elastic tether ($k_t = 40$) shows no oscillation in either the x or y directions. Note that the main direction of oscillation for the inelastically tethered sphere is the third (z) direction.

The phase plots of total forces ($C_x - C_y$) in the xy plane are given in figure 6.19. The phase plots for each k_t and U^* show lengths proportional to those of the xy trajectory, except at $U^* = 3.2$ for $k_t = 0$ and 2 . The apparent irregular pattern of $C_x - C_y$ at $U^* = 3.2$ is due to the inelastic or subcritically elastic tether at the low reduced velocity and the layover angle.

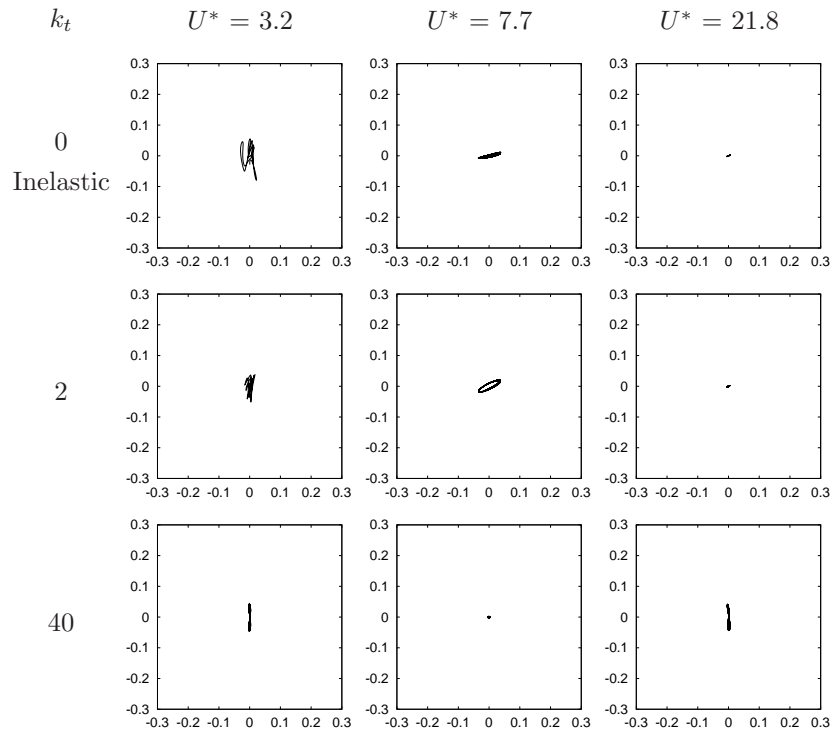


FIGURE 6.19: Phase plot of total forces ($C_x - C_y$) in xy coordinate with varying k_t . The abscissa is C_x and the ordinate is C_y for each subfigure.

Figure 6.20 shows the sphere trajectories in the zx plane. For the range of $U^* = 1 - 34$, the sphere oscillates predominantly in the z direction when inelastically tethered ($k_t = 0$). Due to the predominant z oscillation for buoyant spheres resulting from the gravitational restoring force, some previous experimental studies on VIV of the tethered sphere have focused on the oscillation in the zx plane (Govardhan & Williamson 2005; Jauvtis *et al.* 2001). However, an elastically tethered sphere oscillates in the z direction only

at the intermediate reduced velocities, for example $U^* = 7.7$, when k_t is supercritical. Note that the elastically tethered sphere ($k_t = 40$) oscillates predominantly in the y direction at $U^* = 3.2$ and 21.8, as shown in figure 6.18.

As was reported in previous studies (Govardhan & Williamson 1997; Williamson & Govardhan 1997; Jauvtis *et al.* 2001; Govardhan & Williamson 2005), the zx trajectories with $k_t = 0$ and 2 exhibit a figure-of-eight pattern with much larger z amplitude. It is also known that the aspect ratio of the figure-of-eight trajectory is dependent on the mass ratio (m^*); the sphere of large m^* shows a figure-of-eight pattern of large aspect ratio. For the $k_t = 40$ case, the oscillation amplitude at $U^* = 7.7$ observed in the trajectory is smaller than that for the $U^* = 0$ and 2 cases, as expected from figure 6.16.

The phase plots of the total forces ($C_z - C_x$) in the z and x directions are presented in figure 6.21. The size and pattern of the phase plot of the forces are proportional to the corresponding zx trajectory except at $U^* = 3.2$ for $k_t = 0$ and 2. The irregular pattern of $C_z - C_x$ at $U^* = 3.2$ is due to the inelastic or subcritically elastic tether at the low reduced velocity and the layover angle, as was the case for the xy trajectory and phase plot.

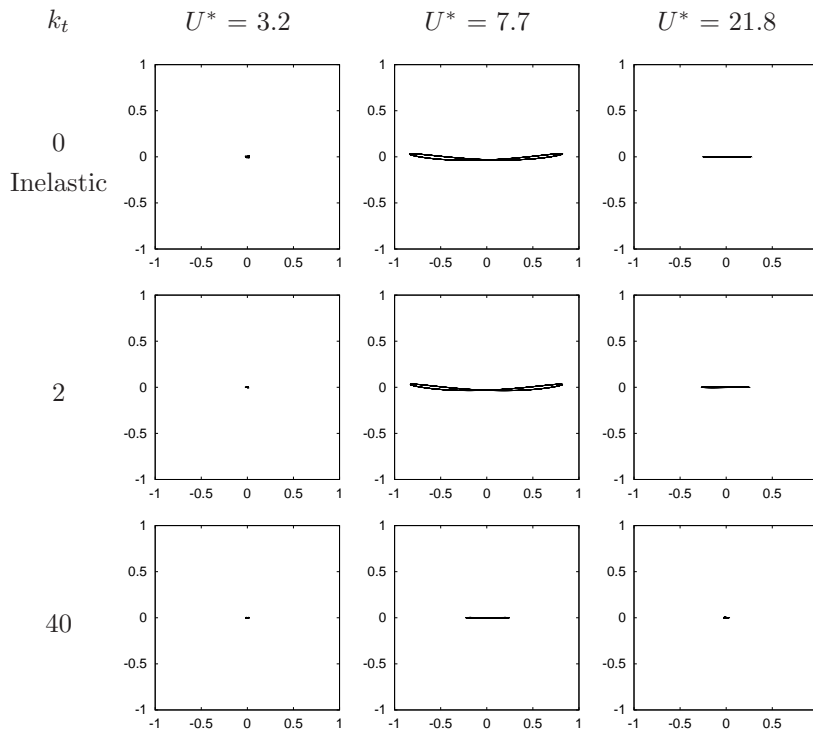


FIGURE 6.20: Trajectory in zx coordinate with varying k_t . The abscissa is z and the ordinate is x for each subfigure. Flow is coming from the bottom.

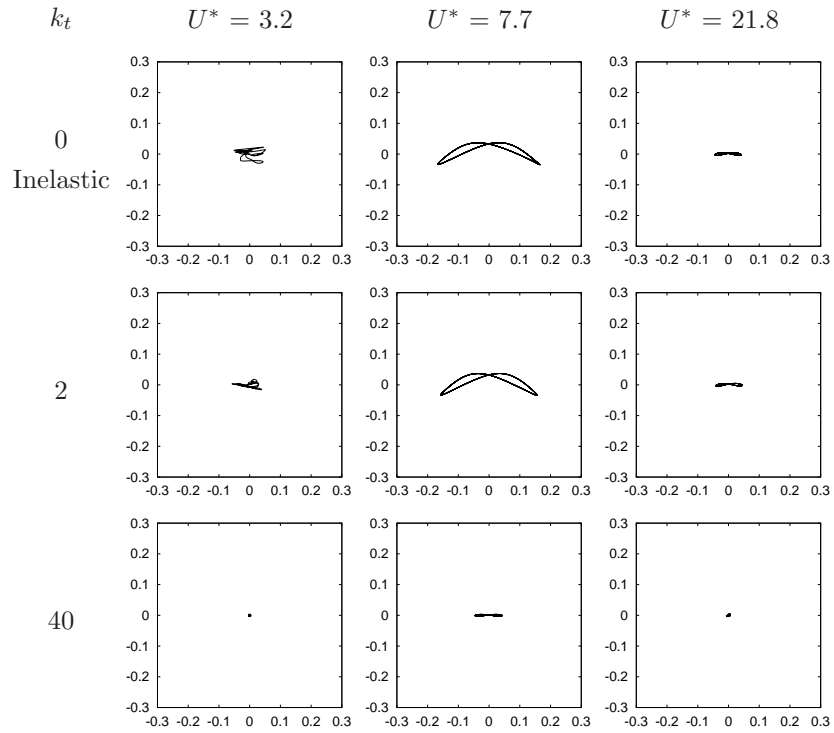


FIGURE 6.21: Phase plot of total forces ($C_z - C_x$) in zx coordinate with varying k_t . The abscissa is C_z and the ordinate is C_x for each subfigure.

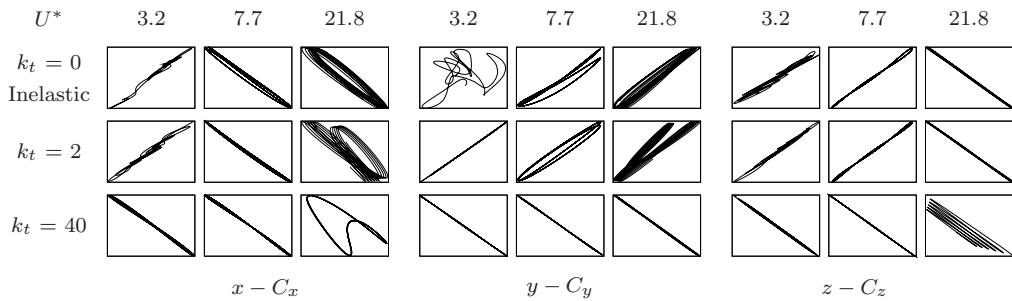


FIGURE 6.22: Phase plot between the displacement and the force. The abscissa is the displacement and the ordinate is the force for each subfigure. The axes are autoscaled to show the pattern more clearly.

Figure 6.22 shows the phase plots between the displacement and the force in both x ($x - C_x$), y ($y - C_y$) and z ($z - C_z$) directions. At each U^* , the inelastic and the $k_t = 2$ cases show essentially the same pattern for all the phase plots. However, the pattern for $k_t = 40$ is different to that for the inelastic and the $k_t = 2$ cases. Therefore, it is clear that the elastically tethered sphere exhibits a different type of VIV when $k_t > 20$, which is the critical value when $m^* = 0.833$ and $L_0 = 10D$.

6.3.3 Vortex structure around the oscillating sphere

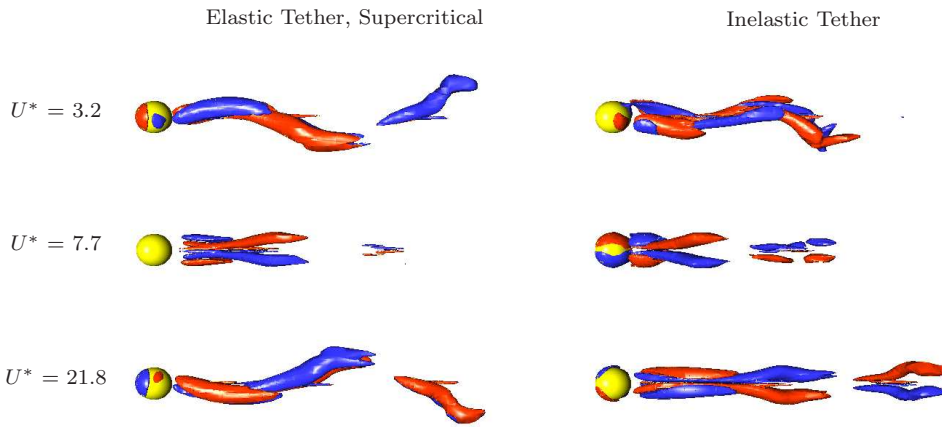


FIGURE 6.23: Streamwise vorticity (xy view) for the elastically tethered sphere ($k_t = 40$) and inelastically tethered sphere at various U^* . The time for each figure is arbitrarily chosen. Flow is coming from left and $Re = 400$.

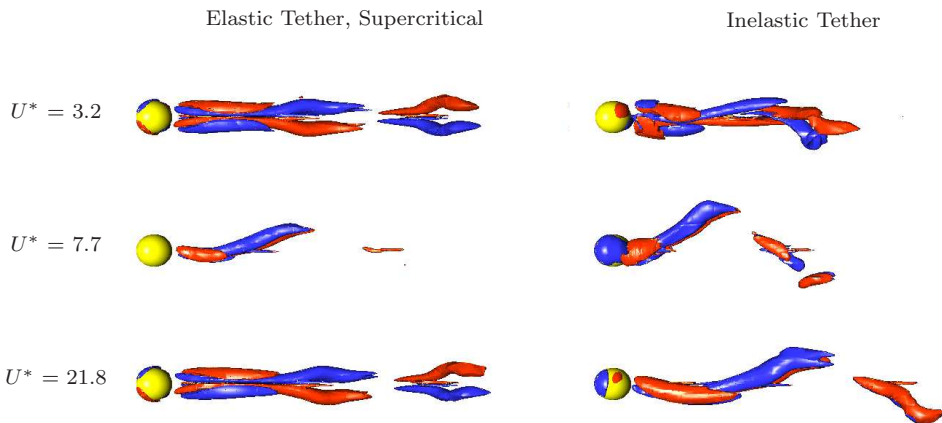


FIGURE 6.24: Streamwise vorticity (zx view) for the elastically tethered sphere ($k_t = 40$) and inelastically tethered sphere at various U^* . The time for each figure is arbitrarily chosen. Flow is coming from left and $Re = 400$.

The vortex structures are rendered by spanwise vorticity and presented in figures 6.23 and 6.24 for the xy view and the zx view, respectively. The main difference in the vortex structure for the inelastic and elastic cases is that, contrary to the inelastic case, the elastically tethered sphere (k_t) maintains planar-symmetry even at low reduced velocities, for example at $U^* = 3.2$. This is clearly shown in the top two subfigures in figure 6.24. These two subfigures demonstrate the higher-amplitude os-

cillation for the supercritically elastic case and the minute oscillation for the inelastic case within the range of $U^* = 1 - 4$.

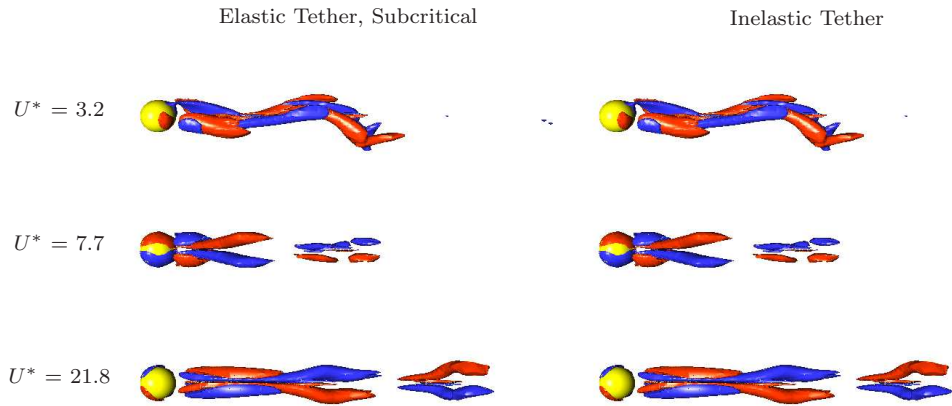


FIGURE 6.25: Streamwise vorticity (xy view) for the elastically tethered sphere ($k_t = 2$) and inelastically tethered sphere at various U^* . The time for each figure is arbitrarily chosen. Flow is coming from left and $Re = 400$.

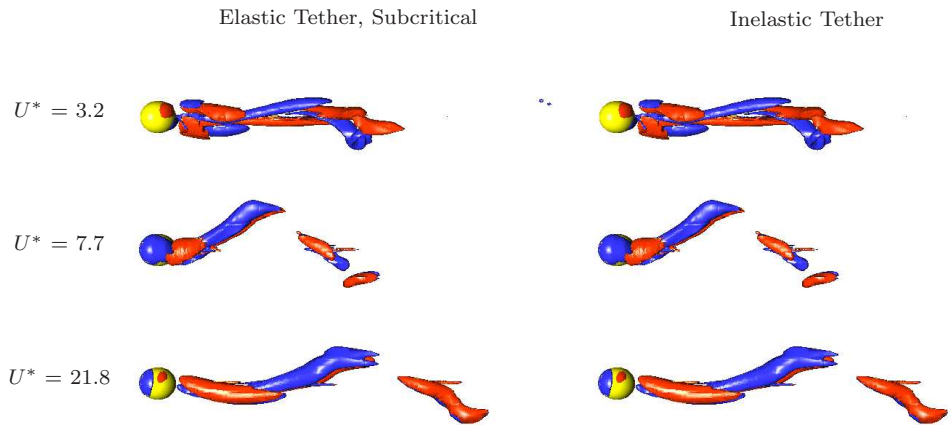


FIGURE 6.26: Streamwise vorticity (zx view) for the elastically tethered sphere ($k_t = 2$) and inelastically tethered sphere at various U^* . The time for each figure is arbitrarily chosen. Flow is coming from left and $Re = 400$.

It is also observed that, within the range $U^* = 5 - 20$, the inelastically tethered sphere oscillates at a higher amplitude than for the other cases. This is indicated by its wider vortex structure in figure 6.24 (see the subfigures for $U^* = 7.7$). One interesting feature is that the oscillation direction is dependent on U^* for the mass ratio considered ($m^* = 0.833$). At high and low reduced velocities, the sphere oscillates mainly in the y direction, while it oscillates mainly in z direction at intermediate reduced velocities,

which is clear from the orientation of the shed vortex structures in figures 6.23 and 6.24.

As was the case of the elastically tethered cylinder, little difference of vortex structure is observed when k_t is subcritical. Figures 6.25 and 6.26 reveal that the vortex structures of a elastically tethered sphere with $k_t = 2$ are almost the same as those of the inelastically tethered sphere at various U^* .

6.4 Chapter Conclusions

The effect of tether elasticity on the VIV of a tethered cylinder and of a tethered sphere is investigated by introducing a linear spring parameter k_t . A mass ratio of $m^* = 0.833$ is chosen both for the cylinder and the sphere to see the effect more clearly and to be consistent with the previous studies of tethered body VIV. A range of reduced velocity $U^* = 1 - 34$ is obtained by changing the parameter α , which is inversely proportional to the square of the Froude number. Only the gravity term is varied allowing the Reynolds number to remain constant and remove its effect on the VIV of the tethered bodies.

For the tethered cylinder, a critical value of the parameter k_t is found to be $k_t = 2$, beyond which the response of the tethered cylinder with an elastic tether greatly differs to that of the inelastically tethered cylinder. The responses of the layover angle and the total RMS value of the oscillation in the x and y directions have been compared, considering their links to the trends of mean C_x and C_y . It is found that, for the elastically tethered cylinder, the trajectory at the low reduced velocities ($U^* = 1 - 4$) shows a figure-of-eight pattern. This is due to the additional freedom to move allowed by the elastic tether. At the low reduced velocities, the elastically tethered cylinder oscillates mainly in the y direction, whereas the cylinder with an inelastic tether oscillates mainly in the x direction with a minute amplitude of oscillation. Due to the large oscillations at low reduced velocities for the elastically tethered cylinder, the wake width is greater than that of the inelastically tethered cylinder. Considering the small difference in the layover angles between the elastic and inelastic cases, it is concluded that this huge difference in vortex structure is due to the change of oscillation direction relative to the tether and from the change of oscillation amplitude.

A critical value of $k_t = 20$ is found for the tethered sphere. However, the responses of the layover angle and the amplitude are different to the cylinder case, particularly in terms of the oscillation amplitude. In the range of $U^* = 5 - 20$, the inelastically teth-

ered sphere exhibits larger amplitude oscillation than that for the elastically tethered sphere when k_t is supercritical. Within the whole range of $U^* = 1 - 34$, the amplitude of the oscillation for the elastically tethered sphere ($k_t = 40$) shows little change, consistent with the same trends of the mean C_x , C_y and C_z . Interestingly, it is found that the sphere oscillates in the y direction at the low and high reduced velocities, whereas the sphere oscillates mainly in the z direction at the intermediate reduced velocities. From the trajectories, it is verified that the tethered sphere with an inelastic tether oscillates mainly in the z direction with a figure-of-eight pattern for the whole U^* range. The main difference in the vortex structure for the inelastic and elastic cases is that, contrary to the inelastic case, the elastically tethered sphere maintains planar-symmetry even at low reduced velocities, for example at $U^* = 3.2$. The vortex structure at the intermediate reduced velocities, for example $U^* = 7.7$, demonstrates the inelastically tethered sphere exhibits a wider wake, consistent with its oscillation amplitude being larger than that for the elastically tethered sphere.

In conclusion, it is found that, both for the cylinder and the sphere, there is a critical value of k_t above which the response is significantly different to that of inelastically tethered bodies. When the k_t exceeds its critical value ($k_t = 2$ for the cylinder and $k_t = 20$ for the sphere), the oscillation amplitude is greatest at low U^* , whereas the amplitude is greatest at high U^* (for the cylinder) or at intermediate U^* (for the sphere) for the inelastic tethered case.

Chapter 7

Conclusions and Future Work

Tethered Cylinders

Numerical simulations of VIV for a neutrally buoyant tethered cylinder have shown that there exist three flow regimes (Regimes I, II and III) in terms of the layover angle ϑ , oscillation amplitude and frequency within the range of Reynolds number $Re = 10-300$.

Regime I covers $10 \leq Re < 40$, and is steady with $\vartheta = 90^\circ$. Regime II exists over $40 \leq Re < 200$, and shows unsteady and periodic oscillation with growing amplitude and frequency as Re increases, whereas ϑ decreases with increasing Re . Regime III, starting at Re 200, exhibits much larger amplitude than that of Regime II, with slowly varying components on its principal oscillation. The frequency of this regime is saturated at $St \approx 0.17$, which is lower than that for a fixed cylinder reported in Williamson (1988a). The history and phase of the displacements and forces in the x and y directions, together with their power spectra, reveal that the principal oscillation in both displacements is dominated by a fluctuating y force C_y , with secondary oscillations affected by subharmonic frequencies of the x force C_x , particularly in Regime II.

Simulations of VIV for buoyant tethered cylinders, where the buoyancy is acting in the y (crossflow) direction, have been carried out to find any similarity or dissimilarity to the neutrally buoyant ($m^* = 1$) case. A range of mass ratios of $m^* = 0.1 - 1.11$ is covered. Similarities to the neutrally buoyant case of the number of regimes, the Re range of each regime and the oscillation frequency are found. However, remarkable differences are also found to exist, particularly in the two oscillating regimes: Regimes II and III. As expected, due to the buoyancy effect, the layover angle is no longer close to 90° , even for the steady Regime I, and decreases continuously across Regime I and II for mass ratios up to 0.5. However, unlike the neutrally buoyant case, the oscillation amplitude grows smoothly across Regime II and III and maintains periodicity in Regime

III. Moreover, there is no subharmonic oscillation in the displacements for Regime II. It is found that the difference in response to the neutrally buoyant case stems from the buoyancy changing the layover angle considerably. Additionally, it is found that there is a critical mass ratio beyond which the response and phase of the forces and displacements change. From the mass ratios considered for the tether length of $10D$, the critical mass ratio exists within $0.5 \leq m^* \leq 0.667$.

VIV of a vertically tethered cylinder where the buoyancy is acting parallel to the flow is also investigated to identify the resemblance to the neutrally buoyant sphere. The vertically tethered cylinder has the same force balance as the neutrally buoyant cylinder except for the difference of magnitude of the force in the x (parallel) direction, and thus might be expected to reveal a close link to the neutrally buoyant cylinder. Virtually the same response, phase portraits and power spectra are observed for the vertically tethered cylinder and the neutrally buoyant cylinder, in particular, featuring a doubling of the figure-of-eight trajectory in the phase plots. Due to effectively increased drag on the vertically tethered cylinder, Regime II starts at a slightly higher Re than the neutrally buoyant case, and the cylinder oscillates periodically at the end of Regime II, whereas the cylinder with neutral buoyancy shows less periodic oscillation with a slowly varying low frequency component. Based on these results, it is concluded that the VIV of a tethered cylinder is dependent not only on the magnitude of buoyancy (i.e. mass ratio) but also on the direction of buoyancy, and VIV of a neutrally buoyant cylinder is closer to that of a vertically tethered cylinder than that of a horizontally tethered buoyant cylinder.

Tethered Spheres

For the neutrally buoyant sphere, both from numerical and experimental studies, it is found that there exist seven different flow regimes within the Reynolds number range of $Re = 50 - 8000$. The transitions for the sphere between the regimes are comparable to those for a fixed sphere, and in the shedding regimes the flow structures exhibit two-sided shedding of hairpin-shaped vortices.

The first regime, Regime I, covers the range of $Re = 50 - 205$, and the sphere remains steady with layover angle $\vartheta = 90^\circ$. Within Regime II, for $Re = 210 - 250$, the flow is steady but asymmetric. Due to this asymmetry, the sphere offsets from the symmetry axis with decreasing layover angles. As Re increases further, the sphere

starts to vibrate at $Re = 270$, the start of Regime III. Regime IV begins at $Re = 300$. It shows a steep decrease of the layover angle indicating the body offsets more from the pivot axis than other regimes. The sphere predominantly oscillates in the azimuthal direction with a frequency of $St = 0.111$, which is close to that of the stationary sphere ($St = 0.134$) but much higher than its natural frequency ($St \approx 0.029$).

In Regime V covering $Re = 335 - 500$, the layover angle comes back to $\vartheta = 90^\circ$, and the sphere oscillates predominantly in the radial direction with increasing amplitude as Re increases. The frequency of the radial displacement for Regime V is 0.104, and is also close to, but less than, that of the fixed sphere ($St = 0.134$). In Regime VI, the vibrations become chaotic and the sphere undertakes chaotic wandering, having no restoring forces. The range of Re for Regime VI covers both simulations and experiments, and the existence of the regime is verified by observing the irregular pattern in the experiments. In Regime VII ($Re \geq 3000$), the oscillation becomes quasi-circular following an irregular pattern. As Re is raised further, the sphere motion exhibits more clearly a circular shape.

The effect of changing the mass ratio has been examined for the mass ratios of $m^* = 0.909$ and 0.667. Response characteristics within the regimes, even though the corresponding Re ranges are dependent on the mass ratio, are similar to that of a neutrally buoyant tethered sphere for all the mass ratios considered. On the other hand, a neutrally buoyant tethered sphere also exhibits a difference in oscillation response to that of a buoyant tethered sphere, in particular for Regime III ($Re = 270 - 300$) and Regime VII ($Re > 3000$). The difference becomes even more evident when the simulations for a vertically tethered sphere are considered.

A comparison between the three types of tethering (horizontal tethering, vertical tethering, and the tethering a neutrally buoyant sphere) reveals that VIV of a neutrally buoyant tethered sphere is closer to that of a non-buoyant tethered sphere with vertical tethering. This is confirmed by finding the *quasi-circular* motion both for the neutrally buoyant tethered sphere and the vertically tethered heavy sphere. This motion results from the similarity of the force balance and the relative magnitude of the forces acting on the sphere. By analysing the phase plots between the force and the displacement, it is also found that the pattern of the trajectory depends on the relative magnitude of the mean forces in each direction, as these mean forces decide the level of force fluctuations.

Simulations for a buoyant sphere at several Reynolds numbers have been conducted.

It is found that the amplitude of oscillation shows dependence on the Reynolds number. The peak amplitude and the range of high-amplitude regime involving $U^* = 5$ undergo a significant change as Re increases. Importantly, the amplitude response at the highest $Re = 800$ shows similarity to that of previous experimental studies at much higher Re within $U^* = [1, 30]$. Based on this, it is highly likely that the difference in amplitude response between the simulations and the experiments for VIV of tethered bodies is due to the difference in the Re ranges.

Elastic Tethers

The effect of tether elasticity on VIV of a tethered cylinder and of a tethered sphere is investigated by introducing a linear spring parameter k_t . A range of reduced velocity $U^* = 1 - 34$ is investigated at fixed Reynolds numbers $Re = 200$ (cylinder) and 400 (sphere).

For the tethered cylinder, a critical value of the parameter k_t is found to be $k_t = 2$, beyond which the response of the tethered cylinder with an elastic tether greatly differs to that of an inelastically tethered cylinder. For the elastically tethered cylinder, the trajectory at the low reduced velocities ($U^* = 1 - 4$) shows a figure-of-eight pattern. This is due to the additional freedom to move allowed by the elastic tether. At these low reduced velocities, the elastically tethered cylinder oscillates mainly in the y direction, whereas the cylinder with an inelastic tether oscillates mainly in the x direction with a minute amplitude of oscillation. Due to the large oscillations at low reduced velocities for the elastically tethered cylinder, the wake width is greater than that of the inelastically tethered cylinder. Considering the small difference in the layover angles between the elastic and inelastic cases, it is concluded that this huge difference in vortex structure is due to the change of oscillation direction relative to the tether and from the change of oscillation amplitude.

Similar to the cylinder case, a critical value of $k_t = 20$ is found for the tethered sphere. However, the responses of the layover angle and the amplitude are different to the cylinder case, particularly in terms of the oscillation amplitude. In the range of $U^* = 5 - 20$, the inelastically tethered sphere exhibits larger amplitude than that for the elastically tethered sphere when k_t is supercritical. Within the whole range of $U^* = 1 - 34$, the amplitude of the oscillation for the elastically tethered sphere ($k_t = 40$) shows little change, consistent with the same trends of the mean C_x , C_y and

C_z . Interestingly, it is found that the sphere oscillates in the y direction at the low and high reduced velocities, whereas the sphere oscillates mainly in the z direction at the intermediate reduced velocities. From the trajectories, it is verified that the tethered sphere with an inelastic tether oscillates mainly in the z direction with a figure-of-eight pattern for the whole U^* range. The vortex structure for the elastically tethered sphere maintains planar-symmetry even at low reduced velocities, whereas that of the inelastically tethered sphere is asymmetric.

In conclusion, it is found that, both for the cylinder and the sphere, there is a critical value of k_t above which the response is significantly different to that of inelastically tethered bodies. When the k_t exceeds its critical value ($k_t = 2$ for the cylinder and $k_t = 20$ for the sphere), the oscillation amplitude is greatest at low U^* , whereas the amplitude is greatest at high U^* (for the cylinder) or at intermediate U^* (for the sphere) for the inelastic tethered case.

Possible Future Work

From this thesis, several findings have been reported that present potential areas of future studies. These include:

- A more detailed study regarding the effect of the Reynolds number on VIV of tethered sphere. Even though the results in chapter 5 indicate an Re effect on the amplitude of oscillation, further studies at higher Re are needed to quantify the effect. This could be done numerically using the Large Eddy Simulation (LES) or Detached Eddy Simulation (DES) as the range of $Re > 10^4$ is well beyond the range for the Direct Numerical Simulation (DNS). Of course, this approach would prove expensive, as both long evolution times and high mesh resolutions are required. Naturally, experimental studies are another way to obtain the high- Re data. A disadvantage is that it is difficult to have independent control of both the reduced velocity and the Reynolds number.
- Stability studies to identify the transitions between the regimes. As this thesis has focused on VIV, i.e., the response of a neutrally buoyant cylinder or sphere and the differences from the response of buoyant tethered bodies, investigating flow transitions and the transition mechanisms would be interesting follow-up studies. Floquet stability analysis and/or Stuart-Landau modelling for the neutrally

buoyant tethered bodies could quantify and elucidate the transitions found in the present study.

- Broader investigation into the effect of elasticity. The studies presented here are restricted in the choice of the spring parameter values selected. Especially for a tethered sphere, the initial investigation on the effect of varying the spring parameter indicated a rich response behaviour, with signs of a direct resonance response at the natural shedding frequency and its first harmonic, as well as an enhanced response at much higher values of the spring parameter. There was also considerable dependence on Reynolds number. It would certainly be interesting to repeat some simulations at considerably higher Reynolds numbers (at least $Re = 800$) to further investigate the response.
- Nonlinearity of the tether elasticity. Remarkable differences in the tethered body response have been presented in chapter 6 when elasticity is introduced to the tether through a linear spring force. As tethering using an elastic tether occurs in real applications, it would be worthwhile to extend this study to consider a nonlinear spring force.

The research directions explored in this thesis are applicable to broader areas. One is ocean and offshore engineering. Offshore exploration is continually moving to deeper sea floors in search of energy resources, which means an understanding of fluid-structure interaction is more crucial than ever. For example, tethered bodies such as deep sea risers connecting between the sea surface platforms and the ocean floor are of considerable importance in extracting subsea resources. Another area where the present research may be beneficial is the fast-growing area of biological engineering, in particular, modelling of circulation processes inside human bodies. For example, white blood cells use tethering to attach to blood vessels walls as part of the immune response, as do much smaller platelets, essential to the clotting response.

Bibliography

- ACHENBACH, E. 1972 Experiments on the flow past spheres at very high Reynolds numbers. *J. Fluid Mech.* **54**, 565–575.
- ACHENBACH, E. 1974 Vortex shedding from spheres. *J. Fluid Mech.* **62**, 209–221.
- ANGRILLI, F., DISILVIO, G. & ZANARDO, A. 1974 *Flow-Induced Structural Vibrations*, chap. Hydroelasticity study of a circular cylinder in a water stream, pp. 502–512. Berlin: Springer Verlag.
- BARKLEY, D. & HENDERSON, R. D. 1996 Three-dimensional Floquet stability analysis of the wake of a circular cylinder. *J. Fluid Mech.* **322**, 215–241.
- BEARMAN, P. W. 1984 Vortex shedding from oscillating bluff bodies. *Annu. Rev. Fluid Mech.* **16**, 195–222.
- BENARD, H. 1908 Formation de centres de giration a l’arriere d’un obstacle en mouvement. *C.R. Acad. Sci. Paris* **147**, 839.
- BISHOP, R. & HASSAN, A. 1964 The lift and drag forces on a circular cylinder in a flowing fluid. *Proc. R. Soc. Lond. Ser. A* **277**, 51–75.
- BLACKBURN, H. & HENDERSON, R. 1999 A study of two-dimensional flow past an oscillating cylinder. *J. Fluid Mech.* **385**, 255–286.
- BLACKBURN, H. M., GOVARDHAN, R. & WILLIAMSON, C. H. K. 2001 A complementary numerical and physical investigation of vortex-induced vibration. *J. Fluids Struct.* **15**, 481–488.
- BLACKBURN, H. M. & LOPEZ, J. M. 2003 On three-dimensional quasi-periodic Floquet instabilities of two-dimensional bluff body wakes. *Phy. Fluids* **15** (8), L57–L60.
- BLACKBURN, H. M., MARQUES, F. & LOPEZ, J. M. 2005 Symmetry breaking of two-dimensional time-periodic wakes. *J. Fluid Mech.* **522**, 395–411.
- BRÜCKER, C. 2001 Spatio-temporal reconstruction of vortex dynamics in axisymmetric wakes. *J. Fluids Struct.* **15**, 543–554.

- CANUTO, C., HUSSAINI, M. Y., QUARTERONI, A. & ZANG, T. A. 2006 *Spectral Methods - Fundamentals in Single Domains*. Springer Verlag.
- CARBERRY, J., GOVARDHAN, R., SHERIDAN, J., ROCKWELL, D. & WILLIAMSON, C. H. K. 2004 Wake states and response branches of forced and freely oscillating cylinders. *Euro. J. Mech. B/Fluids* **23**, 89–97.
- CARBERRY, J. & SHERIDAN, J. 2007 Wake states of a tethered cylinder. *J. Fluid Mech.* **592**, 1–21.
- CHESTER, W. & BREACH, D. R. 1969 On the flow past a sphere at low Reynolds number. *J. Fluid Mech.* **37**, 751–760.
- CHOMAZ, J. M., BONNETON, P. & HOPFINGER, E. J. 1993 The structure of the near wake of a sphere moving horizontally in a stratified field. *J. Fluid Mech.* **254**, 1–21.
- DENNIS, S. C. R. & WALKER, J. D. A. 1971 Calculation of the steady flow past a sphere at low and moderate Reynolds numbers. *J. Fluid Mech.* **48**, 771–789.
- DUŠEK, J., FRAUNIÉ, P. & LE GAL, P. 1994 A numerical and theoretical study of the first Hopf bifurcation in a cylinder wake. *J. Fluid Mech.* **264**, 59–80.
- FENG, C. C. 1968 The measurement of vortex-induced vibrations of a long flexible circular cylinder. Master's thesis, University of British Columbia, Vancouver, Canada.
- GERRITSMAN, M. & PHILLIPS, T. 2000 Spectral element methods for axisymmetric Stokes problems. *J. Comp. Phys.* **164**, 81–103.
- GHIDERSA, B. & DUŠEK, J. 2000 Breaking of axisymmetry and onset of unsteadiness in the wake of a sphere. *J. Fluid Mech.* **423**, 33–69.
- GOTTLIEB, D. & ORSZAG, S. 1977 *Numerical Analysis of Spectral Methods: Theory and Applications*. Philadelphia: SIAM.
- GOTTLIEB, O. 1997 Bifurcations of a nonlinear small-boby ocean-mooring system excited by finite-amplitude waves. *Trans. ASME J. Offshore Mech. Arctic Eng.* **119**, 234–238.
- GOVARDHAN, R. & WILLIAMSON, C. H. K. 1997 Vortex-induced motions of a tethered sphere. *J. Wind Eng. Ind. Aerodyn.* **69–71**, 375–385.
- GOVARDHAN, R. & WILLIAMSON, C. H. K. 2000 Modes of vortex formation and frequency response of a freely vibrating cylinder. *J. Fluid Mech.* **420**, 85–130.
- GOVARDHAN, R. & WILLIAMSON, C. H. K. 2003 Resonance forever: existence of a critical mass and an infinite regime of resonance in vortex-induced vibration. *J. Fluid Mech.* **473**, 147–166.

- GOVARDHAN, R. & WILLIAMSON, C. H. K. 2005 Vortex-induced vibrations of a sphere. *J. Fluid Mech.* **531**, 11–47.
- GRIFFIN, O. M. & RAMBERG, S. E. 1982 Some recent studies of vortex shedding with application to marine tubulars and risers. *Trans. ASME J. Energy Resour. Tech.* **104**, 2–13.
- HARLEMANN, D. & SHAPIRO, W. 1961 The dynamics of a submerged moored sphere in oscillatory waves. *Coastal Eng.* **2**, 746–765.
- HARTUNIAN, R. A. & SEARS, W. R. 1957 On the instability of small gas bubbles moving uniformly in various liquids. *J. Fluid Mech.* **3**, 27–47.
- HENDERSON, R. D. 1997 Non-linear dynamics and pattern formation in turbulent wake transition. *J. Fluid Mech.* **352**, 65–112.
- HOPF, E. 1942 Abzweigung einer periodischen Lösung von einer stationären Lösung eines differentialsystems. *Bericht der Math.-Phys. Klasse der Sächsischen Akademie der Wissenschaften zu Leipzig* **94**, 3–22.
- JAUVTIS, N., GOVARDHAN, R. & WILLIAMSON, C. H. K. 2001 Multiple modes of vortex-induced vibrations of a sphere. *J. Fluids Struct.* **15**, 555–563.
- JAUVTIS, N. & WILLIAMSON, C. H. K. 2003 Vortex-induced vibrations of a cylinder with two degree of freedom. *J. Fluids Struct.* **17**, 1035–1042.
- JAUVTIS, N. & WILLIAMSON, C. H. K. 2004 The effect of two degree of freedom on vortex-induced vibration at low mass and damping. *J. Fluid Mech.* **509**, 32–62.
- JEONG, J. & HUSSAIN, F. 1995 On the identification of a vortex. *J. Fluid Mech.* **285**, 69–94.
- JOHNSON, T. A. & PATEL, V. C. 1999 Flow past a sphere up to a Reynolds number of 300. *J. Fluid Mech.* **378**, 19–70.
- KARNIADAKIS, G. E., ISRAELI, M. & ORSZAG, S. A. 1991 High-order splitting methods of the incompressible NavierStokes equations. *J. Comp. Phys.* **97**, 414–443.
- KARNIADAKIS, G. E. & SHERWIN, S. J. 2005 *Spectral/hp methods for computational fluid dynamics*. Oxford: Oxford University Press.
- KARNIADAKIS, G. E. & TRIANTAFYLLOU, G. S. 1992 Three-dimensional dynamics and transition to turbulence in the wake of bluff objects. *J. Fluid Mech.* **238**, 1–30.
- KHALAK, A. & WILLIAMSON, C. H. K. 1997 Fluid forces and dynamics of a hydroelastic structure with very low mass and damping. *J. Fluids Struct.* **11**, 973–982.

- KHALAK, A. & WILLIAMSON, C. H. K. 1999 Motions, forces and mode transitions in vortex-induced vibrations at low mass-damping. *J. Fluids Struct.* **13**, 813–851.
- KIM, D. & CHOI, H. 2002 Laminar flow past a sphere rotating in the streamwise direction. *J. Fluid Mech.* **461**, 365–386.
- KIM, H. J. & DURBIN, P. A. 1988 Observations of the frequencies in a sphere wake and of drag increase by acoustic excitation. *Phys. Fluids* **31** (11), 3260–3265.
- KIM, I. & PEARLSTEIN, A. J. 1990 Stability of the flow past a sphere. *J. Fluid Mech.* **211**, 73–93.
- KING, R. 1974 Vortex excited oscillations of a circular cylinder in steady currents. In *Proc. Offshore Technology Conference (OTC)*. Houston, Texas, U.S.A.
- LEE, H., THOMPSON, M. C. & HOURIGAN, K. 2008 Vortex-induced vibrations of a tethered sphere with neutral buoyancy. In *Proc. XXII Int. Cong. Theo. Appl. Mech.*, p. 11299. Adelaide, Australia.
- LEONTINI, J. S. 2007 A numerical investigation of transversely-oscillating cylinders in two-dimensional flow. PhD thesis, Monash University, Melbourne, Australia.
- LEONTINI, J. S., THOMPSON, M. C. & HOURIGAN, K. 2007 Three-dimensional transition in the wake of a transversely oscillating cylinder. *J. Fluid Mech.* **577**, 79–104.
- LEWEKE, T., PROVANSAL, M., ORMIÈRES, D. & LEBESCOND, R. 1999 Vortex dynamics in the wake of a sphere. *Phys. Fluids* **11** (9), S12.
- LUNDE, K. & PERKINS, R. 1997 Observations on wakes behind spheroidal bubbles and particles. In *Proc. ASME Fluids Eng. Div. Summer Meeting*, pp. 97–3530. Vancouver, Canada.
- LUNDE, K. & PERKINS, R. 1998 Shape oscillations of rising bubbles. *Appl. Sci. Res.* **58**, 387–408.
- MAGARVEY, R. H. & BISHOP, R. L. 1961a Transition ranges for three-dimensional wakes. *Canadian J. Phy.* **39**, 1418–1422.
- MAGARVEY, R. H. & BISHOP, R. L. 1961b Wakes in liquid-liquid systems. *Phys. Fluids* **4**, 800–805.
- MAGARVEY, R. H. & MACLATCHY, C. S. 1965 Vortices in sphere wakes. *Canadian J. Phy.* **43**, 1649–1656.
- MARQUES, F., LOPEZ, J. M. & BLACKBURN, H. M. 2004 Bifurcations in systems with Z2 spatio-temporal and O(2) spatial symmetry. *Physica D* **189**, 247–276.

- MEIRON, D. I. 1989 On the stability of gass bubbles rising in inviscid fluid. *J. Fluid Mech.* **198**, 101–114.
- MERCIER, J., LYRIO, A. & FORSLUND, R. 1973 Three-dimensional study of the non-rectilinear trajectory of air bubbles rising in water. *Trans. ASME J. Appl. Mech.* **40**, 650–654.
- MITTAL, R. 1999a A Fourier-Chebyshev spectral collocation method for simulating flow past spheres and spheroids. *Int. J. Num. Meth. Fluids* **30**, 921–937.
- MITTAL, R. 1999b Planar symmetry in the unsteady wake of a sphere. *AIAA J.* **37**, 388–390.
- MOE, G. & WU, Z. J. 1990 The lift force on a cylinder vibrating in a current. *Trans. ASME J. Fluids Eng.* **112**, 297–303.
- MONKEWITZ, P. A. 1996 Modeling of self-excited wake oscillations by amplitude equations. *Exp. Therm. Fluid Sci.* **12**, 175–183.
- MORISON, J. R., O'BRIEN, M. P., JOHNSON, J. W. & SCHAAF, S. A. 1950 The force exerted by surface waves on piles. *Petroleum Trans.* **189**, 149–157.
- MOUGIN, G. & MAGNAUDET, J. 2002 Path instability of a rising bubble. *Phys. Rev. Lett.* **88**, 014502.
- MUNSON, B., YOUNG, D. & OKIISHI, T. H. 2006 *Fundamentals of fluid mechanics*. John Wiley and Sons.
- NATARAJAN, R. & ACRIVOS, A. 1993 The instability of the steady flow past spheres and disks. *J. Fluid Mech.* **254**, 323–344.
- NOACK, B. & ECKELMANN, H. 1994 A low-dimensional Galerkin method for the three-dimensional flow around a circular cylinder. *Phys. Fluids* **6**, 124–143.
- ONGOREN, A. & ROCKWELL, D. 1988 Flow structure from an oscillating cylinder. Part 2. mode competition in the near wake. *J. Fluid Mech.* **191**, 225–245.
- ORMIÈRES, D. & PROVANSAL, M. 1999 Transition to turbulence in the wake of a sphere. *Phys. Rev. Lett.* **83**, 80–83.
- PREGNALATO, C. J. 2003 The flow-induced vibrations of a tethered sphere. PhD thesis, Monash University, Melbourne, Australia.
- PROUDMAN, I. & PEARSON, J. R. A. 1957 Expansions at small Reynolds numbers for the flow past a sphere and a circular cylinder. *J. Fluid Mech.* **2**, 237–262.
- PROVANSAL, M., MATHIS, C. & BOYER, L. 1987 Bénard-von Kármán instability: transient and forced regimes. *J. Fluid Mech.* **182**, 1–22.

- PROVANSAL, M., SCHOUVEILER, L. & LEWEKE, T. 2004 From the double vortex street behind a cylinder to the wakes of a sphere. *Euro. J. Mech. B/Fluids* **23**, 65–80.
- RAYLEIGH, L. 1879 Acoustical observations II. *Philosophical Magazine* **VII**, 149–162.
- RIMON, Y. & CHENG, S. I. 1969 Numerical solutions of a uniform flow over a sphere at intermediate Reynolds numbers. *J. Fluid Mech.* **12** (5), 949–959.
- ROOS, F. W. & WILLMARTH, W. W. 1971 Some experimental results on sphere and disk drag. *AIAA J.* **9**, 285–291.
- ROSHKO, A. 1954 On the development of turbulent wakes from vortex streets. *Tech. Rep.* 1191. NACA Report.
- ROSHKO, A. 1993 Perspectives on bluff body aerodynamics. *J. Wind Eng. Ind. Aerodyn.* **49**, 79–100.
- RYAN, K. 2004 The analysis of wake structures behind stationary, freely oscillating and tethered cylinders. PhD thesis, Monash University, Melbourne, Australia.
- RYAN, K., PREGNATALATO, C. J., THOMPSON, M. C. & HOURIGAN, K. 2004a Flow-induced vibrations of a tethered circular cylinder. *J. Fluids Struct.* **19**, 1085–1102.
- RYAN, K., THOMPSON, M. C. & HOURIGAN, K. 2004b Vortex structures in the wake of a buoyant tethered cylinder at moderate to high reduced velocities. *Euro. J. Mech. B/Fluids* **23**, 127–135.
- RYAN, K., THOMPSON, M. C. & HOURIGAN, K. 2005 Variation in the critical mass ratio of a freely oscillating cylinder as a function of Reynolds number. *Phys. Fluids* **17**, 038106.
- RYAN, K., THOMPSON, M. C. & HOURIGAN, K. 2007 The effect of mass ratio and tether length on the flow around a tethered cylinder. *J. Fluid Mech.* **591**, 117–144.
- SAFFMAN, P. G. 1956 On the rise of small air bubbles in water. *J. Fluid Mech.* **1**, 249–275.
- SANCHIS, A., SALEVIK, G. & GRUE, J. 2008 Two-degree-of-freedom vortex-induced vibrations of a spring-mounted rigid cylinder with low mass ratio. *J. Fluids Struct.* **24**, 907–919.
- SARPKAYA, T. 1979 Vortex-induced oscillations. *Trans. ASME J. Appl. Mech.* **46**, 241–258.
- SARPKAYA, T. 1986 Force on a circular cylinder in viscous oscillatory flow at low Keulegan-Carpenter numbers. *J. Fluid Mech.* **165**, 61–71.

- SARPKAYA, T. 1995 Hydrodynamic damping, flow-induced oscillations, and biharmonic response. *Trans. ASME J. Offshore Mech. Arctic Eng.* **117**, 232–238.
- SCHOUVEILER, L. & PROVANSAL, M. 2002 Self-sustained oscillations in the wake of a sphere. *Phys. Fluids* **14**, 3846–3854.
- SHEARD, G. J., THOMPSON, M. C. & HOURIGAN, K. 2003 From spheres to circular cylinders: The stability and flow structures of bluff ring wakes. *J. Fluid Mech.* **492**, 147–180.
- SHEW, W. L., PONCET, S. & PINTON, J.-F. 2006 Force measurements on rising bubbles. *J. Fluid Mech.* **569**, 51–60.
- SHI-IGAI, H. & KONO, T. 1969 Study on vibration of submerged spheres caused by surface waves. *Coastal Engineering Japan* **12**, 29–40.
- SHIELS, D., LEONARD, A. & ROSHKO, A. 2001 Flow-induced vibrations of a circular cylinder at limiting structure parameters. *J. Fluids Struct.* **15**, 3–21.
- STOKES, G. G. 1851 On the effect of the internal friction of fluids on the motion of pendulums. *Trans. Cambridge Phil. Soc.* **9**, 8–106.
- STROUHAL, V. 1878 Uber eine besondere art der tonerregung. *Annu. Phys. und Chemie* **5 (New Series)**, 216–251.
- STUART, J. 1958 On the non-linear mechanics of hydrodynamic instability. *J. Fluid Mech.* **4**, 1–21.
- STUART, J. 1960 On the non-linear mechanics of wave disturbances in stable and unstable parallel flows. Part 1: The basic behaviour in plane Poiseuille flow. *J. Fluid Mech.* **9**, 353–370.
- TANEDA, S. 1956 Experimental investigation of the wakes behind cylinders and plates at low Reynolds numbers. *J. Phys. Soc. Japan* **11**, 302–307.
- TANEDA, S. 1978 Visual observations of the flow past a sphere at Reynolds numbers between 10^4 and 10^6 . *J. Fluid Mech.* **85**, 187–192.
- THOMPSON, M. C., HOURIGAN, K. & SHERIDAN, J. 1995 Three-dimensional mode development in low reynolds number flow over a cylinder. In *Proc. 12th Australasian Fluid Mech. Conf.*, pp. 513–516. Sydney, Australia.
- THOMPSON, M. C., HOURIGAN, K. & SHERIDAN, J. 1996 Three-dimensional instabilities in the wake of a circular cylinder. *Exp. Therm. Fluid Sci.* **12**, 190–196.
- THOMPSON, M. C. & LE GAL, P. 2004 The Stuart–Landau model applied to wake transition revisited. *Euro. J. Mech B/Fluids* **23**, 219–228.

- THOMPSON, M. C., LEWEKE, T. & PROVANSAL, M. 2001 Kinematics and dynamics of sphere wake transition. *J. Fluids Struct.* **15**, 575–585.
- TOMBOULIDES, A. G. & ORSZAG, S. A. 2000 Numerical investigation of transitional and weak turbulent flow past a sphere. *J. Fluid Mech.* **416**, 45–73.
- TOMBOULIDES, A. G., ORSZAG, S. A. & KARNIADAKIS, G. E. 1993 Direct and large-eddy simulation of axisymmetric wakes. *Tech. Rep.* 93-0546. AIAA Paper.
- TRITTON, D. 1970 A note on vortex streets behind circular cylinders at flow Reynolds numbers. *J. Fluid Mech.* **45**, 203–208.
- VAN DYKE, M. 1982 *An Album of Fluid Motion*. Stanford: Parabolic Press.
- VON KÁRMÁN, T. 1911 Über den mechanismus des widerstands, den ein bewegter Körper in einer Flüssigkeit erfährt. *Göttingen Nach. Math. Phys. Kl.* pp. 509–519.
- WARBURTON, T. C. & KARNIADAKIS, G. E. 1996 The wake of an oscillating cylinder close to a free surface. *Buul. Amer. Phys. Soc.* **41**, 1732.
- WEGENER, P. P. & PARLANGE, J. Y. 1973 Spherical-cap bubbles. *Annu. Rev. Fluid Mech.* **5**, 79–100.
- WILLIAMSON, C. H. K. 1988a Defining a universal and continuous Strouhal-Reynolds number relationship for the laminar vortex shedding of a circular cylinder. *Phys. Fluids* **31**, 2742–2744.
- WILLIAMSON, C. H. K. 1988b The existence of two stages in the transition to three-dimensionality of a cylinder wake. *Phys. Fluids* **31**, 3165–3168.
- WILLIAMSON, C. H. K. 1989 Oblique and parallel mode of vortex shedding in the wake of a circular cylinder at low Reynolds numbers. *J. Fluid Mech.* **206**, 579–627.
- WILLIAMSON, C. H. K. 1992 The natural and forced formation of spot-like ‘vortex dislocations’ in the transition of a wake. *J. Fluid Mech.* **243**, 393–441.
- WILLIAMSON, C. H. K. 1996a Three-dimensional wake transition. *J. Fluid Mech.* **328**, 345–407.
- WILLIAMSON, C. H. K. 1996b Vortex dynamics in the cylinder wake. *Annu. Rev. Fluid Mech.* **28**, 477–539.
- WILLIAMSON, C. H. K. & BROWN, G. L. 1998 A series in $1 / \sqrt{Re}$ to represent the Strouhal-Reynolds number relationship of the cylinder wake. *J. Fluids Struct.* **12**, 1073–1085.
- WILLIAMSON, C. H. K. & GOVARDHAN, R. 1997 Dynamics and forcing of a tethered sphere in a fluid flow. *J. Fluids Struct.* **11**, 293–305.

- WILLIAMSON, C. H. K. & GOVARDHAN, R. 2004 Vortex-induced vibrations. *Annu. Rev. Fluid Mech.* **36**, 413–455.
- WILLIAMSON, C. H. K. & ROSHKO, A. 1988 Vortex formation in the wake of an oscillating cylinder. *J. Fluids Struct.* **2**, 355–381.
- WU, M. & GHARIB, M. 2002 Experimental studies on the shape and path of small air bubbles rising in clean water. *Phys. Fluids* **14** (7), L49–L52.
- ZDRAVKOVICH, M. M. 1982 Modifications of vortex shedding in the synchronization range. *Trans. ASME J. Fluids Eng.* **104**, 513–517.
- ZHANG, H. Q., FEY, U., NOACK, B. R., KÖNIG, M. & ECKELMANN, H. 1995 On the transition of the cylinder wake. *Phys. Fluids* **7**, 779–794.